The Schwinger model in the canonical formulation

Inaugural dissertation
of the Faculty of Science,
University of Bern

presented by

Patrick Bühlmann

from Ruswil LU

Supervisor of the doctoral thesis:

Prof. Dr. Urs Wenger

Institute for Theoretical Physics
Albert Einstein Center for Fundamental Physics
University of Bern

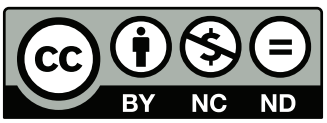

The Schwinger model in the canonical formulation

Inaugural dissertation
of the Faculty of Science,
University of Bern

presented by

Patrick Bühlmann

from Ruswil LU

Supervisor of the doctoral thesis:

Prof. Dr. Urs Wenger

Institute for Theoretical Physics
Albert Einstein Center for Fundamental Physics
University of Bern

Accepted by the Faculty of Science.

Bern, July 26, 2022

The Dean

Prof. Dr. Zoltán Balogh

Abstract

We investigate the Schwinger model in the canonical formulation with fixed fermion numbers. For this, Wilson fermions and a formalism which describes the determinant of the Dirac operator in terms of dimensionally reduced canonical determinants are used. These canonical determinants are built from sums over principal minors of canonical transfer matrices.

We consider the 1-flavour Schwinger model in a regime where the sign problem is absent and investigate several structural properties of the canonical determinants and their transfer matrices.

Next, we discuss the 2-flavour Schwinger model in the canonical formulation. The transfer matrices allow the direct examination of arbitrary multi-particle (meson) sectors and the determination of the corresponding ground state energies. We determine the ground state energies and utilize them to perform some basic scattering theory and investigate finite volume effects in the meson mass. From the 2-meson energies the scattering phase shifts as a function of the volume were determined. Using a low-energy scattering theory, we describe the scattering process in terms of a few physical parameters. We use the scattering phase shifts to solve 3-particle quantization conditions which allow us to make predictions for the 3-meson energies at finite volume. These predictions are compared to direct measurements of the 3-meson energies.

Contents

1 Introduction

In recent years non-perturbative lattice calculations of Quantum Chromodynamics (QCD) at zero density have provided remarkable results. However, lattice simulations for non-zero quark or baryon density remain a problem. At non-zero density the grand-canonical partition function obtains complex-valued weights, which do not allow for standard Monte Carlo importance sampling. These difficulties make it impossible to fully explore the QCD phase diagram [1].

One approach to QCD at finite density is to make use of the canonical formulation, where the net quark number (or baryon number) is fixed. In the canonical formulation, we split the grand-canonical partition function into canonical ones which allow us to investigate the physics of the system with fixed fermion content. Quantities in the standard grand-canonical formulation of QCD can be obtained by averaging over canonical partition functions. The canonical formulation has been used in the context of QCD with staggered and Wilson fermions, see Refs. [2, 3, 4] and [5], respectively, but also in the context of supersymmetric Yang-Mills quantum mechanics [6]. The canonical formalism has also been used as a tool to solve sign problems as in Refs. [7, 8, 9]. The computation of the canonical determinants on the lattice is based on the dimensional reduction of the fermion determinant in terms of transfer matrices [10]. Using those transfer matrices one can construct the canonical determinants, which are the building blocks of the canonical partition functions.

In order to gain a deeper understanding of the canonical formalism we use the Schwinger model as a toy model which allows us to investigate the properties and benefits of the canonical formulation. We define the Schwinger model as Quantum Electrodynamics in two dimensions (QED_2), the number of flavours will be explicitly mentioned. The name Schwinger model originates from Julian Schwinger, who investigated the 1-flavour Schwinger model with massless fermions and presented it as a solvable model in 1962 [11, 12]. In this work we also utilize the 1-flavour variant of the Schwinger model to investigate basic properties of the canonical formulation, before turning to the 2-flavour variant.

The 2-flavour Schwinger model is of great interest since it shares many similarities with Quantum Chromodynamics (QCD), such as confinement, chiral symmetry breaking, charge shielding, and a topological θ-vacuum [13, 14]. We perform numerical calculations in the 2-flavour Schwinger model using the canonical formulation. The corresponding canonical partition functions allow us to investigate the physics of the system at a fixed number of quarks. Those quarks form (multi-)meson states characterized by their isospin content I. Consequently, the lowest-lying energy state in the isospin $I = n$ sector is given by a state of n mesons with maximal isospin. By forming appropriate ratios of canonical partition functions we can determine the ground state energies of those multi-meson states. This allows us to completely circumvent the use of correlators, which become more complex with an increasing number of mesons [15]. In contrast, the complexity for the computation of ground state energies using the canonical formulation is independent of the number of mesons involved.

In this work, we discuss several topics related to the Schwinger model in the canonical formulation. The thesis is written to be as complete and pedagogical as possible, however, for the sake of readability, many details will be postponed to the appendix. The structure is as follows:

In the first part of chapter 2, we introduce the 1- and 2-flavour Schwinger model and consider the most important properties. The second part of the chapter is dedicated to the implementation of the Schwinger model on the Euclidean lattice and the discussion of several effects which arise when discussing a gauge theory on the lattice. In particular, the review of scattering phenomena in a finite periodic box is of major importance for chapter 5.

Chapter 3 is dedicated to the discussion of the Schwinger model in the canonical formulation. We introduce the canonical partition function for the 1-flavour Schwinger model and perform the dimensional reduction on the Wilson Dirac determinant. Next, we present the 2-flavour variant of the Schwinger model in the canonical formalism. We introduce the needed formulas for the extraction of the ground state energies in the different isospin sectors and explain that these (multi-)meson ground states can be identified as (multi-)pion states.

We discuss some qualitative results related to the canonical formalism in chapter 4. First, we compare autocorrelation effects for the topological charge between quenched and dynamical simulations. Next, we turn to the 1-flavour Schwinger model and investigate some interesting quantities related to the intrinsic

structure of the canonical formalism. We finish this chapter by going to the 2-flavour Schwinger model. We show empiric evidence for the one-to-one correspondence between the ground state energies extracted from the canonical formalism and the ground state energies extracted by using π^+, $\pi^+\pi^+$ and $\pi^+\pi^+\pi^+$ correlators.

In chapter 5 we follow up with the main part of this thesis, where we use the extracted (multi-)pion ground state energies to perform some basic pion scattering analysis. To perform scattering in a finite volume L, we start with the extraction of the ground state energy of the isospin $I = 1$ sector yielding the pion mass as a function of the volume $m_\pi(L)$. We calculate $m_\pi(L)$ for a variety of different volumes in order to investigate the finite volume effects on the pion mass and extract interesting parameters, such as the 3-pion coupling. We proceed by measuring the ground state energies of the isospin $I = 2$ sector, which is used to determine the scattering phase shift δ. From the scattering phase shifts we use 3-particle quantization conditions to make predictions for the 3-pion ground state energy $E^{\delta}_{3\pi}(L)$. Finally, we compare these predictions to the direct measurements of the ground state energies in the isospin $I = 3$ sector.

We summarize the results and conclude this thesis in chapter 6.

2 The Schwinger model - 2D QED

In this section we examine the Schwinger model and its properties. We start the discussion by having a look at the continuum model before turning to the discretized Schwinger model on the lattice. The original Schwinger model was first introduced by Julian Schwinger in 1962 who discussed 2-dimensional Quantum Electrodynamics with one massless fermion [11, 12]. The Schwinger Model (respectively QED_2) describes a quantum field theory in $1+1$ dimensions, with a $U(1)$ gauge symmetry. The Lagrangian is given by

$$\mathcal{L}[\bar{\psi},\psi,A_\mu] = \sum_{k=1}^{N_f} \bar{\psi}^k(x)[i\not{D} - m_k]\psi^k(x) - \frac{1}{4}F_{\mu\nu}F^{\mu\nu}, \tag{2.1}$$

where $D_\mu = \partial_\mu + igA_\mu$ is the covariant derivative, g denotes the bare gauge coupling and $\bar{\psi} = \psi^\dagger\gamma_0$ are 2-spinors. The gauge field is described by $A_\mu(x)$ and $F_{\mu\nu} = \partial_\mu A_\nu(x) - \partial_\nu A_\mu(x)$ is the Abelian field strength tensor. The field of the k'th particle is denoted by ψ^k and its corresponding mass by m_k, where k runs over the total number of flavours, $k \in \{1, 2, \ldots, N_f\}$. Since we are dealing with QED in two dimensions the Lorentz indices μ, ν run over 0 and 1. The Schwinger model in Minkowski spacetime uses the metric

$$g = \begin{pmatrix} 1 & 0 \\ 0 & -1 \end{pmatrix} = \mathrm{diag}[1,-1]. \tag{2.2}$$

We construct the γ matrices in terms of Pauli matrices, such that

$$\gamma^0_{\mathrm{M}} = \begin{pmatrix} 1 & 0 \\ 0 & -1 \end{pmatrix} = \sigma_z, \qquad \gamma^1_{\mathrm{M}} = -i\begin{pmatrix} 0 & 1 \\ 1 & 0 \end{pmatrix} = -i\sigma_x, \qquad \text{satisfying } \{\gamma^\mu,\gamma^\nu\} = 2g^{\mu\nu}, \tag{2.3}$$

where the subscript M denotes the fact that we are dealing with γ matrices in Minkowski spacetime. Additionally, one defines the matrix

$$\gamma^5 = \gamma^0\gamma^1 = \sigma_y. \tag{2.4}$$

Due to our choice of γ-matrices γ^0 and γ^5 are hermitian whereas γ^1 is antihermitian, in complete analogy to the 4-dimensional chiral representation (or Weyl representation). One can verify that γ^5 is anticommuting with the other gamma matrices, such that $\{\gamma^\mu,\gamma^5\} = 0$ for $\mu \in \{0,1\}$.

We first discuss the 1-flavour Schwinger model with $N_f = 1$, before turning to the 2-flavour case with $N_f = 2$.

2.1 1-flavour Schwinger model

In this section we have a brief look at the 1-flavour Schwinger model.

Confinement only allows for uncharged particles, therefore the 1-flavour Schwinger model was considered to be a model where the vacuum polarization yields complete charge screening. This was then further discussed by Rothe et al. in Ref. [16] and has become known as "quark trapping". The Lagrangian of the 1-flavour Schwinger model is given by

$$\mathcal{L}[\bar{\psi},\psi,A_\mu] = \bar{\psi}(x)[i\not{D} - m_0]\psi(x) - \frac{1}{4}F_{\mu\nu}F^{\mu\nu}, \tag{2.5}$$

and can be used to compute the Euler-Lagrange equations, which yield the equations of motion

$$\partial_\mu\bar{\psi}\gamma^\mu = ig\bar{\psi}\not{A} + im_0\bar{\psi} \quad \text{and} \quad \not{\partial}\psi = -ig\not{A}\psi - im_0\psi. \tag{2.6}$$

The action of the 1-flavour Schwinger model in Minkowski spacetime is given by

$$S[\bar{\psi},\psi,A_\mu] = \int d^2x\mathcal{L}[\bar{\psi},\psi,A_\mu], \tag{2.7}$$

where we integrate over 2-dimensional spacetime $d^2x = dx^0dx^1$.

2.1.1 Gauge symmetry

To show the local $U(1)$ symmetry we start with the free fermionic action

$$\mathcal{L}[\bar{\psi},\psi] = \bar{\psi}(x)[i\partial\!\!\!/ - m_0]\psi(x). \tag{2.8}$$

This action has a global $U(1)$ symmetry, i.e. a transformation

$$\psi(x) \to G\psi(x), \tag{2.9}$$
$$\bar{\psi}(x) \to \bar{\psi}(x)G^{-1}, \tag{2.10}$$

where $G \in U(1)$ leaves the Lagrangian invariant. The group element G can be written as $G = \mathrm{e}^{i\Lambda}$, where Λ is independent of the spacetime x.

The next step consists in modifying the action in such a way that it becomes invariant under local $U(1)$ transformations i.e. transformations where $\Lambda = \Lambda(x)$. This can be accomplished by introducing a 2-vector potential $A_\mu(x)$, and replacing the ordinary derivative $\partial_\mu = (\frac{\partial}{\partial x^0}, \frac{\partial}{\partial x^1})$ by the covariant one

$$\partial_\mu \to D_\mu = \partial_\mu + igA_\mu(x). \tag{2.11}$$

The Lagrangian then stays invariant if we apply a local $U(1)$ transformation and transform the 2-vector potential $A_\mu(x)$ accordingly

$$\begin{aligned}
&\psi(x) \to G(x)\psi(x),\\
&\bar{\psi}(x) \to \bar{\psi}(x)G(x)^{-1},\\
&A_\mu(x) \to G(x)A_\mu G^{-1}(x) - \frac{i}{g}G(x)\partial_\mu G^{-1}(x),
\end{aligned} \tag{2.12}$$

where $G(x) = e^{i\Lambda(x)}$. Since $G(x)$ is just a $U(1)$ phase, we can simplify the transformation behaviour for the gauge fields A_μ such that

$$A_\mu(x) \to A_\mu(x) - \frac{1}{g}\partial_\mu\Lambda(x). \tag{2.13}$$

We introduced gauge fields to ensure local gauge invariance, but now we also need to add a kinetic term for said gauge fields. This term needs to be invariant under local gauge transformations and is given by

$$-\frac{1}{4}F_{\mu\nu}F^{\mu\nu}, \tag{2.14}$$

which basically leads to our starting point, eq. (2.5). Noether's Theorem tells us that a symmetry also has a corresponding conserved quantity. In this case we obtain the conserved vector current J_V^μ given by

$$J_V^\mu = \bar{\psi}\gamma^\mu\psi, \quad \text{such that} \quad \partial_\mu J_V^\mu = 0. \tag{2.15}$$

2.1.2 Chiral symmetry

We showed that the Schwinger model is constructed in such a way that it has a local $U(1)$ symmetry. However, it also acquires an additional symmetry in the massless limit $m_0 \to 0$. To see this we introduce some new quantities. Consider the orthogonal projectors

$$P_L = \frac{1}{2}(1-\gamma^5) \qquad \text{and} \qquad P_R = \frac{1}{2}(1+\gamma^5), \tag{2.16}$$

satisfying $P_L^2 = P_L$, $P_R^2 = P_R$, $P_L P_R = P_R P_L = 0$, $P_L + P_R = 1$. We decompose the fermion field into a left-handed and a right-handed part where P_L and P_R are the corresponding projection operators, such that

$$\psi = \psi_L + \psi_R, \quad \text{where} \quad \psi_L = P_L\psi \quad \text{and} \quad \psi_R = P_R\psi. \tag{2.17}$$

Using the commutation rules the Lagrangian can be written as

$$\mathcal{L} = \bar{\psi}(iD\!\!\!/ - m_0)\psi - \frac{1}{4}F_{\mu\nu}F^{\mu\nu} \tag{2.18}$$
$$= \bar{\psi}_L iD\!\!\!/\psi_L + \bar{\psi}_R iD\!\!\!/\psi_R - m_0(\bar{\psi}_L\psi_R + \bar{\psi}_R\psi_L) - \frac{1}{4}F_{\mu\nu}F^{\mu\nu}, \tag{2.19}$$

where we used

$$\bar{\psi}\gamma^\mu\psi = \bar{\psi}_L\gamma^\mu\psi_L + \bar{\psi}_R\gamma^\mu\psi_R \quad \text{and} \quad \bar{\psi}\psi = \bar{\psi}_L\psi_R + \bar{\psi}_R\psi_L. \tag{2.20}$$

From the previous expression we can see that the mass term mixes the chiralities. In the chiral limit $m_0 \to 0$, the global $U(1)$ symmetry we had for ψ extends to a separate symmetry for the left-handed and for the right-handed fields ψ_L and ψ_R. The new symmetry group is given by $U(1)_L \times U(1)_R$. Hence in the massless case the global transformations

$$(\bar{\psi}_L, \psi_L) \to (\bar{\psi}_L e^{-i\alpha}, e^{i\alpha}\psi_L) \quad \text{and} \quad (\bar{\psi}_R, \psi_R) \to (\bar{\psi}_R e^{-i\beta}, e^{i\beta}\psi_R) \tag{2.21}$$

leave the action invariant. The corresponding conserved quantities belonging to this symmetry are the left-handed and the right-handed currents given by

$$j_L^\mu = \bar{\psi}\gamma^\mu P_L\psi \quad \text{and} \quad j_R^\mu = \bar{\psi}\gamma^\mu P_R\psi, \tag{2.22}$$

satisfying $\partial_\mu j_L^\mu = 0$ and $\partial_\mu j_R^\mu = 0$. It is useful to form the linear combinations

$$J_V^\mu = j_L^\mu + j_R^\mu = \bar{\psi}\gamma^\mu\psi \quad \text{and} \quad J_A^\mu = j_R^\mu - j_L^\mu = \bar{\psi}\gamma^\mu\gamma^5\psi, \tag{2.23}$$

which are called vector current and axial current. As a result instead of a $U(1)_L \times U(1)_R$ symmetry we work with a $U(1)_V \times U(1)_A$ symmetry in the massless limit. The two currents J_V^μ and J_A^μ are the Noether currents corresponding to the two transformations

$$(\bar{\psi}, \psi) \to (\bar{\psi}e^{-i\Lambda}, e^{i\Lambda}\psi) \quad \text{and} \quad (\bar{\psi}, \psi) \to (\bar{\psi}e^{i\tilde{\Lambda}\gamma^5}, e^{i\tilde{\Lambda}\gamma^5}\psi). \tag{2.24}$$

The first one of these symmetries has already been discussed in the previous section, where we introduced the vector current J_V^μ in eq. (2.15). The second transformation is called a chiral transformation and is a symmetry of the Lagrangian in the massless limit. This can be seen by just carrying out the divergence on j_A^μ and by using the equation of motions given in eq. (2.6). One obtains

$$\partial_\mu j_A^\mu = 2im_0\bar{\psi}\gamma^5\psi, \tag{2.25}$$

which vanishes in the massless limit.

2.1.3 Axial anomaly

Consider a classical field theory which has a symmetry, giving us some conserved quantity. In order to do Quantum Field Theory (from now on QFT) we want to quantize the fields, which means that we impose equal-time-commutation relations on the fields and treat these fields as operators acting on physical states (e.g. the vacuum). When a symmetry is present in the classical theory, but is absent in any regularization of the full QFT, a symmetry is said to be anomalous. We have seen in the previous section that the axial current is conserved in the massless limit

$$\partial_\mu j_A^\mu = 0, \text{ for } m_0 = 0, \tag{2.26}$$

a result which holds true in the classical picture, using classical field theory. However, trying to derive this result from a QFT point of view does not yield the same result, which is a consequence of the so-called chiral anomaly. This anomaly can be derived in different ways, for example by using explicit calculations of loop integrals or by using Ward identities. We give the explicit derivation using Ward identities in appendix G.1, resulting in

$$\partial_\mu j_A^\mu = \frac{g}{2\pi}\epsilon^{\mu\nu}F_{\mu\nu}, \tag{2.27}$$

where $\epsilon^{\mu\nu}$ is the totally antisymmetric tensor in two dimensions with $\epsilon^{01} = +1$.

2.1.4 Properties of the 1-flavour Schwinger model

The 1-flavour model was extensively discussed by Coleman in Refs. [13, 14]. The massless 1-flavour Schwinger model has no free quarks, nor are there any photons, since a $1+1$ dimensional theory does not allow for any transversal modes. Despite starting from a massless theory, it can be shown that there

is a massive free scalar meson η with mass $m_\eta = \frac{g}{\sqrt{\pi}}$. The dynamics of the system can therefore be described by a Hamiltonian, which takes into account the bosonic nature of the theory. The bosonized Hamiltonian[1] of the massless 1-flavour Schwinger model reads,

$$\mathcal{H} = \frac{1}{2} : \Pi^2 + (\nabla\phi)^2 + m_\eta^2\phi^2 :_{m_\eta}, \tag{2.28}$$

where Π denotes the conjugate momenta of the scalar field ϕ and :: denotes the conventional normal ordering, with respect to m_η.

For the massive 1-flavour Schwinger model Coleman has shown that its bosonized model contains an angular parameter θ, independent of the quark mass m_0 and the bare coupling g. He derived the Hamiltonian density given by

$$\mathcal{H} = \mathcal{H}_\theta = \frac{1}{2} : \Pi^2 + (\nabla\phi)^2 + m_\eta^2\phi^2 + cm_0m_\eta\cos(2\sqrt{\pi}\phi + \theta) :_{m_\eta}, \tag{2.29}$$

where $c = \frac{e^\gamma}{2\pi}$ is a numerical constant and $\gamma \approx 0.577$ the Euler number. The Hilbert space of states has an infinite number of orthonormal vacuum states, which are labelled by this particular parameter θ. The appearance of this somewhat arbitrary angle θ is related to the existence of a constant electric background field, which can appear in 2-dimensional QED, but is absent in 4-dimensional QED. This form of the Hamiltonian density for the massive 1-flavour Schwinger model explicitly displays the structure of the massless model, furthermore it also reveals that the parameter θ might be physically significant (for example in mass perturbation theory, the mass of the meson depends non-trivially on θ).

An interesting additional feature is the appearance of a non-vanishing vacuum condensate [12, 18]

$$\frac{\langle\bar{\psi}\psi\rangle(m_0 = 0)}{g} = \frac{e^\gamma}{2\pi^{3/2}} \approx 0.1599. \tag{2.30}$$

2.2 2-flavour Schwinger model

Up to this moment we considered the 1-flavour Schwinger model. Now we turn to the 2-flavour Schwinger model, which is of great interest since it shares many similarities with Quantum Chromodynamics, such as confinement, chiral symmetry breaking, charge shielding and a topological θ-vacuum [13, 14, 16]. We consider two fermions an up quark u and a down quark d, in complete analogy to QCD, which shall be mass degenerate $m_u = m_d = m_0$. Since we have two flavours the Dirac spinor now forms a doublet $\psi = (u, d)$. The Lagrangian of the 2-flavour theory reads

$$\mathcal{L}[\bar{\psi}, \psi, A_\mu] = \bar{\psi}^k(x)[i\not{D} - m_0]\psi^k(x) - \frac{1}{4}F_{\mu\nu}F^{\mu\nu} \tag{2.31}$$

$$= \bar{u}(x)[i\not{D} - m_0]u(x) + \bar{d}(x)[i\not{D} - m_0]d(x) - \frac{1}{4}F_{\mu\nu}F^{\mu\nu}, \tag{2.32}$$

where, in the first line, a summation over the quark flavours $k \in \{u, d\}$ is implied.

2.2.1 Symmetries

The up and down quarks form an isospin doublet with quantum numbers presented in table 2.1. The 2-flavour Lagrangian is now invariant under global transformations in flavour space with a matrix $U \in U(2)$. This symmetry can be split up into two parts

$$U(2) = SU(2)_V \times U(1)_V. \tag{2.33}$$

The $U(1)_V$ part corresponds to the gauge symmetry, which is already present in the 1-flavour Schwinger model (see subsection 2.1.1). The $U(1)_V$ part is covariantized as in the 1-flavour case and the gauge transformation can easily be generalized, the fields transform as

$$\psi \to e^{i\Lambda(x)}\psi \qquad \text{and} \qquad \bar{\psi} \to \bar{\psi}e^{-i\Lambda(x)}. \tag{2.34}$$

[1] The basis of bosonization is the equivalence between the Sine-Gordon model and the massive Thirring model as explained in Ref. [17].

The corresponding conserved vector current is given by

$$J_V^\mu = \bar{\psi}\frac{\mathbb{1}_{2\times 2}}{2} \otimes \gamma^\mu \psi, \quad \text{with } \partial_\mu J_V^\mu = 0, \quad \text{for } U(1)_V. \tag{2.35}$$

The 2-flavour version of the Schwinger model acquires an additional internal $SU(2)_V$ symmetry, which corresponds to a rotation in flavour space. Consider the generators of the $su(2)$ Lie algebra in the Cartan-Weyl form

$$T^0 = \frac{1}{2}\sigma_3, \qquad T^1 = \frac{1}{2}(\sigma_x + i\sigma_y) \stackrel{!}{=} T^+, \qquad T^2 = \frac{1}{2}(\sigma_x - i\sigma_y) \stackrel{!}{=} T^-. \tag{2.36}$$

Then, a non-trivial global $SU(2)_V$ transformation in flavour space is characterized by

$$\psi \to e^{i\omega^a T^a}\psi \qquad \text{and} \qquad \bar{\psi} \to \bar{\psi}e^{-i\omega^a T^a}, \tag{2.37}$$

the resulting Noether currents are given by

$$J_V^{a\mu} = \bar{\psi}T^a \otimes \gamma^\mu \psi, \quad \text{with } \partial_\mu J_V^{a\mu} = 0, \quad \text{for } SU(2)_V. \tag{2.38}$$

Similar to the 1-flavour case, also the 2-flavour Schwinger model acquires an additional symmetry in the chiral limit $m_0 \to 0$. In the chiral limit the axial $U(1)_A$ symmetry is present as well and also spoiled by an anomaly, similarly to the 1-flavour Schwinger model. Consider a global chiral transformation, which is trivial in flavour space

$$\psi \to e^{i\tilde{\Lambda}\gamma^5}\psi \qquad \text{and} \qquad \bar{\psi} \to \bar{\psi}e^{i\tilde{\Lambda}\gamma^5}. \tag{2.39}$$

Then the axial current is conserved in the massless limit, up to an anomaly

$$J_A^\mu = \bar{\psi}\frac{\mathbb{1}_{2\times 2}}{2} \otimes \gamma^\mu\gamma^5\psi, \quad \text{with } \partial_\mu J_A^\mu = 2im_0\bar{\psi}\frac{\mathbb{1}_{2\times 2}}{2} \otimes \gamma^5\psi + \text{ anomaly}, \quad \text{for } U(1)_A. \tag{2.40}$$

Also the $SU(2)_A$ symmetry is broken for massive quarks. Consider a global chiral transformation, which also acts in flavour space

$$\psi \to e^{i\tilde{\omega}^a T^a\gamma^5}\psi \qquad \text{and} \qquad \bar{\psi} \to \bar{\psi}e^{i\tilde{\omega}^a T^a\gamma^5}, \tag{2.41}$$

then the Noether currents read

$$J_A^{a\mu} = \bar{\psi}T^a \otimes \gamma^\mu\gamma^5\psi, \quad \text{with } \partial_\mu J_A^{a\mu} = 2im_0\pi^a, \quad \text{for } SU(2)_A, \tag{2.42}$$

where we introduced the pion correlator $\pi^a = (\bar{\psi}T^a \otimes \gamma^5\psi)$. Contrary to the $U(1)_A$ case the $SU(2)_A$ symmetry does not have an anomaly, due to an additional trace in flavour space, which cancels the axial anomaly (appendix G.1).

flavour	Isospin I	I_z
u	$\frac{1}{2}$	$\frac{1}{2}$
d	$\frac{1}{2}$	$-\frac{1}{2}$

Table 2.1: Isospin quantum numbers.

2.2.2 Spectrum

Due to confinement the up and down quarks do not appear as free particles in the theory, but rather form meson states which make up the spectrum of the theory. We follow mostly the results from Coleman in Ref. [14] and label the mesons as proposed in Refs. [19, 20, 21]. In order to investigate the spectrum of the massive 2-flavour Schwinger model, we write down its bosonized form similar to the 1-flavour case. The bosonization of the up and down quark fields allows us to express the quark fields (u, d) by two

bosonic fields (ϕ_+, ϕ_-) and their corresponding conjugate momenta $\Pi_\pm$. The Hamiltonian of this theory reads

$$\begin{aligned}\mathcal{H}_\theta =& \frac{1}{2} :\Pi_+^2 + (\partial_1\phi_+)^2 + m_\eta^2\phi_+^2 + \Pi_-^2 + (\partial_1\phi_-)^2 :_{m_0} \\ & - 2cm_0^2 :\cos(\sqrt{2\pi}\phi_+ - \frac{\theta}{2}) :_{m_0} :\cos(\sqrt{2\pi}\phi_-) :_{m_0} \qquad (2.43)\\ =& \frac{1}{2} :\Pi_+^2 + (\partial_1\phi_+)^2 + m_\eta^2\phi_+^2 :_{m_\eta} + \frac{1}{2} :\Pi_-^2 + (\partial_1\phi_-)^2 :_{m_0} \\ & - 2cm_0^{3/2}m_\eta^{1/2} :\cos(\sqrt{2\pi}\phi_+ - \frac{\theta}{2}) :_{m_\eta} :\cos(\sqrt{2\pi}\phi_-) :_{m_0}, \qquad (2.44)\end{aligned}$$

where m_0 denotes the mass of the original up and down quarks and we used $m_\eta^2 = \frac{2g^2}{\pi}$. The objects $::_{m_0}$ / $::_{m_\eta}$ denote normal-ordering w.r.t. the free fields with masses m_0 and m_η. The relation between those two types of normal-ordering are elaborated in Ref. [17] and given by

$$\begin{aligned}&\frac{1}{2} :\Pi_+^2 + (\partial_1\phi_+)^2 + m_\eta^2\phi_+^2 :_{m_0} = \frac{1}{2} :\Pi_+^2 + (\partial_1\phi_+)^2 + m_\eta^2\phi_+^2 :_{m_\eta} \\ \text{and} \quad &:\cos(\sqrt{2\pi}\phi_+ - \frac{\theta}{2}) :_{m_0} = \left(\frac{m_\eta}{m_0}\right)^{1/2} :\cos(\sqrt{2\pi}\phi_+ - \frac{\theta}{2}) :_{m_\eta} .\end{aligned}$$

The expression for the Hamiltonian displays a theory of a heavy scalar field ϕ_+ (which retains mass m_η in the massless limit $m_0 \to 0$) and a light scalar field ϕ_-. The original isospin invariance has been obscured but is still present. Based on the transformation behaviour one can show that ϕ_+ represents an iso-singlet (η boson), while the ϕ_- has a more complicated transformation behaviour. In order to make further statements about the spectrum of the massive 2-flavour Schwinger model, we consider the strong coupling limit, i.e. we take the limit where

$$\frac{m_0}{g} \to 0 \quad \Leftrightarrow \quad \frac{m_0}{m_\eta} \to 0. \qquad (2.45)$$

The strong coupling limit is equivalent to a situation, where the mass of the ϕ_- field is negligible compared to the mass of the η boson and therefore the influence of the field ϕ_+ on the dynamics of the field ϕ_- can be dismissed. If we ignore the ϕ_+ fields altogether and introduce a new mass term $m' = (2cm_0m_\eta^{1/2}\cos(\frac{\theta}{2}))^{2/3}$, we end up with a reduced form of the theory

$$\begin{aligned}\mathcal{H}_\theta &= \frac{1}{2} :\Pi_-^2 + (\partial_1\phi_-)^2 :_{m_0} - 2cm_0^{3/2}m_\eta^{1/2}\cos\left(\frac{\theta}{2}\right) :\cos(\sqrt{2\pi}\phi_-) :_{m_0} \\ &= \frac{1}{2} :\Pi_-^2 + (\partial_1\phi_-)^2 :_{m'} - (m')^2 :\cos(\sqrt{2\pi}\phi_-) :_{m'}, \qquad (2.46)\end{aligned}$$

where we used the normal ordering rules

$$:\Pi_-^2 + (\partial_1\phi_-)^2 :_{m_0} = :\Pi_-^2 + (\partial_1\phi_-)^2 :_{m'} \quad \text{and} \quad :\cos(\sqrt{2\pi}\phi_-) :_{m_0} = \left(\frac{m'}{m_0}\right)^{1/2} :\cos(\sqrt{2\pi}\phi_-) :_{m'} .$$

The only mass parameter in the theory is now m', which carries the dependence on the angular parameter θ. Numerical calculations performed by Gutsfeld et al. in Ref. [21] suggest that $\theta \approx 0$, therefore we set $\theta = 0$ from now on. The Hamiltonian $\mathcal{H}_\theta$ presented in eq. (2.46) can be related to the Hamiltonian of the Sine-Gordon model (see Refs. [17, 22]), that is

$$\mathcal{H}_{SG}[\alpha_0, \beta_0, \gamma_0] = \frac{1}{2}\left[\pi^2 + (\partial_1\varphi)^2\right] - \frac{\alpha_0}{\beta_0}\cos(\beta\varphi) - \gamma_0, \qquad (2.47)$$

by identifying $\alpha_0 = \sqrt{2\pi}(m')^2$, $\beta_0 = \sqrt{2\pi}, \gamma_0 = 0$. We conclude that the Schwinger model turns into the Sine-Gordon model in the strong coupling limit

$$\boxed{\text{2-flavour Schwinger model} \quad \overset{\frac{m_0}{g}\to 0}{\longrightarrow} \quad \text{Sine-Gordon model}}.$$

Hence, it is possible to obtain the spectrum of the 2-flavour Schwinger model at strong coupling by using known results from the Sine-Gordon model. The Sine-Gordon model describes a theory of a scalar field

in two dimensions and has been extensively discussed by Dashen et al. in Ref. [22], who computed the particle spectrum for arbitrary values of β_0 based on the WKB approximation. It was shown that the Sine-Gordon model contains two particles, a soliton A and an antisoliton $\bar{A}$ of equal mass M. In addition, the theory has soliton-antisoliton bound states, with masses

$$M_n = 2M \sin\left(\tilde{\beta}^2 \frac{n}{16}\right), \quad \text{where} \quad \tilde{\beta}^2 = \frac{\beta_0^2}{1 - \frac{\beta_0^2}{8\pi}}. \tag{2.48}$$

The number of these bound states is restricted by $\tilde{\beta}$, with $n = 1, 2, \ldots, < \frac{8\pi}{\tilde{\beta}^2}$. In our specific case we have $\beta_0^2 = 2\pi$, which yields two bound states B_1, B_2, with masses

$$M_{B_1} = M \quad \text{and} \quad M_{B_2} = \sqrt{3}M. \tag{2.49}$$

With the identification of particle B_1 we have completed an isospin triplet $(A, \bar{A}, B_1)$, which corresponds to a pion triplet in the 2-flavour Schwinger model (see Refs. [14, 21]). The mass and quantum numbers (isospin, parity, G-parity) of said pion triplet are given by

$$M = 6\sqrt{\frac{2}{\pi}} c^{2/3} \left(\frac{m_0}{g}\right)^{2/3} g \overset{!}{=} m_\pi \quad \text{and} \quad I^{PG} = 1^{-+}. \tag{2.50}$$

We additionally found a particle B_2, which has no partner with non-zero I_3, therefore it must be an iso-singlet, which will be called f_0 meson with mass and quantum number

$$m_{f_0} = \sqrt{3} m_\pi \quad \text{and} \quad I^{PG} = 0^{++}. \tag{2.51}$$

The next particle in line is the η meson resulting from the fields ϕ_+, with mass and quantum numbers

$$m_\eta = \sqrt{\frac{2}{\pi}} g + \text{corrections} \quad \text{and} \quad I^{PG} = 0^{--}. \tag{2.52}$$

It was argued by Gutsfeld et al. [21], that the mass corrections to the η meson are given by

$$\frac{m_\eta}{g} = \sqrt{\frac{2}{\pi}} + A \left(\frac{m_0}{g}\right)^p, \tag{2.53}$$

with $A \approx 1.73$ and $p \approx 1$. Note that for vanishing quark mass ($m_0 \to 0$) the mass-corrections to the η boson vanish. We conclude that in the strong coupling limit the three lightest particles of the massive 2-flavour Schwinger model are given by the pion triplet π, the f_0 meson and the η meson. It can be shown (see Ref. [14]) that in the weak coupling regime, the mass hierarchy changes. The lightest meson is still the pion, however, the next lightest state is the η instead of the f_0 meson. The heaviest 1-meson state is given by a scalar triplet with quantum numbers $I^{PG} = 1^{+-}$, which is being referred to as the a_0 meson (see Refs. [14, 19]).

2.2.3 Spectrum summary

Here we summarize the 1-meson states in the massive 2-flavour Schwinger model and present them in a well-arranged way. We encountered four different meson states so far, which are summarized in table (2.2).

Operator	Meson	Quantum numbers (I^{PG})	Meson Interpolator $J(x,t)$
Pseudo-scalar Triplet	π	1^{-+}	$\bar{\psi}(T^0, T^+, T^-) \cdot \gamma^5 \psi$
Pseudo-scalar Singlet	η	0^{--}	$\bar{\psi} \mathbb{1} \cdot \gamma^5 \psi$
Scalar Triplet	a_0	1^{+-}	$\bar{\psi}(T^0, T^+, T^-) \cdot 1\psi$
Scalar Singlet	f_0	0^{++}	$\bar{\psi} \mathbb{1} \cdot 1\psi$

Table 2.2: Summary of the 1-meson states, including the quantum number and the meson interpolators, which are used for spectroscopy (appendix chapter B).

The lightest meson of the theory is the pion $|\pi\rangle$, which shows up in a mass-degenerate triplet with mass m_π

$$|\pi\rangle = \begin{cases} |\pi^+\rangle = |u\bar{d}\rangle, \\ |\pi^0\rangle = \frac{1}{\sqrt{2}}(|u\bar{u}\rangle - |d\bar{d}\rangle), \\ |\pi^-\rangle = |\bar{u}d\rangle. \end{cases} \tag{2.54}$$

Depending on whether we are working in the strong or weak-coupling regime, the order of the meson masses looks different, however, the pion triplet is always the lightest one. We present a visual representation of the 1-meson spectrum in figure (2.1).

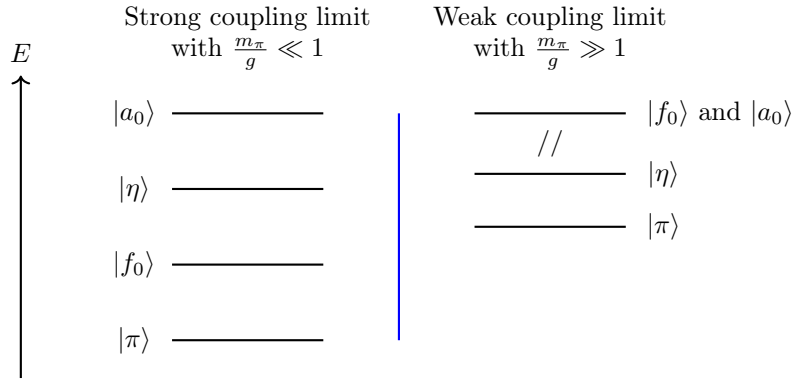

Figure 2.1: Graphical representation of the mass hierarchy of the 1-meson states in the 2-flavour Schwinger model.

2.3 Dimensional analysis

The Schwinger model is super-renormalizable, i.e. only a finite number of Feynmann diagrams superficially diverge. Consequently, all divergences can be removed in order to obtain a physically meaningful, finite theory. One can see this by explicitly showing that the coupling parameter g has positive mass dimension. Consider the action of the Schwinger model in d dimensions (in the end we set $d = 2$, the number of flavours does not play a pivotal role here) and let $[\mathcal{O}]$ denote the mass dimension of an operator $\mathcal{O}$. The action

$$S = \int \mathrm{d}^d x \mathcal{L} = \int \mathrm{d}^d x \left(\bar{\psi}(i\not{D} - m_0)\psi - \frac{1}{4} F_{\mu\nu} F^{\mu\nu} \right), \tag{2.55}$$

is dimensionless and since $[\mathrm{d}x] = -1$, we conclude that $\mathcal{L}$ has dimension d ($[\mathcal{L}] = d$). Using $[m_0] = 1$ and $[\frac{\partial}{\partial x}] = 1$, one immediately gets all the mass dimensions for the Lagrangian

$$[\bar{\psi}] = [\psi] = \frac{d-1}{2}, \qquad [F_{\mu\nu}] = \frac{d}{2}, \qquad [A_\mu] = \frac{d}{2} - 1, \tag{2.56}$$

and $[g] = 2 - \frac{d}{2}$. In the case of $d = 2$ the coupling parameter g has positive mass dimension, therefore the theory is super-renormalizable according to Peskin in Ref. [23].

2.4 Introducing the lattice

So far we discussed general properties of the Schwinger model in 2-dimensional continuous Minkowski spacetime. In order to numerically examine the Schwinger model we have to implement this theory on an Euclidean lattice. Here we briefly sketch the procedure, further details are given in the appendix chapter A, for a more in depth discussion we recommend Rothe [24].

- We start by performing a so-called Wick rotation, i.e. we let the time-variable go to $t \to -i\tau$. As a consequence the action picks up a factor i and the complex path integral Z can be identified as

a well-behaved, real valued partition function $\mathcal{Z}$

$$t \to -i\tau \implies S_M \to iS_E \implies Z = \int \mathcal{D}\bar{\psi}\mathcal{D}\psi\mathcal{D}U e^{iS_M} \to \mathcal{Z} = \int \mathcal{D}\bar{\psi}\mathcal{D}\psi\mathcal{D}U e^{-S_E}.$$

- After the transformation to Euclidean spacetime, we discretize the Lagrangian on a square lattice with spacing a and physical extent $L \times L_t$, with periodic boundary conditions in spatial direction and antiperiodic ones in temporal direction for the fermion fields. The partition function $\mathcal{Z}$ is a function of the temperature T, which is related to the temporal extent of the lattice via $T = 1/L_t$.
- We introduce Wilson lines for the gauge fields $U_{n,n+\hat{\mu}} \in U(1)$ and include a Wilson term in the fermion action to circumvent the fermion doubling problem.

Numerical simulations on the lattice are not a perfect representation of the real world and have systematic errors, which need to be taken care of. One of these systematics are so-called lattice artefacts, which arise due to the non-zero lattice spacing and can be examined by taking the continuum limit $a \to 0$, while keeping all other parameters fixed.

Another problem is the already mentioned fermion doubling problem, which appears upon discretizing fermions on the lattice [25]. The added Wilson term breaks chiral invariance, which makes the definition of the fermion mass more complicated. To define the quark mass in the 2-flavour Schwinger model we use the so-called PCAC mass, which is explained in the next section 2.5.

Finite volume effects arise due to the finite spatial extent of the lattice and will be elaborated in section 2.6.

For the rest of this chapter, we restrict ourselves to the 2-flavour Schwinger model as introduced in section 2.2, on an Euclidean square lattice with spacing $a = 1$ and physical extent $L \times L_t$.

2.5 PCAC mass

The bare fermion mass m_0, which is a parameter in the Lagrangian $\mathcal{L}$, is related to the "true" quark mass m_q by some relation

$$m_q = Z_M m_0, \tag{2.57}$$

where Z_M denotes a multiplicative renormalization factor. The Wilson fermions, which are being introduced to circumvent the fermion doubling problem (see appendix A.2), lead to an additional additive correction to the quark mass such that

$$m_q = Z_M(m_0 - m_{\text{crit}}) = Z_M m_{(q,b)}, \tag{2.58}$$

where $m_{(q,b)}$ defines the bare subtracted quark mass. The critical quark mass m_{crit} is defined as the value of the bare quark mass m_0, where the physical quark mass vanishes. To determine the chiral limit we use the so-called PCAC mass (PCAC stands for *partially conserved axial current*).

In order to obtain the PCAC-relation, we require the $SU(2)_A$-Ward identity for the 2-flavour Schwinger model, given by eq. (2.42). We utilize a lattice version of said relation, which holds in Euclidean spacetime, that is

$$\partial_\mu J_A^{a\mu} = 2m_0\pi^a, \qquad \text{with} \qquad \pi^a = \bar{\psi}T^a \otimes \gamma^5\psi. \tag{2.59}$$

Both, the naive discretization (which has a fermion doubling problem) as well as the Wilson-discretization lead to the same $SU(2)_A$ lattice operator identity. Hence, the parameter m_0 can be considered to be the bare mass regardless of the discretization, allowing us to identify $m_0 \sim m_{(q,b)}$ in eq. (2.59).

We sandwich the operator relation eq. (2.59), between suitable states such that

$$2m_{(q,b)} = \frac{\langle 0|\pi^{a,\dagger}\partial_\mu J_A^{\mu a}|0\rangle}{\langle 0|\pi^{a,\dagger}\pi^a|0\rangle}. \tag{2.60}$$

We can now compute the chiral limit by tuning m_0 in the numerical simulations in such a way that $m_{(q,b)}$ vanishes in eq. (2.60). This then defines the critical bare mass m_{crit}, where also the physical quark mass m_q vanishes. For more details we refer to Hip et al. in Ref. [26].

2.6 Finite volume effects

In order to discuss finite volume effects (FVE) consider a lattice of extent $L \times L_t$, ideally the temporal lattice extent is chosen to be infinite, such that the temperature of the system is zero ($L_t = \frac{1}{T} = \infty$). Consider a particle with non-zero momentum which is allowed to propagate freely within the 1-dimensional box. Once this particle reaches the boundaries, it will show up at the opposite side of the box, due to the periodic boundary conditions. The Schrödinger wave function of such a particle state spreads out within the box if the box size L is big enough. However, if we shrink the box, the wavefunction gets squeezed and laps over via the boundaries, meaning that the particle interacts "with itself" via the boundaries. Lüscher appropriately called these kinds of effects "interactions around the world" [27, 28, 29]. These kinds of interactions also have an effect on the spectrum of the theory. Since the lightest particle of the massive 2-flavour Schwinger model is the pion, we identify the mass gap with the pion mass and denote the mass gap by m_π. The mass gap does not only depend on the input parameters of the theory like the bare coupling g or the bare mass of the fermion m_0, but also, as mentioned, on the size of the box L. The infinite volume mass gap m_π can be extracted from finite volume calculations by extrapolating to infinite volume

$$m_\pi = \lim_{L\to\infty} m_\pi(L), \tag{2.61}$$

while keeping all the other parameters fixed. Lüscher showed that for a 4-dimensional massive quantum field theory the finite volume corrections to the mass gap are given by the three Feynman diagrams depicted in figure 2.2.

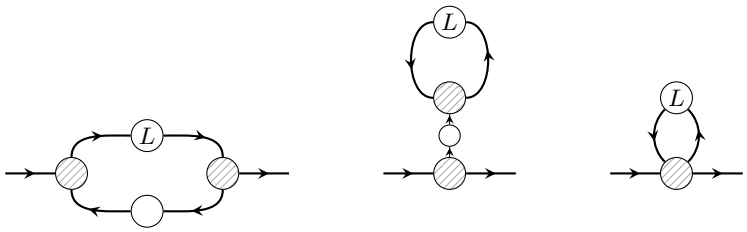

Figure 2.2: Graphical representation of the Feynman diagrams contributing to the finite volume effects. It is worth noticing that only the first diagram yields contributions related to the 3-particle coupling λ. The circles which include an L denote a crossing of the spatial boundaries.

However, he also argued that the same corrections arise for a 2-dimensional massive quantum field theory [29]. After calculating those diagrams one obtains the finite volume corrections to the mass gap

$$m_\pi(L) = m_\pi - \lambda^2 m_\pi^{-3} \frac{1}{8\pi} (\frac{4\pi}{\sqrt{3}}\xi)^{\frac{1}{2}} K_{-\frac{1}{2}}(\frac{\sqrt{3}}{2}\xi) - \frac{1}{2m_\pi} \int \frac{dq}{(2\pi)2q_0} e^{-q_0 L} F(iq_1), \tag{2.62}$$

where λ denotes the effective 3-particle coupling, K_l the modified Besselfunction, $\xi = m_\pi L$ and $F(iq_1)$ denotes the forward scattering amplitude. After some simplifications, approximations and rescaling, assuming sufficiently large volumes L, one obtains

$$m_\pi(L) = m_\pi + \left(\frac{\lambda^2}{4\sqrt{3}m_\pi^3}\right) e^{-\frac{\sqrt{3}}{2}\xi} + \frac{1}{\sqrt{\xi}} \left(\frac{F(0)}{4m_\pi\sqrt{2\pi}}\right) e^{-\xi}. \tag{2.63}$$

The interested reader is referred to the appendix G.2 for more details. Some comments with respect to the 3-particle coupling need to be made. Contrary to QCD, the pion triplet in the 2-flavour Schwinger model has positive G-parity (see subsection 2.2.2, also Refs. [30, 31]), which means that a 3-pion vertex is allowed[2] and appears in the topological Wess-Zumino-Witten term [32]. This means that when considering finite volume effects, we are not allowed to dismiss the contribution arising from the 3-particle coupling.

Note that the Schwinger model turns into the Sine-Gordon Model in the strong coupling limit $\frac{m_\pi}{g} \to 0$. Since the Sine-Gordon model does not exhibit any 3-particle coupling (i.e. $\lambda = 0$), one expects a decreasing 3-particle coupling when approaching the strong coupling limit.

[2]Of course other quantum numbers must not be violated.

2.7 Scattering phase shift

In this section we consider scattering phenomena in $1+1$ dimensions on the lattice and introduce the scattering phase shift. Literature discussing scattering theory in $3+1$ dimensions is available en masse, Griffiths [33] for example provides a very nice introductory read and Lüscher examines scattering in $3+1$ dimensions on the lattice in Ref. [34]. Scattering phenomena for $1+1$ dimensions in a finite box are discussed by Lüscher [27, 29], Guo for a more extensive discussion [35, 36], Eberly [37] or Barlette et al. in Refs. [38, 39].

So far we considered finite volume effects on a single particle in a box and saw that the mass gap (resp. the pion mass) m_π of the 2-flavour Schwinger model is affected by finite volume corrections. Now we discuss the effects of adding a second particle to the box. Having two particles in the box, it should be intuitively clear that finite volume effects become more severe. In a 1-dimensional box scattering processes are inevitable and the mean free path decreases if we shrink the box.

Due to the finite volume of the box the relative wave-function of the 2-particle state requires a correction at the boundaries, which is being taken care of by the so-called scattering phase shift $\delta(k)$. The derivation of the scattering phase shift is straightforward and can be understood using simple quantum mechanics. Consider two identical spinless bosons with mass m moving within a 1-dimensional box of size L with positions and momenta (x_1, x_2) and (p_1, p_2), respectively. The wavefunction is then given by

$$\psi(x_1, x_2), \qquad \text{with } x_1, x_2 \in [0, L], \tag{2.64}$$

and the Schrödinger wavefunction reads

$$\left[-\frac{1}{2m}\frac{d^2}{dx_1^2} - \frac{1}{2m}\frac{d^2}{dx_2^2} + V(x_1 - x_2) - E\right]\psi(x_1, x_2) = 0, \tag{2.65}$$

where E denotes the total energy of the system $E = \frac{p_1^2}{2m} + \frac{p_2^2}{2m}$ and V denotes some symmetric short ranged potential, which depends on the spatial difference between the two particles only. Since the two bosons are identical the wavefunction has to be the same under the exchange of x_1 and x_2, except for an irrelevant complex phase which drops out from physical observables. Let us now introduce the center of mass position R, the relative position r, together with the total momentum P and the relative momentum k via

$$R = \frac{x_1 + x_2}{2}, \qquad r = x_1 - x_2, \qquad P = p_1 + p_2, \qquad k = \frac{p_1 - p_2}{2}, \text{ respectively.} \tag{2.66}$$

Due to the translational invariance of the center of mass motion, the total wavefunction can be written as a product of a plane wave e^{iPR} and a relative wavefunction $\psi(r, k)$, which only depends on the relative motion between the two particles

$$\psi(x_1, x_2) = e^{iPR}\psi(r, k). \tag{2.67}$$

After this transformation of variables, the Schrödinger equation reads

$$\left[-\frac{1}{m}\frac{d^2}{dr^2} - \frac{1}{4m}\frac{d^2}{dR^2} + V(r) - E\right]e^{iPR}\psi(r, k) = 0 \tag{2.68}$$

$$\left[-\frac{1}{m}\frac{d^2}{dr^2} + \frac{P^2}{4m} + V(r) - E\right]e^{iPR}\psi(r, k) = 0. \tag{2.69}$$

Upon restricting ourselves to the center of mass frame with total vanishing momentum ($P = 0$), we obtain

$$\left[-\frac{1}{m}\frac{d^2}{dr^2} + V(r) - E\right]\psi(r, k) = 0, \tag{2.70}$$

with energy $E = \frac{k^2}{m}$. The scattering potential shall be short-ranged and symmetric $V(r) = V(-r)$ such that we have even and odd solutions to the Schrödinger equation. Using an exchange-symmetric ansatz we can immediately find a stationary (time-independent) scattering solution for large r, where the potential $V(r)$ is negligible

$$\psi_0(r, k) \overset{r\to\infty}{\sim} \cos(k|r| + \delta(k)). \tag{2.71}$$

If the particle is now confined within a box of size L, some modifications need to be made, due to the periodicity of the box. We take into account the periodicity of the system by making the replacement

$$V(|r|) \to V_L(|r|) = \sum_{\nu} V(|r + \nu L|), \tag{2.72}$$

and by modifying the stationary solution $\psi_0(r, k)$. We require that the wavefunction is continuous and differentiable at the boundaries such that

$$\psi_0\left(-\frac{L}{2}, k\right) = \psi_0\left(\frac{L}{2}, k\right) \quad \text{and} \quad \psi_0'\left(-\frac{L}{2}, k\right) = \psi_0'\left(\frac{L}{2}, k\right) = 0, \text{ respectively,} \tag{2.73}$$

where the $\psi'(r, k)$ denotes a derivative with respect to r. Both equations yield the same result, which is the quantization condition for the relative momentum k of two particles in a 1-dimensional box

$$2\delta(k) = -kL + 2\pi n, n \in \mathbb{Z}. \tag{2.74}$$

Note that this quantization condition holds true for any short-range interaction $V(|r|)$ and directly links the phase shifts to the finite volume L. The physical interpretation of this quantization condition and the correction term δ can be understood by comparing the free case (with $V = 0$) to the interacting case. In the free case (where no interaction happens) the relative momentum is given by some $k = \frac{2\pi n}{L}$ with $n \in \mathbb{Z}$ and the relative wavefunction smoothly connects at the boundaries. However, in the interacting case the wave function gets distorted by the influence of the potential at $r \approx 0$, and does not connect nicely to itself at the boundaries. The scattering phase shift in the quantization condition (2.74) corrects for this, by adding a correction to the relative momentum [27].

It was argued by Lüscher (also in Ref. [27]) that the quantization conditions presented above are only valid for a lattice field theory where certain conditions are fulfilled. It is required that the lattice spacing is small enough, such that we are close to the continuum limit. This ensures that corrections to the quantization condition eq. (2.74) based on the lattice spacing can be neglected. Furthermore, the box of size L must be chosen large enough such that virtual particle exchanges "around the world" are strongly suppressed. The box size L also needs to be chosen larger than the interaction range of the potential, such that the particles can travel freely, before scattering again off each other. Additionally, we must work with energies below a certain threshold, where only elastic scattering occurs and no new particles are being created.

The derivation of the quantization conditions becomes more involved once we leave the center of mass frame. A generalization of the quantization condition eq. (2.74) has been derived by Guo [35, 36] and reads

$$\cot(\delta(k)) + \cot\left(\frac{PL}{4} + \frac{kL}{2}\right) = 0, \tag{2.75}$$

where $P = p_1 + p_2$ and $k = \frac{p_1 - p_2}{2}$ denote the center of mass and the relative momenta of the two particles. The total momentum is quantized due to the periodic boundary conditions

$$P = \frac{2\pi}{L} d, d \in \mathbb{Z}. \tag{2.76}$$

Note, that eq. (2.75) reduces to Lüscher's quantization condition eq. (2.74) by going into the center of mass frame with $P = 0$.

2.7.1 Partial wave decomposition

So far we have been concerned with the physical interpretation of the scattering phase shift and followed a simple intuitive example presented by Lüscher.

In this section we present a self-contained discussion about non-relativistic quantum scattering. We focus on the partial wave expansion, the effective range expansion and their relation to the scattering phase shift $\delta(k)$. We closely follow Barlette et al., for a more elaborate discussion we refer to Ref. [38].

We adopt the notation introduced in section 2.7 and consider scattering solutions to the Schrödinger equation (eq. (2.70)), that is

$$\left[-\frac{1}{m}\frac{d^2}{dr^2} + V(r) - E\right]\psi(r, k) = 0, \tag{2.77}$$

where $V(r) = V(-r)$ denotes a centrally symmetric potential and the energy is given by $E = \frac{k^2}{m}$. The asymptotic behaviour of the wavefunction can be written as

$$\lim_{r\to\infty} \psi(r,k) = e^{ikr} + \frac{i}{k} f_k(\epsilon) e^{ik|r|}, \tag{2.78}$$

where $\epsilon = \frac{r}{|r|}$, $f_k(\epsilon)$ denotes the scattering amplitude, e^{ikr} the incident wave and $e^{ik|r|}$ the scattered outgoing wave. In one spatial dimension there are only two scattering directions, forward scattering (with $\epsilon = 1$) and backwards scattering (with $\epsilon = -1$), contrary to scattering in 3 dimensions, where we have an infinite number of scattering directions. The total cross-section σ_{tot} is given by a sum of those two contributions, such that

$$\sigma_{tot} = \sum_{\epsilon} \sigma_\epsilon = \frac{1}{k^2} \left[|f_k(+1)|^2 + |f_k(-1)|^2 \right]. \tag{2.79}$$

Analogous to the 3-dimensional case one can expand the wavefunction in partial waves with corresponding scattering phase shifts. Since we are working with a symmetric potential in $1+1$ dimension the expansion in partial waves is heavily restricted and allows for two partial waves only. We have an even-parity wavefunction (symmetric, $L = 0$) and an odd-parity wavefunction (antisymmetric, $L = 1$), in the asymptotic limit we obtain

$$\lim_{r\to\infty} \psi(r,k) = \sum_{L=0,1} \epsilon^L \psi_L(r,k). \tag{2.80}$$

In order to derive those two required wavefunctions ψ_L with $L = 0, 1$, we use

$$e^{ikr} = \cos(k|r|) + i\epsilon \sin(k|r|), \tag{2.81}$$

and expand the scattering amplitude such that

$$f_k(\epsilon) = \sum_{L=0,1} \epsilon^L e^{i\delta_L(k)} \sin(\delta_L(k)) \stackrel{!}{=} \sum_{L=0,1} \epsilon^L f_L, \tag{2.82}$$

where we introduced the scattering phase shifts for the two partial waves $\delta_0(k)$ and $\delta_1(k)$, respectively. Note, that the expansions presented in eq. (2.80) and (2.82), are standard expansions which show up in a similar form in 3-dimensional scattering theory. Using eqs. (2.81) and (2.82) and plugging them into eq. (2.80) yields the partial wave expansion in the asymptotic limit

$$\lim_{r\to\infty} \psi(r,k) = \sum_{L=0,1} \epsilon^L A_L \cos(k|r| + \frac{L\pi}{2} + \delta_L(k)), \tag{2.83}$$

with $A_L = (-i)^L e^{i\delta_L(k)}$. This result should not come as a surprise after the derivation of the symmetric solution in section 2.7, here we basically just added an antisymmetric solution to the mix. Using the expansion of the scattering amplitude the total cross-section becomes

$$\sigma_{tot} = 2 \sum_{L=0,1} \sin^2(\delta_L), \tag{2.84}$$

which satisfies the optical theorem

$$\sigma_{tot} = \frac{2}{k} \Im(f_k(\epsilon)), \tag{2.85}$$

where $\Im$ denotes the imaginary part.

2.7.2 Effective range expansion

Next we discuss the derivation of the so-called effective range expansion for both partial waves $L = 0$ and 1, in close analogy to the 3-dimensional case. The effective range expansion can be used in the study and analysis of low-energy scattering problems. It is being used as a functional tool for the description of scattering problems in nuclear [40, 41] and atomic physics [42], but it can also be used for the description of scattering phenomena on the lattice, see Refs. [38, 39].

Consider the same scattering scenario as introduced in section 2.7. In most cases, the exact form of the scattering potential $V(r)$ is unknown to us, which impedes a sophisticated discussion of the scattering behaviour. The basic idea of the effective range expansion is to describe the low-energy scattering theory using just a few parameters, similar to an effective theory.

We start the derivation by rescaling the Schrödinger equation for the relative wavefunction and introducing $r_0 = |r|$. Now we can write down the Schrödinger equation for the two partial waves separately

$$\left[-\frac{d^2}{dr_0^2} + \tilde{V}(r_0) - k^2\right] \psi_L(r_0, k) = 0, \tag{2.86}$$

with $\tilde{V} = mV$. The full symmetric and antisymmetric solutions (with $L = 0$ and $L = 1$, respectively) can be found by solving eq. (2.86) and by imposing the asympotic behaviour given by eq. (2.83). Close to the interaction range $r_0 \approx 0$, those solutions behave like simple cosines and sines

$$\psi_0(r_0, k) \sim \cos(kr_0) \quad \text{and} \quad \psi_1(r_0, k) \sim \sin(kr_0), \tag{2.87}$$

while in the asympotic region we have the solutions presented in eq. (2.83)

$$\psi_0(r_0, k) \sim \cos(kr_0 + \delta_0(k)) \quad \text{and} \quad \psi_1(r_0, k) \sim \sin(kr_0 + \delta_1(k)), \quad \text{for } r_0 \to \infty. \tag{2.88}$$

For the sake of readability, we define

$$\chi_L(z) \sim \begin{cases} \cos(z), & \text{for } L = 0, \\ \sin(z), & \text{for } L = 1. \end{cases} \tag{2.89}$$

Consider two solutions $u_1(r_0)$ and $u_2(r_0)$ of eq. (2.86) with energies k_1^2, k_2^2, respectively. We normalize them in such a way, that they retain

$$\lim_{r_0 \to \infty} u_i(r_0) \to \frac{\chi_L(r_0 k_i + \delta_L(k_i))}{\chi_L(r_0 k)}, \qquad \text{for } i = 1, 2 \text{ and } L = 0, 1, \tag{2.90}$$

in the asympotic limit. We write down the Schrödinger equation for one solution u_1 and multiply it with the second one u_2, the same is being done vice-versa. Upon subtracting both equations from each other, one obtains

$$[u_1(r_0)u_2''(r_0) - u_2(r_0)u_1''(r_0)] = (k_1^2 - k_2^2)u_1(r_0)u_2(r_0), \tag{2.91}$$

where u_i' denotes a derivative with respect to r_0. After integrating over all relative positions r_0 between 0 and some radial distance $R > 0$, we obtain

$$[u_1(r_0)u_2'(r_0) - u_2(r_0)u_1'(r_0)]\,\big|_0^R = (k_1^2 - k_2^2) \int_0^R dr_0 u_1(r_0)u_2(r_0). \tag{2.92}$$

The same construction can be made for the free Schrödinger equation (with $\tilde{V} = 0$) yielding two free-particle solutions $v_1(r_0), v_2(r_0)$ which take the form

$$v_i(r_0) = \frac{\chi_L(r_0 k_i + \delta_L(k_i))}{\chi_L(r_0 k)}, \qquad \text{for } i = 1, 2 \text{ and } L = 0, 1. \tag{2.93}$$

Performing the same kind of manipulations, we end up with the same equation just as in the interacting case (2.92). Subtracting both equations from each other, leads to a "master equation" which reads

$$\begin{aligned}(k_2^2 - k_1^2) \int_0^R dr_0 (v_1(r_0)v_2(r_0) - u_1(r_0)u_2(r_0)) = \\ (v_1'(r_0)v_2(r_0) - v_1(r_0)v_2'(r_0) + u_1(r_0)u_2'(r_0) - u_1'(r_0)u_2(r_0))\big|_0^R.\end{aligned} \tag{2.94}$$

Let us first consider the odd-parity solutions, with $L = 1$. We let $R \to \infty$ and have $u_i(0) \approx \sin(0) = 0$, for $i = 1, 2$. Evaluating the master equation then leads to

$$(k_2^2 - k_1^2) \int_0^\infty dr_0 \,[v_1(r_0)v_2(r_0) - u_1(r_0)u_2(r_0)] = -k_1 \cot(\delta_1(k_1)) + k_2 \cot(\delta_1(k_2)). \tag{2.95}$$

After setting $k_1 = 0$ and $k_2 = k$, we make the following changes in notation

$$(u_1, u_2, v_1, v_2) \to (u_0, u_k, v_0, v_k), \tag{2.96}$$

where the subscript now denotes the energy. Consequently, we obtain

$$k \cot(\delta_1(k)) = -\frac{1}{a_1} + k^2 \int_0^\infty dr_0 \left[v_0(r_0) v_k(r_0) - u_0(r_0) u_k(r_0) \right], \tag{2.97}$$

where we defined the $L = 1$ scattering length a_1, similarly as in three dimensions, via

$$-\frac{1}{a_1} = \lim_{k \to 0} k \cot(\delta_1(k)). \tag{2.98}$$

After a Taylor expansion of the integral for small momenta k, we obtain the effective range expansion for the $L = 1$ partial wave

$$k \cot(\delta_1(k)) = -\frac{1}{a_1} + \frac{r_1}{2} k^2 + \mathcal{O}(k^4), \tag{2.99}$$

where we introduced the effective range for $L = 1$, which is given by

$$r_1 = 2 \int_0^\infty dr_0 \left[v_0(r_0)^2 - u_0(r_0)^2 \right]. \tag{2.100}$$

Similarly, we can derive the effective range expansion for the even-parity solutions (with $L = 0$). Again, we start with the master equation eq. (2.94) and utilize the boundary conditions $u_1'(0) = u_2'(0) = 0$, which yields

$$(k_2^2 - k_1^2) \int_0^\infty dr_0 \left[v_1(r_0) v_2(r_0) - u_1(r_0) u_2(r_0) \right] = k_1 \tan(\delta_0(k_1)) - k_2 \tan(\delta_0(k_2)). \tag{2.101}$$

After doing the same replacements and calculations (as in the $L = 1$ case), we end up with

$$\boxed{k \tan(\delta_0(k)) = \frac{1}{a_0} + \frac{r_0}{2} k^2 + \mathcal{O}(k^4)}, \tag{2.102}$$

where we defined the $L = 0$ scattering length a_0 via

$$\frac{1}{a_0} = \lim_{k \to 0} k \tan(\delta_0(k)), \tag{2.103}$$

and the coefficient r_0 denotes the effective range for the $L = 0$ partial wave, given by

$$r_0 = -2 \int_0^\infty dr_0 \left[v_0(r_0)^2 - u_0(r_0)^2 \right]. \tag{2.104}$$

We conclude this section with two effective range expansions, one for the even-parity wave (with $L = 0$) and one for the odd-parity wave (with $L = 1$). In order to describe the low-energy scattering theory we used effective parameters a_i and r_i, if we expand further ($\mathcal{O}(k^4)$ etc.) more contributions arise and more parameters need to be introduced.

When discussing scattering phenomena in the 2-flavour Schwinger model we consider two bosons scattering off each other via a short-ranged, symmetric interaction potential. Following Guo [35], the wavefunction for two bosons is of even parity. Therefore, to describe meson scattering in this thesis, we use the effective range expansion for the $L = 0$ partial wave, i.e. eq. (2.102) with parameters a_0 and r_0.

The physical meaning of the effective range r_0 is somewhat complicated and will not be discussed here, the interested reader is referred to Barlette in Refs. [38, 39]. The meaning of the scattering length a_0 can be understood in terms of a simple toy model, for example, the symmetric 1-dimensional square well with potential

$$V(r) = \begin{cases} V_0, \text{ for } r \in [-\frac{R}{2}, \frac{R}{2}], \\ 0, \text{ else.} \end{cases} \tag{2.105}$$

The corresponding scattering length for the $L = 0$ partial wave is given by

$$a_0(R, V_0) = \frac{R}{2} + \frac{\cot(\frac{R}{2}\sqrt{-V_0})}{\sqrt{-V_0}}, \tag{2.106}$$

and can be derived using quantum mechanical considerations or by looking up Barlette in Ref. [38]. The scattering length is real for all values of $V_0 \in \mathbb{R}$, the potentially complex phases in the numerator and denominator cancel each other out.

For an attractive potential $V_0 < 0$ we can have bound states in our system, the number of these bound states scales with the strength of the potential and the width of the square well. There is at least one bound state for all values of

$$z = \frac{R\sqrt{-V_0}}{2}, \tag{2.107}$$

and new bound states appear as z crosses $n\pi$, where n is a positive integer. As a result we have n number of bound states for $z \in ((n-1)\pi, \pi]$. Their appearance can be observed in the scattering length a_0 as well, which diverges whenever z crosses a multiple of π. The scattering length a_0 can be either negative or positive, depending on the characteristics of the square well.

For a repulsive potential $V_0 > 0$ no bound states appear and the discussion of the scattering length a_0 becomes easier. The scattering length a_0 is positive and gives us information about the strength of the repulsion caused by the potential $V(r)$.

In the 2-flavour Schwinger model we can investigate elastic scattering processes, such as two pions scattering off each other. Therefore our physical situation is comparable to the repulsive square well presented above, meaning that we expect the scattering length a_0 to be positive and scale with the strength of the interaction potential.

2.8 3-particle scattering

So far we discussed scenarios with either one or two particles in the box and considered finite volume effects thereof. We saw that for 2-particle states the relative momentum is quantized and requires a correction due to the periodic nature of the finite box. This leads to a quantization condition for 2-particle scattering which is given by eq. (2.75) and a power series expansion of the scattering phase shift given by eq. (2.102). By adding more particles to the system we augment the number of degrees of freedom, which increases the difficulty for studying interactions between the particles. However, scattering processes with three particles in the box can be understood if one is willing to make some simplifying assumptions. In order to make the problem as simple as possible, we ignore relativistic effects and continue working with a 1-dimensional box of size L. We restrict ourselves to a scenario where we only allow for short-ranged 2-particle interactions, such that multi-particle interactions can only occur as a sequence of 2-particle interactions. This allows us to discuss 3-particle interactions in terms of quantities used for the 2-particle scattering process, such as the scattering phase shift $\delta(k)$. Under these aforementioned assumptions Guo [35, 36] was able to derive quantization conditions by following those three steps:

- Construct the free space 3-particle wavefunction.
- Construct the finite volume 3-particle wavefunction (i.e. the wavefunction bounded by the box of size L), using the free space wavefunction.
- Match those two expressions against each other and derive the desired quantization conditions for the 3-particle interaction.

Using this strategy, Guo derived the following quantization conditions

$$\begin{aligned}
\cot\left(\delta(-q_{31}) - \delta(-q_{23})\right) + \cot\left(\frac{PL - p_3 L}{2}\right) &= 0, \\
\cot\left(-\delta(-q_{31}) - \delta(q_{12})\right) + \cot\left(\frac{PL - p_1 L}{2}\right) &= 0, \\
\cot\left(\delta(-q_{23}) + \delta(q_{12})\right) + \cot\left(\frac{PL - p_2 L}{2}\right) &= 0,
\end{aligned} \tag{2.108}$$

where δ denotes the 2-particle scattering phase shift and L is the box size. The total momentum is given by P, while q_{ij} denote the relative momenta between particle i and j. The parameter q_k denotes some modified relative momentum between the particle k and the remaining two particles. Concretely, we have

$$P = \sum_{i=1}^{3} p_i, \qquad q_{ij} = \frac{p_i - p_j}{2} \qquad \text{and} \qquad q_k = \frac{p_i + p_j - 2p_k}{3}. \tag{2.109}$$

Again the center of mass momentum P is quantized within the box and takes values given by $P = \frac{2\pi}{L} d$ with $d \in \mathbb{Z}$. Note, that out of the three equations, only two are independent.

3 Canonical formulation

In this chapter we introduce the canonical formulation for the 1- and 2-flavour Schwinger model and discuss some related subjects. We start from the grand-canonical partition function for the 1-flavour Schwinger model and recapitulate some details of the Wilson Dirac formulation. We proceed with the dimensional reduction of the determinant of the Wilson Dirac operator, which establishes the connection between the grand-canonical partition function and the canonical one. Next, we discuss several topics related to the dimensional reduction and the resulting quark sectors. We finish this chapter by generalizing the introduced concepts to the 2-flavour variant of the Schwinger model and setting the framework needed for further calculations.

Throughout this chapter, we will be working on the lattice as introduced in section 2.4 and explained in more detail in the appendix chapter A. The lattice will be of extent $L \times L_t$ (with $T = \frac{1}{L_t}$) and for the sake of readability we set the lattice spacing to one, $a = 1$.

3.1 Partition function for the 1-flavour Schwinger model

Consider the Euclidean lattice action $S[\bar{\psi}, \psi, U, \mu_q]$ for the 1-flavour Schwinger model (we omit the index E), as derived in appendix chapter A. We assume that the reader has read appendix chapter A and is familiar with the notation used in this chapter. The grand-canonical partition function at temperature T and quark chemical potential μ_q is defined as

$$\mathcal{Z}_{GC}(T, \mu_q) = \int \mathcal{D}U \mathcal{D}\bar{\psi} \mathcal{D}\psi e^{-S[\bar{\psi}, \psi, U, \mu_q]} \tag{3.1}$$

$$= \int \mathcal{D}U \left(\int \mathcal{D}\bar{\psi} \mathcal{D}\psi e^{-S_F[\bar{\psi}, \psi, U, \mu_q]} \right) e^{-S_g[U]} \tag{3.2}$$

$$= \int \mathcal{D}U \, Z_F[U, \mu_q] e^{-S_g[U]}, \tag{3.3}$$

where $S_g[U]$ is the discretized plaquette action, describing the kinetic part of the gauge fields and $Z_F[U, \mu_q]$ is the fermionic part of the action, which can be evaluated explicitly. In order to do so we rewrite the fermionic part S_F. We consider the full Wilson Dirac operator $K_{\alpha,\beta}(n, m)$ given by eq. (A.65), with Dirac indices $\{\alpha, \beta\}$ and spacetime indices $\{n, m\}$ and merge the indices together, such that

$$K_{\alpha,\beta}(n, m) \to K_{i,j}. \tag{3.4}$$

As a result, the fermionic part of the action reads,

$$S_F[\bar{\psi}, \psi, U, \mu_q] = \sum_{\alpha,\beta,n,m} \bar{\psi}_\alpha(n) K_{\alpha,\beta}(n, m) \psi_\beta(m) = \sum_{i,j}^{N} \bar{\psi}_i K_{i,j} \psi_j, \tag{3.5}$$

with $N = 2LL_t$ even. Utilizing the Grassmann integration rules, one can integrate out the fermion fields and obtains

$$Z_F[U, \mu_q] = \int \mathcal{D}\bar{\psi} \mathcal{D}\psi e^{-S_F[\bar{\psi}, \psi, U, \mu_q]} = \det(\mathbf{K}[U, \mu_q]), \tag{3.6}$$

where $\mathbf{K}[U, \mu_q] = K_{\alpha,\beta}(n, m)$ denotes the full Wilson Dirac operator. Consequently, the grand-canonical partition function for the 1-flavour Schwinger model reads

$$\mathcal{Z}_{GC}(T, \mu_q) = \int \mathcal{D}U \det(\mathbf{K}[U, \mu_q]) e^{-S_g[U]}. \tag{3.7}$$

Compared to the canonical partition function, the grand-canonical partition function is a more general object, which not only allows for variation of the energy but also a variation of the particle number. The

parameter for the variation of the particle number is the quark chemical potential μ_q. The canonical partition function at a temperature T and fixed net number of fermions k is given by

$$\mathcal{Z}_k(T) = \int \mathcal{D}U e^{-S_g[U]} \det_k(\mathbf{K}[U]), \tag{3.8}$$

where $\det_k(\mathbf{K}[U])$ denotes the canonical determinant of order k. The grand-canonical partition function can be connected to the canonical ones by using the fugacity expansion

$$\mathcal{Z}_{GC}(T, \mu_q) = \sum_{k=-L}^{L} e^{\mu_q k/T} \mathcal{Z}_k(T). \tag{3.9}$$

The fugacity expansion allows us to decompose the grand-canonical partition function into sectors with different net-fermion numbers, which are characterized by the difference of fermions going forward and antifermions going backwards in time. Note that on the lattice this sum is restricted by the volume. Furthermore, due to the Gauss law, the only non-vanishing canonical contribution arises from the $k = 0$ sector. The fugacity expansion eq. (3.9) makes it evident that the canonical partition function can be written as a Fourier transformation of the grand-canonical partition function, which is accomplished by utilizing

$$\det_k(\mathbf{K}[U]) = \frac{1}{2\pi} \int_0^{2\pi} d\phi e^{-ik\phi} \det(\mathbf{K}[U, \mu_q = i\phi T]), \tag{3.10}$$

such that

$$\mathcal{Z}_k(T) = \frac{1}{2\pi} \int_0^{2\pi} d\phi e^{-ik\phi} \mathcal{Z}_{GC}(T, \mu = i\phi T). \tag{3.11}$$

Those relations establish the connection between the canonical and the grand-canonical partition function of the 1-flavour Schwinger model. We will have a detailed look at the dimensional reduction of the Wilson Dirac operator in section (3.3) and establish the formal connection between the canonical and grand-canonical partition function on the lattice via the corresponding determinants

$$\det(\mathbf{K}[U, \mu_q]) \leftrightarrow \det_k(\mathbf{K}[U]). \tag{3.12}$$

This allows us to gain deeper insight into the structure and symmetries of the partition functions and allows us to show that

$$\mathcal{Z}_k(T) = \mathcal{Z}^*_{-k}(T). \tag{3.13}$$

3.2 Outline of the 1-flavour Schwinger model on the lattice

First, we want to recall the Wilson Dirac formulation for the Schwinger model. As illustrated in the appendix chapter A the fermionic part of the 1-flavour Schwinger model Euclidean action with quark chemical potential μ_q is given by

$$S_F[\bar{\psi}, \psi, U, \mu_q] = \sum_{\alpha,\beta,n,m} \bar{\psi}_\alpha(n) K_{\alpha,\beta}(n, m) \psi_\beta(m), \tag{3.14}$$

where the Dirac operator is given by eq. (A.65), that is

$$\begin{aligned} K_{\alpha,\beta}(n, m) = \delta_{\alpha,\beta}\delta_{n,m}(m_0 + 2r) - \frac{1}{2}\left((r - \gamma_1)_{\alpha,\beta} U_{n,m} \delta_{m,n+\hat{1}} + (r + \gamma_1)_{\alpha,\beta} U_{n,m} \delta_{m,n-\hat{1}}\right) \\ - \frac{1}{2}\left(e^{\mu_q}(r - \gamma_0)_{\alpha,\beta} U_{n,m} \delta_{m,n+\hat{0}} + e^{-\mu_q}(r + \gamma_0)_{\alpha,\beta} U_{n,m} \delta_{m,n-\hat{0}}\right). \end{aligned} \tag{3.15}$$

The gamma matrices γ_0, γ_1 are given by $\gamma_0 = \sigma_z$ and $\gamma_1 = \sigma_x$. The vectors n and m are 2-component vectors denoting points on the spacetime lattice. A point n reads $n = (n_0, n_1)$, where $n_0 \in \{1, 2, 3, \ldots, L_t\}$ denotes the Euclidean time-component and $n_1 \in \{1, 2, 3 \ldots, L\}$ the space-component. The gauge-links

are represented by the factors $U_{n,m} \in U(1)$, fulfilling $U_{n,m} = U^{\dagger}_{m,n}$. Spatial shifts are indicated by $\pm\hat{1}$ and temporal shifts are indicated $\pm\hat{0}$, such that

$$n + \hat{\mu} = \begin{cases} (n_0 \pm 1, n_1), \text{ if } \hat{\mu} = \pm\hat{0}, \\ (n_0, n_1 \pm 1), \text{ if } \hat{\mu} = \pm\hat{1}. \end{cases} \tag{3.16}$$

In the first step we are going to rescale the theory by a factor $2\kappa = \frac{1}{m_0+2r}$, such that $\frac{1}{\sqrt{2\kappa}}\psi \to \psi$. We define the projectors in temporal direction by $P(\pm 0) = \frac{1}{2}(1 \mp \sigma_z)$ and the projectors in spatial direction by $P(\pm 1) = \frac{1}{2}(1 \mp \sigma_x)$. Finally, we can write down the massive 1-flavour Wilson Dirac operator in the form

$$\begin{aligned} K_{\alpha,\beta}(n,m) = \delta_{\alpha,\beta}\delta_{n,m} &- 2\kappa \left(P(1)_{\alpha,\beta} U_{n,m} \delta_{m,n+\hat{1}} + P(-1)_{\alpha,\beta} U_{n,m} \delta_{m,n-\hat{1}} \right) \\ &- 2\kappa \left(P(0)_{\alpha,\beta} U_{n,m} \delta_{m,n+\hat{0}} e^{\mu_q} + P(-0)_{\alpha,\beta} U_{n,m} \delta_{m,n-\hat{0}} e^{-\mu_q} \right), \end{aligned} \tag{3.17}$$

which is a matrix of size $N^2 = (2LL_t)^2$. We impose periodic boundary conditions in spatial direction and antiperiodic boundary conditions for the fermions in temporal direction.

3.3 Dimensional reduction of the Wilson Dirac operator

In the previous section we introduced the rescaled Wilson Dirac operator. The determinant of the Wilson Dirac operator describes the set of all possible closed paths on the lattice, weighted and restricted by the specific form of the Dirac operator. Note that the dimensional reduction we perform here also works - slightly modified - for the Dirac operator of the QCD-action [10], however, in this section we will only consider the reduction for the 1-flavour Schwinger model specifically. For convenience we introduce $P_{\pm} = P(\pm 0)$ and $A^{+}_{t} = e^{\mu_q} \cdot \mathbb{1}_{2,2} \otimes U_t = (A^{-}_{t})^{-1}$, where U_t is diagonal and represents all the temporal gauge-links on the lattice from time-slice t to timeslice $t+1$. Note that these two objects commute since $A^{\pm}_{i}$ acts trivial in Dirac space, s.t. $[A^{\pm}_{i}, P_s] = 0, \forall s \in \{+,-\}$. The first line of eq. (3.17) describes the spatial part of the Wilson Dirac operator. Plugging in $P(\pm 1)$, this part can be expressed in terms of a spatial matrix B_t (for a fixed time-slice t), which is given by

$$B_t = \begin{pmatrix} D & C \\ C & D \end{pmatrix}, \tag{3.18}$$

with the matrices C and D, each of size L^2, given by

$$D = \delta_{n,m} - \kappa(U_{n,m}\delta_{m,n+\hat{1}} + U_{n,m}\delta_{m,n-\hat{1}}) \tag{3.19}$$

$$C = \kappa(U_{n,m}\delta_{m,n+\hat{1}} - U_{n,m}\delta_{m,n-\hat{1}}). \tag{3.20}$$

Using the spatial matrices B_t the Wilson Dirac operator is given by

$$\mathbf{K} = \begin{pmatrix} B_1 & -2\kappa P_+ A^{+}_{1} & & & & \pm 2\kappa P_- A^{-}_{L_t} \\ -2\kappa P_- A^{-}_{1} & B_2 & -2\kappa P_+ A^{+}_{2} & & & \\ & -2\kappa P_- A^{-}_{2} & B_3 & -2\kappa P_+ A^{+}_{3} & & \\ & & \ddots & \ddots & \ddots & \\ & & & -2\kappa P_- A^{-}_{L_t-2} & B_{L_t-1} & -2\kappa P_+ A^{+}_{L_t-1} \\ \pm 2\kappa P_+ A^{+}_{L_t} & & & & -2\kappa P_- A^{-}_{L_t-1} & B_{L_t} \end{pmatrix}, \tag{3.21}$$

where we used the short hand notation

$$\mathbf{K} = \mathbf{K}[U, \mu_q] = K_{\alpha,\beta}(n,m). \tag{3.22}$$

We denoted the boundary conditions in time-direction by a factor ± 1 on the very off-diagonal elements, i.e. the very top right and the very bottom left entries. Antiperiodic boundary conditions require a $+1$, periodic ones a -1. For the sake of convenience, we will work with periodic boundary conditions and make the replacement $A^{\pm}_{L_t} \to -A^{\pm}_{L_t}$ in the end. Some more objects are needed, namely a projection

matrix

$$\mathbf{P} = \begin{pmatrix} P_+ & P_- & & & & \\ & P_+ & P_- & & & \\ & & P_+ & P_- & & \\ & & \ddots & \ddots & \ddots & \\ & & & & P_+ & P_- \\ P_- & & & & & P_+ \end{pmatrix}, \tag{3.23}$$

which is of size $(2LL_t)^2$ and fulfills $\det(\mathbf{P}) = 1$. Furthermore, we need the following matrices of size $(2L)^2$

$$R_i = B_i P_+ - 2\kappa A_{i-1}^- P_- = (B_i P_+ + P_-).(P_+ - 2\kappa A_{i-1}^- P_-) = Q_i^-.(P_+ - 2\kappa A_{i-1}^- P_-), \tag{3.24}$$

$$S_i = B_i P_- - 2\kappa A_i^+ P_+ = (B_i P_- + P_+).(P_- - 2\kappa A_i^+ P_+) = Q_i^+.(P_- - 2\kappa A_i^+ P_+), \tag{3.25}$$

which describe hops forward (S_i) and backwards in time (R_i). Note that the $Q_i^\pm$ are completely independent of any temporal gauge fields.

After setting up all the needed definitions, we perform the dimensional reduction on the Wilson Dirac operator. In a first step we rewrite the Wilson Dirac operator into the form

$$\begin{aligned} \mathbf{K} = &\begin{pmatrix} B_1 & 0 & & & & & -2\kappa P_- A_{L_t}^- \\ -2\kappa P_- A_1^- & B_2 & 0 & & & & \\ & -2\kappa P_- A_2^- & B_3 & 0 & & & \\ & & \ddots & \ddots & \ddots & & \\ & & & -2\kappa P_- A_{L_t-2}^- & B_{L_t-1} & 0 & \\ 0 & & & & -2\kappa P_- A_{L_t-1}^- & B_{L_t} \end{pmatrix} P_- \\ + &\begin{pmatrix} B_1 & -2\kappa P_+ A_1^+ & & & & & 0 \\ & B_2 & -2\kappa P_+ A_2^+ & & & & \\ & & B_3 & -2\kappa P_+ A_3^+ & & & \\ & & \ddots & \ddots & \ddots & & \\ & & & & B_{L_t-1} & -2\kappa P_+ A_{L_t-1}^+ & \\ -2\kappa P_+ A_{L_t}^+ & & & & & B_{L_t}. \end{pmatrix} P_+, \end{aligned} \tag{3.26}$$

where we just took advantage of the properties of the projection operators. The multiplication with the matrices $P_\pm$ is meant to be componentwise. The object of interest which is the determinant of the Wilson Dirac operator then fulfills

$$|\mathbf{K}| = |\mathbf{K}.\mathbf{P}|, \tag{3.27}$$

where we introduced a shorthand notation for the determinant in terms of vertical lines

$$|\mathbf{K}| := \det(\mathbf{K}). \tag{3.28}$$

The product $\mathbf{K}.\mathbf{P}$ is given by

$$\mathbf{K}.\mathbf{P} = \begin{pmatrix} R_1 & S_1 & & & & \\ 0 & R_2 & S_2 & & & \\ & 0 & R_3 & S_3 & & \\ & & \ddots & \ddots & \ddots & \\ & & & & R_{L_t-1} & S_{L_t-1} \\ S_{L_t} & & & & & R_{L_t} \end{pmatrix}. \tag{3.29}$$

After defininining the block-diagonal matrix $\mathbf{R} = \mathrm{diag}[R_1, \ldots, R_{L_t}]$, one concludes that the determinant of $\mathbf{K}$ can be written as

$$|\mathbf{K}| = |\mathbf{R}.\mathbf{R}^{-1}.\mathbf{K}.\mathbf{P}| = |\mathbf{R}||\mathbf{R}^{-1}.\mathbf{K}.\mathbf{P}|, \tag{3.30}$$

where $|\mathbf{R}|$ is a bulk factor and can be written as $|\mathbf{R}| = \prod_{i=1}^{L_t} |R_i|$. We continue working with $\mathbf{R}^{-1}.\mathbf{K}.\mathbf{P}$ and notice that

$$\mathbf{R}^{-1}.\mathbf{K}.\mathbf{P} = \begin{pmatrix} 1 & T_1 & & & & & \\ 0 & 1 & T_2 & & & & \\ & 0 & 1 & T_3 & & & \\ & & \ddots & \ddots & \ddots & & \\ & & & & 1 & T_{L_t-1} & \\ T_{L_t} & & & & & 1 & \end{pmatrix}, \tag{3.31}$$

where T_i is defined as $T_i = R_i^{-1} S_i$ and can be interpreted as a transfer matrix from time-slice i to timeslice $i+1$. Furthermore, we see that $\mathbf{R}^{-1}.\mathbf{K}.\mathbf{P}$ has the form needed in order to utilize the Schur complement formula (see appendix section D.2), that is

$$\det \begin{pmatrix} A & B \\ C & D \end{pmatrix} = (\det A) \det(D - CA^{-1}B). \tag{3.32}$$

Using the Schur complement formula with $A = \mathbb{1}$, $B = (T_1, 0, \ldots, 0)$, $C = (0, \ldots, T_{L_t})^T$ and

$$D = \begin{pmatrix} 1 & T_2 & & & & & \\ 0 & 1 & T_3 & & & & \\ & 0 & 1 & T_4 & & & \\ & & \ddots & \ddots & \ddots & & \\ & & & & 1 & T_{L_t-1} & \\ & & & & & 1 & \end{pmatrix}, \tag{3.33}$$

we obtain for the determinant

$$|\mathbf{R}^{-1}.\mathbf{K}.\mathbf{P}| = \begin{vmatrix} 1 & T_2 & & & & & \\ 0 & 1 & T_3 & & & & \\ & 0 & 1 & T_4 & & & \\ & & \ddots & \ddots & \ddots & & \\ & & & & 1 & T_{L_t-1} & \\ -T_{L_t}.T_1 & & & & & 1 & \end{vmatrix}. \tag{3.34}$$

Applying the Schur complement formula $L_t - 1$ times then leads to

$$|\mathbf{R}^{-1}.\mathbf{K}.\mathbf{P}| = |1 + (-1)^{L_t-1} T_{L_t}.T_1.T_2 \ldots T_{L_t-1}| \tag{3.35}$$

$$= |1 + (-1)^{L_t-1} T_1.T_2 \ldots T_{L_t-1}.T_{L_t}|. \tag{3.36}$$

For the sake of convenience we will assume L_t to be even such that we obtain

$$|\mathbf{K}| = |\mathbf{R}||\mathbf{R}^{-1}.\mathbf{K}.\mathbf{R}| \tag{3.37}$$

$$= |\mathbf{R}||1 - T_1.T_2 \ldots T_{L_t-1}.T_{L_t}| \tag{3.38}$$

$$\overset{\substack{\text{ap.}\\ \text{bc.}}}{=} |\mathbf{R}||1 + \prod_{i=1}^{L_t} T_i|. \tag{3.39}$$

In the last step, that is line (3.39), we took into account the antiperiodic boundary condition by replacing $T_{L_t} \to -T_{L_t}$ (which is equivalent to making the replacement $A_{L_t}^{\pm} \to -A_{L_t}^{\pm}$). In order to separate the dependence of the chemical potential μ_q from the gauge fields A_t we examine the bulk factor $|\mathbf{R}|$ and the factor $|1 + \prod_{i=1}^{L_t} T_i|$ separately.

3.3.1 Examination of the bulk factor |R|

The complex-valued bulk factor $|\mathbf{R}|$ contains an $e^{-\mu_q}$ factor which can be factorized out by using the block structure of R_i

$$|\mathbf{R}| = \prod_{i=1}^{L_t} |R_i| = \prod_{i=1}^{L_t} |B_i P_+ - 2\kappa A_{i-1}^- P_-| = \prod_{i=1}^{L_t} |B_i||2\kappa A_{i-1}^-| \tag{3.40}$$

$$= \prod_{i=1}^{L_t} |B_i||2\kappa U_i^\dagger| e^{-\mu_q L} = e^{-\mu_q L_t L} \prod_{i=1}^{L_t} |B_i||2\kappa U_i^\dagger|. \tag{3.41}$$

Although we were able to factorize out the quark chemical potential, the bulk factor still contains a complex phase of the form

$$|\mathbf{R}| \propto \prod_{i=1}^{L_t} |U_i^\dagger|, \tag{3.42}$$

which will be of importance once we demonstrate the reflection symmetry of the canonical determinant in appendix section G.4.

3.3.2 Examination of $|1 + \prod_{i=1}^{L_t} T_i|$

We note that each transfer matrix T_i can be computed as

$$T_i = R_i^{-1}.S_i = (P_+ - 2\kappa P_- A_{i-1}^-)^{-1}.(Q_i^-)^{-1}.Q_i^+.(P_- - 2\kappa P_+ A_i^+), \tag{3.43}$$

where we used the expressions for R_i and S_i in eqs. (3.24) and (3.25). The inverse of $(P_+ - 2\kappa P_- A_{i-1}^-)$ can be evaluated to be

$$(P_+ - 2\kappa P_- A_{i-1}^-)^{-1} = (P_+ - \frac{1}{2\kappa} P_- A_{i-1}^+), \tag{3.44}$$

which yields a simplified expression for two consecutive transfer matrices $T_i T_{i+1}$, such that

$$T_i T_{i+1} \propto (P_- - 2\kappa P_+ A_i^+).(P_+ - \frac{1}{2\kappa} P_- A_i^+) = -(2\kappa P_+ + \frac{1}{2\kappa} P_-) A_i^+. \tag{3.45}$$

After recalling the definition of A_i^+ and defininig

$$\tilde{U}_i = (2\kappa P_+ + \frac{1}{2\kappa} P_-).(\mathbb{1}_{2,2} \otimes U_i) \tag{3.46}$$

we realize that the μ_q-dependence can be factorized out such that

$$-(2\kappa P_+ + \frac{1}{2\kappa} P_-) A_i^+ = -\tilde{U}_i e^{\mu_q}. \tag{3.47}$$

Since we assumed L_t to be even, we have an even number of these minus signs. Upon combining all contributions we obtain

$$|1 + \prod_{i=1}^{L_t} T_i| = |1 + \prod_{i=1}^{L_t} (Q_i^-)^{-1} Q_i^+ \tilde{U}_i e^{\mu_q}| = |1 + e^{\mu_q L_t} \mathcal{T}|, \tag{3.48}$$

where in the last step we implicitely defined the full transfer matrix $\mathcal{T}$

$$\boxed{\mathcal{T} = \prod_{i=1}^{L_t} (Q_i^-)^{-1} Q_i^+ \tilde{U}_i}. \tag{3.49}$$

Note, that we use the definition of a transfer matrix interchangeably, it can either mean the transfer matrix T_i on a fixed time-slice i or the product presented above. Additionally, it is worth noticing that for vanishing quark chemical potential $\mu_q = 0$ the full transfer matrix can be written as product of the time-slice transfer matrices T_i

$$\mathcal{T} = \prod_{i=1}^{L_t} (Q_i^-)^{-1} Q_i^+ \tilde{U}_i \overset{!}{=} \prod_{i=1}^{L_t} T_i \Big|_{\mu_q = 0}. \tag{3.50}$$

After recalling that the transfer matrix is of size $(2L)^2$ and using the multilinearity of the determinant, one obtains

$$|1 + \prod_{i=1}^{L_t} T_i| = |1 + e^{\mu_q L_t} \mathcal{T}| = e^{2\mu_q L_t L} |e^{-\mu_q L_t} + \mathcal{T}|. \tag{3.51}$$

3.3.3 Constructing the full Wilson Dirac determinant

Combining the two factors we obtain

$$\begin{aligned}|\mathbf{K}| &= |\mathbf{R}||1+\prod_{i=1}^{L_t} T_i| \\ &= \left(\prod_{i=1}^{L_t} |B_i||2\kappa U_i^\dagger|\right) e^{\mu_q L_t L}|e^{-\mu_q L_t}+\mathcal{T}|. \end{aligned} \tag{3.52}$$

The last factor can be simplified using the algebraic formulas for the characteristic polynomial derived in the appendix chapter D. Specifically, we will use the characteristic polynomial (D.23), that is

$$p_A(t) = |t\mathbb{1} - A| = t^n - E_1(A) + \cdots + (-1)^n E_n(A), \tag{3.53}$$

where A denotes a $n \times n$ matrix and the factor $E_k(A)$ denotes the sum over all principal minors of size k

$$E_k(A) = \sum_{I,|I|=k} \det(A^{II}). \tag{3.54}$$

We use the characteristic polynomial with $t = e^{-\mu_q L_t}$, $A = -\mathcal{T}$ and $n = 2L$. Upon using the multilinearity of the determinant we conclude that

$$E_k(-\mathcal{T}) := \sum_{I,|I|=k} \det(-\mathcal{T}^{II}) = (-1)^k \sum_{I,|I|=k} \det(\mathcal{T}^{II}) = (-1)^k E_k(\mathcal{T}). \tag{3.55}$$

As a result, we obtain

$$|\mathbf{K}| = \left(\prod_{i=1}^{L_t} |B_i||2\kappa U_i^\dagger|\right) e^{\mu_q L_t L}|e^{-\mu_q L_t}+\mathcal{T}| \tag{3.56}$$

$$= \left(\prod_{i=1}^{L_t} |B_i||2\kappa U_i^\dagger|\right) e^{\mu_q L_t L}(e^{-\mu_q L_t 2L} + E_1(\mathcal{T})e^{-\mu_q L_t(2L-1)} + \cdots + E_{2L-1}(\mathcal{T})e^{-\mu_q L_t} + E_{2L}(\mathcal{T})). \tag{3.57}$$

After simplifying this expression, we obtain

$$\boxed{\det(\mathbf{K}[U,\mu_q]) = \sum_{k=-L}^{L} e^{\mu_q L_t k} \det{}_k(\mathbf{K}[U])}, \tag{3.58}$$

where we implicitely defined the canonical determinant $\det_k(\mathbf{K}[U])$ as

$$\boxed{\det{}_k(\mathbf{K}[U]) = \left(\prod_{i=1}^{L_t} |B_i||2\kappa U_i^\dagger|\right) E_{k+L}(\mathcal{T}) = \left(\prod_{i=1}^{L_t} |B_i||2\kappa U_i^\dagger|\right) \sum_{I,|I|=k+L} \det(\mathcal{T}^{II})}, \tag{3.59}$$

where the full transfer matrix $\mathcal{T}$ is given by eq. (3.49). These last two equations conclude the derivation of the canonical determinant for the 1-flavour Schwinger model. In order to establish the connection between the canonical and the grand-canonical partition function (see section 3.1), we simply plug in eq. (3.58) into the formula for the grand-canonical partition function, that is eq. (3.7).

3.3.4 The structure of the transfer matrix $\mathcal{T}$

In this subsection we want to have a closer look at the transfer matrix $\mathcal{T}$ and its components. We already established that the basic form of $\mathcal{T}$ is given by

$$\mathcal{T} = \prod_{i=1}^{L_t} (Q_i^-)^{-1} Q_i^+ \tilde{U}_i, \quad \text{where} \quad \tilde{U}_i = (2\kappa P_+ + \frac{1}{2\kappa} P_-).(\mathbb{1}_{2,2} \otimes U_i), \tag{3.60}$$

is diagonal and represents all the temporal gauge-links on time-slice i. First we want to have a closer look at the $Q_i^{\pm}$'s which are of size $(2L)^2$. Utilizing the explicit form of B_i and $P_{\pm}$ one obtains

$$Q_i^- = B_i P_+ + P_- = \begin{pmatrix} \mathbb{1} & C_i \\ 0 & D_i \end{pmatrix} \quad \text{and} \quad Q_i^+ = B_i P_- + P_+ = \begin{pmatrix} D_i & 0 \\ C_i & \mathbb{1} \end{pmatrix}. \tag{3.61}$$

This simplified form is of great utility, since it allows us to compute the inverse of Q_i^- in a straightforward way, such that

$$(Q_i^-)^{-1} = \begin{pmatrix} \mathbb{1} & -C_i D_i^{-1} \\ 0 & D_i^{-1} \end{pmatrix}. \tag{3.62}$$

Next we will have a look at the specific form of $\tilde{U}_i$. Assume that all the temporal $U(1)$ gauge-links on time slice i are described by L angles $\{\varphi_1, \ldots, \varphi_L\}$, then the matrix $\tilde{U}_i$ is diagonal with entries

$$\tilde{U}_i = \operatorname{diag}\left[\frac{1}{2\kappa}e^{i\varphi_1}, \frac{1}{2\kappa}e^{i\varphi_2}, \ldots, \frac{1}{2\kappa}e^{i\varphi_L}, 2\kappa e^{i\varphi_1}, 2\kappa e^{i\varphi_2}, \ldots, 2\kappa e^{i\varphi_L}\right]. \tag{3.63}$$

The objects $Q_t^{\pm}$ describe spatial hops of fermions on time-slice t, while $\tilde{U}_t$ describes fermions hopping forward in time from time-slice t to $t+1$. The first odd thing we notice is the factor $\frac{1}{2\kappa}$ in the first L entries and the factor 2κ in the last L entries, which appear naturally when deriving this contribution.

3.3.5 Spectrum of the transfer matrix $\mathcal{T}$

In the construction of the reduced Wilson Dirac operator the object of importance is the transfer matrix $\mathcal{T}$. In particular the spectrum of the transfer matrix, denoted by $\sigma(\mathcal{T})$, has some interesting properties, which we would like to explore. First, we have a look at the determinant of $\mathcal{T}$, which can easily be computed

$$\det \mathcal{T} = \prod_{i=1}^{L_t} \det((Q_i^-)^{-1}) \det(Q_i^+) \det(\tilde{U}_i) \tag{3.64}$$

$$= \prod_{i=1}^{L_t} \det(U_i)^2, \tag{3.65}$$

where we used the specific form of $\tilde{U}$ and $\det((Q_i^-)^{-1}) \det(Q_i^+) = \det D^{-1} \det D = 1$. Secondly one can show that the eigenvalues of $\mathcal{T}$ come in pairs. In order to see this we first convince ourselves that the combination $(Q_i^-)^{-1} Q_i^+$ can be written as

$$(Q_i^-)^{-1} Q_i^+ = \begin{pmatrix} 1 & -C_i \\ 0 & 1 \end{pmatrix} \begin{pmatrix} D_i & 0 \\ 0 & D_i^{-1} \end{pmatrix} \begin{pmatrix} 1 & 0 \\ C_i & 1 \end{pmatrix}. \tag{3.66}$$

In this form it is easy to compute the inverse

$$[(Q_i^-)^{-1} Q_i^+]^{-1} = \begin{pmatrix} 1 & 0 \\ -C_i & 1 \end{pmatrix} \begin{pmatrix} D_i^{-1} & 0 \\ 0 & D_i \end{pmatrix} \begin{pmatrix} 1 & C_i \\ 0 & 1 \end{pmatrix}. \tag{3.67}$$

Utilizing the fact that D is hermitian and $C = -C^\dagger$ we obtain

$$([(Q_i^-)^{-1} Q_i^+]^{-1})^\dagger = \begin{pmatrix} 1 & 0 \\ -C_i & 1 \end{pmatrix} \begin{pmatrix} D_i^{-1} & 0 \\ 0 & D_i \end{pmatrix} \begin{pmatrix} 1 & C_i \\ 0 & 1 \end{pmatrix}, \tag{3.68}$$

and find

$$([(Q_i^-)^{-1} Q_i^+]^{-1})^\dagger = S(Q_i^-)^{-1} Q_i^+ S^{-1}, \text{ with } S = S^{-1} = \begin{pmatrix} 0 & 1 \\ 1 & 0 \end{pmatrix}. \tag{3.69}$$

Furthermore, also the gauge fields transform similarly as

$$(\tilde{U}_i^{-1})^\dagger = S \tilde{U}_i S^{-1}. \tag{3.70}$$

Using these previous results one obtains for the full transfer matrix $\mathcal{T}$

$$(\mathcal{T}^{-1})^\dagger = ([(Q_1^-)^{-1}Q_1^+]^{-1})^\dagger(\tilde{U}_1^{-1})^\dagger \dots ([(Q_{L_t}^-)^{-1}Q_{L_t}^+]^{-1})^\dagger(\tilde{U}_{L_t}^{-1})^\dagger \tag{3.71}$$

$$= S[(Q_1^-)^{-1}Q_1^+]\tilde{U}_1 \dots [(Q_{L_t}^-)^{-1}Q_{L_t}^+]\tilde{U}_{L_t}S^{-1}, \tag{3.72}$$

$$(\mathcal{T}^{-1})^\dagger = S\mathcal{T}S^{-1}. \tag{3.73}$$

Consequently, the transfer matrix $\mathcal{T}$ shares its eigenvalue-spectrum with $(\mathcal{T}^{-1})^\dagger$ i.e. $\sigma(\mathcal{T}) = \sigma((\mathcal{T}^{-1})^\dagger)$, which indicates that for every eigenvalue $\lambda \in \sigma(\mathcal{T})$ we have an eigenvalue $\frac{1}{\lambda^*} \in \sigma(\mathcal{T})$. This symmetry hints that one could further reduce the transfer matrix by a factor 2 without losing information. The spectrum of the transfer matrix $\mathcal{T}$ can be written down as

$$\sigma(\mathcal{T}) = \{\lambda_1, \dots, \lambda_L, \frac{1}{\lambda_1^*}, \dots, \frac{1}{\lambda_L^*}\}, \tag{3.74}$$

respectively

$$\sigma(\mathcal{T}) = \{r_1 e^{i\phi_1}, \dots, r_L e^{i\phi_L}, \frac{1}{r_1}e^{i\phi_1}, \dots, \frac{1}{r_L}e^{i\phi_L}\}, \tag{3.75}$$

where we introduced radii and angles to describe the spectrum of the transfer matrix. If we write the determinant of $\mathcal{T}$ as a product of the eigenvalues, we obtain

$$\det \mathcal{T} = \prod_{i=1}^{L} \frac{\lambda_i}{\lambda_i^*} = e^{2i\Phi}, \quad \text{with} \quad \Phi = \sum_{i=1}^{L} \phi_i, \tag{3.76}$$

where Φ denotes the sum over all angles. Utilizing above relation for the determinant of $\mathcal{T}$, one can show that the canonical determinant fulfills a reflection symmetry, such that

$$\det_k^*(\mathbf{K}) = \det_{-k}(\mathbf{K}) \quad \forall k \in \{0, \dots, L\}. \tag{3.77}$$

The details of this derivation are given in the appendix section G.4.

3.4 Discussion and interpretation of the canonical determinant

Each entry in the Wilson Dirac operator can be interpreted as a fermion hopping from one lattice site to another one. These entries are now processed into the canonical determinant and still retain their meaning. We discussed the derivation of the reduced matrix, which allows us to directly compute the determinant of the Wilson Dirac operator by using eqs. (3.58) and (3.59), that is

$$\det(\mathbf{K}[U, \mu_q]) = \sum_{k=-L}^{L} e^{\mu_q L_t k} \det_k(\mathbf{K}[U]), \quad \text{with} \tag{3.78}$$

$$\det_k(\mathbf{K}[U]) = \left(\prod_{i=1}^{L_t} |B_i| |2\kappa U_i^\dagger|\right) \sum_{I, |I|=k+L} \det(\mathcal{T}^{II}). \tag{3.79}$$

The summation over all principal minors of a canonical sector is quite trivial if one is interested in cases of "extreme" fermion numbers, i.e. a system which is saturated either by fermions or antifermions. In order to have a close look at these cases, one fixes the net-fermion number to either $k = L$ (saturation with L fermions propagating forward in time) or $k = -L$ (saturation with L antifermions going backwards in time). Here we discuss these cases, the computational aspects for the calculations of the canonical determinant are elaborated in the appendix chapter E.

3.4.1 Saturation with antifermions $k = -L$

Let us first consider the extreme case, where we saturate the system with L antifermions propagating backwards in time. Each of those antifermions wraps around the lattice at the temporal boundary, which yields a factor $(e^{-\mu_q})^{L_t}$. Taking into account not one, but all the L antifermions we end up with an overall factor $(e^{-\mu_q})^{L_t L}$, which is exactly the prefactor of the canonical determinant $\det_{-L}(\mathbf{K}[U])$ in eq. (3.78). To obtain the canonical determinant $\det_{-L}(\mathbf{K}[U])$ we compute a sum over all principal

minors of size $|I| = -L + L = 0$. However, an index set I of size 0 is just the empty set $I = \varnothing$ and by convention, the empty principal minor is 1 (see appendix chapter D). Consequently we end up with the bulk factor only

$$\det_{-L}(\mathbf{K}[U]) = \left(\prod_{i=1}^{L_t} |B_i||2\kappa U_i^\dagger| \right) \cdot 1, \tag{3.80}$$

which factorizes nicely into a spatial and temporal contribution. Only the first component of the Dirac fermion ψ_1 (from $\psi = (\psi_1, \psi_2)$) can propagate backwards in time, while only the second component ψ_2 propagates forward in time. The backwards propagating fields pick up all the L possible gauge field contributions when passing through a time-slice i, hence we obtain the determinant of $2\kappa U_i^\dagger$. Since those antifermions pass through all time-slices we end up with a factor

$$\prod_{i=1}^{L_t} |2\kappa U_i^\dagger|. \tag{3.81}$$

The fields ψ_2 also need to be saturated for the Grassmann integration. Since we fixed the net-fermion number externally, the fields ψ_2 can only move within a fixed time-slice. The determinant $|B_i|$ takes into account all the possible closed paths of the fields ψ_2 on a fixed time-slice $t = i$. In the end the contributions from all the different time-slices read

$$\prod_{i=1}^{L_t} |B_i|. \tag{3.82}$$

The origin of these contributions stems from the bulk factor $|\mathbf{R}|$

$$\prod_{i=1}^{L_t} |R_i| = \prod_{i=1}^{L_t} |B_i P_+ + A_{i-1}^- P_-| \stackrel{!}{=} \prod_{i=1}^{L_t} |B_i||U_i^\dagger 2\kappa e^{-\mu_q}|, \tag{3.83}$$

which displays very nicely all the discussed contributions and shows their affiliation to the corresponding fields $\psi_{1,2}$ via the projection matrices $P_\pm$.

3.4.2 Saturation with fermions $k = L$

Let us now consider the opposite scenario, where the lattice is saturated with $k = L$ fermions going forward in time. Now the summation over all principal minors reduces to a summation over all index sets I of size $|I| = 2L$. Since the transfer matrix $\mathcal{T}$ is of size $(2L)^2$ itself, there is only one possible index set which comes into play, given by $I = \{1, 2, \ldots, 2L\}$, yielding the full determinant

$$E_{2L}(\mathcal{T}) = \sum_{I, |I|=2L} \det(\mathcal{T}^{II}) = \det(\mathcal{T}). \tag{3.84}$$

As a result one obtains

$$\begin{aligned} \det_L(\mathbf{K}) &= \prod_{i=1}^{L_t} |B_i||2\kappa U_i^\dagger| \cdot \det(\mathcal{T}) && (3.85)\\ &= \prod_{i=1}^{L_t} |B_i||2\kappa U_i^\dagger| \cdot \prod_{i=1}^{L_t} |U_i|^2 && (3.86)\\ &= \prod_{i=1}^{L_t} |B_i||2\kappa U_i|. && (3.87) \end{aligned}$$

Similar to before, this expression makes sense. We have L fermions travelling forward in time and consequently, the corresponding canonical determinant comes with a prefactor $(e^{\mu_q})^{LL_t}$ in the fugacity expansion. Along the way the fermions pick up all the contributions from the gauge field resulting in a multiplicative factor of $\prod_{i=1}^{L_t} |2\kappa U_i|$. Similar to before the factor $\prod_{i=1}^{L_t} |B_i|$ arises in order to take into account the spatial hops of the remaining fermionic degrees of freedom on each time-slice.

3.5 Canonical formalism with two flavours

From now on we consider the 2-flavour Schwinger model on the lattice as introduced in section 2.2. In order to discuss the 2-flavour Schwinger model in the canonical formulation some simple generalizations need to be made. We denote the two mass-degenerate quark flavours with u and d (up and down quarks) which turns the fermion wave-function into a doublet $\psi = (u, d)$. The continuum Lagrangian in Minkowski spacetime is then given by eq. (2.31)

$$\mathcal{L}[\bar{\psi}, \psi, A_\mu] = \bar{\psi}^k(x)[i\not{D} - m_0]\psi^k(x) - \frac{1}{4}F_{\mu\nu}F^{\mu\nu} \tag{3.88}$$

$$= \bar{u}(x)[i\not{D} - m_0]u(x) + \bar{d}(x)[i\not{D} - m_0]d(x) - \frac{1}{4}F_{\mu\nu}F^{\mu\nu}, \tag{3.89}$$

where a summation over the quark flavours $k \in \{u, d\}$ is implied. After performing a Wick rotation and discretizing the quark fields we implement this theory on the lattice, similar as in the 1-flavour case. We introduce quark-chemical potentials for the up and down quark (μ_u, μ_d) and define the isospin chemical potential μ_I via $\frac{\mu_I}{2} = \mu_u = -\mu_d$. The grand-canonical partition function for the 2-flavour Schwinger model then reads

$$\mathcal{Z}_{GC}(T, \mu) = \int \mathcal{D}U \det(\mathbf{K}[U, \mu_I]) \det(\mathbf{K}[U, -\mu_I]) e^{-S_g[U]}. \tag{3.90}$$

Similar to the 1-flavour case, we can now perform a dimensional reduction on each of the Wilson Dirac operators, which yields

$$\mathcal{Z}_{GC}(T, \mu) = \int \mathcal{D}U e^{-S_g[U]} \sum_{n_u=-L}^{L} \sum_{n_d=-L}^{L} e^{\frac{\mu_I}{2} L_t (n_u - n_d)} \det{}_{n_u}(\mathbf{K}[U]) \det{}_{n_d}(\mathbf{K}[U]) \tag{3.91}$$

$$= \sum_{n_u=-L}^{L} \sum_{n_d=-L}^{L} e^{\frac{\mu_I}{2} L_t (n_u - n_d)} \mathcal{Z}_{(n_u, n_d)}(T). \tag{3.92}$$

Here we introduced the 2-flavour canonical partition function

$$\mathcal{Z}_{(n_u, n_d)}(T) = \int \mathcal{D}U \det{}_{n_u}(\mathbf{K}[U]) \det{}_{n_d}(\mathbf{K}[U]) e^{-S_g[U]}, \tag{3.93}$$

which describes the quark-sector with n_u up quarks and n_d down quarks. The number of up and down quarks in our system is restricted by the Gauss' law. It requires that the total electric charge Q is zero, while the total isospin charge I is not restricted, i.e.

$$Q = n_u + n_d = 0, \quad \text{and} \quad I = \frac{n_u - n_d}{2} \quad \text{arbitrary.} \tag{3.94}$$

As a result a canonical sector with n up quarks also contains n antidown quarks (resp. $-n$ down quarks) which bind together to form n-meson states. The collection of all states with n up and $-n$ down quarks forms the canonical partition function $\mathcal{Z}_{(n,-n)}(T)$. The vacuum sector contains flavour singlet states and meson-antimeson states with isospin $I = 0$ and is described by the partition function $\mathcal{Z}_{(0,0)}(T)$.

Using the canonical formalism, we can draw a connection between the ground states of the n-meson sectors in the 2-flavour Schwinger model and the particle-spectrum thereof. The partition function $\mathcal{Z}_{(1,-1)}$ describes a theory consisting of an up quark and an antidown quark which are used to build up mesons with isospin $I = 1$. The ground state of this 1-meson sector is just the 1-meson state $|u\bar{d}\rangle$ at zero momentum constructed from the two available components.

However, the 1-meson ground state $|u\bar{d}\rangle$ is just the well-known pion state $|\pi^+\rangle$, which is a member of the pion-triplet introduced in subsection (2.2.3)!

This argument displays the one-to-one correspondence between the lightest particle of the system, which is the pion $|\pi\rangle$ and the ground state of the 1-meson sector. Using this line of argument one can immediately assign each member of the pion-triplet to its corresponding canonical partition function

$$|\pi\rangle = \begin{cases} |\pi^+\rangle = |u\bar{d}\rangle & \in \mathcal{Z}_{(1,-1)}, \\ |\pi^0\rangle = \frac{1}{\sqrt{2}}(|u\bar{u}\rangle - |d\bar{d}\rangle) & \in \mathcal{Z}_{(0,0)}, \\ |\pi^-\rangle = |\bar{u}d\rangle & \in \mathcal{Z}_{(-1,1)}. \end{cases} \tag{3.95}$$

This game can be played for any n-meson ground state. In analogy to before, the lowest energy state of the n-meson sector is constructed by taking n up quarks and n antidown quarks. The simplest state one can build with these components is the multi-pion bound state constructed from n π^+-pions

$$|(\pi^+)^n\rangle = |(u\bar{d})(u\bar{d})\dots(u\bar{d})\rangle \quad \in \mathcal{Z}_{(n,-n)}, \tag{3.96}$$

which is a member of a pion multiplet with Isospin $I = n$ and $I_z = n$.

In theory, one can build arbitrarily complicated states with more exotic quark number configurations such as $|u\bar{d}u\bar{u}\rangle$ etc., however, these are considered to be higher order energy states.

3.6 Ground state energies of the 2-flavour Schwinger model

We are interested in finding the energy of the lowest state in each n-meson sector, that is the ground state energies of the n-pion states. In order to do so, one has to examine the low-temperature behaviour of the free energy corresponding to that canonical sector

$$F(n) := F_{(n,-n)}(T) = -T\log(\mathcal{Z}_{(n,-n)}), \tag{3.97}$$

as explained by Fodor et al. in Ref. [4]. The free energy can also be used in order to define the isospin-chemical potential μ_I, a quantity which describes the response of the system, when introducing a new meson to the system. After labelling the number of mesons with n we can introduce the isospin chemical potential as

$$\mu_I(n) = F(n+1) - F(n). \tag{3.98}$$

The canonical partition function of the n-meson sector can be expressed as a sum over all energy states

$$\mathcal{Z}_{(n,-n)}(T) = \sum_{k=0}^{\infty} m_n^{(k)} e^{-E_n^{(k)}/T}, \tag{3.99}$$

where $m_n^{(k)}$ denotes the multiplicity and $E_n^{(k)}$ the energy of the k-th state of the n-meson sector. We assume these energies to be ordered, such that $E_n^{(k+1)} > E_n^{(k)}$, for all k and n. In the vacuum sector $(n_u, n_d) = (0,0)$ the lowest energy state is the vacuum state, which is assumed to be non-degenerate $(m_0^{(0)} = 1)$, such that

$$\mathcal{Z}_{(0,0)}(T) = e^{-E_0^{(0)}/T} + \sum_{k=1}^{\infty} m_0^{(k)} e^{-E_0^{(k)}/T}. \tag{3.100}$$

Using the expansion of the canonical partition function, the free energy difference can be written down as

$$\begin{aligned} F_{(n,-n)}(T) - F_{(0,0)}(T) &= -T\log\left(\frac{\mathcal{Z}_{(n,-n)}}{\mathcal{Z}_{(0,0)}}\right) \\ &= -T\log\left(\frac{m_n^{(0)} e^{-E_n^{(0)}/T}(1 + \sum_{k=1}^{\infty} \frac{m_n^{(k)}}{m_n^{(0)}} e^{-(E_n^{(k)} - E_n^{(0)})/T})}{e^{-E_0^{(0)}/T}(1 + \sum_{k=1}^{\infty} m_0^{(k)} e^{-(E_0^{(k)} - E_0^{(0)})/T})}\right) \\ &= E_{n\pi} - T\log(m_n^{(0)}) - T\log\left(\frac{1 + \sum_{k=1}^{\infty} \frac{m_n^{(k)}}{m_n^{(0)}} e^{-(E_n^{(k)} - E_n^{(0)})/T}}{1 + \sum_{k=1}^{\infty} m_0^{(k)} e^{-(E_0^{(k)} - E_0^{(0)})/T}}\right), \end{aligned} \tag{3.101}$$

where we introduced the ground state energy of the n-meson sector as

$$E_{n\pi} = (E_n^{(0)} - E_0^{(0)}) \tag{3.102}$$

and the last term in eq. (3.101) denotes corrections from higher order energy states.[1] One can define the temperature-dependent ground state energy of the n-meson sector, as a difference of the corresponding free energies

$$E_{n\pi}(T) = F_{(n,-n)}(T) - F_{(0,0)}(T). \tag{3.103}$$

[1] We denoted the ground state energies with an additional subscript π, since we established that the ground state energies of the different n-meson sectors are multi-pion states.

The true ground state energy $E_{n\pi}$ of the n-meson sector, can be obtained by extrapolating to zero temperature ($T \to 0$), such that

$$\boxed{E_{n\pi} = \lim_{T\to 0} E_{n\pi}(T) = -\lim_{T\to 0} T \log\left(\frac{\mathcal{Z}_{(n,-n)}(T)}{\mathcal{Z}_{(0,0)}(T)}\right)}. \tag{3.104}$$

Throughout chapter 4 and 5 above equation will be referred to as the "master formula".

3.6.1 Bosonic dispersion relation on the lattice

Consider now the 2-flavour Schwinger model as introduced in section 3.5 on a lattice of extent $L \times L_t$. The spectrum consists of multi-meson states as discussed in subsection 2.2.2. In order to describe the energy of those multi-meson states we write down the bosonic dispersion relation [43]. The bosonic dispersion relation for n mesons with momenta $p_i, i \in \{1, \ldots, n\}$ reads

$$E_n(p_1, p_2, \ldots, p_n) = \sum_{i=1}^{n} \cosh^{-1}\left(\cosh(m_\pi) + 1 - \cos(p_i)\right), \tag{3.105}$$

where the total momentum P is quantized on the lattice

$$P = \sum_{i=1}^{n} p_i = \frac{2\pi}{L} d, \quad \text{with} \quad d \in \mathbb{Z}. \tag{3.106}$$

One can show, that by taking the continuum limit $a \to 0$, one reproduces the well-known bosonic dispersion relation in the continuum

$$E_n(p_1, p_2, \ldots, p_n) = \sum_{i=1}^{n} \sqrt{m_\pi^2 + p_i^2}. \tag{3.107}$$

However, for our purposes the correct dispersion relation is given by eq. (3.105).

3.6.2 Examination of the vacuum sector with isospin content $I = 0$

Upon discussing the extraction of ground state energies and the bosonic dispersion relations, we are sufficiently equipped to examine the expansion for the canonical sectors

$$\mathcal{Z}_{(n,-n)}(T) = \sum_{k=0}^{\infty} m_n^{(k)} e^{-E_n^{(k)}/T}, \tag{3.108}$$

and write down explicit expressions for the multiplicities $m_n^{(k)}$ and the energies $E_n^{(k)}$. This allows us to describe the finite temperature behaviour of the system as precisely as possible. In the last part of this chapter, we derive simplified and applicable expressions for the canonical partition functions in the isospin sectors $I = 0, 1, 2$ and $I = 3$, which will be used for the numerical investigations in chapter 5.

First, let us consider the vacuum sector $\mathcal{Z}_{(0,0)}$ which has isospin content $I = 0$ and contains the vacuum state, which is the lowest lying energy state of the theory (assumed to be non-degenerate) such that

$$\mathcal{Z}_{(0,0)}(T) = e^{-E_0^{(0)}/T} + \sum_{k=1}^{\infty} m_0^{(k)} e^{-E_0^{(k)}/T}. \tag{3.109}$$

All other energy states have to be taken relative to the vacuum energy $E_0^{(0)}$. Since the overall lightest particle of the system is given by the pion-triplet, the π^0 pion at rest denotes the ground state of the vacuum sector, above the vacuum state itself. The multplicity of the π^0 state is $m_0^{(1)} = 1$, similar to the vacuum state. For the tower of states we have

$$\begin{aligned} &\text{vacuum state } \mathcal{Z}_{(0,0)} : |0\rangle, && E_0^{(0)}, m_0^{(0)} = 1, \\ &\text{ground state } \mathcal{Z}_{(0,0)} : |\pi^0\rangle, && E_{\pi^0}^{(0)}, m_0^{(1)} = 1, \end{aligned} \tag{3.110}$$

so far, where the energy of the ground state is taken as a difference to the vacuum energy

$$E_{\pi^0}^{(0)} = E_0^{(1)} - E_0^{(0)} = m_\pi. \tag{3.111}$$

The next particles which could be in line are the pseudo-scalar singlet state η or the scalar singlet state f_0. For the sake of simplicity we assume, that the η meson and the f_0 meson are much heavier than the pion. There is also a member of the a_0 triplet state presented in subsection 2.2.2 and 2.2.3, which is included in the vacuum sector. However, it is much heavier than the two singlet states and will be omitted as well.

Upon making these assumptions higher order energy states of the vacuum sector are given by excited states of the π^0 pion, which are basically π^0 pions with additional momenta $p_1 \neq 0$. The total momentum is quantized on the lattice, it is therefore straightforward to write down those excited states. Since the moving π^0 pion can only go in two directions the multiplicity of these states is just 2 i.e. $m_0^{(k)} = 2, k \geq 2$. We can now finish the list of states we started before, by writing down all states, their energy and multiplicity. Note that the number of excited π^0 states is restricted on the lattice by the volume L. We obtain

$$\begin{aligned}
\text{vacuum state } \mathcal{Z}_{(0,0)} &: |0\rangle, & E_0^{(0)}, m_0^{(0)} &= 1, \\
\text{ground state } \mathcal{Z}_{(0,0)} &: |\pi^0\rangle, & E_{\pi^0}^{(0)}, m_0^{(1)} &= 1, \\
\text{1st. excited state of } \mathcal{Z}_{(0,0)} &: |\pi^0\rangle^{(1)}, & E_{\pi^0}^{(1)}, m_0^{(2)} &= 2, \\
\text{2nd. excited state of } \mathcal{Z}_{(0,0)} &: |\pi^0\rangle^{(2)}, & E_{\pi^0}^{(2)}, m_0^{(2)} &= 2, \\
&\vdots & &\vdots \\
\frac{L}{2}\text{'th excited state of } \mathcal{Z}_{(0,0)} &: |\pi^0\rangle^{(\frac{L}{2})}, & E_{\pi^0}^{(\frac{L}{2})}, m_0^{(\frac{L}{2})} &= 2,
\end{aligned}$$

where we implicitely defined the energies of the π^0 pion states as

$$E_{\pi^0}^{(k)} = E_0^{(k+1)} - E_0^{(0)} = \cosh^{-1}\left(\cosh(m_\pi) + 1 - \cos(p^{(k)})\right), \qquad \text{with } p^{(k)} = \frac{2\pi}{L} \cdot k. \tag{3.112}$$

For the sake of illustration we show the tower of excited states in figure 3.1.

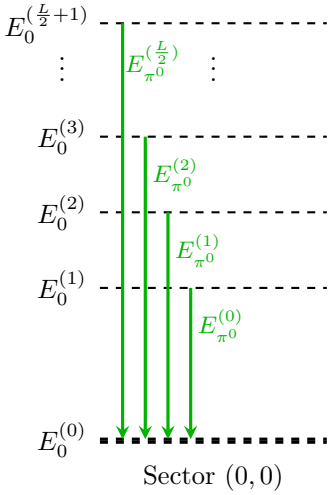

Figure 3.1: Graphical representation of the energies of the π^0 states.

Under these aforementioned assumptions the canonical partition function of the vacuum sector can be written as

$$\mathcal{Z}_{(0,0)}(T) = e^{-E_0^{(0)}/T}\left(1 + e^{-m_\pi/T} + 2\sum_{k=1}^{\frac{L}{2}} e^{-E_{\pi^0}^{(k)}/T} + \mathcal{O}\right), \tag{3.113}$$

where $\mathcal{O}$ denotes contributions from higher order energy states. We finish this section by emphasizing once again, that we only derived leading contributions to the vacuum sector. We assumed that secondary particles are of much higher energy, which allowed us to just write down the contributions arising from the π^0 pion.

3.6.3 Examination of the isospin $I = 1$ sector

Let us now examine the isospin $I = 1$ sector

$$\mathcal{Z}_{(1,-1)}(T) = \sum_{k=0}^{\infty} m_1^{(k)} e^{-E_1^{(k)}/T}, \tag{3.114}$$

and characterize the states, which are living within this sector. We have already established that the lightest particles of the 2-flavour Schwinger model are given by members of the pion-triplet $|\pi\rangle$. One member of the pion-triplet, the $|\pi^+\rangle$ state lives in the isospin $I = 1$ sector and denotes the ground state thereof. As before we can write down the tower of excited states for the π^+ pion, that is

$$\begin{aligned}
\text{ground state } \mathcal{Z}_{(1,-1)} &: |\pi^+\rangle, & E^{(0)}_{\pi^+}, m_0^{(0)} &= 1,\\
\text{1st. excited state of } \mathcal{Z}_{(1,-1)} &: |\pi^+\rangle^{(1)}, & E^{(1)}_{\pi^+}, m_0^{(1)} &= 2,\\
\text{2nd. excited state of } \mathcal{Z}_{(1,-1)} &: |\pi^+\rangle^{(2)}, & E^{(2)}_{\pi^+}, m_0^{(2)} &= 2,\\
&\vdots & &\vdots\\
\frac{L}{2}\text{'th excited state of } \mathcal{Z}_{(1,-1)} &: |\pi^+\rangle^{(\frac{L}{2})}, & E^{(\frac{L}{2})}_{\pi^+}, m_0^{(\frac{L}{2})} &= 2,
\end{aligned}$$

which differs slightly from the tower of states in the isospin $I = 0$ sector. In the Isospin $I = 0$ sector the vacuum state takes up the first state and all energy states are considered relative to that vacuum state. In the isospin $I = 1$ sector, the lowest state is given directly by the ground state of the π^+ pion. The energies are taken relative to the vacuum energy $E_0^{(0)}$ again

$$E^{(k)}_{\pi^+} = E_1^{(k)} - E_0^{(0)} = \cosh^{-1}\left(\cosh(m_\pi) + 1 - \cos(p^{(k)})\right), \qquad \text{with } p^{(k)} = \frac{2\pi}{L}\cdot k. \tag{3.115}$$

Also here, the appearance of additional particles cannot be excluded. Contrary to the $I = 0$ case, we will take into account a second particle, which yields higher order energy contributions to the isospin $I = 1$ sector. We presented in subsection 2.2.2 the existence of an additional scalar triplet state a_0, which (similar to the pion state) has a member living in $\mathcal{Z}_{(1,-1)}$, the a_0^+ meson. The tower of states is analogous to the π^+ pion tower of states and given by

$$E^{(k)}_{a_0} = E_1^{(k+1+\frac{L}{2})} - E_0^{(0)} = \cosh^{-1}\left(\cosh(m_{a_0}) + 1 - \cos(p^{(k)})\right), \qquad \text{with } p^{(k)} = \frac{2\pi}{L}\cdot k. \tag{3.116}$$

The precise order of the excited energy states is not really relevant here - changing the order of energy states in the partition function boils down to a rearrangement of summands in $\mathcal{Z}_{(1,-1)}$. However, the correct identification of the ground state is important.

After factorizing out the lowest energy state $E_1^{(0)}$ in $\mathcal{Z}_{(1,-1)}$ we obtain energy differences which need to be taken relative to the vacuum energy

$$E_1^{(k)} - E_1^{(0)} = (E_1^{(k)} - E_0^{(0)}) - (E_1^{(0)} - E_0^{(0)}) = (E_1^{(k)} - E_0^{(0)}) - m_\pi, \tag{3.117}$$

where we implicitely defined the ground state energy of the 1-pion state, which is simply given by the pion mass

$$E_\pi = E_1^{(0)} - E_0^{(0)} \stackrel{!}{=} m_\pi. \tag{3.118}$$

Furthermore, the contribution $(E_1^{(k)} - E_0^{(0)})$ is given either by $E^{(k)}_{\pi^+}$ or by $E^{(k)}_{a_0}$, depending on the value of k. This allows us to write down the partition function as

$$\mathcal{Z}_{(1,-1)}(T) = e^{-E_1^{(0)}/T}\left(1 + 2\sum_{k=1}^{\frac{L}{2}} e^{-(E^{(k)}_{\pi^+} - m_\pi)/T} + e^{-(m_{a_0} - m_\pi)/T} + 2\sum_{k=1}^{\frac{L}{2}} e^{-(E^{(k)}_{a_0} - m_\pi)/T} + \mathcal{O}\right), \tag{3.119}$$

where the third and fourth term in the brackets are contributions from the a_0^+ meson and $\mathcal{O}$ again denotes higher order energy contributions.

3.6.4 Examination of higher order isospin sectors

The examination of higher order isospin sectors unfortunately puts forth some problems. We follow the procedure as executed for the isospin $I = 0$ and $I = 1$ sector and continue with the isospin sector $I = 2$. The difficulties which we are going to illustrate arise for all isospin sectors $I \geq 2$. Consider the partition function for the isospin $I = 2$ sector

$$\mathcal{Z}_{(2,-2)}(T) = \sum_{k=0}^{\infty} m_2^{(k)} e^{-E_2^{(k)}/T}, \tag{3.120}$$

then the ground state of that sector is given by the 2-pion state $|\pi^+\pi^+\rangle$ at rest and its tower of excited states. Here we omit other possible particle states for the sake of simplicity. Consider two pions with momenta (p_1, p_2). In order to construct the lowest-lying energy state we go into the center of mass frame, such that the total and the relative momenta are given by

$$P = p_1 + p_2 = 0, \qquad \text{and} \qquad k = \frac{p_1 - p_2}{2}, \text{ respectively.} \tag{3.121}$$

The energy of a 2-pion state with momentum k is then given by

$$E_{2\pi}(k) = 2\cosh^{-1}(\cosh(m_\pi) + 1 - \cos(k)). \tag{3.122}$$

Naively, one would think that the ground state is given by two π^+ pions at rest with relative momentum $k = 0$. However, from section 2.7 we know that the two pions in a box scatter off each other, which results in a correction to the relative momentum k.

The relative momenta of the 2-pion states are not multiples of $\frac{2\pi}{L}$, but follow a quantization condition which is given by eq. (2.74), that is

$$2\delta(k) = -kL + 2\pi n, n \in \mathbb{Z}. \tag{3.123}$$

All the relative momenta k need to fulfill said non-trivial quantization condition, unfortunately, we do not have any information for the scattering phase shift $\delta(k)$ in the 2-flavour Schwinger model. If we build the tower of states and write down the expansion of the isospin $I = 2$ sector in terms of excited $|\pi^+\pi^+\rangle$ states we obtain

$$\mathcal{Z}_{(2,-2)}(T) = e^{-E_2^{(0)}/T} \left(1 + 2 \sum_{k=1}^{\frac{L}{2}} e^{-(E_{2\pi^+}^{(k)} - E_{2\pi})/T} + \mathcal{O} \right), \tag{3.124}$$

where the energies $E_{2\pi^+}^{(k)}$ are given by

$$E_{2\pi^+}^{(k)} = 2\cosh^{-1}(\cosh(m_\pi) + 1 - \cos(k^{(k)})) \tag{3.125}$$

and we defined the 2-pion ground state energy as

$$E_{2\pi} = E_2^{(0)} - E_0^{(0)} \stackrel{!}{=} E_{2\pi^+}^{(0)}. \tag{3.126}$$

In above equations the relative momenta $k^{(i)}$ fulfill the quantization conditions presented in eq. (3.123). The relative momentum $k^{(0)}$, belonging to the ground state energy of the $|\pi^+\pi^+\rangle$ state, is the smallest relative momentum fulfilling said quantization condition. Note that we denote the multiplicity of the ground state with $m_2^{(0)} = 1$, since its continuum analogon, would not have any momentum at all $k^{(0)} = 0$.

Above formula for the expansion of the isospin $I = 2$ sector is not really suitable to determine the ground state energy $E_{2\pi}$, since the relative momenta $k^{(i)}$ cannot be determined beforehand and we are left with many free variables. In order to have a description of the temperature behaviour we propose an effective ansatz, where we express the partition function $\mathcal{Z}_{(2,-2)}(T)$ with as few parameters as possible. We only consider the ground state $|\pi^+\pi^+\rangle$ and its energy $E_{2\pi}$ and summarize all excited state contributions into an effective correction term. We propose for the partition function

$$\mathcal{Z}_{(2,-2)}(T) = e^{-E_2^{(0)}/T} \left(1 + A_2 e^{-A_1/T} \right), \tag{3.127}$$

where the second term in the bracket denotes the effective corrections with $A_1, A_2 > 0$.

Similar arguments hold true when examining the isospin $I = 3$ sector. Also here, the 3-pion states $E^{(k)}_{3\pi^+}$ rely on quantized momenta due to scattering phenomena in a finite box. To obtain a description for the partition function of the isospin $I = 3$ sector we use again an effective description. The only physical state we consider is the 3-pion ground state $|\pi^+\pi^+\pi^+\rangle$ with energy

$$E_{3\pi} = E^{(0)}_3 - E^{(0)}_0, \tag{3.128}$$

higher order contributions are summarized in an effective correction term. The used effective description for the partition function of the isospin $I = 3$ sector reads

$$\mathcal{Z}_{(3,-3)}(T) = e^{-E^{(0)}_3/T}\left(1 + B_2 e^{-B_1/T}\right), \tag{3.129}$$

where $B_1, B_2 > 0$ parametrize these effective corrections.

3.6.5 Conclusion

So far we had a closer look at the partition functions of the isospin $I = 0, I = 1, I = 2$ and $I = 3$ sectors. Upon making some simplifying assumptions about the spectrum, we considered the dominant contributions to each partition function and wrote down the expansion thereof. We can now write down a heuristic ansatz for the ground state energies of those sectors using the free energy difference. These expressions will be used to numerically determine the temperature dependence of the ground state energies.

Using the master formula eq. (3.104) with $n = 1$ and upon omitting higher order corrections $\mathcal{O}$ we obtain for the temperature dependence of the pion mass $E_\pi(T)$

$$\boxed{E_\pi(T) \approx m_\pi - T\log\left(\frac{1 + 2\sum_{k=1}^{\frac{L}{2}} e^{-(E^{(k)}_{\pi^+} - m_\pi)/T} + e^{-(m_{a_0} - m_\pi)/T} + 2\sum_{k=1}^{\frac{L}{2}} e^{-(E^{(k)}_{a_0} - m_\pi)/T}}{1 + e^{-m_\pi/T} + 2\sum_{k=1}^{\frac{L}{2}} e^{-E^{(k)}_{\pi^0}/T}}\right).} \tag{3.130}$$

Similarly, we obtain expressions for the temperature dependent ground state energies of 2- and 3-pion states

$$\boxed{E_{2\pi}(T) \approx E_{2\pi} - T\log\left(\frac{1 + A_2 e^{-A_1/T}}{1 + e^{-m_\pi/T} + 2\sum_{k=1}^{\frac{L}{2}} e^{-E^{(k)}_{\pi^0}/T}}\right)} \tag{3.131}$$

and

$$\boxed{E_{3\pi}(T) \approx E_{3\pi} - T\log\left(\frac{1 + B_2 e^{-B_1/T}}{1 + e^{-m_\pi/T} + 2\sum_{k=1}^{\frac{L}{2}} e^{-E^{(k)}_{\pi^0}/T}}\right).} \tag{3.132}$$

We show the tower of states in figure 3.2 for the sake of clarity.

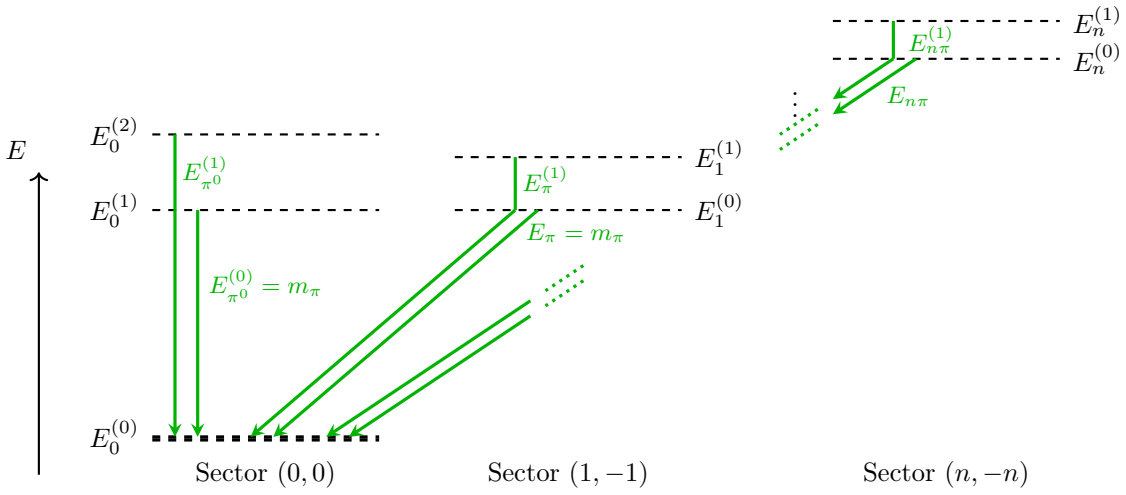

Figure 3.2: Graphical representation of the energy levels of the different canonical sectors.

4 Numerical studies - Qualitative results

In this chapter we discuss some general topics related to the Schwinger model in the canonical formalism. First, we examine autocorrelation effects of the topological charge, which arise when performing quenched ($N_f = 0$) and dynamical simulations ($N_f = 2$). Next, we discuss the average plaquette, which will be used in order to confirm the validity of our quenched simulations.

We use quenched simulations to discuss aspects of the 1-flavour Schwinger model in the canonical formalism. A big part of this chapter is dedicated to canonical determinants, transfer matrices and the interesting properties which come with them. We show that the principal minors of a canonical sector arrange themselves nicely into "classes", yielding a very interesting substructure.

We finish this chapter with the 2-flavour Schwinger model. We present some results confirming the correspondence between the ground state energies of the 1-, 2- and 3-meson sectors and the direct measurements of the corresponding energies extracted from correlators formed with π^+, $\pi^+\pi^+$ and $\pi^+\pi^+\pi^+$ operators. We also examine condensation phenomena in the 2-flavour Schwinger model using the canonical formulation.

Throughout this chapter we work on a lattice of extent $L \times L_t$, where we set the lattice spacing to one, i.e. $a = 1$, if not mentioned otherwise.

4.1 Topological charge and autocorrelation effects

Since there is no efficient prescription on how to perform canonical simulations yet, we utilize quenched ($N_f = 0$) and dynamical simulations ($N_f = 2$) instead. To access the canonical sectors one must perform a reweighting procedure, as explained in the appendix section C.9.

Here we want to discuss the autocorrelation effects of the topological charge Q, which arise when working with quenched and dynamical simulations. An explanatory description of autocorrelation effects is given in the appendix section C.4.

The sampling of decorrelated configurations in lattice simulations can be very tedious, if large energy barriers exist between regions in configuration space. In the Schwinger model energy barriers separate the so-called topological sectors, which are characterized by the topological charge of the gauge configuration. We use the geometrical definition of the topological charge [44, 45], that is

$$Q = \frac{1}{2\pi} \sum_P \log(U_P), \qquad U_P = e^{i\theta_P}, \tag{4.1}$$

where U_P denotes the gauge plaquette and θ_P is the plaquette angle as introduced in eq. (A.61). With increasing β the tunnelling rate between different topological sectors decreases, which yields an ergodicity problem. This effect is known as "topological freezing" and also occurs in other lattice gauge theories such as QCD, see Refs. [46, 47]. Although the autocorrelation time for the topological charge increases drastically with augmenting β (see figure 4.1 for a Monte Carlo history of the topological charge in quenched simulations), other observables seem to be less affected.

Nonetheless one needs to be attentive with measurements originating from different topological sectors. For example, it was hinted that different topological sectors yield different pion masses [21]. Furthermore, one can show that in the chiral limit dynamical simulations (i.e. simulations performed with 2 flavours.) also exhibit the same kind of topological freezing.

4.2 Plaquette

Albeit having access to quenched and dynamical simulations we work almost exclusively with quenched simulations, in particular, the computations in chapter 5, have all been done using quenched simulations. Quenched simulations are quick to generate and allow more flexibility, for example when reweighting to different masses. Preliminary examinations have also shown that quenched simulations in general have a higher rate of change between topological sectors and access topological sectors with large charges

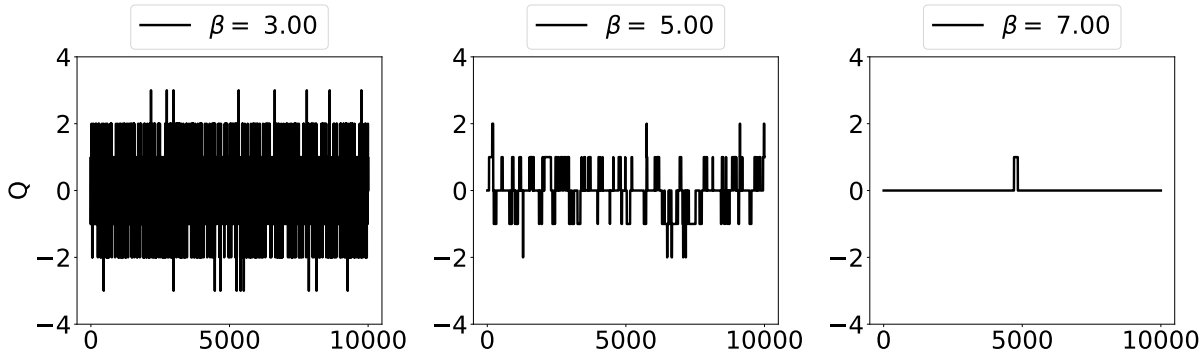

Figure 4.1: Monte Carlo history for topological charge Q. Quenched simulations with $L = L_t = 8$, were used here. We made $10'000$ thermalization steps and $10'000$ measurements afterwards. Between each measurement we skipped 100 metropolis update steps.

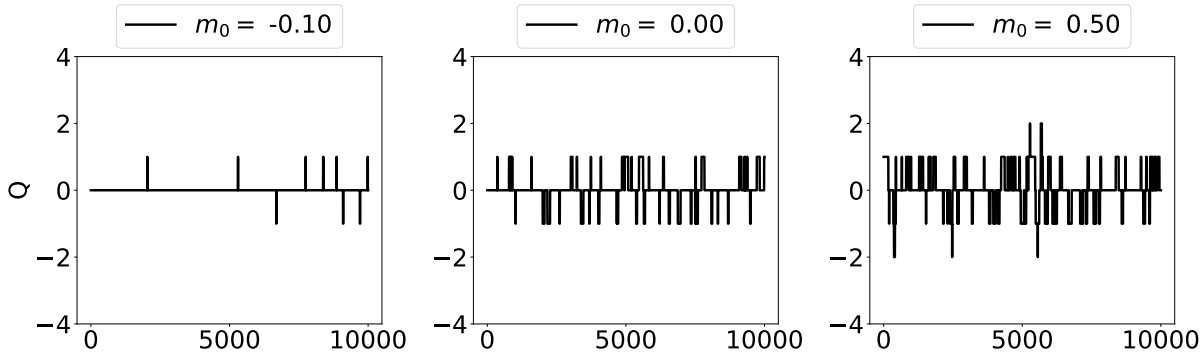

Figure 4.2: Monte Carlo history for topological charge Q. Dynamical simulations ($N_f = 2$) with $L = L_t = 8$, fixed coupling $\beta = 5.0$. Similar to the quenched simulations, these simulations have been performed with a simple metropolis algorithm, for the sake of comparison. We made $10'000$ thermalization steps and $10'000$ measurements afterwards. Between each measurement we skipped 100 metropolis update steps. We approach the chiral limit by approaching small negative bare mass m_0, such that $m_0 \to m_{\text{crit}}$, as explained in section 2.5.

$|Q|$. Therefore, we believe that quenched simulations cover a larger subset of configuration space. To confirm the validity of our simulations analytical results are useful for numerical checks, in our case, these analytical results will be provided by the average plaquette. The average plaquette is defined as

$$\langle P \rangle = \langle \frac{1}{2\Omega} \sum_P (U_P + U_P^\dagger) \rangle = \langle \frac{1}{\Omega} \sum_P \cos(\theta_P) \rangle, \tag{4.2}$$

where $\Omega = L \cdot L_t$ denotes the number of plaquettes on the lattice. For quenched simulations one can show (appendix section (G.3)) that the average plaquette is given by

$$\langle P \rangle = \frac{\frac{I_1(\beta)}{I_0(\beta)} + \sum_{n=1}^{\infty} \left[\left(\frac{I_n(\beta)}{I_0(\beta)} \right)^{\Omega - 1} \left(\frac{I_{n-1}(\beta)}{I_0(\beta)} + \frac{I_{n+1}(\beta)}{I_0(\beta)} \right) \right]}{1 + 2 \sum_{n=1}^{\infty} \left(\frac{I_n(\beta)}{I_0(\beta)} \right)^{\Omega}}. \tag{4.3}$$

Our simulations have been cross-checked with those analytic predictions, as shown for example in figure 4.3.

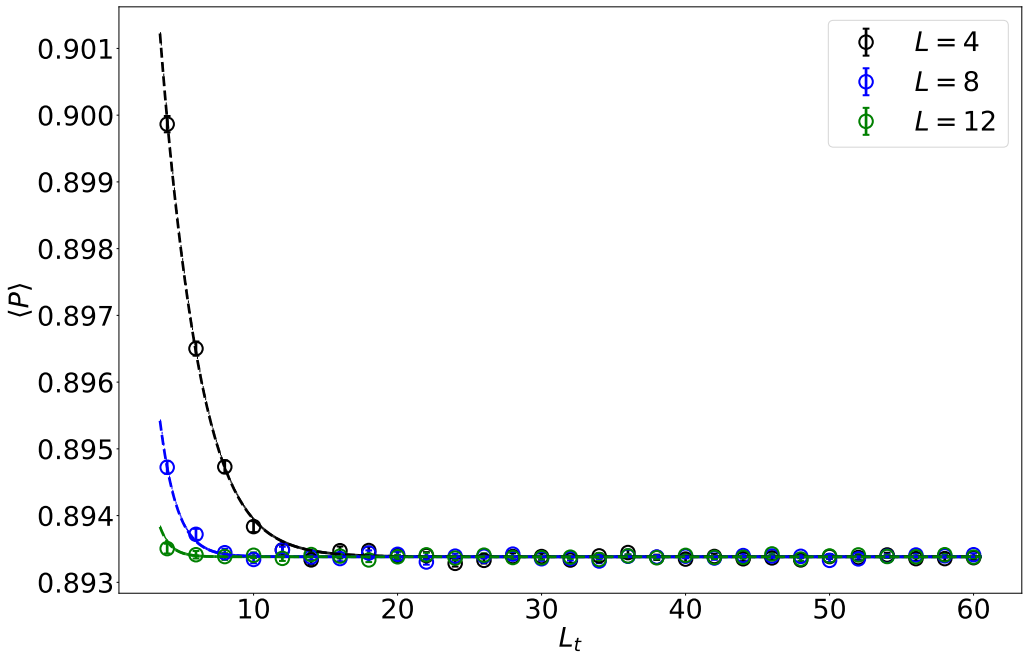

Figure 4.3: Comparison between the average measured plaquette $\langle P \rangle$ and the analytical results (dashed lines). We used quenched simulations with coupling $\beta = 5.0$ and three different volumes $L = 4, 8, 12$.

4.3 Comparison between grand-canonical and canonical weights

For the next discussion, we take the quenched simulations and reweight them to the 1-flavour Schwinger model in the canonical formulation. Although the 1-flavour Schwinger model has a sign problem it can be ignored if we choose the bare mass m_0 of the quark to be sufficiently large. A more careful discussion of the sign problem in the 1-flavour Schwinger model is given in section C.8, but for the following considerations we consider the bare mass to be large enough (resp. the coupling κ to be small enough) such that the sign problem is absent.

The grand-canonical partition function for the 1-flavour Schwinger model has been discussed in detail in section 3.1. The fugacity expansion reads

$$\mathcal{Z}_{GC}(T,\mu) = \int \mathcal{D}U \det(\mathbf{K}[U,\mu_q]) e^{-S_g[U]} \tag{4.4}$$

$$\stackrel{!}{=} \sum_{k=-L}^{L} e^{\mu_q k/T} \mathcal{Z}_k(T), \tag{4.5}$$

where $\mathcal{Z}_k(T)$ denotes the canonical partition function given by

$$\mathcal{Z}_k(T) = \int \mathcal{D}U e^{-S_g[U]} \det_k(\mathbf{K}[U]). \tag{4.6}$$

The connection between the two partition functions is established via the dimensional reduction of the determinant of the Wilson Dirac operator, which has been extensively discussed in section 3.3.

The final result of said reduction is given by eq. (3.58), that is

$$\det(\mathbf{K}[U,\mu_q]) = \sum_{k=-L}^{L} e^{\mu_q L_t k} \det_k(\mathbf{K}[U]). \tag{4.7}$$

From now on, we set the quark chemical potential to zero $\mu_q = 0$ and introduce a new notation for the sake of readability. We use

$$\det(\mathbf{K}) = \det(\mathbf{K}[U,\mu_q]) \quad \text{and} \quad \det_k(\mathbf{K}) = \det_k(\mathbf{K}[U]), \tag{4.8}$$

such that above relation simply reads

$$\det(\mathbf{K}) = \sum_{k=-L}^{L} \det_k(\mathbf{K}). \tag{4.9}$$

The canonical weights $\det_k(\mathbf{K})$ fix the number of fermions (resp. quarks) in the system, while $\det(\mathbf{K})$ takes into account all contributions with varying quark numbers.

By taking the ratio between the weights

$$\frac{\det_k(\mathbf{K})}{\det(\mathbf{K})}, \tag{4.10}$$

we can make statements about how much the canonical sectors contribute to the overall grand-canonical system. Note, that the Gauss law states that the total charge of the system on the lattice needs to be zero. Since we are only working with 1 quark flavour, the Gauss law simply states that

$$\langle \det_k(\mathbf{K}) \rangle = 0, \quad \forall k \neq 0, \tag{4.11}$$

indicating, that the only non-vanishing canonical contribution is coming from the vacuum sector with no quark content ($k = 0$). However, for individual configurations we can have non-zero contributions from other quark sectors, which means that for a single configuration we can have a naive look at the relative weights given by eq. (4.10). In order to do so, we introduce the quark density

$$\rho(k) = \frac{k}{L}, \quad k \in \{-L, \ldots, \ldots, L\}, \tag{4.12}$$

where k denotes the number of quarks and L denotes the volume. Note, that the resolution of the quark density increases with the volume L. The lattice can be completely saturated with L anti quarks or L quarks, resulting in

$$\rho(-L) = -1, \quad \text{and} \quad \rho(L) = 1, \quad \text{respectively.} \tag{4.13}$$

The vacuum sector with no quark content is then described by $\rho(0) = 0$. For the full real determinant of the Wilson Dirac operator eq. (4.9), the complex phases in the canonical determinant cancel each other out, due to the reflection symmetry

$$\det{}_k^*(\mathbf{K}) = \det{}_{-k}(\mathbf{K}) \quad \forall k \in \{0, \dots, L\}. \tag{4.14}$$

This allows us to restrict ourselves to the real part of the canonical determinants and consider the ratio

$$\frac{\Re[\det_k(\mathbf{K})]}{\det(\mathbf{K})}, \tag{4.15}$$

as a function of the quark density. We only consider a single thermalized configuration for two different volumes $L = 10$ and $L = 20$. The results are given in figure 4.4, we expressed the volume using the dimensionless combination gL, where the two couplings g and β are related to each other via $\beta = 1/(ag)^2$.

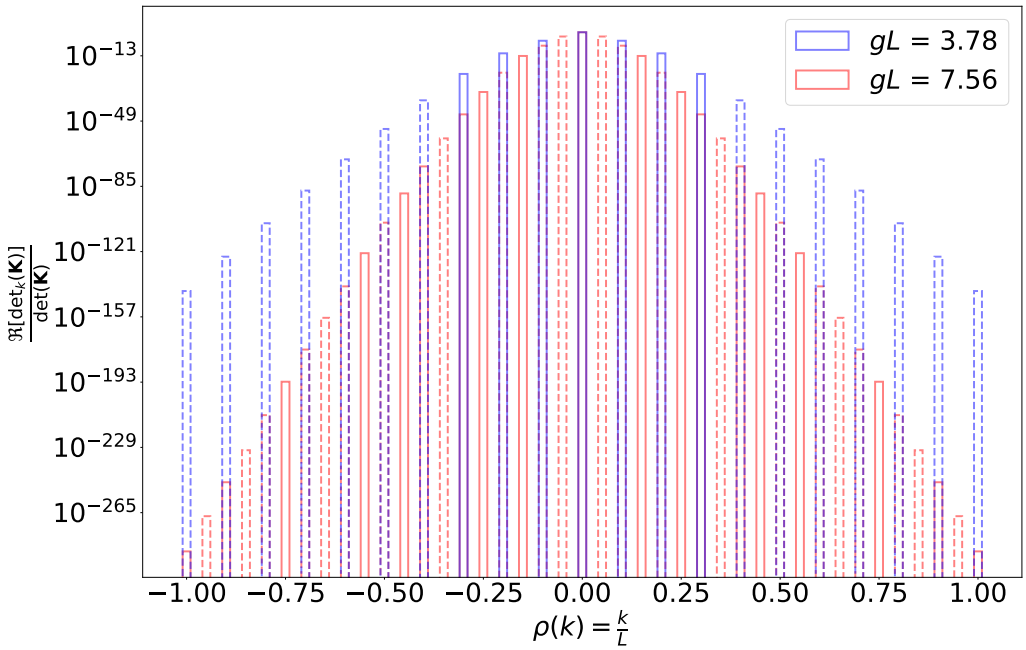

Figure 4.4: We plot here the contribution $\frac{\Re[\det_k(\mathbf{K})]}{\det(\mathbf{K})}$ for a single configuration with $\beta = 7.0, m_0 = 0.0266$ and fixed temperature $gL_t \approx 15.12$. The continuous bars denote positive contributions, while the dashed ones denote negative contributions.

There are a few interesting phenomena one can observe. As expected the dominant contribution is given by the vacuum sector with no quark content $\rho(k) = 0$, where $\frac{\Re[\det_k(\mathbf{K})]}{\det(\mathbf{K})}$ becomes approximately one (difficult to see in figure 4.4 due to the scaling of the plot). For the neighbouring sectors the contributions are continuously decreasing and either positive or negative (continuous bars represent positive contributions, dashed ones represent negative contributions). This ambiguity in the sign makes sense, the Gauss law states that the only surviving contribution in the ensemble average should be coming from the vacuum sector, see eq. (4.11).

It is also very interesting to examine the differences between the two volumes. It seems that for larger volumes the distribution is more sharply peaked around the vacuum sector. This means that neighbouring sectors become more suppressed with increasing quark density.

Since we established the non-trivial behaviour of the canonical weights, we consider the ratio

$$\frac{\det_0(\mathbf{K})}{\det(\mathbf{K})} - 1, \tag{4.16}$$

and examine lattice artefacts by fixing the volume gL and the temperature gL_t. We vary the coupling β, which is related to the lattice spacing a via $\beta = 1/(ag)^2$. We measure the ratio given by eq. (4.16), bin the results and present them in a histogramm given in figure (4.5). We see that the results fluctuate around 0, as expected. However, there is no visible difference between the three lattice spacings, indicating that lattice artefacts are very well under control. We obtain a seemingly universal behaviour for the distribution.

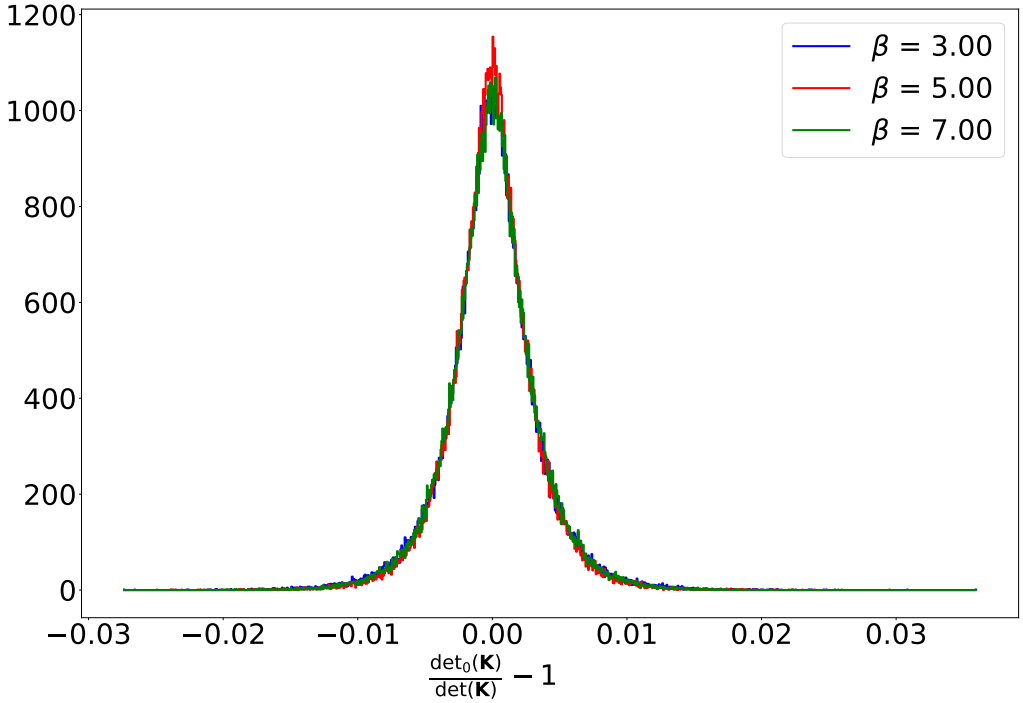

Figure 4.5: Examination of lattice artefacts for the distribution of $\frac{\det_0(\mathbf{K})}{\det(\mathbf{K})} - 1$, for fixed volume and temperature $gL = gL_t \approx 15.10$. The measurements correspond to $L = 26$ for $\beta = 3.0$, $L = 34$ for $\beta = 5.0$ and $L = 40$ for $\beta = 7.0$. The bare masses were chosen in such a way that the infinite volume pion mass in the 2-flavour Schwinger model would be fixed, $m_\pi/g \approx 0.75$.

Next, we examine the same fluctuations given by eq. (4.16) at fixed lattice spacing β and fixed temperature gL_t. This time we vary the volume dependence instead. We present the results in figure 4.6, where we see that with increasing volume the distribution becomes wider until eventually saturating.

The y-axis in figure 4.6 is log-scaled, the fact that the distribution approaches a triangle-shape indicates clearly that the original distribution is exponentially decaying.

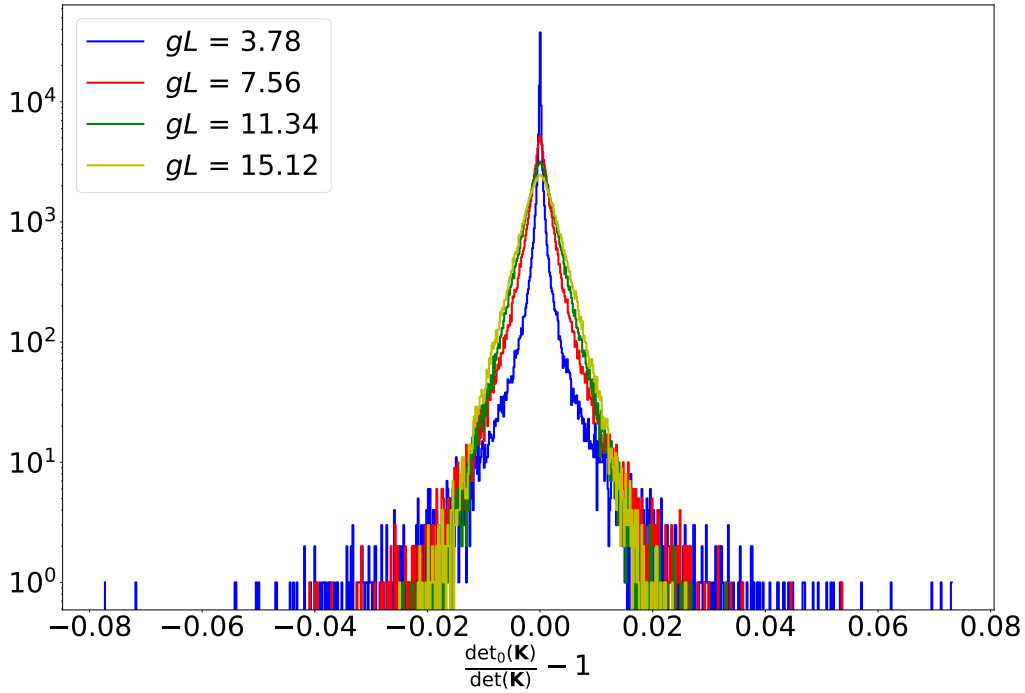

Figure 4.6: Distribution of the ratio $\frac{\det_0(\mathbf{K})}{\det(\mathbf{K})} - 1$, with fixed lattice spacing β, fixed temperature $gL_t \approx 15.12$ and for different volumes.

4.4 Spectrum of the transfer matrix $\mathcal{T}$

We continue with the 1-flavour Schwinger model in the canonical formulation and consider now the spectrum of the transfer matrix $\mathcal{T}$. The derivation of the full transfer matrix is given in subsection 3.3.2 and the examination of the spectrum $\sigma(\mathcal{T})$ has been done in subsection 3.3.4. Here we briefly recapitulate the most important details and give some results. The transfer matrix is related to the canonical determinants via eq. (3.59), that is

$$\det_k(\mathbf{K}) = \left(\prod_{i=1}^{L_t} |B_i||2\kappa U_i^\dagger|\right) \sum_{I,|I|=k+L} \det(\mathcal{T}^{II}), \tag{4.17}$$

and is constructed by using the building blocks from the Wilson Dirac operator

$$\mathcal{T} = \prod_{i=1}^{L_t} (Q_i^-)^{-1} Q_i^+ \tilde{U}_i. \tag{4.18}$$

One interesting property, which has been derived in subsection 3.3.4, is the symmetry property of the spectrum. We argued, that

$$\sigma(\mathcal{T}) = \{\lambda_1, \ldots, \lambda_L, \frac{1}{\lambda_1^*}, \ldots, \frac{1}{\lambda_L^*}\} = \{r_1 e^{i\phi_1}, \ldots, r_L e^{i\phi_L}, \frac{1}{r_1} e^{i\phi_1}, \ldots, \frac{1}{r_L} e^{i\phi_L}\}, \tag{4.19}$$

which means that the eigenvalues split up nicely into two sectors, either

$$|\lambda| < 1.0, \quad \text{or} \quad |\lambda| > 1.0. \tag{4.20}$$

In figures 4.7 and 4.8 we show the distribution of the eigenvalues for 100 thermalized configurations. Close to the circle with radius $r = 1$ (denoted by a blue line on the right plot in figure 4.7 and 4.8) one can find partnered eigenvalues, which are related to each other via

$$\lambda_i = r_i e^{i\phi_i} \quad \text{and} \quad \frac{1}{\lambda_i^*} = \frac{1}{r_i} e^{i\phi_i}. \tag{4.21}$$

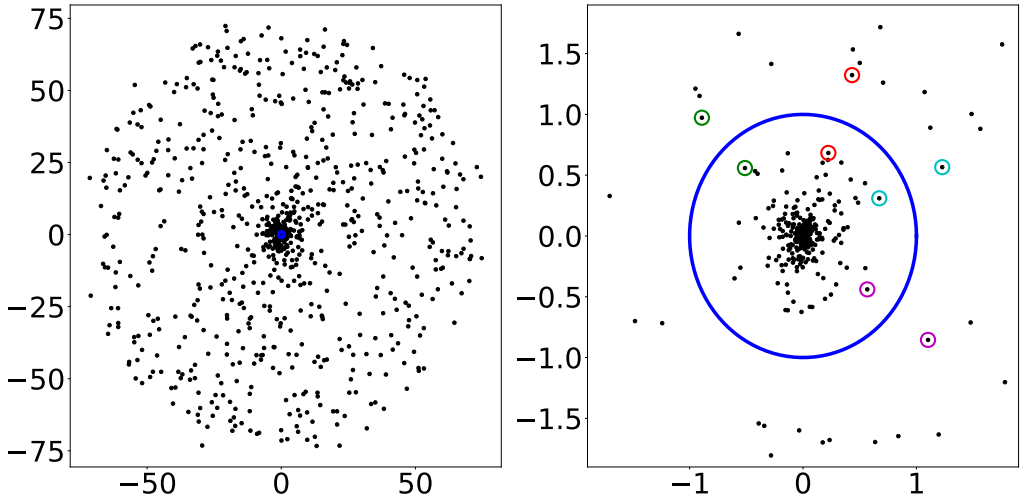

Figure 4.7: Distribution of the eigenvalue spectrum for 100 thermalized configurations with $\beta = 5.0, m_0 = 0.0220$ and $(L, L_t) = (8, 4)$. The blue circle denotes the boundary, which separates the eigenvalues into two subsets - if $|\lambda_i| > 1.0$, then that eigenvalue is outside the blue circle and has a partner $\frac{1}{\lambda_i^*}$ living inside the circle. We denote some examples of partnered eigenvalues with coloured circles.

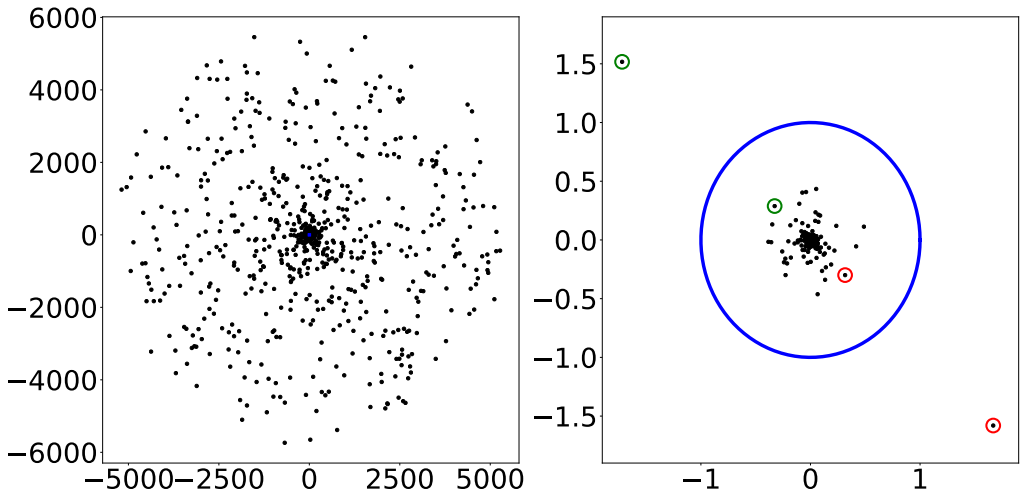

Figure 4.8: Distribution of the eigenvalue spectrum for 100 thermalized configurations with $(L, L_t) = (8, 8)$, $\beta = 5.0, m_0 = 0.0220$. We denote some examples of partnered eigenvalues with coloured circles.

4.5 Distribution of the principal minors

After investigating the spectrum of the transfer matrix, we want to discuss the principal minors related to the transfer matrix. For the sake of simplicity (and if not mentioned otherwise) we combine the principal minor with its prefactor and redefine the principal minor as

$$P^{II} = \left(\prod_{i=1}^{L_t} |B_i||2\kappa U_i^\dagger| \right) \det(\mathcal{T}^{II}). \tag{4.22}$$

We consider the quark sector with k quarks in our system, corresponding canonical partition function $\mathcal{Z}_k(T)$ and canonical determinant $\det_k(\mathbf{K})$. Then the complete number of principal minors $\mathcal{N}[P^{II}]$ is given by the number of possible index sets one can build, such that

$$\mathcal{N}[P^{II}] = \binom{2L}{L+k}, \quad \text{for} \quad |I| = L + k, \quad \text{and} \quad k \in \{-L, \ldots, L\}. \tag{4.23}$$

We hinted, in the end of subsection 3.3.4, that the canonical determinants fulfill some sort of reflection symmetry, such that

$$\det{}_k^*(\mathbf{K}) = \det{}_{-k}(\mathbf{K}) \quad \forall k \in \{0, \ldots, L\}, \tag{4.24}$$

which was also used in the previous section. This symmetry can be confirmed on the level of the principal minors, which has been done in the appendix section G.4. There we showed that for each principal minor P^{II}, belonging to the canonical sector $\det_k(\mathbf{K})$,

$$P^{II} = \left(\prod_{i=1}^{L_t} |B_i||2\kappa U_i^\dagger| \right) \det(\mathcal{T}^{II}), \quad \text{with} \quad |I| = k + L \tag{4.25}$$

there is a complex conjugated partner $\tilde{P}^{JJ}$ living in the canonical sector $\det_{-k}(\mathbf{K})$

$$\tilde{P}^{JJ} = \left(\prod_{i=1}^{L_t} |B_i||2\kappa U_i^\dagger| \right) \det(\mathcal{T}^{JJ}), \quad \text{with} \quad |J| = -k + L, \tag{4.26}$$

such that

$$\tilde{P}^{JJ} = (P^{II})^\dagger. \tag{4.27}$$

This relationship ensures that the reflection symmetry eq. (4.24), is fulfilled. Interestingly, this also means that the canonical determinant corresponding to the vacuum sector with $k = 0$ is real

$$\det{}_0(\mathbf{K}) \in \mathbb{R}, \tag{4.28}$$

and that each principal minor of $\det_0(\mathbf{K})$ is either real or has a complex-conjugate partner, which is also in $\det_0(\mathbf{K})$.

In figure 4.9 we show the values of the principal minors in the vacuum sector $\det_0(\mathbf{K})$ for a single configuration, which displays nicely the mentioned symmetry on the level of the principal minors.

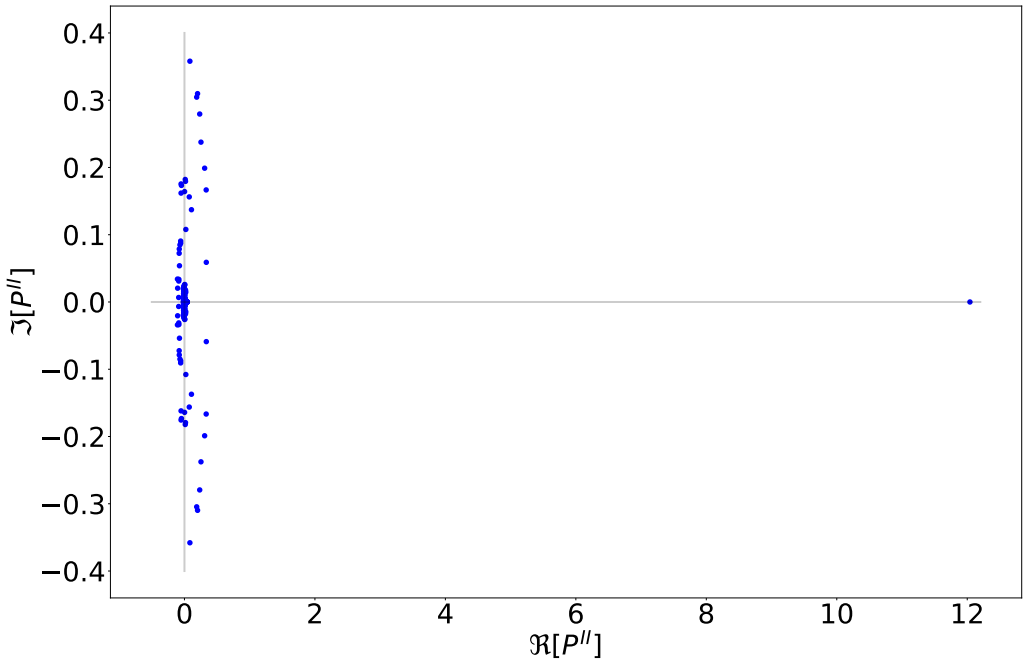

Figure 4.9: Principal minors in the vacuum sector (no quark content) for a single configuration, with $\beta = 5.0$, $m_0 = 0.0220$ and $(L, L_t) = (8, 8)$. We have a lone principal minor to the far right, which seems completely isolated from the rest. This principal minor shows up in each configuration, belongs to the index set $\{1, 2, 3, \ldots, L\}$, and is always real and positive.

One interesting observation we make is that the contributions seem to be dominated by a single principal minor sitting on the real axis, to the very right. This principal minor shows up in the vacuum sector $\det_0(\mathbf{K})$ on all configurations and is described by the index set $I = \{1, 2, 3, \ldots, L\}$, we refer to it as the maximal principal minor. Its contribution will be discussed in detail later when illustrating the division of the principal minors into different classes.

Each principal minor in the vacuum sector is either real or has a complex conjugate partner. If we interpret these contributions as weights, we can consider the real parts only and examine the overall distribution of the weights. Since the principal minors can differ several orders of magnitude we take the logarithm for the sake of illustration. We consider the distributions of the positive and negative principal minors separately and use

$$\log(\Re[P^{II}]) \quad \text{for} \quad \Re[P^{II}] > 0 \quad \text{and} \quad \log(-\Re[P^{II}]) \quad \text{for} \quad \Re[P^{II}] < 0. \tag{4.29}$$

The distributions belonging to the positive principal minors $\Re[P^{II}] > 0$ are denoted with continuous lines, while the distributions belonging to negative principal minors $\Re[P^{II}] < 0$ are denoted with dotted lines, which allows us to compare both distributions in a much cleaner way.

In figure 4.10 we show the distribution of the principal minors in the vacuum sector, for two different temperatures. Our results display nicely that the positive contributions outnumber the negative ones, indicating that potential sampling algorithms using principal minors would only encounter a minor sign problem.

In figure 4.11 we show the distribution of the principal minors for a variety of different temperatures. We see that -especially for high temperatures (i.e. small L_t)- the distributions seem to have an additional substructure, indicated by the multiple spikes. Upon decreasing the temperature the distributions become smoother until the substructure is not recognizable anymore. For the remainder of this thesis, we label these substructures as classes. These classes are characterized by their index sets and will be discussed in the next section. However, it is worth noting, that we have already encountered one of these classes characterized by the maximal principal minor with index set $\{1, 2, 3, \ldots, L\}$.

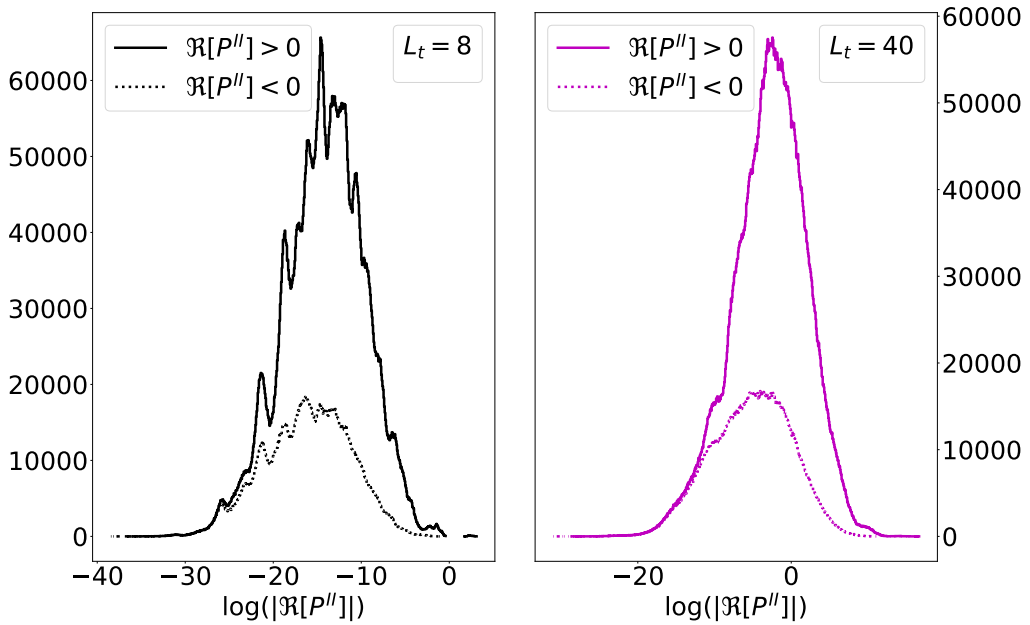

Figure 4.10: Histogram of all the contributions from the principal minors P^{II} in the vacuum sector, we keep $\beta = 5.0, m_0 = 0.0220, L = 8$ fix and consider two different temperatures L_t. The plot on the left has been done at a high temperature $L_t = 8$, while the plot on the right has been done at a low temperature $L_t = 40$. For each plot we used $1'000$ configurations and the dotted lines indicate the negative weights with $\Re[P^{II}] < 0.0$. The distribution of the principal minors becomes smoother for increasing L_t (decreasing temperature), for high temperature the distribution displays an interesting substructure.

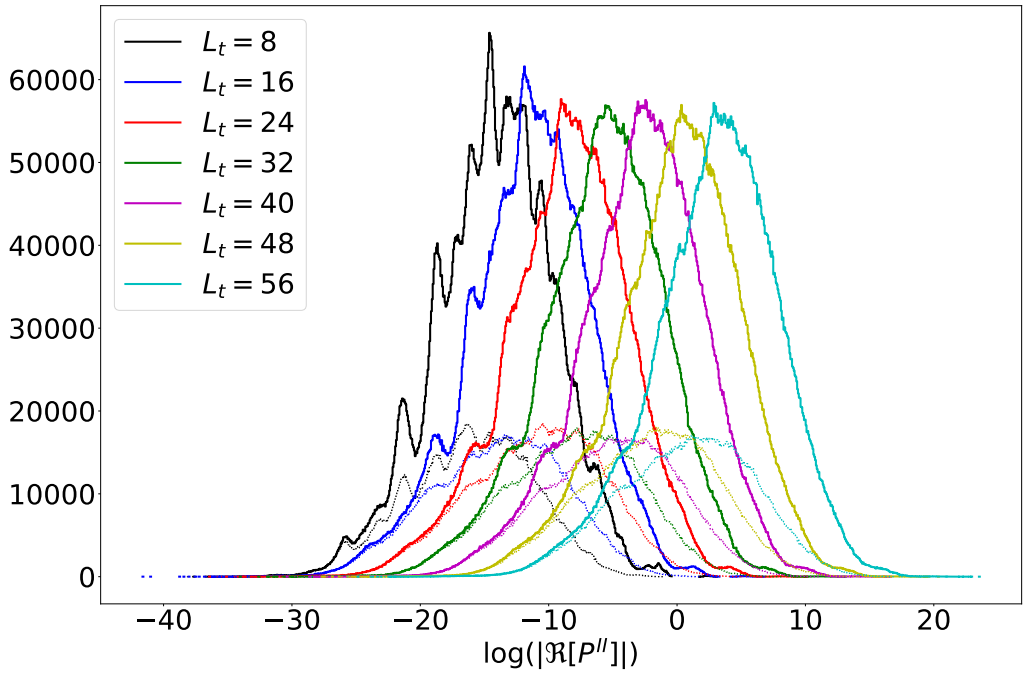

Figure 4.11: Distribution of the principal minors P^{II} in the vacuum sector, we keep $\beta = 5.0, m_0 = 0.0220, L = 8$ fix and vary the temperature L_t. The dotted lines indicate negative contributions, that is $\Re[P^{II}] < 0.0$. If we compare the positive with the negative contributions we see that the net-weight is always positive. Similar as in figure 4.10, the distributions become smoother with decreasing temperature.

4.6 Class structure of the principal minors

The appearance of the class structure has already been mentioned in the previous sections and will be elaborated in more detail here, meaning that we continue with the 1-flavour Schwinger model in the canonical formulation. In this section we work exclusively with the vacuum sector, that is $\mathcal{Z}_0(T)$, and its corresponding canonical determinant

$$\det_0(\mathbf{K}) = \sum_{I,|I|=L} \left[\left(\prod_{i=1}^{L_t} |B_i||2\kappa U_i^\dagger| \right) \det(\mathcal{T}^{II}) \right] \stackrel{!}{=} \sum_{I,|I|=L} P^{II}, \tag{4.30}$$

where the full transfer matrix $\mathcal{T}$ is given by

$$\mathcal{T} = \prod_{i=1}^{L_t} (Q_i^-)^{-1} Q_i^+ \tilde{U}_i. \tag{4.31}$$

The principal minor P^{II}

$$P^{II} = \left(\prod_{i=1}^{L_t} |B_i||2\kappa U_i^\dagger| \right) \cdot \det(\mathcal{T}^{II}), \tag{4.32}$$

decomposes into a bulkfactor and the original principal minor of the transfer matrix $\mathcal{T}$. The principal minors of the transfer matrix $\mathcal{T}$, respectively the index sets thereof, cause the appearance of the aforementioned class structure.

We give a heuristic argument, explaining the reasoning behind the appearance of said class structure and show that it is indeed related to the index sets.

For the following discussion we choose the coupling in such a way that

$$0 < \kappa \ll 1, \quad \text{resp.} \quad \left(\frac{1}{2\kappa} \right) \stackrel{!}{=} m_0 + 2 \gg \frac{1}{2}. \tag{4.33}$$

Furthermore, we consider a simplified scenario, where we set the temporal extent of the lattice to $L_t = 1$,[1] such that

$$\mathcal{T} = (Q_1^-)^{-1} Q_1^+ \tilde{U}_1. \tag{4.34}$$

The last factor $\tilde{U}_1$ has been discussed in subsection 3.3.4 and is given by a block-diagonal matrix with two submatrices $\tilde{U}_{11}, \tilde{U}_{22}$ of size $L \times L$

$$\tilde{U}_{11} = \mathrm{diag}[\left(\frac{1}{2\kappa} \right) e^{i\varphi_1}, \ldots, \left(\frac{1}{2\kappa} \right) e^{i\varphi_L}] \quad \text{and} \quad \tilde{U}_{22} = \mathrm{diag}[(2\kappa)e^{i\varphi_1}, \ldots, (2\kappa)e^{i\varphi_L}], \tag{4.35}$$

such that $\tilde{U}_1$ can be written as

$$\tilde{U}_1 = \begin{pmatrix} \tilde{U}_{11} & \mathbb{0} \\ \mathbb{0} & \tilde{U}_{22} \end{pmatrix} \sim \begin{pmatrix} \mathcal{O}(\frac{1}{2\kappa}) & 0 \\ 0 & \mathcal{O}(2\kappa) \end{pmatrix}. \tag{4.36}$$

In the last step, we recognized that the contributions are either of order $\mathcal{O}(\frac{1}{2\kappa})$ or $\mathcal{O}(2\kappa)$. Consider now the first two factors of this transfer matrix, which have been discussed in subsection 3.3.5 and are given by

$$(Q_1^-)^{-1} Q_1^+ = \begin{pmatrix} D_1 - C_1.D_1^{-1}.C_1 & -C_1 D_1^{-1} \\ D_1^{-1} C_1 & D_1^{-1} \end{pmatrix}. \tag{4.37}$$

Upon reminding ourselves of the definitions of C_1 and D_1

$$D_1 = \delta_{n,m} - \kappa(U_{n,m}\delta_{m,n+\hat{1}} + U_{n,m}\delta_{m,n-\hat{1}}) \tag{4.38}$$

$$C_1 = \kappa(U_{n,m}\delta_{m,n+\hat{1}} - U_{n,m}\delta_{m,n-\hat{1}}), \tag{4.39}$$

[1] We ignore any kind of additional minus signs, which might arise with an odd L_t.

We can express $(Q_1^-)^{-1}.Q_1^+$ in terms of contributions of order 1 or order κ

$$(Q_1^-)^{-1}Q_1^+ = \begin{pmatrix} D_1 - C_1.D_1^{-1}.C_1 & -C_1 D_1^{-1} \\ D_1^{-1}C_1 & D_1^{-1} \end{pmatrix} \sim \begin{pmatrix} 1+\mathcal{O}(\kappa) & \mathcal{O}(\kappa) \\ \mathcal{O}(\kappa) & 1+\mathcal{O}(\kappa) \end{pmatrix}. \tag{4.40}$$

Multiplying all contributions together yields

$$\mathcal{T} = (Q_1^-)^{-1}Q_1^+\tilde{U}_1 \sim \begin{pmatrix} \mathcal{O}(\frac{1}{2\kappa}) + \mathcal{O}(\frac{1}{2}) & \mathcal{O}(2\kappa^2) \\ \mathcal{O}(\frac{1}{2}) & \mathcal{O}(2\kappa) + \mathcal{O}(2\kappa^2) \end{pmatrix}. \tag{4.41}$$

Since we restricted ourselves to a regime with $\kappa \ll 1$, it is evident, that the dominant contribution is coming from the upper left part of the transfer matrix corresponding to a principal minor with index set $I = \{1, 2, 3, \ldots, L\}$. The same line of argument holds for arbitrary $L_t > 1$.

The presented argument shows that index sets containing numbers from 1 to L are favoured, while index sets containing numbers from $L+1$ to $2L$ are seemingly unfavoured. The extreme case, which we have already encountered before, is the maximal principal minor

$$P^{II}, \quad \text{with} \quad I = \{1, 2, 3, \ldots, L\}. \tag{4.42}$$

The "next"-extreme case, would be with a principal minor P^{II} with $L-1$ indices chosen from 1 to L and one index choosen in between $L+1$ and $2L$. We continue this construction of index sets until ending up with the smallest principal minor

$$P^{II}, \quad \text{with} \quad I = \{L+1, L+2, L+3, \ldots, 2L\}. \tag{4.43}$$

Following this explanation we define the classes based on the number of dominant indices in the index set I.

We emphasize once again that this discussion holds in the vacuum sector, i.e. the canonical sector with no quark content $k = 0$, where the total number of principal minors is given by

$$\mathcal{N}[P^{II}] = \binom{2L}{L}, \quad \text{for} \quad |I| = L. \tag{4.44}$$

We define "class 0" to be the dominant class, that is the class describing the maximal principal minor with index set $I = \{1, 2, \ldots, L\}$. Since we only have one index set we denote $\mathcal{N}_0[P^{II}] = 1$. Class 1 shall be the class, where the index set is chosen in such a way that

$$I = \{\underbrace{i_1, i_2, \ldots, i_{L-1}}_{\substack{\text{Choice between} \\ 1 \text{ and } L}}, \underbrace{i_L}_{\substack{\text{Choice between} \\ L+1 \text{ and } 2L}} \}. \tag{4.45}$$

The number of index sets in class 1 is therefore just given by $\mathcal{N}_1[P^{II}] = L^2$. We have L choices of which index to include in $\{L+1, \ldots, 2L\}$ and L choices of which index to exclude from $\{1, \ldots, L\}$. Following this kind of argument, we can build up the tower of classes and write down the number of principal minors belonging to each class. The general formula describing the number of principal minors for class J with $J \in \{0, 1, 2, \ldots, L\}$, reads

$$\text{Class } J \qquad\qquad \mathcal{N}_J[P^{II}] = \binom{L}{J}\binom{L}{L-J}.$$

If we sum up all the principal minors of each class, we obtain, as expected, the total number of principal minors of $\det_0(\mathbf{K})$, that is

$$\binom{2L}{L} = \sum_{J=0}^{L} \binom{L}{J}\binom{L}{L-J}, \tag{4.46}$$

where we used Vandermonde's identity. Note, that the splitting of the principal minors into classes is not an exclusive feature of the vacuum sector, but also shows up in the other canonical sectors.

Next, we can split up all the principal minors of the vacuum sector into those classes and examine the distribution of the principal minors for each class separately. As before we consider $\log(\Re[P^{II}])$ for positive principal minors and $\log(-\Re[P^{II}])$ for negative principal minors. The results for the distributions for a high temperature of $L_t = 8$, are given in figure 4.12.

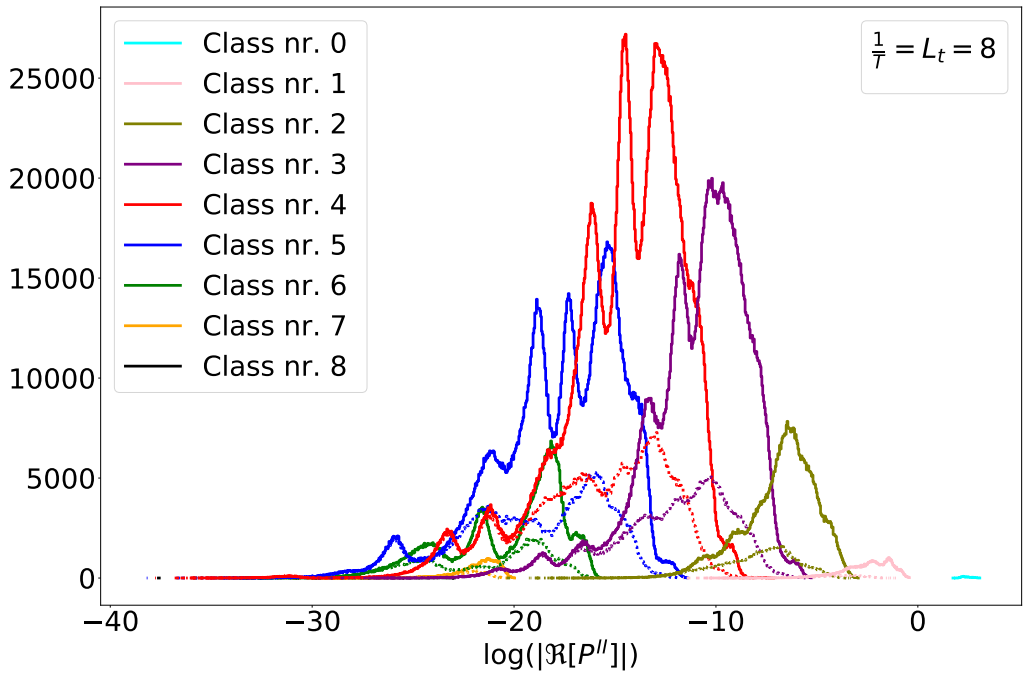

Figure 4.12: Class structure of the principal minors in the vacuum sector, with $\beta = 5.0$, $m_0 = 0.0220$, $L = 8$ fix and $L_t = 8$. The continuous lines represent the positive contributions, while the dotted lines (below the continuous ones) represent the negative contributions. We see that the dominant class 0 (cyan-coloured, collection of all dominant prinicipal minors), is presented to the far right with a little bump. Each class seems to have "subclasses", denoted by bumps again.

As expected, the dominant class, that is class 0, can be found to the very far right and is always positive - giving the largest relative contribution to the positive determinant of the Wilson Dirac operator. With increasing "class-number" the principal minors become smaller and smaller and the contributions from the highest class $L = 8$, are sitting to the very left. Additionally, we notice that there seems to be some kind of substructure to each class, indicating that there is more information hidden within those classes. For decreasing temperatures, the classes smoothen out and become almost log-normal. We show the division of principal minors into classes for a low temperature of $L_t = 40$ in figure 4.13.

Upon examining the figures it seems that for low temperatures the distributions for the dominant classes become smoother, almost Gaussian. This might be an indication, that the principal minors are log-normal distributed at low temperatures. We investigate this further, by restricting ourselves to the dominant class, that is class 0 and investigating its distribution for various temperatures in figure 4.14. We see very nicely how for decreasing temperature the distribution becomes "smoother" and "rounder" and the overall contribution shifts to the right.

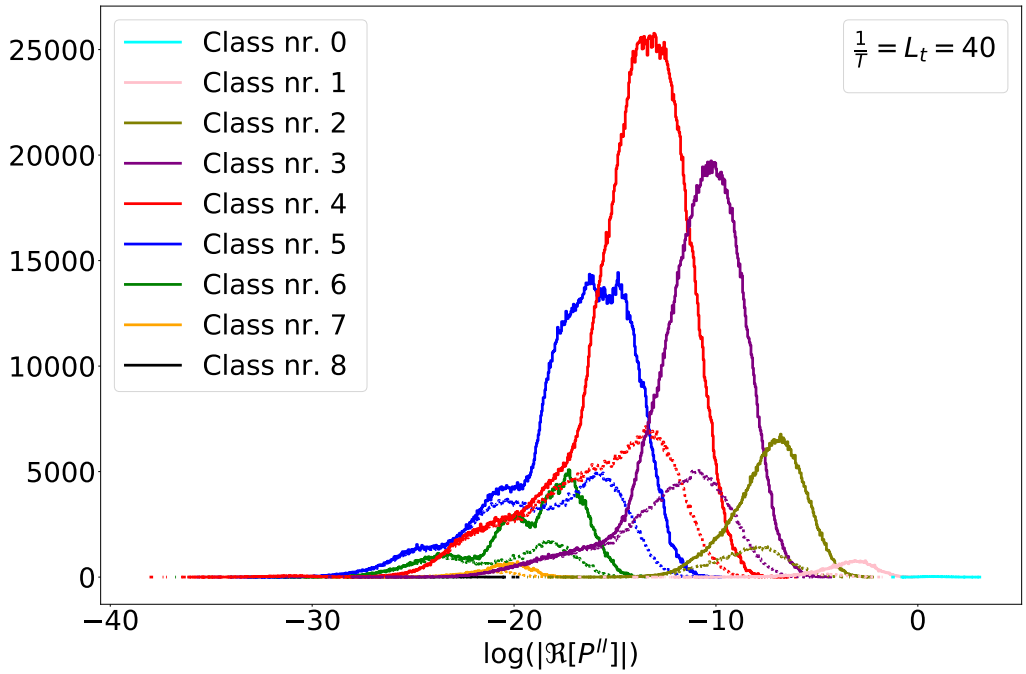

Figure 4.13: Class structure of the principal minors in the vacuum sector, with $\beta = 5.0$, $m_0 = 0.0220$, $L = 8$ fix and $L_t = 40$. With decreasing temperature the subclass structure seems to get "washed out".

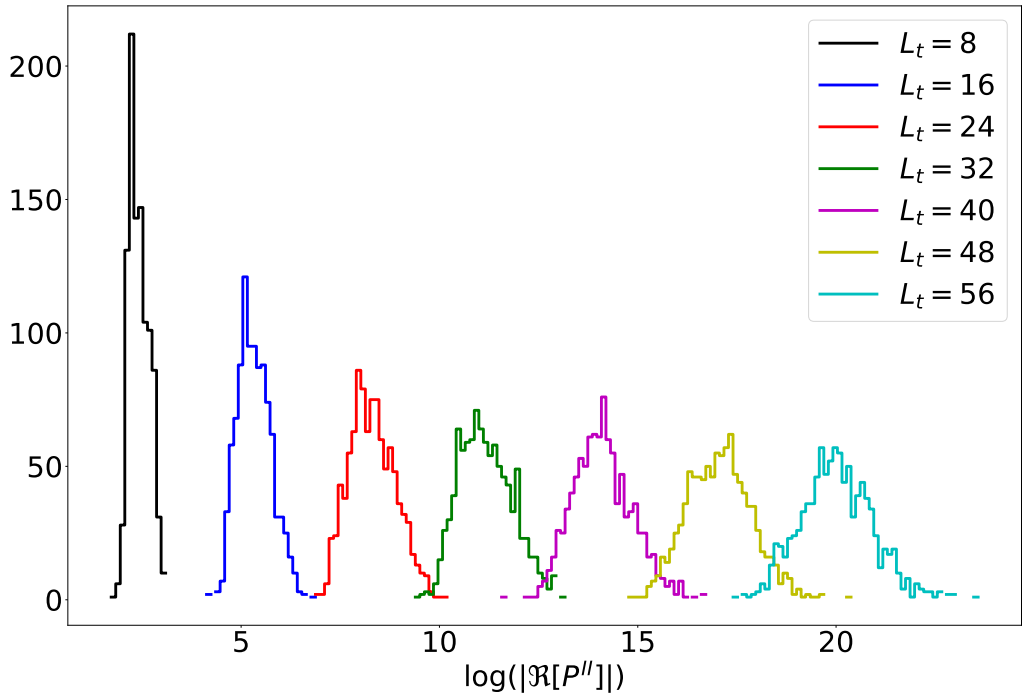

Figure 4.14: Distribution of the maximal principal minor (class 0) in the vacuum sector for fixed $\beta = 5.0$, $m_0 = 0.0220$, $L = 8$ and varying L_t. We can see, that for decreasing temperature the distribution looks very much normal-distributed.

4.7 Spectroscopy with the canonical formalism

So far we worked in this chapter with the quenched Schwinger model ($N_f = 0$), as well as with 1-flavour Schwinger model ($N_f = 1$). Throughout this section and the next section, we turn to the 2-flavour Schwinger model. We extract ground state energies of multi-pion states, by using the canonical formalism as illustrated in section 3.5. By using the master formula (eq. (3.104))

$$E_{n\pi} = \lim_{T\to 0} E_{n\pi}(T) = -\lim_{T\to 0} T \log\left(\frac{\mathcal{Z}_{(n,-n)}(T)}{\mathcal{Z}_{(0,0)}(T)}\right), \tag{4.47}$$

we can compute the pion masses $m_\pi(L)$, the 2-pion ground state energies $E_{2\pi}(L)$ and the 3-pion ground state energies $E_{3\pi}(L)$ as a function of the volume L. The details of these computations are a main part of this thesis and will be elaborated in detail in chapter 5.

These energies can also be extracted by using the correlators formed with π^+, $\pi^+\pi^+$ and $\pi^+\pi^+\pi^+$ operators. This is explained in more detail in the appendix chapter B.

We argued in section 3.5 that the energies coincide with each other, here want to provide some empirical evidence for that statement. We compare the ground state energies $m_\pi^{can.}(L), E_{2\pi}^{can.}(L)$ and $E_{3\pi}^{can.}(L)$ to energies extracted from π^+, $\pi^+\pi^+$ and $\pi^+\pi^+\pi^+$ correlators.

Note, that the canonical results have been obtained by reweighting quenched simulations onto the canonical sectors, while the results obtained from traditional spectroscopy were done separately using dynamical simulations with two flavours. We used a publicly available code, provided by Urbach et al. in [48], which simulates the 2-dimensional Schwinger model with $N_f = 2$ quarks using a Hybrid Monte Carlo (HMC) algorithm. Those simulations were performed with different volumes L and for fixed $L_t = 120$.

Despite being from completely different simulations, we obtain a very nice agreement between the measurements, as can be seen in figure 4.15. The only differences seem to stem from the pion mass at extremely small volume L. We believe that this discrepancy stems from reweighting difficulties, as elaborated in the appendix section C.9.

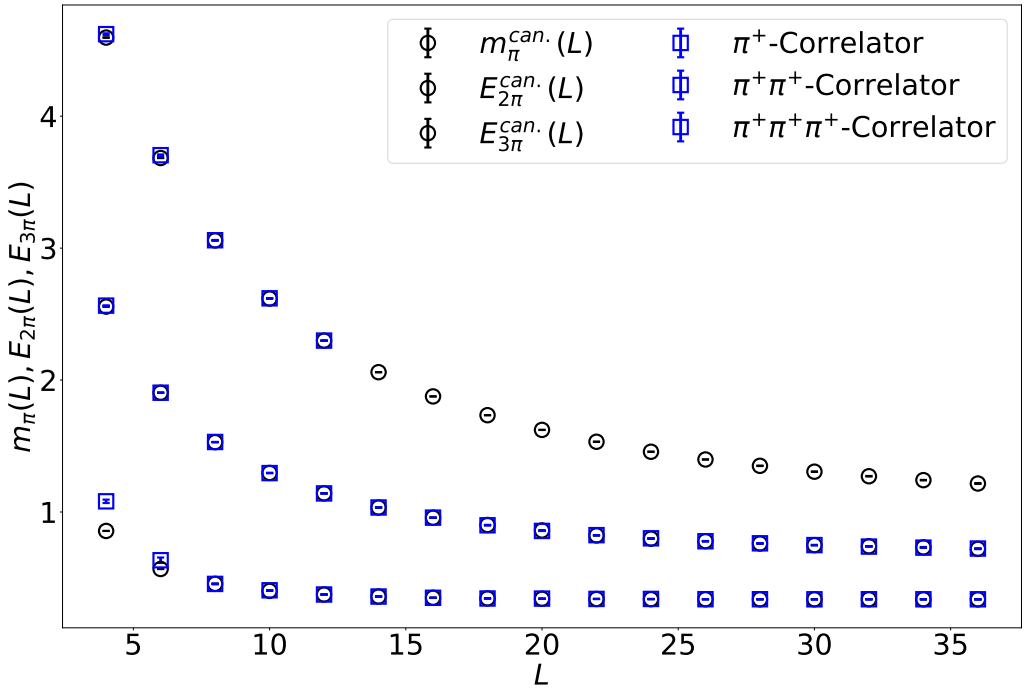

Figure 4.15: We use different volumes and compare the ground state energies $m_\pi^{can.}(L), E_{2\pi}^{can.}(L)$ and $E_{3\pi}^{can.}(L)$ to the direct measurements using correlation functions. We use $\beta = 5.00$ and $m_0 = 0.0220$ such that $m_\pi/g \approx 0.75$.

4.8 Saturating the lattice with mesons

The biggest advantage of the canonical formalism is the direct access to ground state energies of multi-meson sectors. This allows us to directly investigate the condensation of pions in the 2-flavour Schwinger model, circumventing the use of correlators, as explained in the previous section.

To illustrate said condensation phenomenon, we determine the expectation value of the isospin density, resp. pion density as a function of the isospin chemical potential μ_I

$$\rho_\pi(\mu_I) = \frac{\langle n \rangle}{L}, \tag{4.48}$$

where n denotes the number of pions. We compute the pion density by using reweighting methods as explained in section C.9, where the pion number $\langle n \rangle$ can be expressed using simulations of the 2-flavour Schwinger model, such that

$$\langle n \rangle = \frac{\langle \sum_{k=-L}^{L} k \cdot \mathcal{R}[N_f = 2, k] \cdot e^{\mu_I k L_t} \rangle_{N_f=2}}{\langle \sum_{k=-L}^{L} \mathcal{R}[N_f = 2, k] \cdot e^{\mu_I k L_t} \rangle_{N_f=2}}. \tag{4.49}$$

In above equation we used a reweighting factor, which allows us to reweight to the canonical sectors of the 2-flavour Schwinger model

$$\mathcal{R}[N_f = 2, k] = \frac{\det_k(\mathbf{K}[U]) \det_{-k}(\mathbf{K}[U])}{|\det(\mathbf{K}[U, \mu_I = 0])|^2}. \tag{4.50}$$

We show results for a fixed volume $L = 24$ and varying temperatures $L_t = \frac{1}{T} = \{20, 60, 180\}$ in figure 4.16. As expected, we see condensation where the number of pions - and therefore the pion density - rises as a function of μ_I. We also notice that the behaviour of the pion density depends heavily on the temperature. For low temperatures $L_t = 60, 180$ the pion density rises from $\rho = 0$ to $\rho = \frac{1}{24}$ at some critical chemical potential μ_1 which can be identified as the pion mass $\mu_1 = m_\pi$. If we increase the isospin chemical potential further, a second pion condensates at some critical value μ_2. With increasing chemical potential more and more pions condensate until eventually saturating the lattice.

This condensation behaviour is different for all three temperatures, at high temperature (given by $L_t = 20$) the line is "washed out" denoting a slow continuous change of the pion-density. However, for low temperatures the behaviour becomes much more distinct, basically resembling a step-function. For zero temperature one expects discontinuous jumps.

It was shown in Ref. [49] that at very low temperatures the condensation thresholds μ_i are related to physical multi-pion energies, i.e.

$$m_\pi(L) = \mu_1(L) \quad \text{and} \quad E_{n\pi}(L) = \sum_{i=1}^{n} \mu_i(L), \tag{4.51}$$

where we explicitly take into account the volume dependence.

The symbols (circle, square, triangle) in figure 4.16 denote the direct calculations of the isospin chemical potentials via

$$\mu_I(n) = F(n) - F(n-1) = -T \log\left(\frac{\mathcal{Z}_{(n,-n)}}{\mathcal{Z}_{(n-1,-(n-1))}}\right). \tag{4.52}$$

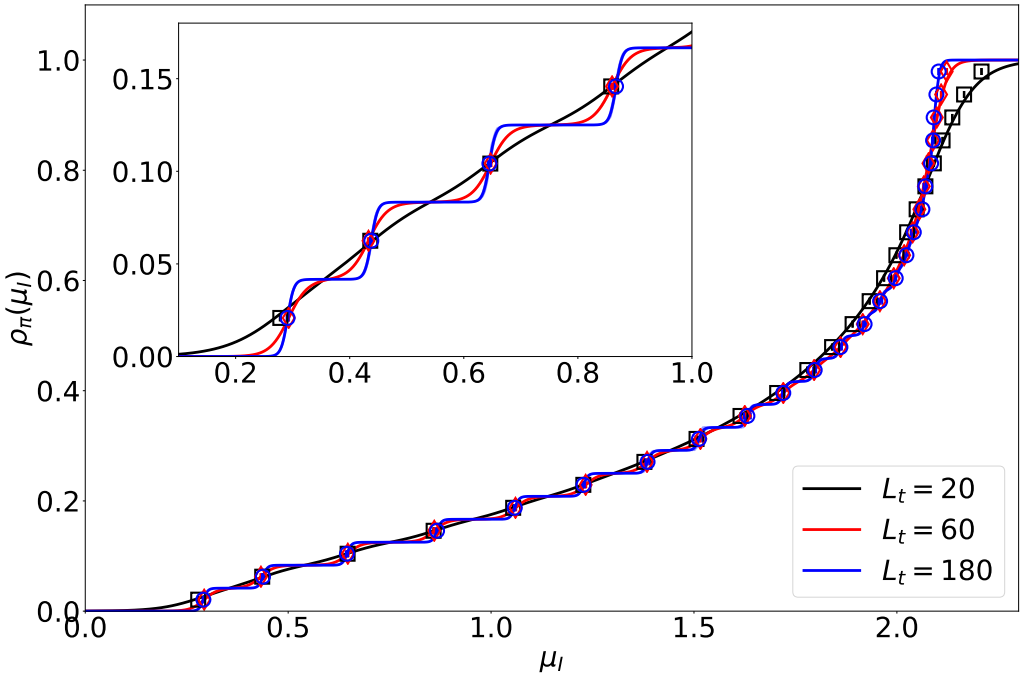

Figure 4.16: Pion condensation in the 2-flavour Schwinger model. We used dynamical simulations (HMC), with $\beta = 5.00, m_0 = 0.00$, fixed volume $L = 24$ and 3 different temperatures $L_t = 20, 60, 80$.

5 Numerical studies - Pion scattering using the canonical partition functions

In this chapter we will be working exclusively with the 2-flavour variant of the Schwinger model in the canonical formulation on the lattice, as introduced in section 3.5. We consider two mass-degenerate quarks, an up quark u and a down quark d. The fugacity expansion on the lattice then reads

$$\mathcal{Z}_{GC}(T,\mu) = \sum_{n_u=-L}^{L} \sum_{n_d=-L}^{L} e^{\frac{\mu_I}{2} L_t (n_u - n_d)} \mathcal{Z}_{(n_u,n_d)}(T), \tag{5.1}$$

where the isospin chemical potential μ_I, is related to the quark chemical potentials via

$$\frac{\mu_I}{2} = \mu_u = -\mu_d, \tag{5.2}$$

and the canonical partition functions

$$\mathcal{Z}_{(n_u,n_d)}(T) = \int \mathcal{D}U \det{}_{n_u}(\mathbf{K}[U]) \det{}_{n_d}(\mathbf{K}[U]) e^{-S_g[U]}, \tag{5.3}$$

fix the number of up and down quarks in our system with the subscript (n_u, n_d). The number of up and down quarks is restricted due to the Gauss law, such that the total quark number is zero, while the isospin is not restricted

$$Q = n_u + n_d = 0, \quad \text{and} \quad I = \frac{n_u - n_d}{2} \quad \text{arbitrary.} \tag{5.4}$$

Consequently, the meson sectors can be completely characterized by their isospin I. We have argued in section 3.6, that the ground states of n-mesons sectors are actually multi-pion states, with quantum numbers $I = n$. In the canonical formalism it is straightforward to compute the ground state energies of those multi-pion states $E_{n\pi}$, by taking the free energy difference between the corresponding canonical sectors

$$\boxed{E_{n\pi} = -\lim_{T\to 0} T \log\left(\frac{\mathcal{Z}_{(+n,-n)}(T)}{\mathcal{Z}_{(0,0)}(T)}\right)}. \tag{5.5}$$

Formula (5.5) is of major importance, it will be used to compute multi-pion ground state energies, instead of correlators. Throughout this chapter we refer to eq. (5.5) as the "master formula".

The basis of the calculations presented here is given by a range of measurements for multi-pion ground state energies, where we vary multiple parameters. The simulations are performed for different couplings $\beta = \frac{1}{(ag)^2}$ and different bare quark masses m_0, given in table 5.1. From now on, if not mentioned otherwise, we set the lattice spacing to one, that is $a = 1$.

Dataset	β	am_0	κ	am_π	m_π/g
A3	3.0	0.0000	0.5000	0.4330(3)	0.7500(5)
A5	5.0	0.0220	0.4892	0.3387(2)	0.7574(3)
A7	7.0	0.0266	0.4870	0.2859(1)	0.7564(3)
B5	5.0	-0.0400	0.5208	0.1921(4)	0.4296(8)
B7	7.0	-0.0220	0.5112	0.1701(6)	0.450(2)

Table 5.1: Datasets which have been used throughout this chapter.

For the first three and the remaining two datasets we tuned the bare mass m_0 in such a way that the infinite volume pion mass is more or less the same

$$\{\text{A3, A5, A7}\} \Rightarrow \frac{m_\pi}{g} \approx 0.75, \qquad \text{and} \qquad \{\text{B5, B7}\} \Rightarrow \frac{m_\pi}{g} \approx 0.44. \tag{5.6}$$

By fixing the infinite volume pion mass we can make statements about the continuum limit.

In order to outline the strategy of this work, we restrict ourselves to a single dataset from table 5.1, for the sake of simplicity.

For said dataset, we perform quenched simulations for different volumes L and different temperatures $L_t = \frac{1}{T}$. We extract 1-, 2- and 3-pion ground state energies, such that we obtain a set of measurements

$$E_{n\pi}(L, L_t), \qquad \text{with} \qquad n \in \{1, 2, 3\}, \quad L \in \{4, 6, 8, \ldots, 40\}, \quad L_t \in \{4, 6, 8, \ldots, 60\}. \tag{5.7}$$

A summary of the performed simulations is given in the appendix H.1. Here we give a short superficial description of how these measurements will be processed, the details follow suit in the corresponding sections.

- We first discuss the temperature behaviour of the 1-pion ground state energies $E_\pi(T)$, for fixed small and large volumes.

  For each volume L, we compute the ground state energies $E_\pi(L)$ by performing the extrapolation to zero temperature, using the master formula eq. (5.5) with $n = 1$. Note, that the ground state energy for the 1-pion state corresponds to the pion mass

  $$E_\pi(L) \stackrel{!}{=} m_\pi(L). \tag{5.8}$$

  Using the pion mass for different volumes $m_\pi(L)$, we can discuss finite volume effects, as explained in section 2.6. By utilizing Lüschers formula eq. (2.62) we determine the pion mass in the infinite volume

  $$m_\pi = \lim_{L\to\infty} m_\pi(L). \tag{5.9}$$

- We use the master formula with $n = 2$ and extract the ground state energies of the isospin $I = 2$ sector. We obtain the finite volume dependence of the 2-pion ground state energy $E_{2\pi}(L)$.

- With these two measurements we can compute the scattering phase shift (see section 2.7) via

  $$2\delta(k) = -kL + 2\pi n, n \in \mathbb{Z}, \tag{5.10}$$

  for each volume L. The relative momentum $k = k(L)$ can be extracted via the bosonic dispersion relation for two bosons in the center of mass frame

  $$E_{2\pi}(L) = 2\cosh^{-1}(\cosh(m_\pi) + 1 - \cos(k(L))). \tag{5.11}$$

  We obtain discrete measurements for the scattering phase shifts for each volume L

  $$\delta(k(L)) \equiv \delta(L). \tag{5.12}$$

- These values $\delta(k(L)) \equiv \delta(L)$ can be fitted to an effective range expansion presented in subsection 2.7.2. In our particular case, we use the bosonic ansatz (labelled with $L = 0$), which allows us to obtain a heuristic ansatz for the scattering phase shift $\delta(k)$.

- Using the previously determined scattering phase shift $\delta(k)$ and the 3-particle quantization conditions presented in section (2.8), we can make predictions for the 3-pion ground state energies. Since these predictions are based on the scattering phase shift, we will denote them with an additional superscript $E^\delta_{3\pi}(L)$.

- Finally the determinations of $E^\delta_{3\pi}(L)$ can be compared to the direct measurements of the 3-pion ground state energies, which have been extracted using the master formula with $n = 3$.

5.1 Isospin $I = 1$ sector and extraction of the pion mass $m_\pi(L)$

Let us briefly recapitulate the most important properties of the isospin $I = 1$ sector, for further information we refer to section 3.6. The lightest particle in the massive 2-flavour Schwinger model is given by the mass-degenerate pion triplet $|\pi\rangle = \{|\pi^-\rangle, |\pi^0\rangle, |\pi^+\rangle\}$. Within this triplet, the state with maximal z-component of the isospin is built from an up and antidown quark $|\pi^+\rangle = |u\bar{d}\rangle$. It can be identified as the ground state of the isospin $I = 1$ sector described by the canonical partition function in eq. (5.3) with $(n_u, n_d) = (1, -1)$. Hence, the ground state energy of the 1-meson sector, i.e., the mass of the pion, is determined by using the master equation eq. (5.5) with $n = 1$.

For the sake of simplicity, we consider a single dataset from table 5.1, that is dataset A5, the discussion we present here is analogous to all the other datasets. The objective is to understand the finite temperature behaviour of the ground state energy

$$E_\pi(T), \text{ resp. } m_\pi(T), \quad \text{for a fixed volume } L. \tag{5.13}$$

We illustrate the finite temperature behaviour of the pion mass for small volumes in figure 5.1 and for large volumes in figure 5.2.

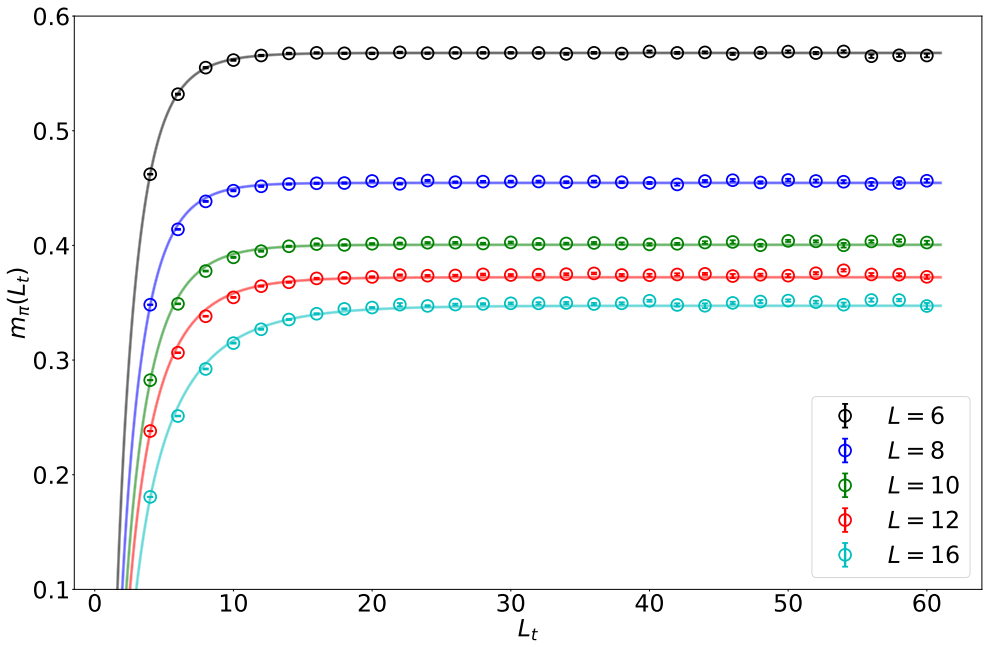

Figure 5.1: Dataset A5. Finite temperature behaviour of the pion mass $m_\pi(L_t)$, for different small volumes. The lines with error bands represent fits including excited state contributions from the $I = 1$ and the vacuum sector. The temperature is related to the temporal extent of the lattice via $T = 1/L_t$.

For a fixed volume, we can examine the behaviour of the ground state energy as a function of the temperature (reminder: $T = \frac{1}{L_t}$). According to the discussion in subsection 3.6.5, we obtain

$$E_\pi(T) \approx m_\pi - T \log\left(\frac{1 + 2\sum_{i=1}^{\frac{L}{2}} e^{-(E^{(i)}_{\pi^+} - m_\pi)/T} + e^{-(m_{a_0} - m_\pi)/T} + 2\sum_{i=1}^{\frac{L}{2}} e^{-(E^{(i)}_{a_0} - m_\pi)/T}}{1 + e^{-m_\pi/T} + 2\sum_{i=1}^{\frac{L}{2}} e^{-E^{(i)}_{\pi^0}/T}}\right). \tag{5.14}$$

We deduce that the behaviour of the pion mass towards high temperatures ($L_t \to 0$) is dominated by contributions from the isospin $I = 1$ sector. These dominant contributions arise from excited π^+ states and possibly from a_0^+ states. However, we can also see that upon approaching small temperatures, those higher order contributions vanish fast and the asymptotic behaviour can easily be described by a constant.

At large volumes, a similar behaviour can be observed (figure 5.2). For large volumes higher order contributions from the isospin $I = 1$ sector are more dominant than for small volumes, negative corrections and the resulting curvatures are already visible at small temperatures.

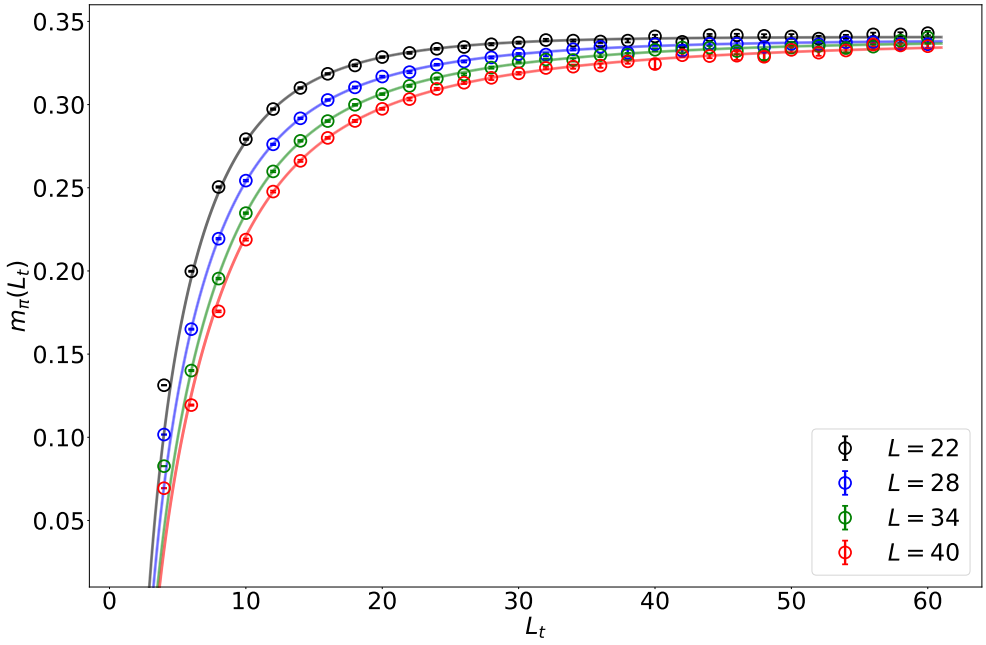

Figure 5.2: Dataset A5. Finite temperature behaviour of the pion mass $m_\pi(L_t)$, for different large volumes. The lines with error bands represent fits including excited state contributions from the $I = 1$ and the vacuum sector. The temperature is related to the temporal extent of the lattice via $T = 1/L_t$.

The reason for this effect lies in the spectrum of the theory. The energy differences for subsequent excited states differ between small and large volumes due to the quantization of the momenta. To explain this argument in more detail, consider the first excited state contribution arising from the π^+ pion in the isospin $I = 1$ sector, that is

$$E^{(1)}_{\pi^+} = \cosh^{-1}(\cosh(m_\pi) + 1 - \cos(p^{(1)})), \qquad \text{with } p^{(1)} = \frac{2\pi}{L} \cdot 1. \tag{5.15}$$

We can see that the energy gap to the pion mass m_π becomes larger the smaller the volume is. Vice-versa this gap becomes smaller the larger the volume is. This means, that for large volumes contributions from high energy states become noticeable already at low temperatures.

This finite temperature behaviour of the pion mass $m_\pi(L)$ puts forth some problems when trying to take the zero temperature limit. These problems can be summarized as "model-selection" problems, which describe an unsatisfactory ambiguity when it comes to choosing fit models and fit ranges which are used to extrapolate to zero temperature.

To circumvent this ambiguity and obtain feasible model-independent results we use a combination of Bayesian model averaging as described in the appendix F and what we call "systematic averaging" as described in section F.4.

For each volume L we consider three possible fit functions, which are truncations of the function presented in eq. (5.14) and allow us to extrapolate to zero temperature. We utilize the following three models

$$\begin{aligned}
\mathrm{M}_{m_\pi,1}(T, m_\pi) &= m_\pi, \\
\mathrm{M}_{m_\pi,2}(T, m_\pi) &= m_\pi - T \log\left(\frac{1 + 2\sum_{i=1}^{\frac{L}{2}} e^{-(E^{(i)}_{\pi^+} - m_\pi)/T}}{1 + e^{-m_\pi/T} + 2\sum_{i=1}^{\frac{L}{2}} e^{-E^{(i)}_{\pi^0}/T}}\right), \\
\mathrm{M}_{m_\pi,3}(T, m_\pi, m_{a_0}) &= m_\pi - T \log\left(\frac{1 + 2\sum_{i=1}^{\frac{L}{2}} e^{-(E^{(i)}_{\pi^+} - m_\pi)/T} + e^{-(m_{a_0} - m_\pi)/T} + 2\sum_{i=1}^{\frac{L}{2}} e^{-(E^{(i)}_{a_0} - m_\pi)/T}}{1 + e^{-m_\pi/T} + 2\sum_{i=1}^{\frac{L}{2}} e^{-E^{(i)}_{\pi^0}/T}}\right).
\end{aligned} \tag{5.16}$$

The first and second models depend on one fit parameter m_π, while the third one also takes into account contributions from an a_0 state, yielding an additional parameter m_{a_0}.

For each model we perform a variety of fits with varying fit ranges (the details are given in the appendix H section H.2). The resulting pion masses are being averaged for each fit ansatz using the Bayesian model averaging procedure, yielding model-dependent pion masses, which are then being averaged using systematic averaging. This yields a final model-independent result for the pion mass $m_\pi(L)$. In table 5.2 we show such a calculation for a few selected volumes for the dataset A5.

L	$m_\pi(L)$ from $\mathrm{M}_{m\pi,1}$	$m_\pi(L)$ from $\mathrm{M}_{m\pi,2}$	$m_\pi(L)$ from $\mathrm{M}_{m\pi,3}$	Final results
4	0.85634(29)	0.85626(22)	0.85647(22)	0.85636(25)
6	0.56785(17)	0.56785(17)	0.56795(16)	0.56788(17)
8	0.45550(21)	0.45550(20)	0.45540(18)	0.45546(21)
38	0.33238(82)	0.33805(25)	0.33814(22)	0.3379(11)
40	0.3304(11)	0.33799(33)	0.33808(26)	0.3378(14)

Table 5.2: Dataset A5. Some sample results of the three fitting approaches after the Bayesian model averaging. The last column denotes the results after the systematic averaging.

The resulting pion masses for different volumes $m_\pi(L)$ indicate the appearance of finite volume effects as discussed in section 2.6. We discuss these finite volume effects in the next section.

5.2 Finite volume effects

In the previous section we considered the pion masses as function of temperature for a fixed volume, that is

$$m_\pi(T), \quad \text{for a fixed volume } L. \tag{5.17}$$

After extrapolating to zero temperature we obtain the pion masses as a function of the volume $m_\pi(L)$, which allows us to discuss finite volume effects in detail. As elaborated in section 2.6, finite volume effects arise when the pion wavefunction overlaps at the boundaries of the box and interacts with itself. As a result, the pion mass gets artificially inflated for small volumes. Lüscher appropriately called these kinds of effects "interactions around the world" and provided the needed formula, which can be used to describe these effects. In case of a massive 2-dimensional quantum field theory, this formula is given by eq. (2.63), that is

$$m_\pi(L) = m_\pi + \left(\frac{\lambda^2}{4\sqrt{3}m_\pi^3}\right) e^{-\frac{\sqrt{3}}{2}m_\pi L} + \frac{1}{\sqrt{m_\pi L}}\left(\frac{F(0)}{4m_\pi\sqrt{2\pi}}\right) e^{-m_\pi L}, \tag{5.18}$$

where $m_\pi = \lim_{L\to\infty} m_\pi(L)$ defines the infinite-volume pion mass, $F(0)$ the forward scattering amplitude and λ some effective 3-particle coupling (resp. 3-pion coupling in our case). We use Lüscher's ansatz to describe the finite volume behaviour using $m_\pi, F(0)$ and λ as fit parameters. The results for the two different pion masses $m_\pi/g \approx 0.75$ and $m_\pi/g \approx 0.44$ are presented in figure 5.3 and figure 5.4. The ansatz allows us to describe the measurements of $m_\pi(L)$ down to small volumes. For the datasets A3, A5 and A7 we can go as far as $m_\pi L \gtrsim 3.0$, for the smaller pion mass with datasets B5 and B7 this ansatz is even better, allowing us to describe the finite volume behaviour down to $m_\pi L \gtrsim 2.0$. For the two sets of measurements presented in the two figures 5.3 and 5.4, we separately kept the infinite volume pion mass fixed, which allows us to estimate lattice artefacts. Our results indicate nicely, that lattice artefacts are very well under control, even for small volumes.

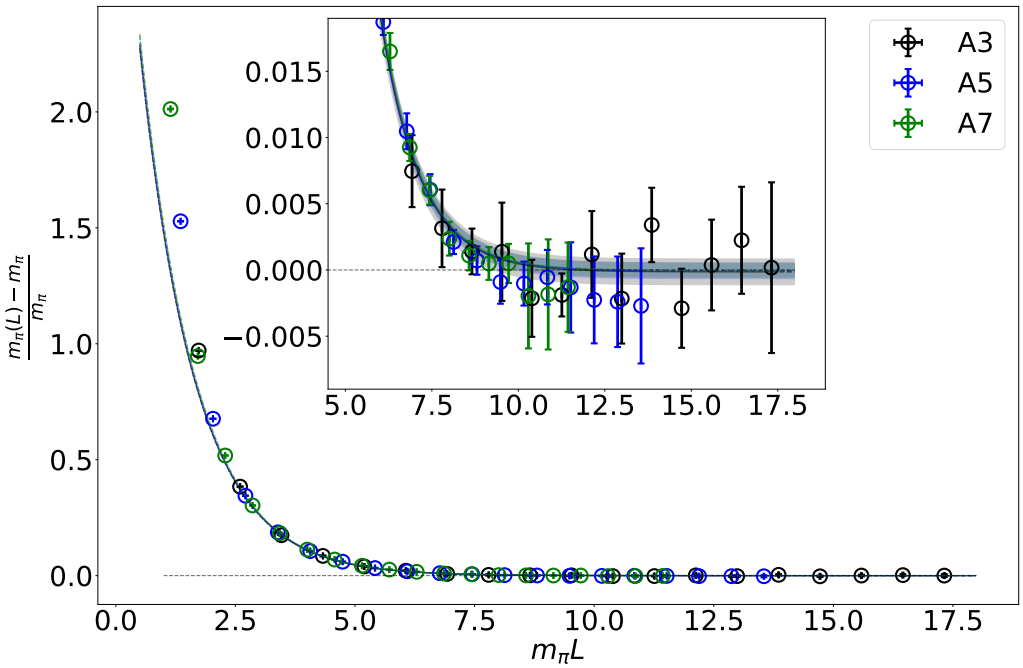

Figure 5.3: Datasets A3, A5 and A7. Rescaled finite volume behaviour of the pion mass $m_\pi(L)$, for $m_\pi/g \approx 0.75$. The lines with errorbands represent finite volume fits using Lüscher's formula.

We extract the dimensionless 3-pion coupling $a^2\lambda$, forward scattering amplitude $a^2F(0)$ and the dimensionless ratio $\frac{\lambda}{g^2}$ for all available datasets, using different fitting approaches. In order to get a final model-independent result, we perform a combination of Bayesian model averaging and systematic averaging, yielding the final results depicted in table 5.3. The details of said calculations are given in the appendix section H.3.

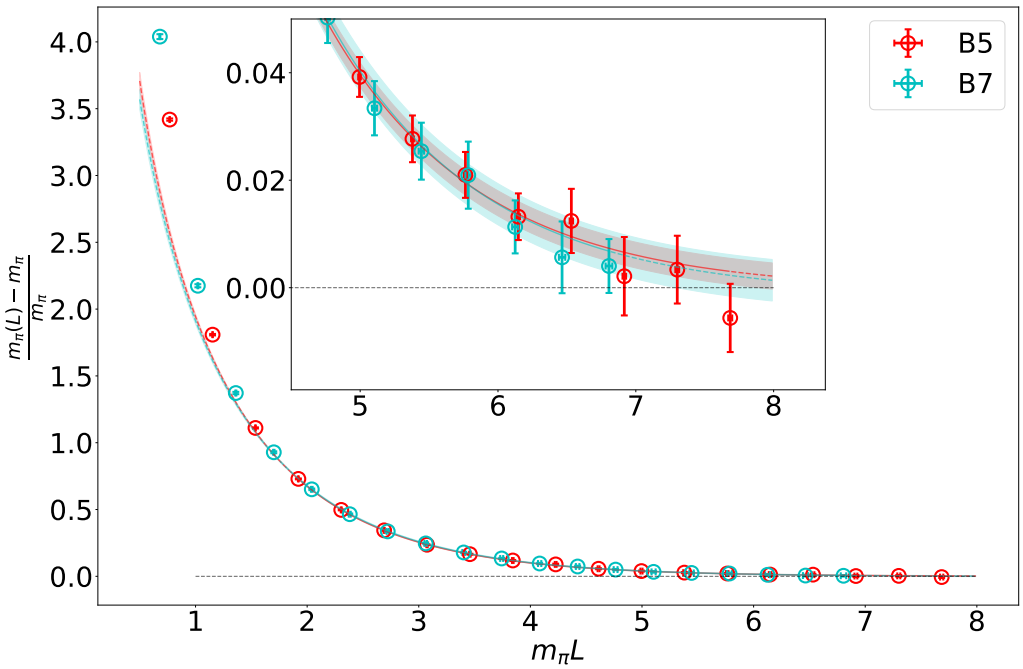

Figure 5.4: Datasets B5 and B7. Rescaled finite volume behaviour of the pion mass $m_\pi(L)$, for $m_\pi/g \approx 0.44$. The lines with errorbands represent finite volume fits using Lüscher's formula.

Dataset	m_π/g	$a^2\lambda$	λ/g^2	$a^2F(0)$
A3	0.7500(5)	0.922(11)	2.765(34)	2.31(35)
A5	0.7574(3)	0.56747(90)	2.8373(45)	N/A
A7	0.7564(3)	0.40796(42)	2.8557(29)	N/A
B5	0.4296(8)	0.1528(18)	0.7639(91)	0.913(49)
B7	0.450(2)	0.1235(19)	0.865(13)	0.644(63)

Table 5.3: Results for the 3-pion coupling $a^2\lambda$, λ/g^2 and $a^2F(0)$. For the datasets A5 and A7 we were not able to extract the forward scattering $a^2F(0)$ due to a lack of good fits.

We perform a continuum extrapolation of the dimensionless parameter λ/g^2, for fixed coupling g and varying pion mass m_π. For the sake of simplicity, we use a linear function for the extrapolation, shown in figure 5.5. The numerical results are given by table 5.4.

We know (from section 2.6) that in the strong coupling limit $m_\pi/g \to 0$ the Schwinger model goes over into the Sine-Gordon model, where the 3-pion coupling λ vanishes. As expected this is reinforced here, we see that for a fixed coupling g the 3-pion coupling λ decreases with the pion mass.

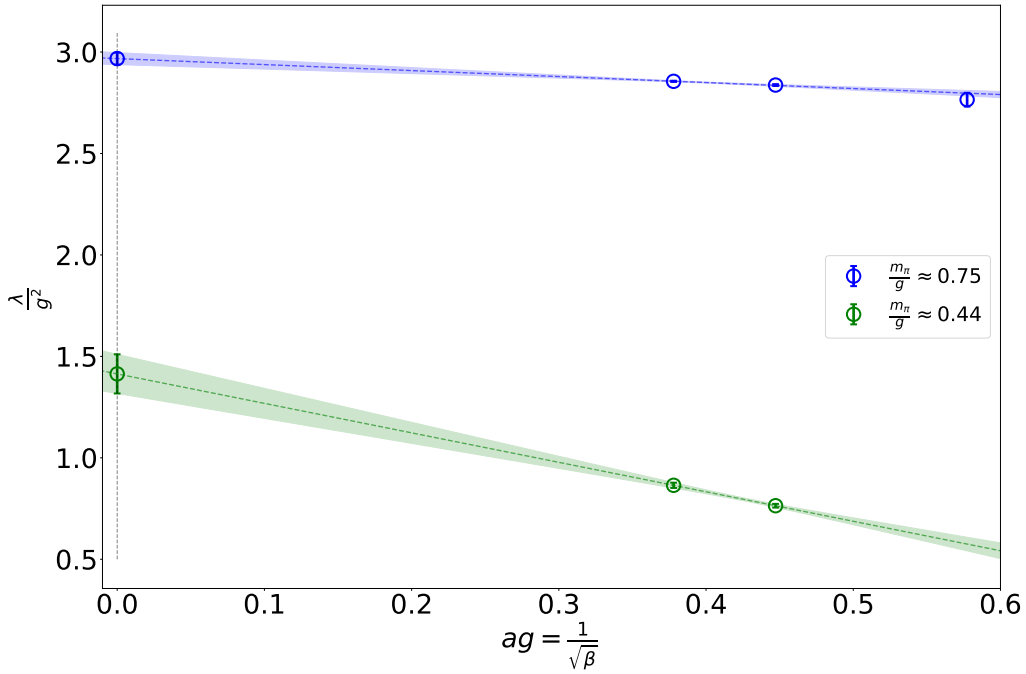

Figure 5.5: Continuum extrapolation of λ/g^2, for fixed coupling g and varying pion mass m_π. A linear function was used for the continuum extrapolation.

m_π/g	λ/g^2
0.75	2.968(30)
0.44	1.414(97)

Table 5.4: Continuum extrapolation of λ/g^2, for fixed coupling g and varying pion mass m_π, numerical results.

5.3 Isospin $I = 2$ sector

So far we used the master formula eq. (5.5) with $n = 1$, to determine the pion masses $m_\pi(L)$ as a function of the volume. In the next step, we can utilize said formula with $n = 2$ to determine the ground state energy of the isospin $I = 2$ sector, that is the ground state energy $E_{2\pi}$ of a 2-pion state $|\pi^+\pi^+\rangle$. We first investigate the temperature behaviour of the 2-pion ground state energy

$$E_{2\pi}(T), \quad \text{for a fixed volume } L, \tag{5.19}$$

in figure 5.6 and figure 5.7.

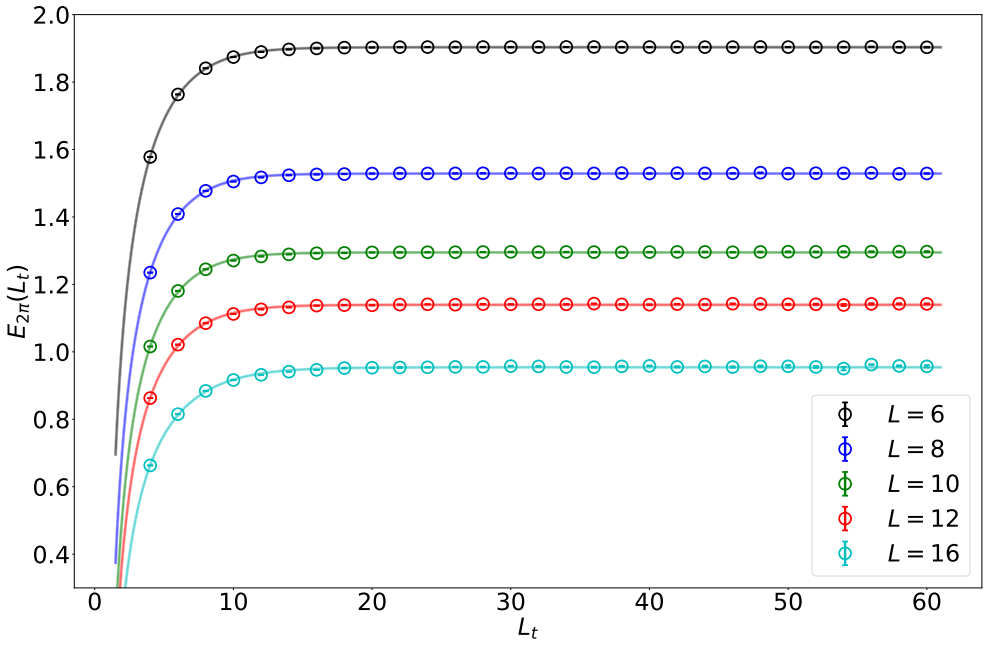

Figure 5.6: Dataset A5. Finite temperature behaviour of the 2-pion ground state energy $E_{2\pi}(L_t)$, for different small volumes. The lines with error bands represent the best fits. The temperature is related to the temporal extent of the lattice via $T = 1/L_t$.

Upon examining the temperature behaviour of the 2-pion ground state energy we encounter all the known effects we have seen when investigating the temperature dependence of the pion mass. For high temperatures $E_{2\pi}(T)$ is governed by corrections arising from excited meson states living in the isospin $I = 2$ sector (for example excited 2-pion states). For decreasing temperature, we obtain the usual plateau, which indicates the desired ground state energy $E_{2\pi}$. Upon comparing the behaviour of $E_{2\pi}(T)$ between the different volumes we see that for large volumes temperature corrections are much more dominant than for small volumes. This is no surprise, also in the isospin $I = 2$ sector the energy levels for subsequent energy states move closer to each other with increasing volume, analogous to the isospin $I = 1$ case.

As before, we extract the ground state energies $E_{2\pi}$ by extrapolating to zero temperature using a combination of Bayesian model averaging and systematic averaging. The proposed fit models are motivated by eq. (3.131) as discussed in subsection 3.6.5

$$\mathrm{M}_{E_{2\pi},1}(T, E_{2\pi}) = E_{2\pi} \tag{5.20}$$

$$\mathrm{M}_{E_{2\pi},2}(T, E_{2\pi}, A_1, A_2) = E_{2\pi} - T \log\left(\frac{1 + A_2 e^{-A_1/T}}{1 + e^{-m_\pi/T} + 2\sum_{i=1}^{\frac{L}{2}} e^{-E_{\pi^0}^{(i)}/T}}\right). \tag{5.21}$$

The parameter $m_\pi = m_\pi(L)$ in the second function $\mathrm{M}_{E_{2\pi},2}$ is determined beforehand from the zero temperature extrapolation of the pion mass. Consequently, the fit models have one and three fit parameters, respectively.

The results for the relative finite volume corrections

$$\frac{E_{2\pi}(m_\pi L) - 2m_\pi}{2m_\pi}, \tag{5.22}$$

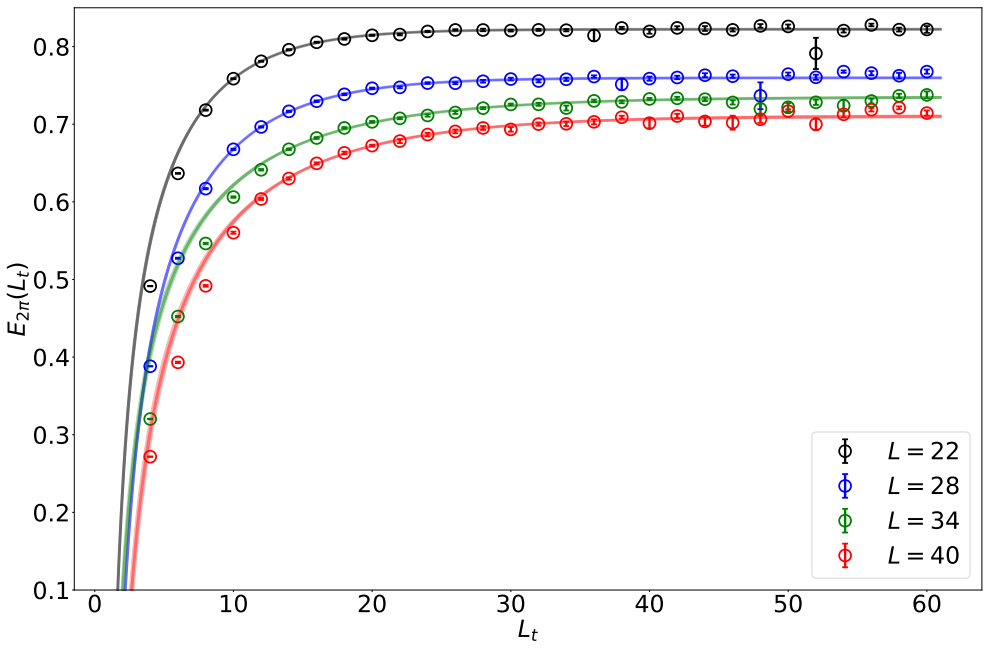

Figure 5.7: Dataset A5. Finite temperature behaviour of the 2-pion ground state energy $E_{2\pi}(L_t)$, for different small volumes. The lines with error bands represent the best fits. The temperature is related to the temporal extent of the lattice via $T = 1/L_t$.

are depicted in figure 5.8 and 5.9. We can see very nicely, how the measurements asymptotically approach the infinite volume limit

$$2m_\pi = 2 \lim_{L\to\infty} m_\pi(L), \tag{5.23}$$

as expected. Furthermore, we can see that lattice artefacts become more dominant, contrary to the examination of the finite volume effects on the pion mass in the previous section. This can especially be seen for the datasets A3, A5 and A7 in figure 5.8, where the data points seem to split up around $m_\pi L \approx 5.0$. The continuous lines and error bands represent fits, which have been made based on the scattering phase shift $\delta(k)$, which will be discussed in the next section.

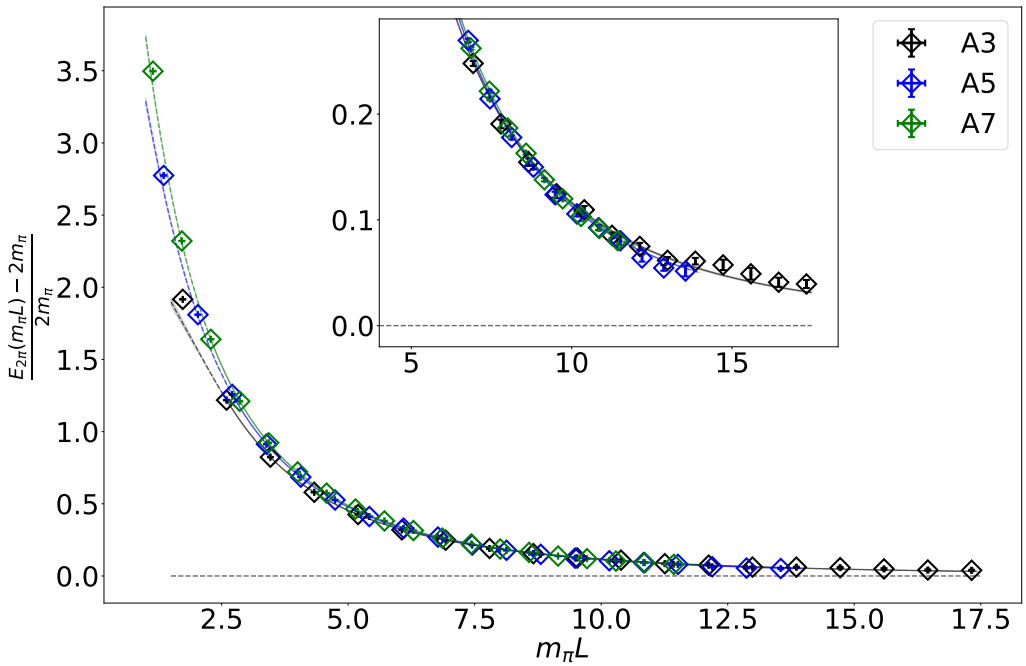

Figure 5.8: Finite volume behaviour of the 2-pion ground state energy $E_{2\pi}(L)$ for three different datasets A3, A5 and A7 with varying lattice spacings and fixed infinite volume pion mass $m_\pi/g \approx 0.75$. Shown are the relative finite volume corrections. The lines with error bars represent fits for the 2-pion ground state energies $E^\delta_{2\pi}$ resulting from a heuristic ansatz for the scattering phase shift $\delta(k)$. Note that we obtain bad agreement between data and fit for the data set A3. This problem originates from the difficulties of fitting the scattering phase shift $\delta(k)$ at large volumes.

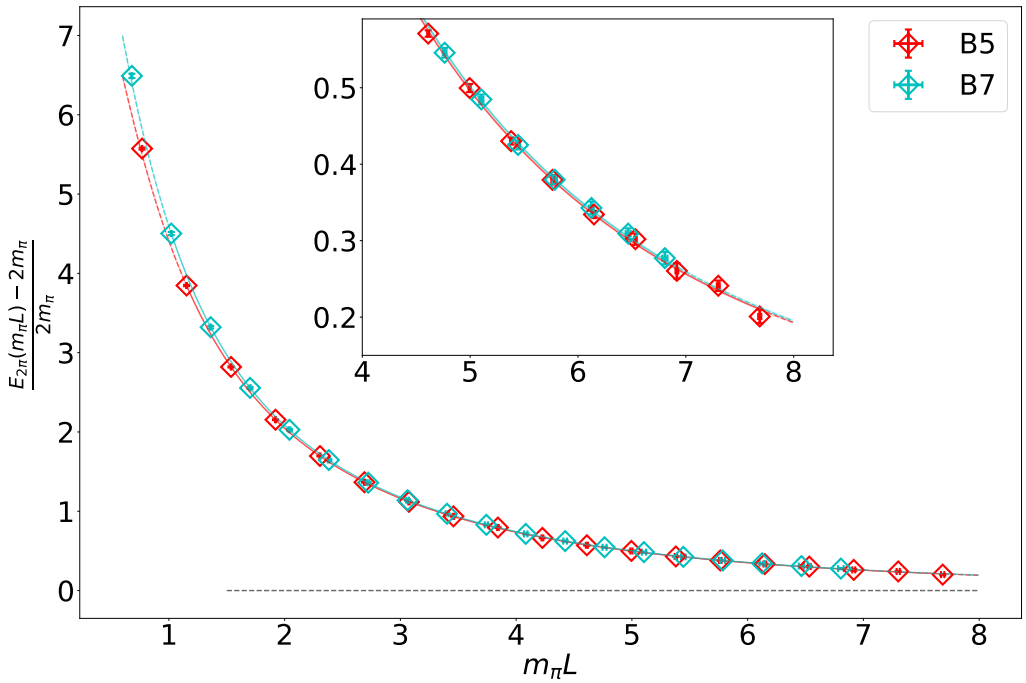

Figure 5.9: Finite volume behaviour of the 2-pion ground state energy $E_{2\pi}(L)$ for two different datasets B5 and B7 with varying lattice spacings and fixed infinite volume pion mass $m_\pi/g \approx 0.44$. Shown are the relative finite volume corrections. The lines with error bars represent fits for the 2-pion ground state energies $E^\delta_{2\pi}$ resulting from a heuristic ansatz for the scattering phase shift $\delta(k)$.

5.4 Extraction of the scattering phase shift $\delta(k) \equiv \delta(L)$

Upon extracting $E_{2\pi}(L)$ we can examine the finite volume behaviour of the 2-pion ground state energy and tackle the extraction of the so-called scattering phase shift, discussed in section 2.7. Consider a situation where one has two pions in a box of size L with equal masses m_π and momenta p_1 and p_2. The lattice dispersion relation for such a state in the center of mass frame ($P = p_1 + p_2 = 0$) has been discussed in subsection 3.6.1 and is given by

$$E_{2\pi}(L) = 2\cosh^{-1}(\cosh(m_\pi) + 1 - \cos(k(L))), \tag{5.24}$$

where the $k(L)$ denote the volume-dependent momenta of the two pions. These momenta have to obey some quantization condition due to the periodic nature of the box. Said quantization condition is related to the scattering phase shift $\delta(k)$ and given by eq. (2.74), that is

$$\delta(k(L)) = -\frac{kL}{2} \equiv \delta(L). \tag{5.25}$$

If the scattering phase shift $\delta(k)$ is known, one can construct the relative momenta $k(L)$ and compute the 2-pion ground state energies for arbitrary volumes L. Conversely, one can determine the scattering phase shift from the 2-pion energies by using the quantization condition eq. (5.25), where the relative momenta $k = k(L)$ are determined by using the dispersion relation eq. (5.24).

Note, that we use the infinite volume pion mass $m_\pi = \lim_{L\to} m_\pi(L)$ instead of the finite volume pion mass in eq. (5.24). Philosophically speaking, it would make more sense to use $m_\pi(L)$, simply because finite volume quantities like $E_{2\pi}(L)$ should not have any information about the infinite volume pion mass - a box of size L only sees $m_\pi(L)$. The literature is not clear about this: Guo et al. who investigated the $2d$ φ^4-model in Ref. [36] used the infinite volume pion mass m_π for the extraction of $E_{2\pi}(L)$, while Romero-López et al. who investigated the $4d$ φ^4-model in Ref. [50] argued for the opposite. Our results indicate clearly that using the infinite volume pion mass in eq. (5.24) yields better results for the scattering phase shift, which is why we proceed to use m_π instead of $m_\pi(L)$ in the dispersion relation.

The discussion of the scattering phase shifts is quite interesting and offers a lot to talk about. We plot the scattering phase shifts for all 5 datasets A3, A5, A7, B5 and B7, such that we can examine lattice artefacts by comparing the results of {A3, A5, A7} and {B5, B7} with each other. We describe the scattering phase shift $\delta(x)$ as a function of the dimensionless variable $x = k/m_\pi$. The measured scattering phase shifts are shown in figure 5.10 and 5.11.

Before turning to the discussion of the scattering phase shift we need to keep in mind that the used 2-particle quantization conditions eq. (5.25) are only valid provided that some conditions are fulfilled. These conditions were discussed in section 2.7, for the sake of completeness we repeat them here once more

- Small enough lattice spacings (close enough to the continuum).
- Large enough volumes, such that the interaction range of the potential is small compared to the volume, and self-interactions of the 2-particle states via the boundaries can be neglected.
- We only consider elastic scattering, i.e. we are working in an energy regime, where no new particles are being created.

Let us now discuss our results for the scattering phase shift, by starting with the large energy regime, that is $\frac{k}{m_\pi} \gg 1$.

Upon approaching large energies (resp. small volumes), the measurements become more precise, since the 2-pion ground state energies $E_{2\pi}(L)$ are easier to extract for small volumes. As a consequence, differences between the measurements for different datasets become much more pronounced. We see that for large energies and fixed pion masses m_π/g the scattering phase shifts start to drift away from each other. This effect can be attributed to many factors since many of Lüscher's conditions are violated here. The discrepancies for large energies are believed to stem from severe finite volume effects. It is also not clear how much credibility should be given to measurements for large energies, given the potential crossing of an inelastic threshold, where 3-pion states could be produced.

Now we turn to the low-energy regime, that is $\frac{k}{m_\pi} \ll 1$.

One universal effect, which holds true for all datasets, are the fluctuations of the scattering phase shift which arise when approaching low energies k/m_π. By approaching small energies, we consider

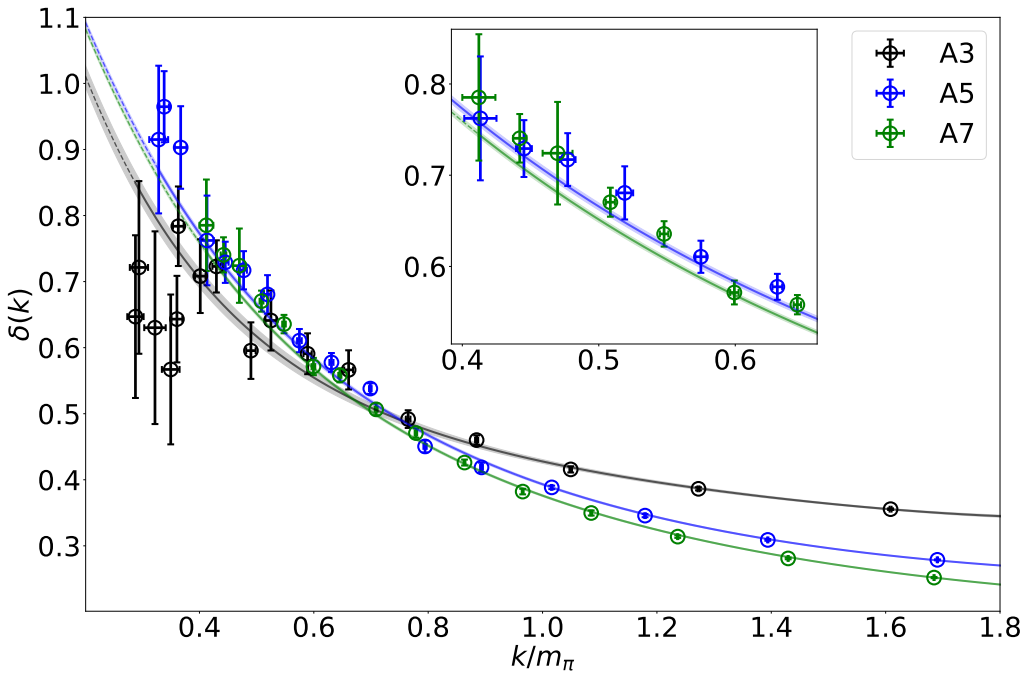

Figure 5.10: Scattering phase shifts $\delta(\frac{k}{m_\pi})$ for the datasets A3, A5 and A7. The lines with errorbands represent fits with an effective ansatz. Note that the measurements for the coarse lattice A3 seem to be problematic for small energies.

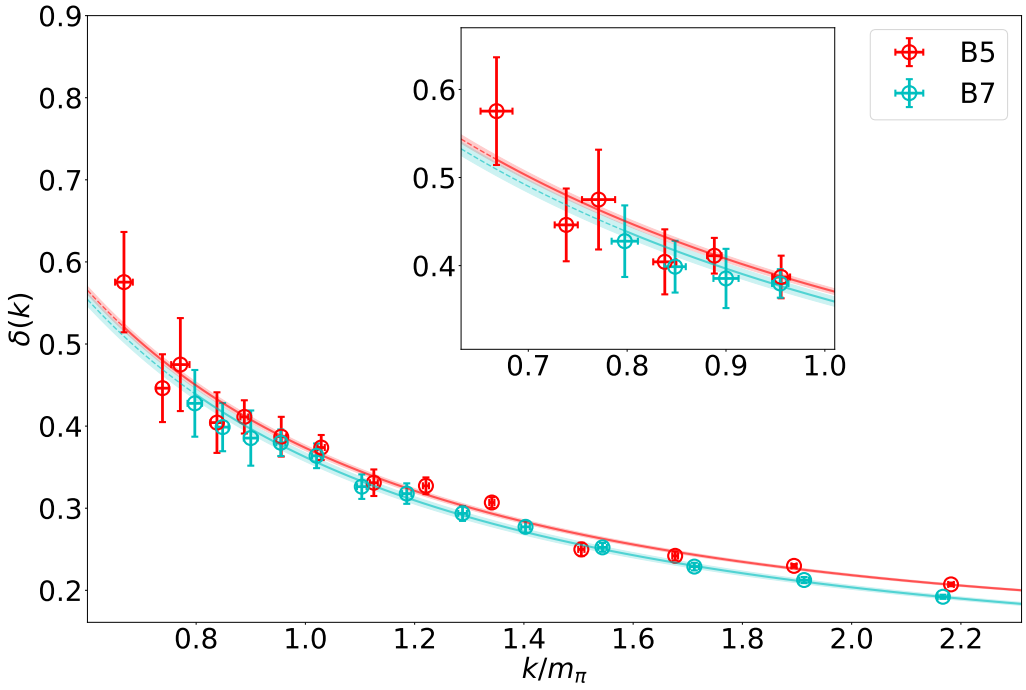

Figure 5.11: Scattering phase shifts $\delta(\frac{k}{m_\pi})$ for the datasets B5 and B7. The lines with errorbands represent fits with an effective ansatz.

measurements of the scattering phase shift for large volumes L. For large volumes, the spectrum of the isospin $I = 2$ sector is very dense, making the extraction of $E_{2\pi}(L)$ more involved and more prone to errors. This explains the increased uncertainty for the scattering phase shifts when approaching small energies. Note that these effects appear for all datasets.

Lattice artefacts, can be investigated by fixing the pion mass m_π/g and the momentum k/m_π and comparing the measurements for {A3, A5, A7} and {B5, B7} with each other (see insetplots in figure 5.10

and 5.11). We immediately notice that the accuracy of the scattering phase shifts becomes better for finer lattices, as expected. In particular, the scattering phase shifts for the dataset A3 (which was conducted at a large lattice spacing) are of bad quality at low energies.

5.5 Effective range expansion of $\delta(k)$

We have extracted the scattering phase shifts $\delta(k(L)) \equiv \delta(L)$ for different volumes which can now be fitted using an effective range expansion. Contrary to the effective range expansion in 3+1 dimensions we do not consider an expansion in $k\cot(\delta(k))$, but an expansion in $k\tan(\delta(k))$ for the bosonic wavefunction, as explained in subsection 2.7.2. The effective range expansion - which is basically a Taylor expansion for small relative momenta k - is given by eq. (2.102), that is

$$\begin{aligned} k\tan(\delta_0(k)) &= \frac{1}{a_0} + \frac{r_0}{2}k^2 + \mathcal{O}(k^4), \text{ resp.} \\ x\tan(\delta_0(x)) &= \frac{1}{a_0 m_\pi} + \frac{r_0 m_\pi}{2}x^2 + \mathcal{O}(x^4), \quad \text{with } x = \frac{k}{m_\pi}, \end{aligned} \tag{5.26}$$

where a_0 denotes the scattering length and r_0 the effective range. By adding more correction terms on the r.h.s. of eq. (5.26), the expansion is also valid for large momenta. Upon fitting $\delta(k)$, resp. $\delta(x)$, we get a heuristic ansatz for the scattering phase shift but also obtain physically relevant parameters like the scattering length a_0 and the effective range r_0.

Let us first consider the extraction of a_0 and r_0. We perform Bayesian model averaging with different fit models motivated by the effective range expansion (5.26), which are then being averaged using systematic averaging.

We fit the dimensionless combination $x\tan(\delta(x))$, with $x = \frac{k}{m_\pi}$, to the following fit functions

$$\mathrm{M}_1^\delta(x, c_0, c_1) = c_0 + c_1 x^2 \tag{5.27}$$

$$\mathrm{M}_2^\delta(x, c_0, c_1, c_2) = c_0 + c_1 x^2 + c_2^2 x^4 \tag{5.28}$$

$$\mathrm{M}_3^\delta(x, c_0, c_1, c_2, c_3) = c_0 + c_1 x^2 + c_2 x^4 + c_3 x^6, \tag{5.29}$$

extract the desired parameters

$$c_0 = \frac{1}{a_0 m_\pi} \quad \text{and} \quad c_1 = \frac{r_0 m_\pi}{2}, \tag{5.30}$$

and therefore also the scattering length a_0 and the effective range r_0.

The obtained results are then averaged using systematic averaging, yielding the final model-independent results for each parameter. The details are given in the appendix section H.5, a summary of the extracted parameters, including the calculation of the rescaled scattering length $a_0 m_\pi$ and rescaled effective range $r_0 m_\pi$ is given in table 5.5.

Dataset	m_π/g	c_0	$a_0 m_\pi$	c_1	$r_0 m_\pi$
A3	0.7500(5)	0.318(25)	3.147(80)	0.157(51)	0.31(10)
A5	0.7574(3)	0.3883(53)	2.576(14)	0.0241(48)	0.0482(96)
A7	0.7564(3)	0.3835(43)	2.607(11)	0.0106(35)	0.0212(71)
B5	0.4296(8)	0.3817(71)	2.620(19)	0.0145(23)	0.0290(46)
B7	0.450(2)	0.3721(85)	2.688(23)	0.0098(18)	0.0195(35)

Table 5.5: All model-independent parameters after taking the systematic average in the very end.

Upon investigating the results in table 5.5, some interesting observations can be made. It is worth mentioning, that one can fit almost the whole range of extracted scattering phase shifts (between 17 to 18 data points) using between 3 and 4 fit parameters only, the best fits are summarized in table H.26.

We also notice that for all datasets (except for dataset A3) the parameters $a_0 m_\pi$ and $r_0 m_\pi$ seem to be somewhat compatible with each other. The vastly different results for dataset A3 can be attributed to lattice artefacts and finite volume effects, which underrate the scattering phase shift at low energies. As a result, the extraction of low-energy parameters such as a_0 and r_0 become unreliable for dataset A3.

By using linear fits, we perform the continuum limit for the parameters $a_0 m_\pi$ and $r_0 m_\pi$ for fixed infinite volume pion mass and two different couplings, as shown in figure 5.12. For these calculations we exclude the data point for dataset A3.

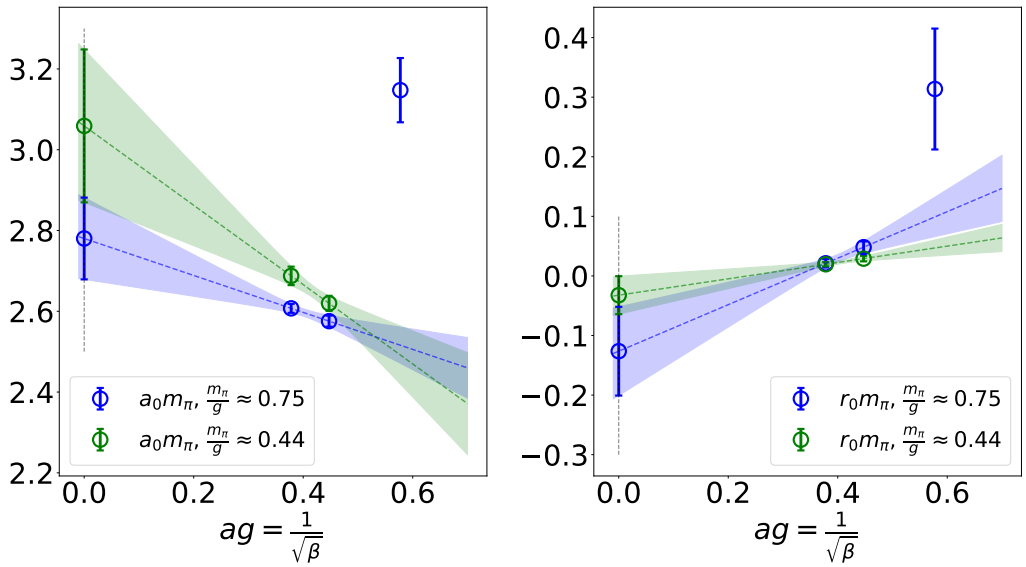

Figure 5.12: Results for $a_0 m_\pi$ and $r_0 m_\pi$ for all 5 datasets. For the continuum extrapolations linear functions in combination with the datasets A5, A7, B5 and B7 have been used.

	$a_0 m_\pi$	$r_0 m_\pi$
$m_\pi/g \approx 0.75$	2.78(10)	-0.126(74)
$m_\pi/g \approx 0.44$	3.06(19)	-0.032(32)

Table 5.6: Scattering length $a_0 m_\pi$ and effective range $r_0 m_\pi$ for two different pion masses extracted from the four datasets A5, A7, B5 and B7 via continuum extrapolation.

The continuum extrapolations show very nicely, that the scattering length $a_0 m_\pi$ is positive as expected, whereas the effective range seems to be compatible with 0. The numerical results are summarized in table 5.6.

Considering these results we ask ourselves, whether the effective range $r_0 m_\pi$ is actually just zero, $r_0 m_\pi = 0$. This can be checked, by performing the continuum extrapolation with a fixed offset 0, such that the fit function is just given by a linear term only. The resulting χ^2 is then a measure for the goodness of the fit. The χ^2 values, given in table 5.7 indicate that for the measurements conducted at pion mass $m_\pi/g \approx 0.44$ the value of $r_0 m_\pi$ is compatible with 0. On the other hand, for $m_\pi/g \approx 0.75$ the value of $r_0 m_\pi$ is not compatible with 0 and is most likely negative. However, these results need to be taken with a grain of salt, since only two data points have been used for the continuum extrapolation.

	$m_\pi/g \approx 0.75$	$m_\pi/g \approx 0.44$
χ^2/d.o.f	3.28	0.90

Table 5.7: Value of χ^2/d.o.f for effective range $r_0 m_\pi$ fitted with a single linear function $y = a \cdot x$ only.

5.6 Isospin $I = 3$ sector

Here we consider three pions in a finite box of size L and determine the ground state energies in the corresponding isospin $I = 3$ sector using the master formula eq. (5.5) with $n = 3$. The ground state is given by a 3-pion state $|\pi^+\pi^+\pi^+\rangle$. Also here, we first examine the finite temperature behaviour of

$$E_{3\pi}(T), \quad \text{for a fixed volume } L, \tag{5.31}$$

in figure 5.13.

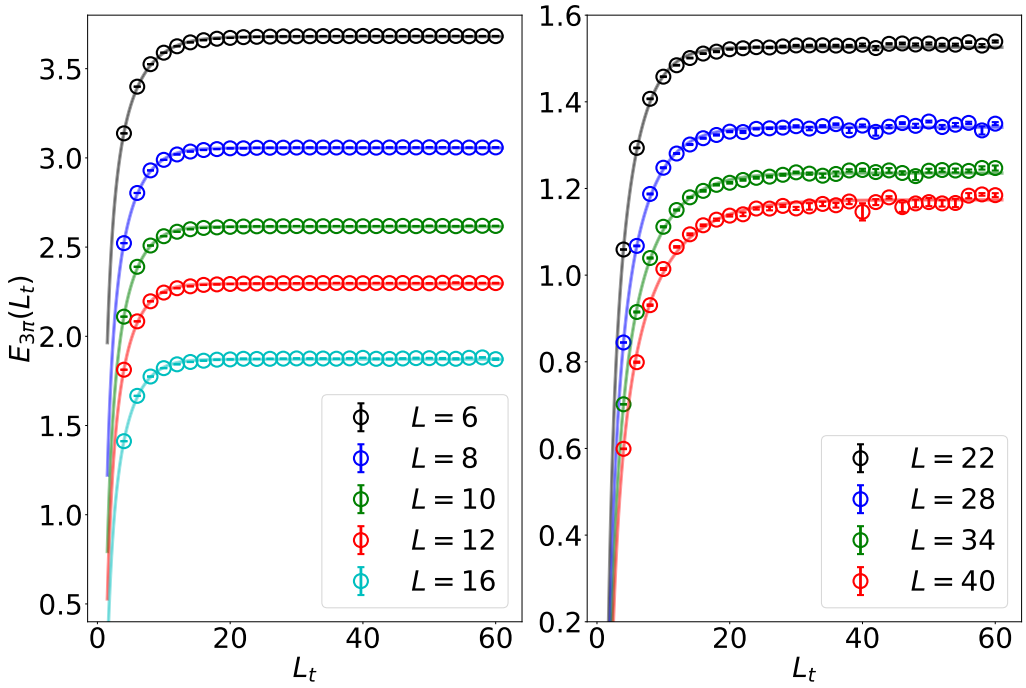

Figure 5.13: Dataset A5. Finite temperature behaviour of the 3-pion ground state energy $E_{3\pi}(L_t)$, for different small and large volumes. The temperature is related to the temporal extent of the lattice via $T = 1/L_t$.

The complete discussion of the temperature behaviour is analogous to the discussion of $m_\pi(T)$ and $E_{2\pi}(T)$:

- Large temperature behaviour is dominated by corrections from the Isospin $I = 3$ sector.
- These corrections become more dominant for larger volumes, due to the volume-dependent structure of the spectrum.

The fit functions used for the extrapolation to zero temperature are the same as for $E_{2\pi}(T)$

$$\mathrm{M}_{E_{3\pi},1}(T, E_{3\pi}) = E_{3\pi} \tag{5.32}$$

$$\mathrm{M}_{E_{3\pi},2}(T, E_{3\pi}, B_1, B_2) = E_{3\pi} - T \log\left(\frac{1 + B_2 e^{-B_1/T}}{1 + e^{-m_\pi/T} + 2\sum_{i=1}^{\frac{L}{2}} e^{-E^{(i)}_{\pi^0}/T}}\right), \tag{5.33}$$

where the parameter $m_\pi = m_\pi(L)$ is extracted beforehand from the zero temperature extrapolation of the pion mass, as explained in section 5.1. As before we first perform Bayesian model averaging and average those results afterwards using systematic averaging.

Upon extracting $m_\pi(L)$, $E_{2\pi}(L)$ and $E_{3\pi}(L)$ we can plot the results, giving us a visual overview of the finite volume behaviour of said quantities. In figure 5.14 we consider the results for the datasets {A3, A5, A7}, minor miss tunings in the pion mass will be omitted for this superficial discussion. We can see very nicely how finite volume effects and lattice artefacts increase with the number of pions in the box. For the pion mass m_π finite volume effects arise around $m_\pi L \approx 4$, for the 2-pion ground state energy those effects already arise around $m_\pi L \approx 8$. Finally, finite volume effects for the 3-pion ground state

energy, are already visible for $m_\pi L \approx 14$. Although somewhat heuristic, these results show very nicely that finite volume effects increase with an increasing number of pions in the box, as expected.

Similar considerations can be made with respect to lattice artefacts. For the pion mass, no lattice artefacts are visible (on that scale), which means that Lüscher's formula for finite volume effects can be used universally, to describe the pion mass as a function of the volume. However, for the 2-pion ground state energies, we can see that lattice artefacts arise around $m_\pi L \approx 4$, where the data points seem to diverge for the three datasets. For the 3-pion ground state energies this situation becomes even worse, lattice artefacts already showing up at $m_\pi L \approx 8$.

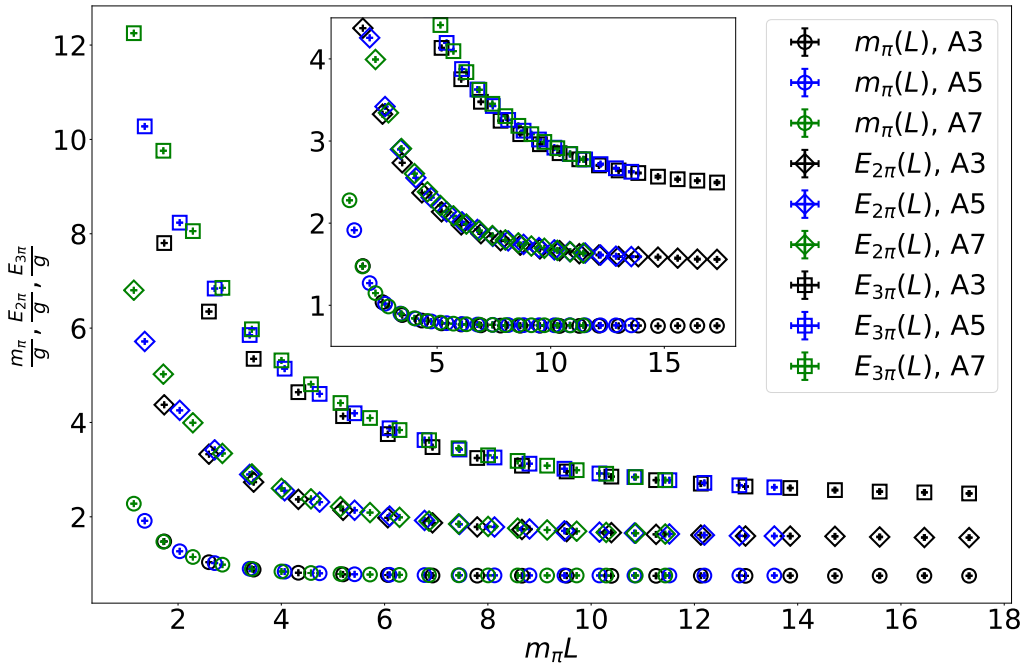

Figure 5.14: Finite volume behaviour of $m_\pi(L)$, $E_{2\pi}(L)$ and $E_{3\pi}(L)$ for the datasets A3, A5 and A7. Finite volume corrections and lattice artefacts increase with the number of pions in the box.

5.7 Computing the 3-pion ground state energy $E_{3\pi}^{\delta}$ based on the scattering phase shifts $\delta(k)$

Up to this point we used the master formula eq. (5.5) with $n = 1$ and $n = 2$, which allowed us to determine $m_\pi(L)$ and $E_{2\pi}(L)$. By using the volume-dependent pion masses we determined the infinite volume pion mass $m_\pi = \lim_{L\to\infty} m_\pi(L)$ and by combining m_π with the 2-pion ground state energies $E_{2\pi}(L)$ we computed the scattering phase shifts $\delta(k(L)) \equiv \delta(L)$ for different volumes. These discrete measurements were used to make a heuristic ansatz for $\delta(k)$ based on the effective range expansion.

The scattering phase shift $\delta(k)$ can be used to make predictions for the 3-pion ground state energies $E_{3\pi}^{\delta}(L)$, where we use the superscript to distinguish between the δ-dependent predictions and the direct computations using the master formula with $n = 3$. We start the discussion by writing down the bosonic lattice dispersion relation for the energy of a 3-pion state

$$E_{3\pi}(L) = \sum_{i=1,2,3} \cosh^{-1}\left(\cosh(m_\pi) + 1 - \cos(p_i(L))\right), \tag{5.34}$$

where the $p_i(L)$ denote the volume-dependent momenta of the 3 pions. Following the discussion in section 2.8 the momenta $p_i(L)$ obey quantization conditions. These quantization conditions are valid in a nonrelativistic setup, where we only assume short-ranged 2-particle interactions. Of course, it is not clear up to which extent, these conditions are fulfilled here. We know for example that a 3-pion coupling λ is present in the 2-flavour Schwinger model. The 3-particle quantization conditions have been discussed in section 2.8 and are given by eq. (2.108), that is

$$\cot\left(\delta(-q_{31}) - \delta(-q_{23})\right) + \cot\left(\frac{PL - p_3 L}{2}\right) = 0, \tag{5.35}$$

$$\cot\left(-\delta(-q_{31}) - \delta(q_{12})\right) + \cot\left(\frac{PL - p_1 L}{2}\right) = 0, \tag{5.36}$$

$$\cot\left(\delta(-q_{23}) + \delta(q_{12})\right) + \cot\left(\frac{PL - p_2 L}{2}\right) = 0, \tag{5.37}$$

where the parameters are given by

$$P = \sum_{i=1}^{3} p_i, \qquad q_{ij} = \frac{p_i - p_j}{2} \qquad \text{and} \qquad q_k = \frac{p_i + p_j - 2p_k}{3}. \tag{5.38}$$

In order to construct the lowest lying energy state we restrict ourselves to the center of mass frame with $P = p_1 + p_2 + p_3 = 0$ and assume the third particle to be at rest $p_3 = 0$, such that $p_2 = -p_1$. This choice of momentum configuration was used by Guo in Ref. [36], to construct the smallest 3-particle energy for the $2d$ φ^4 model. Upon using these assumptions, we are left with one single quantization condition which reads

$$\cot\left(\delta\left(\frac{x}{2}\right) + \delta(x)\right) + \cot\left(\frac{x \cdot (m_\pi L)}{2}\right) = 0, \quad \text{with} \quad x = \frac{p_1}{m_\pi}. \tag{5.39}$$

This quantization condition can now be solved using the previously determined scattering phase shift $\delta(x)$, yielding the momenta $p_i(L)$. This allows us to determine the momentum configuration (p_1, p_2, p_3) and the 3-pion energy, through the bosonic dispersion relation eq. (5.34). As a result, we obtain predictions for the 3-pion ground state energies and the corresponding relative finite volume corrections based on the 3-particle quantization conditions and the scattering phase shift.

We plot the relative finite volume corrections, that is

$$\frac{E_{3\pi}^{\delta}(m_\pi L) - 3m_\pi}{3m_\pi}, \tag{5.40}$$

in figure 5.15 for all datasets A3, A5, A7, B5 and B7.

For increasing volumes, the 3-pion energies approach $3m_\pi$ as expected and lattice artefacts become increasingly more suppressed. For the larger pion mass $m_\pi/g \approx 0.75$ lattice artefacts arise for $m_\pi L \lesssim 8.0$, while for the smaller pion mass $m_\pi/g \approx 0.44$ they arise for $m_\pi L \lesssim 4.0$. In general, the relative finite volume corrections show a very nice continuous behaviour and indicate a universal behaviour for large volumes.

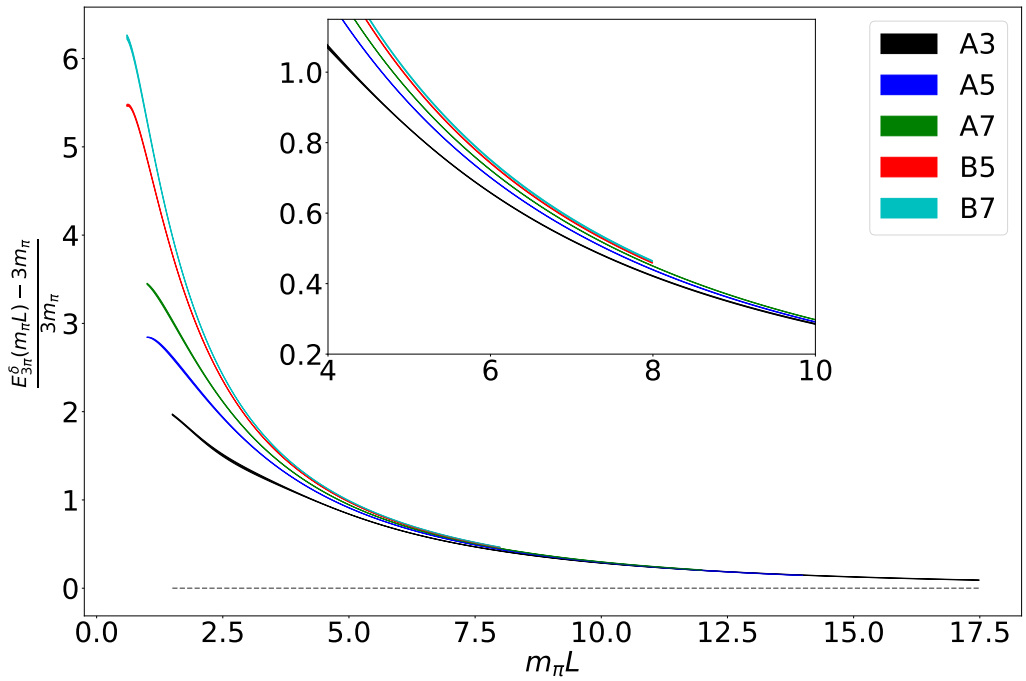

Figure 5.15: Relative finite volume corrections of the predictions $E^{\delta}_{3\pi}$ for all datasets.

So far we considered the relative finite volume corrections of the predicted 3-pion energy $E^{\delta}_{3\pi}$. However, it is far more interesting to compare the predictions of the 3-pion ground state energies $E^{\delta}_{3\pi}$ to the direct measurements $E_{3\pi}$ which have been extracted using the master formula eq. (5.5) with $n = 3$.

This allows us to judge in which regime the predictions hold true and whether our prescription for the 3-pion energy needs to be modified. The relative corrections are given by

$$\frac{E_{3\pi}(m_\pi L) - E^{\delta}_{3\pi}(m_\pi L)}{3m_\pi}, \tag{5.41}$$

and the results are presented in figure 5.16.

The first thing we notice is that the predictions are generally underestimated for smaller volumes. However, for large volumes, it seems that asymptotically the predictions fit the direct measurements perfectly.

For the larger pion mass $m_\pi/g \approx 0.75$ we consider the results for the two datasets A5 and A7 and see that we obtain perfect agreement for $m_\pi L \gtrsim 10.0$. The dataset A3 exhibits strong fluctuations at large volumes which stem from the difficulties of fitting the scattering phase shift for small energies and the problems of extracting $E_{3\pi}(m_\pi L)$ for large volumes.

For the smaller pion mass $m_\pi/g \approx 0.44$ we can see that for increasing volumes the predictions coincide with the direct measurements asymptotically. Unfortunately, the measurements stop around $m_\pi L \approx 8.0$, due to the small pion mass. Having access to more data would most likely confirm the compatibility between the direct measurements and the predictions.

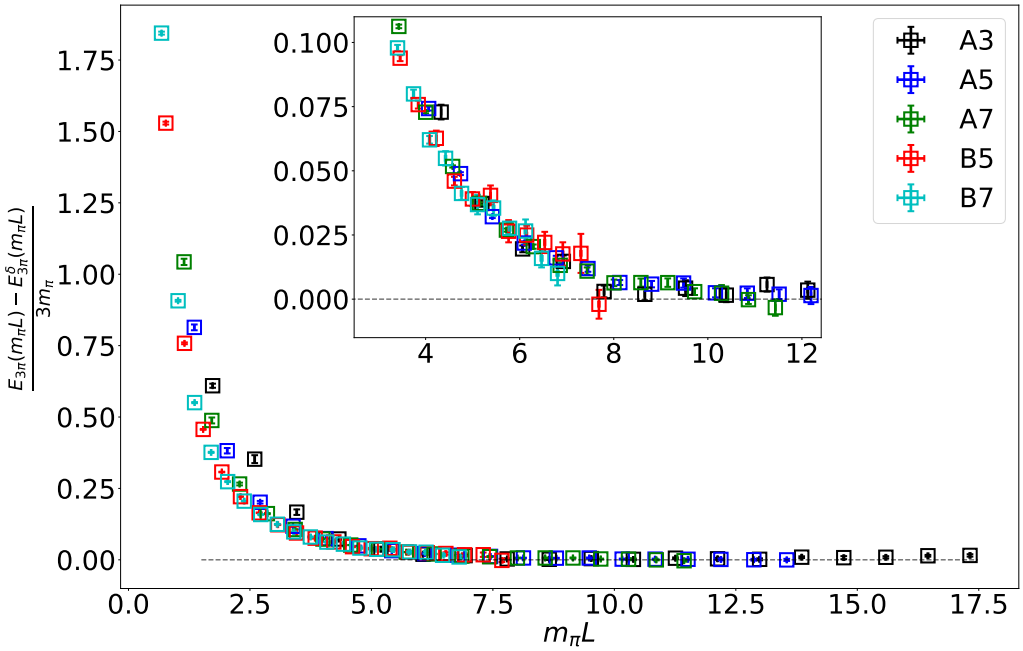

Figure 5.16: Relative differences between the predictions and the direct measurements for the 3-pion energies, for all datasets.

6 Conclusion and outlook

This thesis aimed to investigate the 1- and 2-flavour Schwinger model in the canonical formulation and to illustrate the utility of the canonical formalism, which allows us to investigate the physics of a system with a fixed number of fermions. The fundamental building block of this formalism is the decomposition of the grand-canonical partition function into canonical partition functions with fixed fermion number.

We started this thesis by introducing the 1- and 2-flavour Schwinger model on the lattice and discussing the most important properties of these models.

Next, we focused on the 1-flavour variant of the Schwinger model and derived the relation between the grand-canonical partition function and the canonical ones, by performing a dimensional reduction on the determinant of the Wilson Dirac operator.

We discussed several topics related to the canonical formalism, such as the construction of the transfer matrix $\mathcal{T}$, its properties and the description of the canonical partition functions in terms of principal minors. The distribution of the principal minors showed very interesting properties, which leave room for more research.

In the last part of this thesis, we used the canonical formalism to perform some pion scattering analysis in the 2-flavour Schwinger model. We discussed finite volume effects on the pion mass by using Lüscher's formula for finite volume effects. Utilizing said formula we determined the infinite volume pion mass m_π and showed that the dominant corrections are coming from contributions proportional to a 3-pion coupling. Lüscher's formula allows us to describe the measurements down to small volumes $m_\pi L \approx 3.0$.

The infinite volume pion mass was used in combination with the 2-pion ground state energies $E_{2\pi}(L)$ to determine the scattering phase shift $\delta(k(L))$, based on 2-particle quantization conditions in the finite volume. By using an effective range expansion for the bosonic wavefunction we present a heuristic ansatz, which allows us to describe the scattering phase shift in terms of fundamental physical parameters, such as the scattering length and the effective range. Remarkably, we were able to describe almost the full range of scattering phase shifts $\delta = \delta(L)$ (between 17 and 18 data points) using between 3 and 4 fit parameters only. Difficulties arose for ensembles generated with large lattice spacings, indicating that lattice artefacts are indeed a problem when discussing scattering phase shifts $\delta(k)$.

Upon making some simplifying assumptions and using our ansatz for the scattering phase shift, we can utilize 3-particle quantization conditions to make predictions for the 3-pion ground state energies $E^{\delta}_{3\pi}(L)$. These can be directly compared to the 3-pion ground state energies extracted from the canonical formalism $E_{3\pi}(L)$. Our results show very nicely, that the predictions coincide with the direct measurements for sufficiently large volumes $m_\pi L \approx 10$, as expected. For smaller volumes there seems to be a systematic discrepancy, indicating that our strategy for the prediction of the 3-pion ground state energies is not complete yet. The used quantization conditions for 3-particle scattering (derived by Guo) assume nonrelativistic scattering, where multi-particle interaction can only occur as sequences of short-ranged 2-particle interactions. These assumptions are not necessarily fulfilled in our case. We know, from the finite volume analysis of the pion mass, that we have a non-zero 3-pion coupling, allowing for 3-pion interaction. In order to take these effects into account, we must consider 3-particle quantization conditions, which are better suited to our problem.

In this thesis, we discussed several aspects of the 1- and 2-flavour Schwinger model in the canonical formalism, resulting in many starting points for interesting future studies.

The structural behaviour of the principal minors is a very interesting subject, worth investigating. Once we have a complete understanding of the structure of the principal minors, one could use those principal minors P^{II} to perform canonical simulations. As a starting point, one can interpret the principal minors as weights and perform simulations, where we not only vary the gauge fields but also the index sets I.

In a next step, one could write out the principal minors using Cauchy-Binet (see Ref. [51]), such that for vanishing quark chemical potential,[1] we obtain

$$\det(\mathcal{T}^{I_0 I_0}) = \sum_{I_1, I_2, \ldots, I_{L_t-1}} \det(T_1^{I_0 I_1}) \det(T_2^{I_1 I_2}) \ldots \det(T_{L_t}^{I_{L_t-1} I_0}). \tag{6.1}$$

[1] In this case one can factorize the full transfer matrix $\mathcal{T}$ as a product of time-slice transfer matrices T_i, such that $\mathcal{T} = \prod_{i=1}^{L_t} T_i$.

This allows us to perform simulations, where we sample gauge fields and index sets on a single time-slice while keeping all other time-slices fixed.

The biggest advantage of the canonical formalism is the direct access to ground state energies of multi-meson sectors. This allows us to directly investigate the phase structure of the Schwinger model and completely circumvent the use of correlators, which become more complex with an increasing number of mesons. In this work, we only tipped our toes into this topic, as illustrated in section 4.8.

The scattering analysis performed in chapter 5 can be improved by increasing the number of data points and utilizing suitable 3-particle quantization conditions.

We conclude, that the Schwinger model in the canonical formulation opens up many directions for interesting future research.

Man wird am besten für seine Tugenden bestraft.

F. Nietzsche, Jenseits von Gut und Böse, 1886

Acknowledgement

First and foremost, my thanks go to Urs Wenger for his supervision and for giving me the opportunity to work on this project. Secondly, I would like to thank Andrei Alexandru for accepting the responsibility of being the external referee for this thesis. Uwe-Jens Wiese always had an open ear for me and took me seriously, I am very grateful for that as well.

My gratitude goes to Esther Fiechter, former secretary of our institute and Binia Marti the current one, for their help and dealing with the bureaucracy. I would also like to thank Markus Moser for maintaining the hardware and software of the computers at our institute and especially for maintaining the cluster, I used extensively.

Special thanks go to my fellow PhD students and Postdocs, who lightened up the time at the university, either at lunch, at discussions in the coffeeroom or when playing a round of "Magic the Gathering". I am deeply indebted to the people who proofread my thesis and gave me valuable input such as Tatiana Kochetkova, Raphael Friedli, Nicolas Schalch and David Rohrbach. But also Alessandro Mariani should be mentioned, who provided a proof for a dull little formula I discovered (after investing too much time playing with principal minors). I also thank Samuel Favrod for organizing an apéro for my PhD defence, even though I think that apéros are stupid.

Without any doubt, my biggest thank goes to Sebastian Burri, who shared the office with me throughout my PhD. It was an absolute pleasure to have such a pleasant and competent office mate, with whom I could discuss computer and physics-related problems.

I wish everyone much success in their future careers and private lives.

Last but not least, I thank my family and my girlfriend Tatiana for their support, encouragement and love.

A Fermions on the lattice

In order to perform numerical simulations of the Schwinger model, we require a discretization of the theory, which can be implemented on the lattice. In this part of the appendix, we derive the lattice action for the 1-flavour Schwinger model, in close analogy to Rothe in Ref. [24]. We require the action of the 1-flavour Schwinger model

$$S[\bar{\psi},\psi,A_\mu] = \int d^2x \mathcal{L}[\bar{\psi},\psi,A_\mu], \quad \text{with} \quad \mathcal{L}[\bar{\psi},\psi,A_\mu] = \bar{\psi}(x)[i\not{D} - m_0]\psi(x) - \frac{1}{4}F_{\mu\nu}F^{\mu\nu}, \tag{A.1}$$

as discussed in section 2.1 and some basic knowledge about Grassmann variables, which can also be found in Ref. [24].

We start the derivation by making a transition from Minkowski spacetime to Euclidean spacetime. Next, we discretize the fermion fields and discuss the resulting fermion doubling problem. In order to solve the fermion doubling problem we introduce a Wilson-term which breaks chiral symmetry. We finish the derivation by implementing the gauge fields, eventually leading to the final results given by eqs. (A.63) to (A.65).

A.1 Euclidean field theory

In a quantum field theory the fields $\bar{\psi}(x)$ and $\psi(x)$ in the Lagrangian $\mathcal{L}$ become operators satisfying the equal-time anticommutation relations

$$\{\psi_a(x), \psi_b^\dagger(y)\} = \delta_{ab}\delta(x-y), \quad \text{with} \quad x^0 = y^0. \tag{A.2}$$

The physical information is contained in the Green functions in Minkowski spacetime, given by

$$\langle \psi_\alpha(x)\dots\bar{\psi}_\beta(y)\dots\rangle_{\mathrm{M}} = \langle 0|\mathrm{T}\{\psi_\alpha(x)\dots\bar{\psi}_\beta(y)\dots\}|0\rangle, \tag{A.3}$$

where $|0\rangle$ stands for the ground state of the physical system and T describes the time-ordered product of the operators $(\psi(x)\dots\bar{\psi}(y)\dots)$. This Greens function has a path-integral representation, which reads

$$\langle \psi_\alpha(x)\dots\bar{\psi}_\beta(y)\dots\rangle_{\mathrm{M}} = \frac{\int \mathcal{D}\bar{\psi}\mathcal{D}\psi\mathcal{D}U(\psi_\alpha(x)\dots\bar{\psi}_\beta(y)\dots)e^{i\bar{S}_{\mathrm{M}}[\bar{\psi},\psi,U]}}{\int \mathcal{D}\bar{\psi}\mathcal{D}\psi\mathcal{D}U e^{i\bar{S}_{\mathrm{M}}[\bar{\psi},\psi,U]}}, \tag{A.4}$$

where U describes the gauge field degrees of freedom (related to the original gauge fields A_μ) and $\bar{S}_{\mathrm{M}}$ denotes the path-integral version[1] of the Minkowski action S_{M}. In eq. (A.4) the fields are defined at every point in spacetime and we integrate over all possible field configurations. We will require a careful definition of the integration measure $\mathcal{D}\psi$, however, at the moment our main concern is the weighting factor $e^{i\bar{S}_{\mathrm{M}}}$, which is an oscillating function and therefore unsuitable for numerical simulations.

To get rid of this factor, we rotate the time-axis by an angle of 90° degree i.e. we perform a so-called Wick rotation. This is done by substituting $x_0 \to -i\tau$, where τ denotes the Euclidean time, such that

$$x_M^2 = x_\mu x^\mu = x_0^2 - x_1^2 \to -\tau^2 - x_1^2 = -x_E^2, \tag{A.5}$$

as a result we obtain new Euclidean coordinates x_E. We have to make appropriate changes to other objects as well, in practice the following replacements take place

$$x_0 \to -i\tau, \qquad \partial_0 \to i\partial_\tau, \qquad A_0 \to iA_\tau \tag{A.6}$$

$$\gamma_M^0 \to \gamma_E^0, \qquad \gamma_M^1 \to -i\gamma_E^1, \qquad \text{such that } \gamma_E^1 = i\gamma_M^1. \tag{A.7}$$

[1] i.e. the action is appropriately discretized to be suitable for a path-integral representation.

By making these replacements the new action reads

$$S_{\mathrm{M}}[\bar{\psi},\psi,U] = \int \mathrm{d}^2x\{\bar{\psi}(i\partial\!\!\!/ - gA\!\!\!/ - m_0)\psi - \frac{1}{4}F_{\mu\nu}F^{\mu\nu}\} \tag{A.8}$$

$$= i\int \mathrm{d}\tau\mathrm{d}x^1\{\bar{\psi}(\partial\!\!\!/ + igA\!\!\!/ + m_0)\psi + \frac{1}{4}F_{\mu\nu}F^{\mu\nu}\} \tag{A.9}$$

$$= iS_{\mathrm{E}}[\bar{\psi},\psi,U], \tag{A.10}$$

where S_{E} denotes the action in Euclidean spacetime and the gamma matrices satisfy $\{\gamma_E^\mu,\gamma_E^\nu\} = 2\delta^{\mu\nu}$ with metric $\delta = \mathrm{diag}[1,1]$. In the lattice formulation the gauge field degrees of freedom will be characterized with Wilson lines (denoted by $U_{n,m}$) which will be introduced later. This is why, from now on, we label the gauge field degrees of freedom with U instead of A_μ. Using $\bar{S}_E$ as the path-integral version of S_E, the denominator of the Green's function can be identified with a partition function $\mathcal{Z}$ of a statistical mechanical system

$$\mathcal{Z} = \int \mathcal{D}\bar{\psi}\mathcal{D}\psi\mathcal{D}U e^{-\bar{S}_{\mathrm{E}}[\bar{\psi},\psi,U]}. \tag{A.11}$$

After the Wick-rotation the weighting factor is now positive and suitable for numerical simulations and the Greens function takes the form of a well-behaved correlation function

$$\langle\psi_\alpha(x)\bar{\psi}_\beta(y)\rangle_E = \frac{\int \mathcal{D}\bar{\psi}\mathcal{D}\psi\mathcal{D}U(\psi_\alpha(x)\dots\bar{\psi}_\beta(y)\dots)e^{-\bar{S}_{\mathrm{E}}[\bar{\psi},\psi,U]}}{\int \mathcal{D}\bar{\psi}\mathcal{D}\psi\mathcal{D}U e^{-\bar{S}_{\mathrm{E}}[\bar{\psi},\psi,U]}}, \tag{A.12}$$

with partition function

$$\mathcal{Z} = \int \mathcal{D}\bar{\psi}\mathcal{D}\psi\mathcal{D}U e^{-\bar{S}_{\mathrm{E}}[\bar{\psi},\psi,U]}. \tag{A.13}$$

For the rest of this chapter, we work in Euclidean spacetime. For the sake of readability, we omit the indices E and relabel $\tau \to x^0$.

A.2 Lattice formulation

We showed that the Euclidean action reads

$$S[\bar{\psi},\psi,U] = \int \mathrm{d}^2x\bar{\psi}(x)(D\!\!\!/ + m_0)\psi(x) + \frac{1}{4}F_{\mu\nu}F^{\mu\nu}, \tag{A.14}$$

where x^0, x^1 are continuous variables now describing Euclidean time and space. In order to illustrate the discretization procedure and the fermion doubling problem we start with the free fermionic action, that is

$$S_{\mathrm{f}}[\bar{\psi},\psi] = \int \mathrm{d}^2x\bar{\psi}(x)(\partial\!\!\!/ + m_0)\psi(x). \tag{A.15}$$

We discretize spacetime and consider a lattice of extent $L \times L_t = a\hat{L} \times a\hat{L}_t$, where a is the lattice spacing and $\hat{L}, \hat{L}_t$ are fixed positive integers. The fields $\bar{\psi}$ and ψ live on the lattice sites an, where $n = (n_0, n_1)$ is a 2-vector describing a spacetime point on the lattice, with $n_0 \in \{1,2,3,\dots\hat{L}_t\}$ and $n_1 \in \{1,2,3,\dots\hat{L}\}$. We formally write down the integration measure of the partition function as

$$\mathcal{D}\bar{\psi}\mathcal{D}\psi = \prod_{\alpha,n}\mathrm{d}\bar{\psi}_\alpha(na)\prod_{\beta,m}\mathrm{d}\psi_\beta(ma), \tag{A.16}$$

where α and β denote the Dirac indices, $\alpha,\beta \in \{1,2\}$ and n,m denote spacetime points on the lattice. In order to discretize the partition function we also need to discretize the action. Note, that we are allowed to use any discretization we want, the only requirement being that in the continuum limit (i.e. for $a \to 0$) one retrieves the correct continuum theory. Before applying the most straightforward, naive discretization we are going to introduce dimensionless lattice variables, which can be obtained by scaling

$m, \bar{\psi}, \psi$ according to their canonical dimensions. We make the following replacements:

$$\begin{aligned} m_0 &\to \frac{1}{a}\hat{m}_0, & g &\to \frac{1}{a}\hat{g}, \\ \psi_\alpha(x) &\to \frac{1}{a^{1/2}}\hat{\psi}_\alpha(n), & \bar{\psi}_\alpha(x) &\to \frac{1}{a^{1/2}}\hat{\bar{\psi}}_\alpha(n), \\ \partial_\mu\psi_\alpha(x) &\to \frac{1}{a^{3/2}}\hat{\partial}_\mu\hat{\psi}_\alpha(n), & \int d^2x &\to a^2\sum_n . \end{aligned} \tag{A.17}$$

The antihermitian lattice derivative $\hat{\partial}_\mu$ is given by

$$\hat{\partial}_\mu\hat{\psi}_\alpha(n) = \frac{1}{2}[\hat{\psi}_\alpha(n+\hat{\mu}) - \hat{\psi}_\alpha(n-\hat{\mu})], \tag{A.18}$$

where $\hat{\mu}$ denotes a unit vector pointing in x^0 or x^1 direction. The discretized action in the 1-flavour case can be written as

$$S[\hat{\bar{\psi}}, \hat{\psi}] = \sum_{\alpha,\beta,n,m} \hat{\bar{\psi}}_\alpha(n) K_{\alpha,\beta}(n,m)\hat{\psi}_\beta(m), \tag{A.19}$$

with $K_{\alpha,\beta}(n,m)$ given by

$$K_{\alpha,\beta}(n,m) = \sum_\mu \frac{1}{2}(\gamma_\mu)_{\alpha,\beta}(\delta_{m,n+\hat{\mu}} - \delta_{m,n-\hat{\mu}}) + \hat{m}_0\delta_{m,n}\delta_{\alpha,\beta}. \tag{A.20}$$

A.3 Fermion doubling problem

In order to illustrate the fermion doubling problem we introduce the lattice 2-point function given by

$$\langle\hat{\psi}_\alpha(n)\hat{\bar{\psi}}_\beta(m)\rangle = \frac{\int \mathcal{D}\hat{\bar{\psi}}\mathcal{D}\hat{\psi}\left(\hat{\psi}_\alpha(n)\hat{\bar{\psi}}_\beta(m)\right)e^{-S_{\mathrm{f}}[\hat{\bar{\psi}},\hat{\psi}]}}{\int \mathcal{D}\hat{\bar{\psi}}\mathcal{D}\hat{\psi}e^{-S_{\mathrm{f}}[\hat{\bar{\psi}},\hat{\psi}]}}. \tag{A.21}$$

A complete, detailed derivation of the lattice 2-point function is quite technical, in this section we just briefly sketch the arguments. For a detailed derivation we refer to Rothe in Ref. [24]. We construct the 2-point function by using the generating functional of the partition function, which is obtained by introducing Grassmann-valued fields $\{\bar{\rho}, \rho\}$, such that

$$\mathcal{Z}[\bar{\rho}, \rho] = \int \mathcal{D}\hat{\bar{\psi}}\mathcal{D}\hat{\psi}e^{-S_{\mathrm{f}}[\hat{\bar{\psi}},\hat{\psi}]+\sum_{n,\alpha}[\bar{\rho}_\alpha(n)\hat{\psi}_\alpha(n)+\hat{\bar{\psi}}_\alpha(n)\rho_\alpha(n)]}. \tag{A.22}$$

By using the explicit form of $S_{\mathrm{f}}[\hat{\bar{\psi}}, \hat{\psi}]$ and applying the following substitutions

$$\hat{\psi}_\beta(m) = \hat{\psi}'_\beta(m) + \sum_{\gamma,r} K^{-1}_{\beta,\gamma}(m,r)\rho_\gamma(r) \quad \text{and} \quad \hat{\bar{\psi}}_\alpha(n) = \hat{\bar{\psi}}'_\alpha(n) + \sum_{\delta,s}\bar{\rho}_\delta(s)K^{-1}_{\delta,\alpha}(s,n) \tag{A.23}$$

one obtains

$$\mathcal{Z}[\rho, \bar{\rho}] = \det[\mathbf{K}]e^{\sum_{\alpha,\beta,n,m}\bar{\rho}_\alpha(n)K^{-1}_{\alpha,\beta}(n,m)\rho_\beta(m)}, \tag{A.24}$$

where $\mathbf{K}$ denotes the Dirac operator, given by eq. (A.20) and we used the well-known result for Gaussian integrals over Grassmann variables. In this particular form the generating functional can be used to obtain the numerator of the 2-point function eq. (A.21) by taking derivatives with respect to ρ and $\bar{\rho}$. After some careful calculations using the generating functional and the Grassmann integration rules we obtain

$$\langle\hat{\psi}_\alpha(n)\hat{\bar{\psi}}_\beta(m)\rangle = K^{-1}_{\alpha,\beta}(n,m). \tag{A.25}$$

One can compute $K^{-1}_{\alpha,\beta}(n,m)$ by working in Fourier space and using

$$\sum_{\lambda,l} K^{-1}_{\alpha\lambda}(n,l)K_{\lambda\beta}(l,m) = \delta_{\alpha\beta}\delta_{nm}, \tag{A.26}$$

also here for details we refer to Ref. [24]. The final result for $K^{-1}_{\alpha\beta}(n,m)$ is given by

$$K^{-1}_{\alpha\beta}(n,m) = \int \frac{d^2\hat{k}}{(2\pi)^2} \frac{[-i\sum_\mu(\gamma_\mu)\sin(\hat{k}_\mu) + \hat{m}_0]_{\alpha\beta}}{\sum_\mu \sin^2(\hat{k}_\mu) + \hat{m}_0^2} e^{i\hat{k}(n-m)} =: \tilde{T}(n,m;\hat{m}_0), \tag{A.27}$$

where we used $\hat{k}.\hat{\mu} = \hat{k}_\mu$ and defined a new quantity $\tilde{T}(n,m;\hat{m}_0)$ in the last equation. So far all the calculations went smoothly and there is no reason to believe that our naive lattice discretization would fail. However, one can show that one does not retrieve the correct continuum limit. Let us derive the continuum 2-point function $\langle\psi_\alpha(x)\bar{\psi}_\beta(y)\rangle$ starting from the lattice 2-point function $\langle\hat{\psi}_\alpha(n)\hat{\bar{\psi}}_\beta(m)\rangle$. The the continuum 2-point function can be computed by letting the lattice spacing go to zero $a \to 0$, such that

$$\langle\psi_\alpha(x)\bar{\psi}_\beta(y)\rangle = \lim_{a\to 0}\frac{1}{a}\langle\hat{\psi}_\alpha(n)\hat{\bar{\psi}}_\beta(m)\rangle \tag{A.28}$$

$$= \lim_{a\to 0}\frac{1}{a}\tilde{T}(\frac{x}{a},\frac{y}{a};m_0 a) \tag{A.29}$$

$$= \lim_{a\to 0}\int_{(-\frac{\pi}{a},\frac{\pi}{a}]}\frac{dk_0}{(2\pi)}\int_{(-\frac{\pi}{a},\frac{\pi}{a}]}\frac{dk_1}{(2\pi)}\frac{[-i\sum_\mu(\gamma_\mu)\frac{1}{a}\sin(ak_\mu)+m_0]_{\alpha\beta}}{\sum_\mu(\frac{1}{a}\sin(ak_\mu))^2+m_0^2}e^{ik(x-y)}, \tag{A.30}$$

where we wrote out the integration measure in the last step. As a side-product we obtain the fermion propagator in momentum space which is given by

$$\tilde{S}(k)_{\alpha,\beta} = \frac{[-i\sum_\mu(\gamma_\mu)\frac{1}{a}\sin(ak_\mu)+m_0]_{\alpha\beta}}{\sum_\mu(\frac{1}{a}\sin(ak_\mu))^2+m_0^2}. \tag{A.31}$$

The easiest way to illustrate the fermion doubling problem is to consider a massless theory with $m_0 = 0$. In this case, for fixed momentum k, the momentum space fermion propagator has the correct continuum limit

$$\tilde{S}(k)_{\alpha,\beta}|_{m_0=0} = \frac{[-i\sum_\mu(\gamma_\mu)\frac{1}{a}\sin(ak_\mu)]_{\alpha\beta}}{\sum_\mu(\frac{1}{a}\sin(ak_\mu))^2} \xrightarrow{a\to 0} \frac{[-i\sum_\mu\gamma_\mu k_\mu]_{\alpha\beta}}{k^2}. \tag{A.32}$$

In the continuum the momentum space propagator for massless fermions has a pole at $k = (0,0)$, corresponding to the single fermion, which is described by the continuum Dirac operator.

However, on the lattice this situation is different. Not only do we have the "correct" pole at $k = (0,0)$ but additional unphysical poles at the boundaries of the Brillouin zone

$$k = (\frac{\pi}{a},0), \quad k = (0,\frac{\pi}{a}), \quad \text{and} \quad k = (\frac{\pi}{a},\frac{\pi}{a}). \tag{A.33}$$

We see that these values of k give rise to 3 unwanted poles, the so-called fermion doublers, which have no meaning in the continuum. The appearance of these unwanted fermion doublers is described by the Nielsen-Ninomiya theorem, see Ref. [25], for a more pedagogical explanation we recommend Refs. [52] and [43]. To circumvent the fermion doubling problem we implement so-called Wilson fermions which explicitly break chiral symmetry.

A.4 Wilson fermions

To circumvent the fermion doubling problem we remind ourselves that any discretization of the original action is valid, as long as we retrieve the correct continuum limit. We now exploit this ambiguity by modifying the action in such a way that the pole of the massless propagator is only given by the physical pole at $k = (0,0)$. In order to do this, we add an additional term to the lattice action, such that

$$S^W[\hat{\bar{\psi}},\hat{\psi}] = S[\hat{\bar{\psi}},\hat{\psi}] - \frac{r}{2}\sum_n \hat{\bar{\psi}}(n)\hat{\Box}\hat{\psi}(n), \tag{A.34}$$

where r is the so called Wilson parameter[2] and $\hat{\Box}$ is the 2-dimensional, dimensionless, lattice Laplacian given by

$$\hat{\Box}\hat{\psi}(n) = \sum_\mu[\hat{\psi}(n+\hat{\mu}) + \hat{\psi}(n-\hat{\mu}) - 2\hat{\psi}(n)]. \tag{A.35}$$

[2]Note, that the Wilson parameter will always be set to $r = 1$ in lattice simulations.

Making the inverse replacements as we did in eqs. (A.17) and (A.18) one can see that this additional Wilson term vanishes linearly with a in the continuum limit $a \to 0$. Consequently, we can write down the Wilson action as

$$S^W[\hat{\bar{\psi}}, \hat{\psi}] = \sum_{\alpha,\beta,n,m} \hat{\bar{\psi}}_\alpha(n) K^W_{\alpha,\beta}(n,m) \hat{\psi}_\beta(m), \tag{A.36}$$

where the Wilson Dirac operator $K^W_{\alpha,\beta}(n,m)$ is now given by

$$K^W_{\alpha,\beta}(n,m) = (\hat{m}_0 + 2r)\delta_{mn}\delta_{\alpha,\beta} - \frac{1}{2}\sum_\mu [(r-\gamma_\mu)_{\alpha\beta}\delta_{m,n+\hat{\mu}} + (r+\gamma_\mu)_{\alpha\beta}\delta_{m,n-\hat{\mu}}]. \tag{A.37}$$

The Wilson action leads to the following 2-point function of the continuum theory

$$\langle \psi_\alpha(x)\bar{\psi}_\beta(y)\rangle = \lim_{a\to 0} \int_{-\frac{\pi}{a}}^{\frac{\pi}{a}} \frac{\mathrm{d}^2k}{(2\pi)^2} \frac{[-i\sum_\mu(\gamma_\mu)\frac{1}{a}\sin(ak_\mu) + m(k)]_{\alpha\beta}}{\sum_\mu(\frac{1}{a}\sin(ak_\mu))^2 + m(k)^2}, \tag{A.38}$$

where $m(k)$ is now given by

$$m(k) = m_0 + \frac{2r}{a}\sum_\mu \sin^2\left(\frac{k_\mu a}{2}\right). \tag{A.39}$$

For any fixed value of k, which is not at the edges of the Brillouin zone, we obtain $m(k) \to m$ in the continuum limit. However, at the edges of the Brillouin zone the mass diverges in the continuum limit, giving an infinite mass to the fermion doublers, which then decouple.

A.5 Implementation of the gauge fields

From now on, we will be working with Wilson fermions. Thus, we omit the index W in the Wilson Dirac operator and the corresponding action. For the sake of simplicity, we also drop the hats on the lattice variables. We work with dimensionless variables unless mentioned otherwise. So far we derived the free lattice action

$$S_\mathrm{f}[\bar{\psi}, \psi] = \sum_{\alpha,\beta,n,m} \bar{\psi}_\alpha(n) K_{\alpha,\beta}(n,m) \psi_\beta(m), \tag{A.40}$$

where $K_{\alpha,\beta}(n,m)$ is given by

$$K_{\alpha,\beta}(n,m) = (m_0 + 2r)\delta_{mn}\delta_{\alpha,\beta} - \frac{1}{2}\sum_\mu [(r-\gamma_\mu)_{\alpha\beta}\delta_{m,n+\hat{\mu}} + (r+\gamma_\mu)_{\alpha\beta}\delta_{m,n-\hat{\mu}}]. \tag{A.41}$$

Up to this point, we derived this expression by working in the free formulation only, where no gauge fields exist (i.e. $A_\mu = 0$). However, we know that the continuum Schwinger model has a local $U(1)$ invariance, which was described in subsection (2.1.1). The next step consists in making the discretized lattice action invariant under a local $U(1)$ transformations given by

$$\psi(n) \to G(n)\psi(n), \qquad \bar{\psi}(n) \to \bar{\psi}(n)G(n)^{-1}, \tag{A.42}$$

where $G(n) \in U(1)$ describes a local gauge transformation depending on the lattice site n. Since the group element $G(n)$ does not act on the Dirac degrees of freedom, it is sufficient to look at a bilinear term like $\bar{\psi}(n)\psi(n+\hat{\mu})$. A bilinear combination of fields transforms as

$$\bar{\psi}(y)\psi(x) \to \bar{\psi}(y)G(y)^{-1}G(x)\psi(x), \tag{A.43}$$

which is not invariant. However, it is also known that in the continuum formulation a particle travelling along a path $\mathcal{C}$ picks up a phase of the form

$$U(y,x) = e^{ig\int_y^x dz_\mu A_\mu(z)}, \tag{A.44}$$

which is the so-called Wilson line. The Wilson line is an element of $U(1)$ and fulfills $U(y,x)^\dagger = U(x,y)$. Under a local gauge-transformation $A_\mu(x) \to A_\mu(x) - \frac{1}{g}\partial_\mu \Lambda(x)$ this object transforms as

$$U(y,x) \to G(y)U(y,x)G(x)^{-1}, \tag{A.45}$$

where $G(x) = e^{i\Lambda(x)}$. Consequently the following object is locally gauge-invariant

$$\bar{\psi}(y)U(y,x)\psi(x). \tag{A.46}$$

The above expression can be interpreted as a particle travelling in spacetime from point y to x and picking up all the contributions from the gauge fields. Now, let us construct the discretized Wilson line $U_{n,n+\hat{\mu}} \in U(1)$, starting from the continuum expression $U(x,y) \in U(1)$. In order to build local gauge-invariance into the lattice formulation the following replacements need to be made

$$\begin{aligned} &\bar{\psi}(n)(r-\gamma_\mu)\psi(n+\hat{\mu}) \to \bar{\psi}(n)(r-\gamma_\mu)U_{n,n+\hat{\mu}}\psi(n+\hat{\mu}) \quad \text{and} \\ &\bar{\psi}(n+\hat{\mu})(r+\gamma_\mu)\psi(n) \to \bar{\psi}(n+\hat{\mu})(r+\gamma_\mu)U_{n+\hat{\mu},n}\psi(n), \end{aligned} \tag{A.47}$$

where $U_{n+\hat{\mu},n} = U^\dagger_{n,n+\hat{\mu}}$. These replacements ensure local gauge invariance under the following transformations

$$\psi(n) \to G(n)\psi(n), \qquad \bar{\psi}(n) \to \bar{\psi}(n)G^{-1}(n), \tag{A.48}$$

$$U_{n,n+\hat{\mu}} \to G(n)U_{n,n+\hat{\mu}}G^{-1}(n+\hat{\mu}), \qquad U_{n+\hat{\mu},n} \to G(n+\hat{\mu})U_{n+\hat{\mu},n}G^{-1}(n). \tag{A.49}$$

Now, let us discuss the construction of these new discretized link variables $U_{n,n+\hat{\mu}} \in U(1)$. Take the most general ansatz

$$U_{n,n+\hat{\mu}} = e^{i\phi_\mu(n)}, \text{ with } \phi_\mu(n) \in [0, 2\pi), \tag{A.50}$$

and compare this expression to the Wilson line in the continuum $U(y,x)$. Assume that $x = y + \epsilon\hat{\mu}$, where $\epsilon\hat{\mu}$ describes an infinitesimal shift in $\hat{\mu}$-direction, then the continuum Wilson line can be approximated as

$$U(y, y+\epsilon\hat{\mu}) = e^{ig\int_y^{y+\epsilon\hat{\mu}} dz_\nu A_\nu(z)} \approx 1 + ig\epsilon A_\mu(y). \tag{A.51}$$

After comparison with the continuum expression and making some dimensional considerations we make the ansatz $\phi_\mu(n) = gaA_\mu(n)$ such that for a small lattice spacing a we obtain

$$U_{n,n+\hat{\mu}} \approx 1 + igaA_\mu(n). \tag{A.52}$$

By assuming that the discretized gauge fields transform as

$$A_\mu(n) \to A_\mu(n) - \frac{1}{g}\partial_\mu\Lambda(n) = A_\mu(n) - \frac{1}{g}(\Lambda(n+\hat{\mu}) - \Lambda(n)), \tag{A.53}$$

one can now verify that the discretized link variables transform correctly. The discretized Wilson line also has a graphical representation on the lattice (see figure A.1).

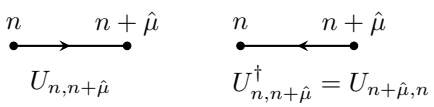

Figure A.1: Wilson line on the lattice.

Upon implementing the Wilson line in the fermionic action, we have

$$S[\bar{\psi},\psi,U] = \sum_{\alpha,\beta,n,m} \bar{\psi}_\alpha(n)K_{\alpha,\beta}(n,m)\psi_\beta(m), \text{ with} \tag{A.54}$$

$$K_{\alpha,\beta}(n,m) = \delta_{\alpha,\beta}\delta_{n,m}(m_0 + 2r) - \frac{1}{2}\sum_\mu [(r-\gamma_\mu)_{\alpha,\beta}U_{n,m}\delta_{m,n+\hat{\mu}} + (r+\gamma_\mu)_{\alpha,\beta}U_{n,m}\delta_{m,n-\hat{\mu}}]. \tag{A.55}$$

To complete the construction of the lattice action, we require a lattice version of the kinetic term

$$\frac{1}{4}F_{\mu\nu}F^{\mu\nu}, \tag{A.56}$$

which should be gauge-invariant as well and depend on the link variables only. Such gauge-invariant quantities can be constructed by taking the product of link-variables around closed loops on the lattice. We consider the smallest possible loop, which is a loop around an elementary plaquette. Its contribution is given by

$$\begin{aligned} U^P_{\mu\nu}(n) &= U_{n,n+\hat{\mu}}U_{n+\hat{\mu},n+\hat{\mu}+\hat{\nu}}U_{n+\hat{\mu}+\hat{\nu},n+\hat{\nu}}U_{n+\hat{\nu},n} \\ &= U_{n,n+\hat{\mu}}U_{n+\hat{\mu},n+\hat{\mu}+\hat{\nu}}U^\dagger_{n+\hat{\nu},n+\hat{\mu}+\hat{\nu}}U^\dagger_{n,n+\hat{\nu}}, \end{aligned} \tag{A.57}$$

where we have path ordered the link variables.

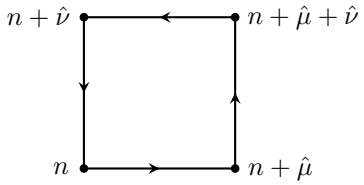

Figure A.2: Plaquette variable $U^P_{\mu\nu}$.

Note, that for an abelian gauge theory the path ordering is irrelevant, since all the link variables commute with each other. Additionally, we also specified the plaquette to be in the $\mu\nu$ plane starting from the point n. However, since we are working with a $1+1$-dimensional theory it should be evident, that every plaquette lies in the x^0x^1-plane. Upon inserting our known expression for the link variables we obtain

$$\begin{aligned} U^P_{\mu\nu} &= e^{igaA_\mu(n)}e^{igaA_\nu(n+\hat{\mu})}e^{-igaA_\mu(n+\hat{\nu})}e^{-igaA_\nu(n)} = e^{iga^2F_{\mu\nu}(n)}, \\ &\text{with } F_{\mu\nu} = \frac{1}{a}[(A_\nu(n+\hat{\mu}) - A_\nu(n)) + (A_\mu(n+\hat{\nu}) - A_\mu(n))]. \end{aligned} \tag{A.58}$$

One can show that for small a one obtains

$$\frac{1}{g^2}\sum_n \sum_{\substack{\mu,\nu \\ \mu<\nu}} (1 - \frac{1}{2}(U^P_{\mu,\nu} + U^{P,\dagger}_{\mu,\nu})) \approx \sum_n \sum_{\substack{\mu,\nu \\ \mu<\nu}} (\frac{1}{2}a^4F_{\mu\nu}F_{\mu\nu}) = \frac{1}{4}\sum_n\sum_{\mu\nu}(a^4F_{\mu\nu}F_{\mu\nu}). \tag{A.59}$$

We conclude that the discretized kinetic part of the action can be written as

$$S_g[U] = \frac{1}{g^2}\sum_P [1 - \frac{1}{2}(U^P + U^{P,\dagger})]. \tag{A.60}$$

For future purposes we also introduce the plaquette angle θ_P, which is related to the plaquette U_P via

$$U_P = e^{i\theta_P}, \tag{A.61}$$

allowing us to rewrite the kinetic part of the action as

$$S_g[U] = \frac{1}{g^2}\sum_P [1 - \cos(U_P)]. \tag{A.62}$$

In the last step, we introduce the quark chemical potential μ_q, which couples to the fermion number and is introduced on the lattice (see e.g. Ref. [53]) by furnishing the forward and backward temporal hopping terms by factors of $e^{\pm\mu_q}$, respectively. We conclude this section by giving the complete grand-canonical partition function for the 1-flavour Schwinger model and the complete discretized lattice action. The grand-canonical partition function of the 1-flavour Schwinger model is given by

$$\mathcal{Z}_{GC}(T,\mu) = \int \mathcal{D}U\mathcal{D}\bar{\psi}\mathcal{D}\psi e^{-S[\bar{\psi},\psi,U,\mu_q]}, \tag{A.63}$$

with Euclidean action

$$\begin{aligned} S[\bar{\psi},\psi,U,\mu_q] &= S_g[U] + S_F[\bar{\psi},\psi,U,\mu_q] \\ &= \frac{1}{g^2}\sum_P [1 - \frac{1}{2}(U^P + U^{P,\dagger})] + \sum_{\alpha,\beta,n,m} \bar{\psi}_\alpha(n) K_{\alpha,\beta}(n,m)\psi_\beta(m), \end{aligned} \tag{A.64}$$

where the Wilson Dirac operator is given by

$$\begin{aligned} K_{\alpha,\beta}(n,m) &= \delta_{\alpha,\beta}\delta_{n,m}(m_0 + 2r) \\ &- \frac{1}{2}[(r-\gamma_1)_{\alpha,\beta} U_{n,m}\delta_{m,n+\hat{1}} + (r+\gamma_1)_{\alpha,\beta} U_{n,m}\delta_{m,n-\hat{1}}] \\ &- \frac{1}{2}[e^{\mu_q}(r-\gamma_0)_{\alpha,\beta} U_{n,m}\delta_{m,n+\hat{0}} + e^{-\mu_q}(r+\gamma_0)_{\alpha,\beta} U_{n,m}\delta_{m,n-\hat{0}}]. \end{aligned} \tag{A.65}$$

B Traditional spectroscopy

In lattice simulations particle masses are traditionally computed from the asymptotic decay of the Euclidean time-correlation function (short correlation functions or correlators). A typical 2-point correlator is formed by taking the vacuum-expectation value of an operator $\mathcal{O}$

$$C(t-t_0) = \langle 0|\mathcal{O}(t)\mathcal{O}(t_0)|0\rangle, \quad \text{with } t \geq t_0. \tag{B.1}$$

Using the Euclidean time-evolution

$$\mathcal{O}(t) = e^{Ht}\mathcal{O}e^{-Ht}, \tag{B.2}$$

and inserting a complete set of eigenstates

$$\mathbb{1} = \sum_{n\geq 0} |n\rangle\langle n|, \text{ with energies } E_0 \leq E_1 \leq E_2 \leq \ldots, \tag{B.3}$$

one obtains (after setting $t_0 = 0$ for the sake of simplicity)

$$C(t) = \sum_{n\geq 0} |\langle 0|\mathcal{O}|n\rangle|^2 e^{-(E_n - E_0)t}. \tag{B.4}$$

For big time separations, higher order contributions are suppressed and the Euclidean correlation function reads

$$C(t) \sim |\langle 0|\mathcal{O}|0\rangle|^2 + |\langle 0|\mathcal{O}|1\rangle|^2 e^{-(E_1 - E_0)t}, \tag{B.5}$$

where E_0 is the vacuum energy and E_1 is the energy of the lowest energy state which the operator $\mathcal{O}$ can create from the vacuum. The first part is the vacuum disconnected part, correlation functions are usually defined without it. After defining the mass gap $m = E_1 - E_0$ one obtains

$$C(t) \sim |\langle 0|\mathcal{O}|1\rangle| e^{-mt}. \tag{B.6}$$

If we are extracting particle masses using correlation functions in lattice simulations we also must take into account the periodic nature of the lattice. Assume that the temporal extent of the lattice is t_{max},[1] then the correlator needs to be symmetrized with respect to $t \to t_{max} - t$, such that

$$\begin{aligned} C(t) &= \frac{1}{2}(\langle 0|\mathcal{O}(t)\mathcal{O}(0)|0\rangle + \langle 0|\mathcal{O}(t_{max}-t)\mathcal{O}(0)|0\rangle) \\ &= \frac{1}{2}\sum_{n\geq 0} |\langle 0|\mathcal{O}|n\rangle|^2 e^{-\frac{1}{2}(E_n - E_0)t_{max}} \left(e^{-(E_n-E_0)(t-\frac{t_{max}}{2})} + e^{-(E_n-E_0)(\frac{t_{max}}{2}-t)}\right) \\ &\to |\langle 0|\mathcal{O}|1\rangle|^2 e^{-\frac{mt_{max}}{2}} \cosh\left(m(t-\frac{t_{max}}{2})\right), \text{ for t} \to \frac{t_{max}}{2}. \end{aligned} \tag{B.7}$$

This is the basic way how one finds hadronic masses in lattice gauge theories, the specific form of the operators $\mathcal{O}$, determine the kind of particle we are measuring.

Although most of the following discussion can be held in a more generalized context, we restrict ourselves to the computation of correlators in the 2-flavour Schwinger model, which was introduced in section 2.2. Furthermore, we set the lattice spacing to $a = 1$, for the rest of this chapter.

Let us suppose we want to determine the mass of a meson in the 2-flavour Schwinger model. Then we measure a correlator of the form

$$C_2(t-t_0) = \sum_{x,y} \langle J(x,t)J^\dagger(y,t_0)\rangle, \tag{B.8}$$

[1] On a lattice of extent $L \times L_t$, we have $t_{max} = L_t$.

where we sum over all lattice points $x, y \in \{1, 2, \ldots, L\}$ and $J(x,t)$ denotes a meson interpolator, given by one of the wavefunctions in table (B.1). The meson interpolator $J^\dagger(y, t_0)$ is considered a source operator, where the meson is being created, while $J(x,t)$ is considered to be a sink operator, where the meson is being annihilated. A meson interpolator $J(x,t)$ is of the form

$$J(x,t) = \bar{\psi}(x,t)\Gamma T\psi(x,t) = \bar{\psi}_a^A(x,t)\Gamma_{ab}T^{AB}\psi_b^B(x,t), \tag{B.9}$$

where Γ denotes the gamma structure and T describes the flavour structure of the meson. We labelled the flavour indices with capital letters A, B and Dirac indices with lower case letters a, b. Since we are working with the 2-flavour Schwinger model, the spinor ψ is a doublet in flavour space $\psi = (u, d)$. Depending on whether we are interested in a triplet or a singlet state, we modify the flavour matrix T. For a singlet state we choose $T = \mathbb{1}$, for triplet states we use one the generators of the $su(2)$ algebra in the Cartan-Weyl form

$$T^0 = \begin{pmatrix} \frac{1}{2} & 0 \\ 0 & -\frac{1}{2} \end{pmatrix}, \qquad T^+ = \begin{pmatrix} 0 & 1 \\ 0 & 0 \end{pmatrix}, \qquad T^- = \begin{pmatrix} 0 & 0 \\ 1 & 0 \end{pmatrix}, \tag{B.10}$$

as illustrated in table B.1.

operator	particle name	Quantum numbers (I^{PG})	Meson Interpolator $J(x,t)$
Pseudo-scalar Triplet	π	1^{-+}	$\bar{\psi}(T^0, T^+, T^-) \cdot \gamma^5\psi$
Pseudo-scalar Singlet	η	0^{--}	$\bar{\psi}\mathbb{1} \cdot \gamma^5\psi$
Scalar Triplet	a_0	1^{+-}	$\bar{\psi}(T^0, T^+, T^-) \cdot 1\psi$
Scalar Singlet	f_0	0^{++}	$\bar{\psi}\mathbb{1} \cdot 1\psi$

Table B.1: Summary of the 1-meson states, including the quantum number and the meson interpolators, which are used for spectroscopy. Compared to four dimensions, we only have a finite number of meson interpolators, other potential meson interpolators are related to the ones presented here by the relation $i\gamma_5\gamma_\mu = \epsilon_{\mu\nu}\gamma_\nu$.

The Dirac structure needs to be chosen depending on the quantum numbers of the particle we want to measure. For instance, a positively charged pion π^+, consisting of an up and down quark, is a pseudo-scalar particle and a member of the triplet $\{\pi^-, \pi^0, \pi^+\}$. In order to form the corresponding interpolator J, we choose the corresponding Dirac-structure $\Gamma = \gamma_5$ and the generator $T = T^-$, such that

$$J(x,t) = \bar{\psi}(x,t)T^- \otimes \gamma_5\psi(x,t) = \bar{d}(x,t)\gamma_5 u(x,t) =: \pi^+(x,t). \tag{B.11}$$

We finish this section by mentioning that mesons can have higher order energy states, which are constructed by giving the meson a momentum p. To measure the energy of those states one has to modify the meson interpolator and give it some momentum

$$J(x,t) \to J(x,t)e^{-ip^{(k)}x}, \quad \text{where } p^{(k)} = \frac{2\pi}{L} \cdot k, \tag{B.12}$$

denotes the quantized momentum of the meson on the lattice. The new 2-point correlation function then reads

$$C_2(t - t_0, k) = \sum_{x,y} e^{-\frac{2\pi \cdot k}{L}(x-y)}\langle J(x,t)J^\dagger(y,t_0)\rangle \propto e^{-E_J^{(k)}(t-t_0)}, \tag{B.13}$$

and allows us to extract the energy of the k-th excited energy state of the measured meson belonging to the interpolator J.

B.1 Contractions

For the remainder of this section we restrict ourselves to the computation of ground state energies, i.e. we do not give any momenta to the mesons we measure. Then the most general expression for the 2-point

correlation function reads

$$C_{2,T\Gamma,T'\Gamma'}(t-t_0) = \sum_{x,y}\langle J(x,t)J^\dagger(y,t_0)\rangle \tag{B.14}$$

$$= \sum_{x,y}\sum_{ABCD}\sum_{abcd}\langle\bar{\psi}_a^A(x,t)T^{AB}\Gamma_{ab}\psi_b^B(x,t)\bar{\psi}_c^C(y,t_0)T'^{CD}\Gamma'_{cd}\psi_d^D(y,t_0)\rangle \tag{B.15}$$

$$= \sum_{x,y}\sum_{ABCD}\sum_{abcd} T^{AB}T'^{CD}\Gamma_{ab}\Gamma'_{cd}\langle\psi_b^B(x,t)\bar{\psi}_a^A(x,t)\psi_d^D(y,t_0)\bar{\psi}_c^C(y,t_0)\rangle, \tag{B.16}$$

where we explicitly used the expressions for the source and the sink operators. To evaluate the Wick contractions, we define the fermion propagator

$$S_{ba}^{BA}(x',t',x,t) = \langle 0|\psi_b^B(x',t')\bar{\psi}_a^A(x,t)|0\rangle, \tag{B.17}$$

which is determined from the inverse Dirac operator and denotes a fermion propagating from (x,t) to (x',t'). Making use of the fermion propagator, the Einstein sum convention and implicitely summing over all spatial lattice points x, y one obtains

$$C_{2,T\Gamma,T'\Gamma'}(t-t_0) = T^{AB}T'^{CD}\Gamma_{ab}\Gamma'_{cd}(S_{ba}^{BA}(x,t,x,t)S_{dc}^{DC}(y,t_0,y,t_0) - S_{bc}^{BC}(x,t,y,t_0)S_{da}^{DA}(y,t_0,x,t)). \tag{B.18}$$

For Wilson fermions the fermion propagator is diagonal in flavour space, $S^{AB} \sim \delta^{AB}$, such that the flavour structure can be evaluated separately. Performing the summation over the flavour indices A, B, C, D leads to

$$\begin{aligned} C_{2,T\Gamma,T'\Gamma'}(t-t_0) = {} & \mathrm{Tr}(T)\,\mathrm{Tr}(T')\Gamma_{ab}\Gamma_{cd}S_{ba}(x,t,x,t)S_{dc}(y,t_0,y,t_0) \\ & - \mathrm{Tr}(T.T')\Gamma_{ab}\Gamma_{cd}S_{bc}(x,t,y,t_0)S_{da}(y,t_0,x,t). \end{aligned} \tag{B.19}$$

After summing over all Dirac indices and reintroducing the suppressed summation over the spatial lattice points, the final expression for a 2-point function reads

$$\begin{aligned} C_{2,T\Gamma,T'\Gamma'}(t-t_0) = \sum_{x,y}\{ & \mathrm{Tr}(T)\,\mathrm{Tr}(T')\,\mathrm{Tr}[S(x,t,x,t)\Gamma]\,\mathrm{Tr}[S(y,t_0,y,t_0)\Gamma] \\ & - \mathrm{Tr}(T.T')\,\mathrm{Tr}[S(x,t,y,t_0)\Gamma S(y,t_0,x,t)\Gamma]\}. \end{aligned} \tag{B.20}$$

B.2 1- and 2-pion correlators

In the 2-flavour Schwinger model the pion triplet has fermion number $Q = 0$ and isospin $I = 1$. The three members of the triplet are distinguished by the z-component of their isospin. In our work we are interested in energies of n-meson ground states, which all happen to be multi-pion states. One way to compute the energies of those multi-pion states is by measuring $2n$-point correlation functions (or short n-pion correlators), with the corresponding interpolator J. We start by writing down the complete expression for the correlation function of a single pion π. We restrict ourselves to the calculation of states with maximal isospin $I_z = I = 1$, such that the 1-pion correlator reads

$$C_2(t-t_0) = \langle(\sum_x \pi^-(x,t))(\sum_y \pi^+(y,t_0))\rangle. \tag{B.21}$$

Plugging in the required flavour matrices $T = T^+$, $T' = T^-$ and setting $\Gamma = \Gamma' = \gamma_5$ we obtain

$$C_2(t-t_0) \propto \sum_{x,y}\mathrm{Tr}[S(x,t,y,t_0)\gamma_5 S(y,t_0,x,t)\gamma_5], \tag{B.22}$$

where we omitted the prefactor. It is worth noticing that the flavour triplet does not have any disconnected contribution in the 1-pion correlator, due to the traceless nature of the generators of the $su(2)$ algebra.

For pedagogical reasons let us also compute the 2-pion correlator. Similar to the case for $n = 1$, multi-pion correlation functions do not pick up disconnected contributions. The most general expression for a 4-point function is given by

$$\begin{aligned} C_{4,T\Gamma,T'\Gamma'}(t-t_0) = {} & T^{AB}T^{CD}T'^{EF}T'^{GH}\Gamma_{ab}\Gamma_{cd}\Gamma_{ef}\Gamma_{gh} \\ & \times\langle\psi_b^B(x_1,t)\bar{\psi}_a^A(x_1,t)\psi_d^D(x_2,t)\bar{\psi}_c^C(x_2,t)\psi_f^F(y_1,t_0)\bar{\psi}_e^E(y_1,t_0)\psi_h^H(y_2,t_0)\bar{\psi}_g^G(y_2,t_0)\rangle, \end{aligned} \tag{B.23}$$

where we implicitely sum over all spatial points x_1, x_2, y_1, y_2 and over all Dirac and flavour indices. In order to get the 2-pion correlator we perform the same kind of replacements, as for the 1-pion correlator, that is $T = T^+$, $T' = T^-$ and $\Gamma = \Gamma' = \gamma_5$. Given that $\mathrm{Tr}[T^+] = \mathrm{Tr}[T^-] = 0$ and $T^+.T^+ = T^-.T^- = 0$, many of the Wick contractions vanish and the remaining ones are easily computed. Using

$$\mathrm{Tr}[T^+.T^-] = \mathrm{Tr}[T^+.T^-.T^+.T^-] = 1, \tag{B.24}$$

and relabelling the spatial indices we obtain

$$\begin{aligned} C_4(t-t_0) \propto & \left(\sum_{x_1,y_1} \mathrm{Tr}[S(x_1,t,y_1,t_0)\gamma_5 S(y_1,t_0,x_1,t)\gamma_5] \right)^2 \\ & - \sum_{x_1,x_2,y_1,y_2} \mathrm{Tr}[S(x_1,t,y_1,t_0)\gamma_5 S(y_1,t_0,x_2,t)\gamma_5 S(x_2,t,y_2,t_0)\gamma_5 S(y_2,t_0,x_1,t)\gamma_5] \end{aligned} \tag{B.25}$$

This game can be played for arbitrary n-pion correlators, i.e. correlators of the form

$$C_{2n}(t-t_0) = \langle (\sum_x \pi^-(x,t))^n (\sum_y \pi^+(y,t_0))^n \rangle, \tag{B.26}$$

however, it is quite evident that the calculations become more involved and time-consuming. By realizing that each contribution describes a different type of closed graph on the lattice (see for example figure B.1, for the 2-pion correlator), we can find a generalized formula, which allows us to determine all pion correlators up to arbitrary order. Detmold, Savage et al. did this and wrote down all the n-pion correlators for up to $n = 13$ pions in Ref. [15]. In the next section we present an argument which allows us to compute the very same multi-pion correlator in terms of so-called "quark loop propagators".

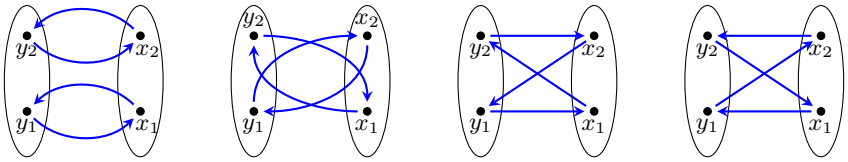

Figure B.1: Graphical representation of the contractions for the 2-pion correlator. The spatial points y_1, y_2 are sitting at the source at time t_0, while the spatial points x_1, x_2 are sitting at the sink at time t. The first two figures on the left show two closed quark loops, corresponding to the contribution T_1^2. The remaining two figures show quarks making a "complete" loop, hopping twice between time-slices, before closing the loop.

B.3 Multi-pion correlators

We would like to derive a generalized formula for n-pion correlators, that is

$$C_{2n}(t-t_0) = \langle (\sum_x \pi(x,t)^-)^n (\sum_y \pi(y,t_0)^+)^n \rangle. \tag{B.27}$$

To do so, we introduce the so-called "quark loop propagator" as

$$\Pi = \sum_{x,y} S(x,t,y,t_0) S^\dagger(x,t,y,t_0) \tag{B.28}$$

$$= \sum_{x,y} S(x,t,y,t_0)\gamma_5 S(y,t_0,x,t)\gamma_5, \tag{B.29}$$

where we used an identity for the path-reversed propagator $S^\dagger(x,t,y,t_0) = \gamma_5 S(y,t_0,x,t)\gamma_5$. Note, that we do not follow any naming conventions, the object Π does not really have a name. We choose to label it quark loop propagator, since it describes a quark being created at spacetime point (y,t_0), visiting spacetime point (x,t), before going back to (y,t_0), completing the loop. Furthermore, we introduce the trace of the quark loop propagator as

$$T_i = \mathrm{Tr}[\Pi^i], \tag{B.30}$$

where the trace is taken over the Dirac indices and the index i denotes the power to which Π is raised. Note, that by raising the power of the quark loop propagator, it is meant that we prolong the path of quark, so for example

$$\Pi^2 = \sum_{x_1,x_2,y_1,y_2} S(x_1,t,y_1,t_0)\gamma_5 S(y_1,t_0,x_2,t)\gamma_5 S(x_2,t,y_2,t_0)\gamma_5 S(y_2,t_0,x_1,t)\gamma_5. \tag{B.31}$$

Upon making these definitions, we identify that the 1- and 2-pion correlators is given by

$$C_2(t-t_0) \propto T_1, \tag{B.32}$$

$$C_4(t-t_0) \propto T_1^2 - T_2, \tag{B.33}$$

respectively. Using intuitive arguments, one can show that n-pion correlators can be computed in terms of the traces of quark loop propagators

$$T_i = \mathrm{Tr}[\Pi^i], \quad \text{with} \quad \Pi = \sum_{x,y} S(x,t,y,t_0)\gamma_5 S(y,t_0,x,t)\gamma_5. \tag{B.34}$$

Consider two time-slices on the lattice, t_0 and t with $t > t_0$, each consisting of L spatial points. Upon having a closer look at the structure of the correlation functions, one comes to understand, that an n-pion correlator describes sets of closed paths on the lattice which alternate between the time slices. The exact spatial points the path visits do not matter, in the end, we sum over all the different possibilities anyway.

Let us revisit the two examples we calculated before. The 1-pion correlator describes the set of all paths, where the pion travels from the source at some spacetime point (y_1, t_0) to the sink at some spacetime point (x_1, t) and back again to the source (y_1, t_0). This path yields an overall factor T_1 and therefore the result for $C_2(t-t_0)$ given by eq. (B.32). The 2-pion correlator has two parts. The first part describes two separate paths with two pions travelling similarly as before, yielding a contribution T_1^2. The second part describes a pion travelling twice between time-slices. Its path[2] is given by something like

$$(y_1,t_0) \to (x_1,t) \to (y_2,t_0) \to (x_2,t) \to (y_1,t_0). \tag{B.35}$$

The second part yields an overall contribution of T_2 and has a minus sign compared to the first one, since the number of quark loops changes from an even number to an odd one. The underlying reasons are of course the commutation rules of the Grassmann fields ψ and $\bar{\psi}$. The two contributions for the 2-pion correlator are shown in figure B.1. Combining those two parts we obtain the well known result for $C_4(t-t_0)$ that is eq. (B.33).

The important quantities which are crucial for the determination of the pion correlators are the number of closed paths and the lengths of each of these paths. The length of a path shall be defined by the number of times, where the pion jumps from time-slice t to t_0 and back. In the next section we give an idea of how to compute arbitrary n-pion correlators using the symmetric group S_n, which describes permutations of n elements, and the so-called integer partitions $\mathrm{IP}(n)$.

B.4 Revisiting 1- and 2-pion correlators and computing 3-pion correlators

Here we present a description, allowing us to determine n-pion correlators using simple algebra. We do this by presenting the calculations of the 1-, 2- and 3-pion correlators, the computations for higher pion numbers follow the same strategy. The needed mathematical background for this section is provided by Dummit and Foote in Ref. [54] and Cameron et al. in Ref. [55].

To describe the different sets of paths mathematically, we utilize the symmetric group S_n, which describes permutations of n elements. The order of S_n is given by the number of ways one can rearrange the elements of the set $\{1, 2, \ldots, n\}$. This is a simple combinatorial task and we conclude that the order of S_n is $n!$. In order to characterize an element $\sigma \in S_n$, the cycle notation is very handy. A cycle is a string of integers which represents the elements of S_n which cyclically permutes these integers (and fixes all other integers). For example, the cycle

$$(a_1, a_2, \ldots, a_m), \tag{B.36}$$

[2]We emphasize, once more, that the specific choice of spatial points the quark visits does not matter.

with $m \leq n$, sends a_i to a_{i+1} for all $i < m$ and a_m to a_1.

For a more concrete example, consider an element $\sigma = (123)$ in S_3 which maps $1 \to 2$, $2 \to 3$ and $3 \to 1$. The element $\sigma = (12)$ in S_3, just exchanges 1 and 2, while keeping 3 fixed.

Throughout this section we use a slightly modified form of the cycle notation, we will explicitly write down the cycles of length 1 for the sake of completeness. This means, that for example a cycle like $\sigma = (12)$ in S_3 becomes $\sigma = (12)(3)$.

Furthermore, so-called integer partitions $\mathrm{IP}(n)$ will be used, in particular, the equivalence between the integer partitions of n and the conjugacy classes of S_n, as illustrated in Ref. [54].

Let us start the computations with the 1-pion correlator $C_2(t - t_0)$. We need the symmetry group $S_1 = \{(1)\}$ which contains just the unit element denoting a "trivial" permutation. In order to obtain the conjugacy classes of S_1 we compute the integer partition of $n = 1$, which are simply given by

$$1 = 1, \tag{B.37}$$

therefore $\mathrm{IP}(1) = \{\{1\}\}$. The element $\{1\}$ can be understood as the conjugacy class of one cycle of length 1, belonging to the unit element of S_1. For the computation of the 1-pion correlator the conjugacy class $\{1\}$ can be interpreted as a path of length 1, which allows us to draw a connection to the trace of the quark loop propagator T_1. We make the assignment

$$\{1\} \to T_1, \tag{B.38}$$

and since we only have one conjugacy class, the final result reads

$$C_2(t - t_0) \propto T_1. \tag{B.39}$$

We turn to the computation of the 2-pion correlator $C_4(t - t_0)$. The corresponding symmetric group

$$S_2 = \{(1)(2), (12)\} \tag{B.40}$$

has two elements, $(1)(2)$ denotes the unit element, while (12) denotes a permutation of the two elements. In order to get the conjugacy classes we compute the integer partitions

$$2 = 1 + 1, \tag{B.41}$$
$$= 2, \tag{B.42}$$

therefore

$$\mathrm{IP}(2) = \{\{1, 1\}, \{2\}\}. \tag{B.43}$$

The first element $\{1, 1\}$ belongs to the conjugacy class corresponding to two cycles of length 1. The only member of this conjugacy class is the unit element of S_2, that is $(1)(2)$. The second element $\{2\}$ belongs to the conjugacy class corresponding to one cycle of length 2, belonging to (12). For the computation of the 2-pion correlator we make the following assignments

$$\{1, 1\} \to T_1^2 \quad \text{and} \quad \{2\} \to T_2. \tag{B.44}$$

To construct $C_4(t - t_0)$ we take into account the number of elements in each conjugacy class and add a minus sign if the number of quark loops changes. Since we have one element for each conjugacy class the computation is straightforward and we obtain our well-known result

$$C_4(t - t_0) \propto T_1^2 - T_2. \tag{B.45}$$

Well, that was fun! Now let us turn to something new, the 3-pion correlator $C_6(t-t_0)$, with the symmetric group

$$S_3 = \{(1)(2)(3), (12)(3), (1)(23), (13)(2), (123), (132)\}. \tag{B.46}$$

As before, we determine the conjugacy classes by computing the integer partitions of $n = 3$

$$3 = 1 + 1 + 1, \tag{B.47}$$
$$= 2 + 1, \tag{B.48}$$
$$= 3, \tag{B.49}$$

such that

$$\mathrm{IP}(3) = \{\{1,1,1\},\{2,1\},\{3\}\}. \tag{B.50}$$

We associate the conjugacy classes to the corresponding traces of quark loop propagators

$$\{1,1,1\} \to T_1^3, \quad \{2,1\} \to T_1 T_2 \quad \text{and} \quad \{3\} \to T_3, \tag{B.51}$$

and compute the number of elements of each conjugacy class, by identifying

$$\{1,1,1\} \sim (1)(2)(3) \qquad \to 1 \text{ element}, \tag{B.52}$$
$$\{2,1\} \sim (12)(3),(1)(23),(13)(2) \qquad \to 3 \text{ elements}, \tag{B.53}$$
$$\{3\} \sim (123),(132) \qquad \to 2 \text{ elements}. \tag{B.54}$$

After adding the mandatory change of sign, we obtain

$$C_6(t-t_0) \propto T_1^3 - 3T_1T_2 + 2T_3. \tag{B.55}$$

We obtain these results using just the traces of the quark loop propagators, without engaging in extensive indices algebra coming from multiple Wick contractions. Following this strategy, one can construct all the n-pion correlators in a straightforward way, but also here, the computations become more complex with an increasing number of pions.

Let us discuss the reason for the increase in complexity. Based on the integer partitions of n, we determine the conjugacy classes and write down the different kinds of contributions in terms of traces of quark loop propagators T_i. However, the prefactors of these contributions are related to the number of elements in the given conjugacy class and are not always easy to determine. It is therefore necessary to have an analytic expression for the number of elements in each conjugacy class. Such an analytic formula for the size of a conjugacy class can be found in Ref. [54] and will be discussed next.

Suppose we want to find the size of a conjugacy class C of S_n, that is $|C|$. Consider an element of that conjugacy class $\sigma \in C$, which can be decomposed into s different cycle types. Then σ can be characterized by the number of cycles k_i and the length of each of these cycles l_i, with $i \in \{1,\dots,s\}$, such that

$$\sum_{i=1}^{s} k_i l_i = n. \tag{B.56}$$

The number of conjugates of σ - and therefore the size of the conjugacy class C - is given by

$$|C| = \frac{n!}{(k_1! l_1^{k_1})(k_2! l_2^{k_2}) \dots (k_s! l_s^{k_s})}. \tag{B.57}$$

If we revisit our computation for the 3-pion correlator we recognize our well-known prefactors from eq. (B.55)

$$C(\{1,1,1\}) = \frac{3!}{3!1^3} = 1, \tag{B.58}$$
$$C(\{2,1\}) = \frac{3!}{(1!2^1)(1!1^2)} = 3, \tag{B.59}$$
$$C(\{3\}) = \frac{3!}{(1!3^1)} = 2, \tag{B.60}$$

confirming the validity of eq. (B.57).

C Monte Carlo simulations

Explicitly evaluating the partition function $\mathcal{Z}$ for a lattice gauge theory of interacting particles is a hopeless task, which is why we resort to numerical methods. The idea of Monte Carlo sampling is to compute physical quantities we are interested in (observables) by numerically generating new configurations, according to their Boltzmann weight. For the Schwinger model on the lattice, the configurations are characterized by the gauge fields

$$[s] := [s[U]] = \{U_{n,n+\hat{\mu}}, \text{ with } n \in \{1, 2, \ldots, \Omega\}, \hat{\mu} \in \{\hat{0}, \hat{1}\}\}, \tag{C.1}$$

where we introduced a lattice with a total of $\Omega = L \cdot L_t$ spacetime points (we set the lattice spacing to one, $a = 1$). In case of the quenched (0-flavour) Schwinger model we simulate a pure $U(1)$ gauge theory with no fermion content, such that the Euclidean action reduces to the kinetic part only

$$S_E[U] = S_g[U]. \tag{C.2}$$

The partition function can then be expressed as sum over all Boltzmann weights

$$\mathcal{Z} = \int \mathcal{D}U e^{-S_g[U]} = \int \mathcal{D}U e^{-\mathcal{H}[U]}, \tag{C.3}$$

where we interpret the action as a measure of the energy of the system. The probability that a configuration $[s]$ is occupied is then given by

$$p[s] = \frac{1}{\mathcal{Z}} e^{-\mathcal{H}[s]}. \tag{C.4}$$

For a more detailed discussion consider Ref. [56].

C.1 Markov chains

The concept of Markov chains is of central importance in Monte Carlo simulations. A Markov chain is a sequence of configurations which begins with an initial configuration $[\mathrm{s}^{(1)}]$ and then evolves from $[\mathrm{s}^{(i)}]$ to $[\mathrm{s}^{(i+1)}]$ recursively by applying some algorithm

$$[\mathrm{s}^{(1)}] \to \cdots \to [\mathrm{s}^{(N)}]. \tag{C.5}$$

In the end, when computing observables the choice of the initial configuration should not matter. After a certain number of Monte Carlo steps (i.e. iterations from $[\mathrm{s}^{(i)}]$ to $[\mathrm{s}^{(i+1)}]$), the system has reached equilibrium; from this point on we start measuring an observable $\mathcal{O}$. The measurement of an observable is carried out by averaging over all measurements after approaching equilibrium. Assuming that equilibrium is reached after M iterations, $\langle \mathcal{O} \rangle$ is estimated as

$$\overline{\mathcal{O}} = \frac{1}{N - M} \sum_{i=M+1}^{N} \mathcal{O}[\mathrm{s}^{(i)}]. \tag{C.6}$$

C.2 Measurements and error estimations

As in experimental physics, when measuring quantities we have to take into account statistical errors. Let the quantity $\mathcal{O}$ be normally distributed with mean value $\langle \mathcal{O} \rangle$ and width $\sigma = \sqrt{\mathrm{Var}(\mathcal{O})}$. Additionally, let us assume that we have N statistically independent observations within equilibrium $\{\mathcal{O}[\mathrm{s}^{(i)}]\}_{i=1}^{N}$ of a certain observable $\mathcal{O}$. An unbiased estimator for the mean value is the sample mean

$$\overline{\mathcal{O}} = \frac{1}{N} \sum_{i=1}^{N} \mathcal{O}[\mathrm{s}^{(i)}], \tag{C.7}$$

such that $\langle\overline{\mathcal{O}}\rangle = \langle\mathcal{O}\rangle$. By using the definition of the variance and assuming that the measurements are independent of each other, the standard deviation of the measurement is given by

$$\Delta\mathcal{O} = \frac{\sigma}{\sqrt{N}}. \tag{C.8}$$

An unbiased estimator of the variance σ^2 is given by the sample variance S^2

$$S^2 = \frac{1}{N-1}\sum_{i=1}^{N}(\mathcal{O}[\mathrm{s}^{(i)}] - \overline{\mathcal{O}})^2. \tag{C.9}$$

Consequently $\Delta\mathcal{O}$ can be written as

$$\Delta\mathcal{O} = \frac{S}{\sqrt{N}} = \frac{1}{\sqrt{N(N-1)}}\sqrt{\sum_{i=1}^{N}(\mathcal{O}[\mathrm{s}^{(i)}] - \overline{\mathcal{O}})^2} = \frac{1}{\sqrt{N-1}}\sqrt{\overline{\mathcal{O}^2} - \overline{\mathcal{O}}^2}. \tag{C.10}$$

C.3 The Bootstrap method

The bootstrap method was introduced as an automated computer-based method to estimate the errors of an observable $\mathcal{O}$. This method does not rely on any assumptions about the underlying distribution of the data and the complexity of the estimator $\hat{\mathcal{O}}$, which makes it a very universal tool for data analysis. For a more detailed discussion, we recommend Efron and Tibshirani in Ref. [57]. The bootstrap method relies on so-called bootstrap samples. Consider a set of n independent measurements, which may or may not be generated from a Monte Carlo simulation

$$\vec{x} = (x_1, x_2, \ldots, x_n). \tag{C.11}$$

We now construct N_B independent bootstrap samples, each one consisting of n data values drawn with replacement from $\vec{x}$. Mathematically speaking, we construct a bootstrap sample $x^\alpha, \alpha = 1, \ldots, N_B$ as

$$x^\alpha = \sum_{i=1}^{n} n_i^\alpha x_i, \tag{C.12}$$

where n^α denotes a vector of random positive integers, such that

$$\sum_{i=1}^{n} n_i^\alpha = n. \tag{C.13}$$

We construct the bootstrap estimator $\hat{\mathcal{O}}$ based on the bootstrap samples

$$\hat{\mathcal{O}}^\alpha = \hat{\mathcal{O}}(x^\alpha), \qquad \alpha = 1, \ldots, N_B. \tag{C.14}$$

Note that in case of a direct error estimation of the measurements, we just set $\hat{\mathcal{O}}^\alpha = x^\alpha$. An estimator of the standard error is given by the sample standard deviation of the N_B bootstrap samples

$$\Delta\mathcal{O}_B = \frac{1}{\sqrt{N_B - 1}}\sqrt{\sum_{\alpha=1}^{N_B}(\hat{\mathcal{O}}^\alpha - \overline{\mathcal{O}})^2}, \tag{C.15}$$

where we implicitely defined

$$\overline{\mathcal{O}} = \frac{1}{N_B}\sum_{\alpha=1}^{N_B}\hat{\mathcal{O}}^\alpha. \tag{C.16}$$

C.4 Autocorrelation

The ideal Monte Carlo algorithm would create a Markov chain of statistically independent configurations, but since a new configuration is generated from the previous one, subsequent configurations may be correlated. This means that the true statistical error is larger than the naive estimate of the standard

deviation. In order to take into account correlations of subsequently generated observations we modify the standard deviation by

$$\Delta\mathcal{O}^2 = \frac{S^2}{N}\left(1+\frac{2\tau_\mathcal{O}}{\delta t}\right) = \Delta\mathcal{O}^2_{\text{naive}}\left(1+\frac{2\tau_\mathcal{O}}{\delta t}\right), \tag{C.17}$$

where we introduced the integrated autocorrelation time $\tau_\mathcal{O}$ which is measured in units of δt. The additional term in $\Delta\mathcal{O}^2$ can be considered as a correction term for the true statistical error. A normalized autocorrelation function is used in order to estimate the number τ of iterations that separate statistically independent configurations. Consider the Markov chain as a statistical system evolving in Monte Carlo time. The normalized autocorrelation function for some observable $\mathcal{O}$ (within equilibrium) is defined as

$$\phi(t) = \frac{\langle\mathcal{O}[\mathrm{s}^{(t_0)}]\mathcal{O}[\mathrm{s}^{(t_0+t)}]\rangle - \langle\mathcal{O}\rangle^2}{\langle\mathcal{O}^2\rangle - \langle\mathcal{O}\rangle^2},$$

with the properties that $\phi(0)=1$, $\lim_{t\to\infty}\phi(t)=0$ and $\phi(t)$ decays monotonically with increasing time t. The long-time behavior of the normalized autocorrelation function is exponential, such that

$$\phi(t) \propto e^{-\frac{t}{\tau}}, \quad \text{for} \quad t\to\infty. \tag{C.18}$$

For the error analysis, the relevant quantity is the integrated autocorrelation time $\tau_\mathcal{O}$, given by

$$\frac{\tau_\mathcal{O}}{\delta t} = \sum_{t=1}^{\infty}\phi(t). \tag{C.19}$$

Note, that if the autocorrelation function was purely exponential $\phi(t)=e^{-t/\tau}$, we would obtain $\tau_\mathcal{O}=\tau$. Since $\phi(t)$ becomes noisy for $t\gg\tau_\mathcal{O}$, the sum in eq. (C.19) can behave badly for large t. Thus, the sum should be truncated self-consistently as the summation proceeds. In our case we truncate the sum at some upper limit $I_{\max}$, which is chosen to be the smallest integer such that

$$0.5+\sum_{t=1}^{I_{\max}}\phi(t) \le \frac{1}{6}I_{\max}. \tag{C.20}$$

C.5 Detailed balance and ergodicity

In order to ensure that a Monte Carlo algorithm converges to the correct equilibrium distribution, it is sufficient that the algorithm obeys ergodicity and detailed balance. Ergodicity means that all possible configurations which contribute to the partition function should theoretically be accessible within a finite number of Monte Carlo steps. This condition is necessary, since we must be able to take into account all possible contributions. Detailed balance means that

$$p[\mathrm{s}]w[\mathrm{s},\mathrm{s}'] = p[\mathrm{s}']w[\mathrm{s}',\mathrm{s}], \tag{C.21}$$

where $p[\mathrm{s}]$ is the probability for the system to be in configuration [s] (see for example eq. (C.4)), and $w[\mathrm{s},\mathrm{s}']$ is the transition probability to turn the configuration [s] into [s′]. The transition probability is normalized to

$$\sum_{[\mathrm{s}']} w[\mathrm{s},\mathrm{s}'] = 1, \tag{C.22}$$

since the algorithm necessarily turns a configuration [s] into some other configuration [s′]. In order to ensure that the algorithm converges towards the correct equilibrium distribution, we require that the distribution $p[\mathrm{s}]$ is an eigenvector of the transition matrix $w[\mathrm{s},\mathrm{s}']$ with eigenvalue 1

$$\sum_{[\mathrm{s}]} p[\mathrm{s}]w[\mathrm{s},\mathrm{s}'] = p[\mathrm{s}']. \tag{C.23}$$

Using the detailed balance condition (C.21), and the normalization of the transition probability we see that this requirement is fulfilled

$$\sum_{[\mathrm{s}]} p[\mathrm{s}]w[\mathrm{s},\mathrm{s}'] = \sum_{[\mathrm{s}]} p[\mathrm{s}']w[\mathrm{s}',\mathrm{s}] = p[\mathrm{s}']. \tag{C.24}$$

By using ergodicity one can show that such an eigenvector exists, is unique, and that the equilibrium distribution is therefore indeed approached asymptotically.

C.6 Metropolis algorithm for the quenched Schwinger model

The Metropolis algorithm is a simple algorithm, which is being used to sample the quenched Schwinger model. In this algorithm we construct a new gauge configuration [s′] based on the old one [s]. This is done by choosing a random spacetime point and direction $\tilde{n}, \tilde{\mu}$ and furnishing the corresponding gauge field with a random phase $e^{i\varphi}$, such that

$$\underbrace{\{U_{1,1+\hat{0}}, \ldots, U_{\tilde{n},\tilde{n}+\tilde{\mu}}, \ldots, U_{\Omega,\Omega+\hat{1}}\}}_{[s]} \to \underbrace{\{U_{1,1+\hat{0}}, \ldots, U_{\tilde{n},\tilde{n}+\tilde{\mu}} e^{i\varphi}, \ldots, U_{\Omega,\Omega+\hat{1}}\}}_{[s']}. \tag{C.25}$$

If the new configuration is energetically favorable, it is accepted which means that if

$$\Delta\mathcal{H} = \mathcal{H}[\mathrm{s}'] - \mathcal{H}[\mathrm{s}] < 0, \quad \text{then} \quad w[\mathrm{s}, \mathrm{s}'] = 1. \tag{C.26}$$

If the new energy is larger, we accept the new configuration with a certain probability

$$\Delta\mathcal{H} = \mathcal{H}[\mathrm{s}'] - \mathcal{H}[\mathrm{s}] > 0, \quad \text{then} \quad w[\mathrm{s}, \mathrm{s}'] = e^{-\beta\Delta\mathcal{H}}. \tag{C.27}$$

The algorithm is ergodic since every configuration of gauge fields is accessible with a non-vanishing probability. In order to show detailed balance consider the case where $\mathcal{H}[\mathrm{s}] - \mathcal{H}[\mathrm{s}'] > 0$, such that $\mathcal{H}[\mathrm{s}'] - \mathcal{H}[\mathrm{s}] < 0$ and $w[\mathrm{s}, \mathrm{s}'] = 1$. Then detailed balance is fulfilled since

$$p[\mathrm{s}']w[\mathrm{s}', \mathrm{s}] = \frac{e^{-\beta\mathcal{H}[\mathrm{s}']}}{Z(\beta)} e^{-\beta(\mathcal{H}[\mathrm{s}] - \mathcal{H}[\mathrm{s}'])} = p[\mathrm{s}] \cdot 1 = p[\mathrm{s}]w[\mathrm{s}, \mathrm{s}']. \tag{C.28}$$

C.7 Hybrid Monte Carlo methods

The Hybrid Monte Carlo method (HMC) is an alternative method for sampling lattice gauge theories. Compared to the Metropolis algorithm, the HMC method reduces correlations between subsequently sampled states by proposing moves to distant states which maintain a high probability of acceptance. This allows us to sample a big portion of configuration space with reduced autocorrelation effects. Due to its efficiency, the HMC is used for the sampling of the 2-flavour Schwinger model. The code we used for the sampling of the 2-flavour Schwinger model is publicly available and provided by Urbach et al. in Ref. [48]. The implementation of the HMC algorithm is quite complicated and a thorough discussion would be beyond the scope of this thesis. For more details about the HMC algorithm, the interested reader is referred to Ref. [24].

C.8 Sign problem

The Metropolis algorithm, but also the Hybrid Monte Carlo algorithm rely on positive Boltzmann weights. However, depending on the kind of simulations one is interested in, certain configurations might have a complex Boltzmann weight, which is known as the infamous "sign problem".

Sign problem in the quenched Schwinger model

Assume that we are interested in simulating the quenched (0-flavour) Schwinger model, with partition function given by eq. (C.3). Then the Boltzmann weight W_B, which is used for numerical simulations, is always strictly real and positive

$$W_B[N_f = 0] = e^{-S_g[U]} > 0, \tag{C.29}$$

which indicates the absence of the sign problem.

Sign problem in the 1-flavour Schwinger model

Let us examine the Boltzmann weight for the grand-canonical partition function of the 1-flavour Schwinger model, with quark chemical potential μ_q and Wilson Dirac operator $\mathbf{K}[U, \mu_q]$. The Euclidean action can then be written as

$$S_E[\bar{q}, q, U, \mu_q] = S_g[U] + \bar{q}.\mathbf{K}[U, \mu_q].q, \tag{C.30}$$

where q denotes the 2-component spinorfield for the quark q. After integrating out the quark fields using Grassmann integration rules, the Euclidean action is

$$S_E[U, \mu_q] = S_g[U] - \log(\det(\mathbf{K}[U, \mu_q])), \tag{C.31}$$

and the corresponding Boltzmann weight is given by

$$W_B[N_f = 1, \mu_q] = \det(\mathbf{K}[U, \mu_q]) e^{-S_g[U]}. \tag{C.32}$$

The known exponential factor is always strictly positive, but the determinant of the Wilson Dirac operator may become negative or even complex. In order to discuss that problematic factor, we first discuss the case for $\mu_q = 0$. For vanishing quark chemical potential the Wilson Dirac operator fulfills γ_5 hermiticity, that is

$$\gamma_5 . \mathbf{K}[U, \mu_q = 0] . \gamma_5 = \mathbf{K}[U, \mu_q = 0]^\dagger, \tag{C.33}$$

then since $\det \gamma_5 = 1$, one obtains

$$\det(\mathbf{K}[U, \mu_q = 0]) = \det(\mathbf{K}[U, \mu_q = 0]^\dagger) = \det(\mathbf{K}[U, \mu_q = 0])^\dagger. \tag{C.34}$$

We conclude that $\mathbf{K}[U, \mu_q = 0]$ always has a real determinant. However, to ensure positivity we need to be working in a regime where the quark masses are positive. Similar to the discussion in section 2.5 also for the 1-flavour Schwinger model with Wilson fermions the true quark mass is given by

$$m_q = Z_M (m_0 - m_{\text{crit}}), \tag{C.35}$$

where Z_M denotes a multiplicative renormalization factor and m_{crit} denotes an additive correction due to the use of Wilson fermions. If we approach the chiral limit $m_0 \to m_{\text{crit}}$ or work in a regime where $m_0 < m_{\text{crit}}$ the sign problem amplifies and simulations become impossible. However, if we work in a regime where the bare quark mass fulfills $m_0 \gg m_{\text{crit}}$ then the determinant of the Wilson Dirac operator is always positive and the sign problem is absent.

If we turn on the quark chemical quark potential $\mu_q \neq 0$, the γ_5 hermiticity is broken and the determinant gets a complex phase

$$\det(\mathbf{K}[U, \mu_q \neq 0]) = e^{i\varphi} |\det(\mathbf{K}[U, \mu_q \neq 0])|. \tag{C.36}$$

One way to remove this unwanted phase is by utilizing a generalized version of the γ_5 hermiticity, which reads

$$\gamma_5 . \mathbf{K}[U, \mu_q] . \gamma_5 = \mathbf{K}[U, -\mu_q^*]^\dagger. \tag{C.37}$$

This equation tells us, that if we complexify the chemical potential $\mu_q = i\tilde{\mu}_q$, with $\tilde{\mu} \in \mathbb{R}$, we obtain once again

$$\det(\mathbf{K}[U, i\tilde{\mu}_q]) = \det(\mathbf{K}[U, i\tilde{\mu}_q])^\dagger. \tag{C.38}$$

We conclude that complexifying the quark chemical potential yields a real determinant and therefore a real weight $W_B[N_f = 1, \mu_q = i\tilde{\mu}_q] \in \mathbb{R}$. However, we still need to choose the bare quark mass m_0 to be sufficiently large to avoid the sign problem.

Note, that we can also derive that $W_B[N_f = 1, \mu_q = i\tilde{\mu}_q]$ is real by using the canonical formalism. Consider the dimensionally reduced Wilson Dirac determinant with complexified quark chemical potential $\mu_q = i\tilde{\mu}_q$, that is

$$\det(\mathbf{K}[U, i\tilde{\mu}]) = \sum_{k=-L}^{L} e^{i\tilde{\mu} L_t k} \det_k(\mathbf{K}[U]). \tag{C.39}$$

The right-hand side of above equation is real due to the reflection symmetry of the canonical determinants,

$$\det_k^*(\mathbf{K}) = \det_{-k}(\mathbf{K}) \quad \forall k \in \{0, \ldots, L\} \tag{C.40}$$

which is shown in section G.4. Therefore also the determinant on the left-hand side, must be real.

We conclude that the Boltzmann weight of the 1-flavour Schwinger model can be constructed to be real and positive if we turn off the quark chemical potential ($\mu_q = 0$) and work with a suitable bare quark mass $m_0 \gg m_{\text{crit}}$.

Sign problem in the 2-flavour Schwinger model

In a final step, we consider the Boltzmann weight of the mass-degenerate 2-flavour Schwinger model with an up and down quark $\psi = (u, d)$, as introduced in section 2.2. We have an isospin chemical potential μ_I, which is related to the quark chemical potentials via $\mu_u = -\mu_d = \frac{\mu_I}{2}$. The Euclidean action decomposes similarly as in the 1-flavour case

$$S_E[\bar{\psi}, \psi, U, \mu_I] = S_g[U] + \bar{u}.\mathbf{K}[U, \mu_I].u + \bar{d}.\mathbf{K}[U, -\mu_I].d, \tag{C.41}$$

and after integrating out the quark fields we have

$$S_E[U, \mu_I] = S_g[U] - \log(\det(\mathbf{K}[U, \mu_I])) - \log(\det(\mathbf{K}[U, -\mu_I])). \tag{C.42}$$

Using relation (C.37), we can show that the Boltzmann weight is always strictly positive

$$W_B[N_f = 2, \mu_I] = e^{-S_g[U]} \det(\mathbf{K}[U, \mu_I]) \det(\mathbf{K}[U, -\mu_I]) \tag{C.43}$$

$$= e^{-S_g[U]} |\det(\mathbf{K}[U, \mu_I])|^2 \geq 0. \tag{C.44}$$

We conclude that the quenched Schwinger model (0 flavour) and the mass-degenerate 2-flavour Schwinger model (with $\mu_u = -\mu_d = \frac{\mu_I}{2}$) can be sampled without a sign problem. The 1-flavour Schwinger model on the other hand exhibits a sign problem, which is more difficult to handle. In this thesis, when working with the 1-flavour Schwinger model, we choose the input parameters in such a way, that the sign problem is absent.

C.9 Reweighting technique

Using Metropolis and Hybrid Monte Carlo (HMC) algorithms we are able to sample the partition functions of the quenched and the 2-flavour Schwinger model, respectively. However, we are interested in sampling the canonical partition functions with a fixed number of up and down quarks (n_u, n_d)

$$\mathcal{Z}_{(n_u,n_d)}(T) = \int \mathcal{D}U \, (\det_{n_u} \mathbf{K}[U]) \, (\det_{n_d} \mathbf{K}[U]) \, e^{-S_g[U]}, \tag{C.45}$$

with the Boltzmann weights

$$W_B[N_f = 2, n = (n_u, n_d)] = (\det_{n_u} \mathbf{K}[U]) \, (\det_{n_d} \mathbf{K}[U]) \, e^{-S_g[U]}. \tag{C.46}$$

The computation of those canonical weights requires the dimensional reduction of the Wilson Dirac determinant discussed in section 3.3, which is very time-consuming and therefore not practical for numerical simulations.

An alternative method is the so-called reweighting technique, which is a standard tool in Monte Carlo approaches. The rough idea of reweighting is to access a certain part of configuration space characterized by some input parameters $\mathcal{P}'$ from an ensemble of configurations which has been created with some different input parameters $\mathcal{P}$. These Input parameters may be very general such as the number of flavours, the coupling β, the bare mass m_0, etc. Let us discuss a concrete example of how we can use this reweighting technique to make measurements with respect to canonical sectors.

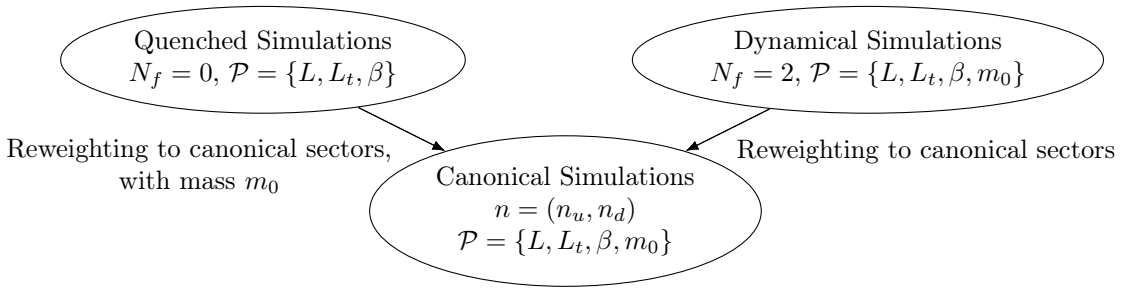

Figure C.1: Reweighting onto canonical sectors from quenched and dynamical simulations. Note that we set $\mu_I = 0$ in both cases.

Assume that we are interested in measuring an observable $\mathcal{O}$ of the 2-flavour Schwinger model in the fixed canonical sector with n_u up and n_d down quarks (n_u, n_d). By using the canonical partition function in eq. (C.45) statistical mechanics tell us that the expectation value for the observable $\mathcal{O}$ reads

$$\langle \mathcal{O} \rangle_{(n_u,n_d)} = \frac{\int \mathcal{D}U \cdot \mathcal{O} \cdot (\det_{n_u} \mathbf{K}[U]) \, (\det_{n_d} \mathbf{K}[U]) \, e^{-S_g[U]}}{\int \mathcal{D}U \, (\det_{n_u} \mathbf{K}[U]) \, (\det_{n_d} \mathbf{K}[U]) \, e^{-S_g[U]}} \tag{C.47}$$

$$= \frac{1}{\mathcal{Z}_{(n_u,n_d)}(T)} \int \mathcal{D}U \cdot \mathcal{O} \cdot (\det_{n_u} \mathbf{K}[U]) \, (\det_{n_d} \mathbf{K}[U]) \, e^{-S_g[U]}. \tag{C.48}$$

After introducing the following abbreviations for the reweighting factors

$$\mathcal{R}[N_f = 0] = (\det_{n_u} \mathbf{K}[U]) \, (\det_{n_d} \mathbf{K}[U]) \quad \text{and} \quad \mathcal{R}[N_f = 2] = \left(\frac{\det_{n_u} \mathbf{K}[U] \det_{n_d} \mathbf{K}[U]}{|\det(\mathbf{K}[U, \mu_I])|^2} \right), \tag{C.49}$$

we can derive these intriguingly simple relations, which are the reweighting formulas used in this thesis

$$\langle \mathcal{O} \rangle_{(n_u,n_d)} = \frac{\langle \mathcal{O}\mathcal{R}[N_f = 0] \rangle_{N_f=0}}{\langle \mathcal{R}[N_f = 0] \rangle_{N_f=0}} \tag{C.50}$$

$$= \frac{\langle \mathcal{O}\mathcal{R}[N_f = 2] \rangle_{N_f=2}}{\langle \mathcal{R}[N_f = 2] \rangle_{N_f=2}}. \tag{C.51}$$

The first equation can be used to reweight from quenched simulations onto canonical sectors of the 2-flavour Schwinger model, with n_u up and n_d down quarks. The second one can be used to reweight from the dynamical 2-flavour simulations onto canonical sectors with n_u up and n_d down quarks.

This result indicates that we can make "measurements" with respect to canonical sectors, by using configurations from quenched and 2-flavour simulations, respectively.

Dangers of reweighting

Although the reweighting formulas derived in eqs. (C.50) and (C.51) are mathematically correct, they do not show the full picture and there are some pitfalls one has to respect. This can be understood by making some simple thought experiments. Consider an ensemble of configurations which has been created from quenched simulations, i.e. with zero fermion-content, and assume that we want to measure some observable $\langle \mathcal{O} \rangle_{(n_u,n_d)}$ with respect to the canonical sector (n_u, n_d). The quenched simulations cover a certain subset of configuration space, that is, the subset of configuration space, where the quenched Boltzmann weight $W_B[N_f = 0]$ is dominant. However, for the measurements of $\langle \mathcal{O} \rangle_{(n_u,n_d)}$ we would like to cover the part of configuration space where the Boltzmann weight for the canonical sectors in the 2-flavour Schwinger model $W_B[N_f = 2, n = (n_u, n_d)]$ is predominant. In general, those two subsets are not overlapping, which means that we are basically "extrapolating" from one subset of configuration space to another one using the reweighting formulas. This idea can be prone to systematical errors and is well-known as the so-called overlap problem [58]. In order to apply reweighting techniques successfully, it is important that the configuration space covered by the original simulations is overlapping as much as possible with the target configuration space.

D Matrix formulas

Here we review some basic formulas needed throughout this thesis without giving any proofs. The interested reader is referred to Horn and Johnson in Ref. [51].

D.1 Partitions of matrices

Let $A \in \mathrm{Mat}(m \times n, \mathbb{C})$ be a $m \times n$-dimensional matrix and $I \subseteq \{1, \ldots, m\}, J \subseteq \{1, \ldots, n\}$ be two sets of index sets. Then we define

$$A^{IJ}, \tag{D.1}$$

to be the submatrix of entries that lie in the rows indexed by I and in columns indexed by J. Consider the following examples

$$A^{IJ} = A_{ij}, \qquad \text{for } I = \{i\}, J = \{j\} \tag{D.2}$$
$$A^{IJ} = \emptyset, \qquad \text{for } I = J = \emptyset \tag{D.3}$$
$$A^{IJ} = A, \qquad \text{for } I = \{1, \ldots, m\}, J = \{1, \ldots, n\}. \tag{D.4}$$

similarly one can also define define a submatrix

$$A^{I\not{J}}, \tag{D.5}$$

which now denotes the submatrix one obtains after deleting all the rows in I and all the columns in J. As a non-trivial example consider

$$A = \begin{pmatrix} a & b & c \\ d & e & f \end{pmatrix}, \quad \text{with} \quad I = \{1\} \quad \text{and} \quad J = \{2, 3\}. \tag{D.6}$$

Then

$$A^{IJ} = \begin{pmatrix} b & c \end{pmatrix}, \quad \text{and} \quad A^{I\not{J}} = \begin{pmatrix} d \end{pmatrix} = d. \tag{D.7}$$

Throughout this thesis, we will be working exclusively with quadratic matrices and with *principal* submatrices. A principal submatrix is a quadratic submatrix A^{IJ} where the two index sets, denoting the selected rows and columns, are equal $J = I$. For a quadratic matrix $A \in \mathrm{Mat}(n, \mathbb{C})$ one has $\binom{n}{k}$, distinct principal submatrices of size $(k \times k)$. The determinant of such a quadratic principal submatrix is called principal minor of size k and denoted by

$$\det(A^{II}), \quad \text{with} \quad |I| = k. \tag{D.8}$$

By convention, the empty principal minor is just one 1, that is $\det A^{\emptyset\emptyset} = 1$. One can also take the sum of all $\binom{n}{k}$ principal minors, which then leads to the following two definitions and a resulting theorem.

Definition: Sum of all principal minors

Let $A \in \mathrm{Mat}(n, \mathbb{C})$, then the sum of all principal minors of size $|I| = k$ is denoted by $E_k(A)$, such that

$$E_k(A) := \sum_{I, |I|=k} \det(A^{II}). \tag{D.9}$$

We mention, once again, that the number of principal minors is given by $\binom{n}{k}$. Note, that for the trivial cases $k = 0, 1, n$ one obtains

$$E_0(A) = 1, \tag{D.10}$$
$$E_1(A) = \mathrm{Tr}[A], \tag{D.11}$$
$$E_n(A) = \det(A). \tag{D.12}$$

Definition: Symmetric functions

Let $\{\lambda_1, \ldots, \lambda_n\}$ be a set of arbitrary complex numbers, then the k'th elementary symmetric function reads

$$S_k(\lambda_1, \ldots, \lambda_n) = \sum_{1 \leq i_1 \leq \cdots \leq i_k \leq n} \prod_{j=1}^{k} \lambda_{i_j}. \tag{D.13}$$

Note that the sum has $\binom{n}{k}$ summands as well. Next consider some $A \in \mathrm{Mat}(n, \mathbb{C})$ and assume that the eigenvalue-spectrum of A is given by $\sigma(A) = \{\lambda_1, \ldots, \lambda_n\}$, then we define $S_k(A) = S_k(\lambda_1 \ldots, \lambda_n)$.

Theorem: Equivalence of $E_k(A)$ and $S_k(A)$

Let $A \in \mathrm{Mat}(n, \mathbb{C})$. Then $E_k(A) = S_k(A)$ for all $k \in \{1, \ldots n\}$.

The previous theorem will be of great use throughout this thesis, since it allows us to make statements about the sum of principal minors, while utilizing properties of the eigenvalue spectrum. The proof is given in Ref. [51].

D.2 Schur complements and determinantal formulae

Let $M \in \mathrm{Mat}(n, \mathbb{C})$ and suppose that $I \subseteq \{1, \ldots, n\}$ is an index set, such that M^{II} is non-singular (and therefore invertible). For the sake of simplicity we define

$$A = M^{II}, \quad B = M^{I\dot{I}}, \quad C = M^{\dot{I}I} \quad \text{and} \quad D = M^{\dot{I}\dot{I}}, \tag{D.14}$$

such that the matrix M can be written in blockform

$$M = \begin{pmatrix} A & B \\ C & D \end{pmatrix}. \tag{D.15}$$

Upon further investigation we see that M can be written as

$$M = \begin{pmatrix} 1 & 0 \\ CA^{-1} & 1 \end{pmatrix} \begin{pmatrix} A & 0 \\ 0 & D - CA^{-1}B \end{pmatrix} \begin{pmatrix} 1 & A^{-1}B \\ 0 & 1 \end{pmatrix}, \tag{D.16}$$

where $D - CA^{-1}B$ denotes the so-called Schur complement. Following this observation we see that the determinant of M can be written as

$$\det M = (\det A) \det(D - CA^{-1}B). \tag{D.17}$$

D.3 Characteristic polynomial

Let $A \in \mathrm{Mat}(n, \mathbb{C})$, $\lambda \in \mathbb{C}$ a scalar and $x \in \mathbb{C}^n$ an non-zero n-dimensional vector. If A, λ and x satisfy the following equation

$$Ax = \lambda x, \tag{D.18}$$

then λ is called an eigenvector of A and x is called an eigenvector of A associated with λ. The set of all eigenvalues of A is called spectrum and denoted by $\sigma(A)$. We rewrite the eigenvalue equation such that

$$(\lambda \mathbb{1} - A)x = 0, \quad \text{for} \quad x \neq 0. \tag{D.19}$$

Thus, $\lambda \in \sigma(A)$ if and only if $\lambda \mathbb{1} - A$ is singular, i.e. $\det(\lambda \mathbb{1} - A) = 0$. Therefore the formal definition of the spectrum is given by

$$\sigma(A) = \{\lambda \in \mathbb{C} : \det(\lambda \mathbb{1} - A) = 0\}. \tag{D.20}$$

The characteristic polynomial for the matrix A is defined as

$$p_A(t) = \det(t \mathbb{1} - A), \tag{D.21}$$

and the characteristic equation is given by

$$p_A(t) = 0. \tag{D.22}$$

The characteristic polynomial $p_A(t)$ has degree n and fulfills the characteristic equation if and only if $t \in \sigma(A)$. We can derive every coefficient of $p_A(t)$, however, the computations are somewhat involved and require a lot of buildup. The interested reader is again referred to Horn in Ref. [51], here we just present the result. One can show that in the end, the expression for the characteristic polynomial $p_A(t)$ is given by

$$\begin{aligned} p_A(t) = \det(t\mathbb{1} - A) &= t^n + (-1)^1 E_1(A) t^{n-1} + \cdots + (-1)^{n-1} E_{n-1}(A) t + (-1)^n E_n(A) && \text{(D.23)} \\ &= t^n + (-1)^1 S_1(A) t^{n-1} + \cdots + (-1)^{n-1} S_{n-1}(A) t + (-1)^n S_n(A), && \text{(D.24)} \end{aligned}$$

where we used the equivalence of $E_k(A) = S_k(A)$ in the last step.

E Computation canonical determinants

In this chapter we discuss the computation of the canonical determinants in detail. As such, this chapter is a direct follow-up to section (3.3). We work with a lattice of extent $L \times L_t$ and set the lattice spacing to one, i.e. $a = 1$. After having discussed the derivation of the reduced matrix, we are now able to compute the determinant of the Wilson Dirac operator using the fugacity expansion (eq. (3.58))

$$\det(\mathbf{K}[U, \mu_q]) = \sum_{k=-L}^{L} e^{\mu_q L_t k} \det{}_k(\mathbf{K}[U]) \tag{E.1}$$

for any quark chemical potential, provided we have an efficient method of calculating the canonical determinants (eq. (3.59)), that is

$$\det{}_k(\mathbf{K}[U]) = \left(\prod_{i=1}^{L_t} |B_i||2\kappa U_i^\dagger| \right) \sum_{I,|I|=k+L} \det(\mathcal{T}^{II}), \quad \forall k \in \{-L, \ldots, L\}. \tag{E.2}$$

The computation of the bulkfactor $\prod_{i=1}^{L_t} |B_i||2\kappa U_i^\dagger|$ is straightforward and does not require any special treatment. However, the construction of the full transfer matrix and the summation over the principal minors thereof require some discussion. For this chapter we set the quark chemical potential to zero $\mu_q = 0$, such that the full transfer matrix can be written as

$$\mathcal{T} = \prod_{i=1}^{L_t} T_i. \tag{E.3}$$

The full transfer matrix $\mathcal{T}$ is of size $(2L)^2$, the precise form of the time-slice transfer matrices T_i is not relevant for the following discussion.

E.1 Construction of the transfer matrix $\mathcal{T}$

Numerical inaccuracy is one of the problems we face when computing canonical determinants. The problems already arise when constructing the full transfer matrix via eq. (E.3). Thankfully, we have analytical results which allow us to verify whether the constructed transfer matrix $\mathcal{T}$ is sufficiently precise or not. For example, one could test whether the symmetry of the eigenvalues ($\lambda \in \sigma(\mathcal{T}) \implies \frac{1}{\lambda^*} \in \sigma(\mathcal{T})$) is fulfilled as described in subsection (3.3.5). However, since we are interested in calculating the canonical determinants, the easiest way to test the accuracy is to see whether we retain the reflection symmetry mentioned in eq. (3.77) and proven in section G.4, that is

$$\det{}_k^*(\mathbf{K}) = \det{}_{-k}(\mathbf{K}) \quad \forall k \in \{0, \ldots, L\}. \tag{E.4}$$

We worked out that double precision is sufficient to construct a transfer matrix $\mathcal{T}$ built up from $L_t \approx 30$ time-slice transfer matrices T_i without losing any significant information. However, in order to extrapolate to zero temperature ($T \to 0 \Leftrightarrow L_t \to \infty$), we need to reach higher values of L_t. This means that we need to add more time-slices to the lattice and thus add more components T_i to the final transfer matrix $\mathcal{T}$. However, this procedure renders the full transfer matrix $\mathcal{T}$ numerically unstable. In order to perform these numerically challenging tasks, we utilize a multi-precision library by Bailey [59], which allows us to convert a transfer matrix T_i to a multi-precision object

$$T_i \to (T_i)_{MP}. \tag{E.5}$$

These multi-precision objects $(T_i)_{MP}$ can be multiplied together without loosing any accuracy, allowing us to perform the delicate task of constructing the full transfer matrix

$$\mathcal{T}_{MP} = \prod_{i=1}^{L_t} (T_i)_{MP} \tag{E.6}$$

without loosing any information. We also use multi-precision routines to compute eigenvalues and canonical determinants, yielding numerical results which retain all the expected symmetries.

E.2 Extensive numbers of principal minors

The summation over all principal minors of a canonical sector is quite trivial if one is interested only in the case of "extreme" quark numbers, i.e. a system which is either saturated by quarks or by antiquarks. In both cases there exists only one principal minor. For saturation with antiquarks ($k = -L$) the corresponding index set is given by $I = \varnothing$, if we have saturation with quarks ($k = L$), the index set is given by $I = \{1, 2, \ldots, 2L\}$. We easily obtain the results which we already discussed in subsection 3.4.1 and 3.4.2, that is

$$\det\nolimits_{-L}(\mathbf{K}) = \prod_{i=1}^{L_t} |B_i||2\kappa U_i^\dagger| \cdot 1, \qquad \text{for } I = \varnothing, \text{ and} \tag{E.7}$$

$$\det\nolimits_{L}(\mathbf{K}) = \prod_{i=1}^{L_t} |B_i||2\kappa U_i^\dagger| \cdot \det(\mathcal{T}), \qquad \text{for } I = \{1, 2, \ldots, 2L\}. \tag{E.8}$$

In order to have a look at an arbitrary canonical sector one fixes the net-quark number to some $k \in \{-L, \ldots, L\}$ and considers the number of possible principal minors $\mathcal{T}^{II}$, with index set I of size $|I| = k+L$. The total number of index sets - and therefore principal minors - shall be denoted by $\mathcal{N}(\mathcal{T}^{II})$. Since the transfer matrix $\mathcal{T}$ is of size $(2L)^2$ we have a total of $2L$ possible indices we can choose from, s.t. $I \subseteq \{1, 2, \ldots, 2L\}$. As a results computing the number of principal minors for each canonical sector is a simple combinatorial task

$$\begin{aligned}
&k = -L && |I| = 0 && \mathcal{N}(\mathcal{T}^{II}) = \binom{2L}{0} = 1,\\
&k = -L+1 && |I| = 1 && \mathcal{N}(\mathcal{T}^{II}) = \binom{2L}{1} = L,\\
&\vdots && \vdots && \vdots\\
&k = 0 && |I| = L && \mathcal{N}(\mathcal{T}^{II}) = \binom{2L}{L},\\
&\vdots && \vdots && \vdots\\
&k = L-1 && |I| = 2L-1 && \mathcal{N}(\mathcal{T}^{II}) = \binom{2L}{2L-1} = L,\\
&k = L && |I| = 2L && \mathcal{N}(\mathcal{T}^{II}) = \binom{2L}{2L} = 1,
\end{aligned}$$

which also includes the two extreme cases discussed before. Note that the sectors which are the most interesting for our calculations are the ones close to quark number $k = 0$, unfortunately these are exactly the ones which require the biggest computational effort. Even for a relative small lattice of volume $L = 8$, the canonical sector $\det_0(\mathbf{K})$ requires the computation of $\binom{16}{8} = 12870$ principal minors. This means that for each principal minor the determinant of an 8×8-matrix needs to be evaluated and summed over. Not only is this task very time-consuming (especially for increasing volumes), but it is also prone to numerical errors. The principal minors can differ from each other by several orders of magnitude, which makes their summation very delicate, especially if only double precision is used. In order to circumvent these problems we suggest an alternative way of calculating the canonical determinants by using the spectrum of the transfer matrix $\sigma(\mathcal{T})$.

E.3 Calculation of the projected determinants

Let us reconsider the expansion in eq. (3.52), that is

$$|\mathbf{K}| \propto e^{\mu_q L_t L} |e^{-\mu_q L_t} + \mathcal{T}|, \tag{E.9}$$

where we omitted the bulkfactor for the sake of simplicity. First we diagonalize the transfer matrix such that

$$\mathcal{T} = D \Lambda D^{-1}, \quad \text{with} \quad \Lambda = \mathrm{diag}[\lambda_1, \ldots, \lambda_{2L}]. \tag{E.10}$$

This allows us to rewrite the determinant of the Wilson Dirac operator as

$$|\mathbf{K}| \propto e^{\mu_q L_t L} |e^{-\mu_q L_t} + \Lambda|, \tag{E.11}$$

which leads to an expansion in $t = e^{-\mu_q L_t}$, such that

$$|\mathbf{K}| \propto t^{-L} \prod_{i=1}^{2L} (t + \lambda_i) = t^{-L} \sum_{k=0}^{2L} c_k t^k = \sum_{k=-L}^{L} c_{k+L} t^k. \tag{E.12}$$

In above equation the c_k's are the coefficients of the expansion and the λ_i belong to the spectrum of $\mathcal{T}$, i.e. $\lambda_i \in \sigma(\mathcal{T})$. After comparing this result to the fugacity expansion in eq. (3.58), it becomes evident that the coefficients are directly related to the canonical determinants. One identifies

$$\begin{aligned} \det\nolimits_{-L}(\mathbf{K}) &\propto c_{2L}, \\ \det\nolimits_{-L+1}(\mathbf{K}) &\propto c_{2L-1}, \\ &\vdots \\ \det\nolimits_{L-1}(\mathbf{K}) &\propto c_1, \\ \det\nolimits_{L}(\mathbf{K}) &\propto c_0. \end{aligned}$$

Some coefficients can be computed easily, for instance $c_0 = \prod_{i=1}^{2L} \lambda_i = \det(\mathcal{T})$ or $c_{2L} = 1$. All other coefficients can be computed recursively by using the partial product defined by

$$\Pi_n(t) = \prod_{i \leq n} (t + \lambda_i) = \sum_{k \leq n} c_k^{(n)} t^k. \tag{E.13}$$

After identifying

$$\Pi_{n+1}(t) = (t + \lambda_{n+1}) \Pi_n(t), \tag{E.14}$$

we obtain a recursive relation for the coefficients

$$\sum_{k \leq n+1} c_k^{(n+1)} t^k = \sum_{k \leq n} c_k^{(n)} t^{k+1} + \lambda_{n+1} \sum_{k \leq n} c_k^{(n)} t^k \tag{E.15}$$

$$\Leftrightarrow c_k^{(n+1)} = c_{k-1}^{(n)} + \lambda_{n+1} c_k^{(n)}, \tag{E.16}$$

for all $0 \leq k \leq n+1$ (we set $c_{-1} = 0$). In order to start we need to calculate $c^{(0)}$, however, a quick look at our definition of $\Pi_0(t)$ tells us that $c_k^{(0)} = 0$ for all $k \in \{1, \ldots, 2L\}$ except for $c_0^{(0)} = 1$.

Starting from $c_k^{(0)}$ we can recursively compute $c_k^{(n+1)}$ from $c_k^{(n)}$ and after $2L$ steps we obtain the desired coefficients $c_k = c_k^{(2L)}$. This method allows us to compute the canonical determinants in a much more efficient way.

Suppose we are interested in the computation of the canonical determinant $\det_0(\mathbf{K})$. Computation of all the principal minors would leave us with the construction of $\binom{2L}{L}$ matrices and the computation of the determinants thereof. Using the formulas presented here, we require only the computation of the $2L$ eigenvalues of $\mathcal{T}$ and some small manageable manipulations thereof. Unfortunately, the eigenvalues can differ several orders of magnitude, meaning that also here multi-precision tools are required. These multi-precision tools are provided by Bailey, see Ref. [59].

F Bayesian theory

After doing experiments one has to perform data analysis to extract the needed physical quantities from the measurements. One part of this analysis concerns statistical modelling, where we take the data and perform a least-squares fit to some physically motivated model. However, this procedure can be quite tricky, since the precise form of the fit model might not always be clear. Bayesian model averaging can be used to extract quantities of a physically motivated model given the measured data, by taking into account the possible fit models at hand and averaging over them.

Let us consider an example, where this problem can be made more evident. Assume that we measured the 1-pion correlator $C_2(t)$ for different times t and we want to extract the pion mass m_π. The full model, expected to describe those correlations, involves an infinite tower of exponentials[1]

$$C_2(t) \propto \sum_{k=0}^{\infty} A_k e^{-E_\pi^{(k)} t}, \tag{F.1}$$

where the A_k's and the energies $E_\pi^{(k)}$'s denote fit parameters. Furthermore, the parameter $E_\pi^{(0)} = m_\pi$ denotes the desired pion mass, while the $E_\pi^{(k)}$'s $k \geq 1$ denote the energies of excited 1-pion states. In practice one picks up the first dominant term (model truncation) and a minimum value for the time t_{min} below which the data is simply ignored (data truncation). Then one proceeds to fit

$$C_2(t) \propto A_0 e^{-m_\pi t}, \quad \text{for} \quad t \geq t_{min}, \tag{F.2}$$

to determine the desired pion mass m_π. This example illustrates perfectly, the ambiguity which arises when performing this kind of data analysis. On one side, one can add additional correction terms to the fit model, without worsening the quality of the fits and on the other hand, there is no precise prescription on how to determine t_{min}. Note, that choosing the appropriate fit domain of the data can also be interpreted as a model selection problem.

Consequently, there is no clear prescription on how to perform these fits in detail, which introduces a kind of unsatisfactory ambiguity. In the end, one is only interested in the pion mass, regardless of truncation parameter t_{min} or the number of correction terms involved in the fit model. From the Bayesian perspective, this problem can be solved by using model averaging methods, which allow us to obtain a probability-weighted average over all potential models and a reasonable error estimation thereof. In this chapter we review some basic concepts of Bayesian theory. For a more elaborate discussion of Bayesian theory, we refer to Sivia in Ref. [60, 61]. Most results we use are motivated by the work of Jay and Neil, for proofs and more details see Refs. [62] and [63].

F.1 Introduction

Assume the following set-up, where we have a set of data $\mathbf{D}$ and N different models $\{M_1, M_2, \dots M_N\}$ which can be used to describe the data. More specifically, we consider the case where all models are an extension of a base model M_1. The base model M_1 describes the data with the smallest number of parameters $\mathbf{a}_0$, all other available models $\{M_2, \dots M_N\}$ are an extension thereof and might include additional parameters $\mathbf{a}_i = (\mathbf{a}_0, \mathbf{a}_{m_i})$. The extended models usually take into account higher order correction terms.

If we revisit the previous example the base model could be given by

$$M_1(A_0, m_\pi) = A_0 e^{-m_\pi t} \tag{F.3}$$

and an extension thereof would be given by

$$M_2(A_0, A_1, m_\pi, E_\pi^{(1)}) = A_0 e^{-m_\pi t} + A_1 e^{-E_\pi^{(1)} t}. \tag{F.4}$$

[1] Note, that here we omit periodic effects on the lattice, for the sake of simplicity.

To obtain the marginalized probabilities for the common parameters, we marginalize over all models, including their additional parameters. As a result we obtain a model-independent posteriori distribution for the desired parameters $\mathbf{a}_0$ given the data $\mathbf{D}$

$$pr(\mathbf{a}_0|\mathbf{D}) = \sum_{i=1}^{N} \int \mathrm{d}\mathbf{a}_{m_i} \frac{pr(\mathbf{D}|\mathbf{a}_i, M_i) pr(\mathbf{a}_i|M_i)}{pr(\mathbf{D})}. \tag{F.5}$$

The posteriori distribution $pr(\mathbf{a}_0|\mathbf{D})$ has all the relevant information needed to make statements about the parameters $\mathbf{a}_0$. Any expectation value of some well-behaved function can be written in the standard way as

$$\langle f(\mathbf{a}_0)\rangle = \int \mathrm{d}\mathbf{a}_0 f(\mathbf{a}_0) pr(\mathbf{a}_0|\mathbf{D}). \tag{F.6}$$

It is also instructive to see that one can write the model-independent expectation value $\langle f(\mathbf{a}_0)\rangle$ as a weighted sum over all individual "model-fixed" expectation values $\langle f(\mathbf{a}_0)\rangle_i$, such that

$$\langle f(\mathbf{a}_0)\rangle = \sum_{i=1}^{N} \langle f(\mathbf{a}_0)\rangle_i \cdot pr(M_i|\mathbf{D}), \tag{F.7}$$

where $\langle f(\mathbf{a}_0)\rangle_i$ is given by

$$\langle f(\mathbf{a}_0)\rangle_i = \int \mathrm{d}\mathbf{a}_0 f(\mathbf{a}_0) pr(\mathbf{a}_0|M_i, \mathbf{D}) \tag{F.8}$$

and $pr(M_i|\mathbf{D})$ are model weights, which are normalized such that

$$\sum_{i=1}^{N} pr(M_i|\mathbf{D}) = 1. \tag{F.9}$$

F.2 Estimation of model parameters

As a specific example, to illustrate how to extract the model parameters, we consider a base model with only a single parameter a_0. Using eq. (F.7) we can write down the best estimate for a_0, which is given by the model average

$$\langle a_0\rangle = \sum_{i=1}^{N} \langle a_0\rangle_i \cdot pr(M_i|\mathbf{D}). \tag{F.10}$$

An estimate for the uncertainty is given by the variance

$$\begin{aligned}
\sigma_{a_0}^2 &= \langle a_0^2\rangle - \langle a_0\rangle^2 && \text{(F.11)}\\
&= \sum_{i=1}^{N} \langle a_0^2\rangle pr(M_i|\mathbf{D}) - \langle a_0\rangle^2 && \text{(F.12)}\\
&= \sum_{i=1}^{N} \sigma_{a_0,i}^2 pr(M_i|\mathbf{D}) + \sum_{i=1}^{N} \langle a_0\rangle^2 pr(M_i|\mathbf{D}) - \langle a_0\rangle^2 && \text{(F.13)}\\
&= \sum_{i=1}^{N} \sigma_{a_0,i}^2 pr(M_i|\mathbf{D}) + \sum_{i=1}^{N} (\langle a_0\rangle_i - \langle a_0\rangle)^2 pr(M_i|\mathbf{D}), && \text{(F.14)}
\end{aligned}$$

where $\sigma_{a_0,i}^2$ denotes the variance of a_0 in the model M_i. We can see, that the variance can be decomposed into two contributions. The first contribution can be interpreted as a statistical error, while the second term can be interpreted as a systematical one, such that $\sigma_{a_0}^2 = \sigma_{\mathrm{stat}}^2 + \sigma_{\mathrm{sys}}^2$, with

$$\sigma_{\mathrm{stat}}^2 = \sum_{i=1}^{N} \sigma_{a_0,i}^2 pr(M_i|\mathbf{D}) \quad \text{and} \quad \sigma_{\mathrm{sys}}^2 = \sum_{i=1}^{N} (\langle a_0\rangle_i - \langle a_0\rangle)^2 pr(M_i|\mathbf{D}). \tag{F.15}$$

Our inference about the parameter a_0 is therefore summarized in the statement

$$a_0 = \langle a_0\rangle \pm \sigma_{a_0}. \tag{F.16}$$

F.3 Model weights for least-square problem

The goal of this section is to discuss the model weight

$$pr(M_i|\mathbf{D}), \tag{F.17}$$

in the context of a least-squares fitting problem. Suppose that our dataset $\mathbf{D}$ consists of d data points characterized by their x and y values

$$(x_1, y_1), (x_2, y_2), \ldots, (x_d, y_d), \tag{F.18}$$

where we summarize the x- and y-values in vectors denoted by $\mathbf{x}$ and $\mathbf{y}$, respectively. The covariance between the measurements shall be described by a covariance matrix $\Sigma \in \mathbb{R}^{d\times d}$. Throughout this section we will be working with a single model M_i, which shall be characterized by its fit function $M_i = M_i(x, \mathbf{a}_i)$ with parameters $\mathbf{a}_i$ and domain $\mathbf{D}$. For the start, we assume that the model M_i takes the full range of data points into account $\mathbf{D}_i = \mathbf{D}$.

The complete derivation of the model weight is very tedious, here we simply discuss the results derived by Jay and Neil in Ref. [62]. After a lengthy calculation one can show that the model weight can be written as

$$pr(M_i|\mathbf{D}) \propto e^{-\frac{GAP_i}{2}}, \tag{F.19}$$

where GAP_i denotes the so called "Gaussian approximate posterior" for the model M_i, given by

$$GAP_i \propto -2\log(pr(M_i|\mathbf{D})) \tag{F.20}$$

$$\propto -2\log(pr(M_i)) + \chi^2_T(\mathbf{a}^*_i) + (\log(\det\tilde{\Sigma}) - \log(\det\Sigma^*)) + 2\,\mathrm{Tr}[J_N^{-1} I_N]. \tag{F.21}$$

Since we skipped the derivation, the terms in the above expression need to be explained. The first term $pr(M_i)$ quantifies our prior preference for a model M_i and the second term is the augmented chi-squared value evaluated at the best fit parameter $\mathbf{a}^*_i$. In our computations we do not discriminate against any model and ignore the contribution coming from $pr(M_i)$. In this work we also do not implement any priors for the fit parameters. As a result the augmented chi-squared is given by the "normal" chi-squared value, one obtains when performing a least squares fit

$$\chi^2_T(\mathbf{a}_i) = \chi^2_0(\mathbf{a}_i) = (\mathbf{y} - M_i(\mathbf{x}, \mathbf{a}_i))^T . \Sigma^{-1} . (\mathbf{y} - M_i(\mathbf{x}, \mathbf{a}_i)), \tag{F.22}$$

where $\mathbf{x} = (x_1, \ldots, x_d)$ and $\mathbf{y} = (y_1, \ldots, y_d)$.

The next two terms are given by the covariance matrix of the fit parameters $\tilde{\Sigma}$ and the best-fit covariance matrix Σ^* related to Σ. The remaining contribution $\mathrm{Tr}[J_N^{-1} I_N]$ is a bias-correction term.

The last three terms for GAP_i are quite tedious to work with, however, in the limit of large sample size $d \to \infty$ they can be simplified. By using a cross-validation argument one can show that in the limit $d \to \infty$, the quantity $(\log(\det\tilde{\Sigma}) - \log(\det\Sigma^*))$ is a correction which behaves like $1/d$. The bias-correction term reduces to a factor $2k$, where k denotes the number of fit parameters for the model M_i. This leads to the so-called Akaike information criterion (AIC) given by

$$GAP_i \xrightarrow{d\to\infty} AIC_i = -2\log(pr(M_i)) + \chi^2_T(\mathbf{a}^*_i) + 2k. \tag{F.23}$$

This result requires some correction in case one does not only vary the fit function but also the domain $\mathbf{D}$ thereof. Following the discussion at the beginning of this chapter, we want to consider cases where we restrict the fit ranges and omit data points. The number of ignored data points will be denoted by N_{cut}. Following the construction of Jay and Neil in Ref. [62] the Akaike-Information Criterion receives an additional term such that

$$AIC_i = -2\log(pr(M_i)) + \chi^2_T(\mathbf{a}^*_i) + 2k + 2N_{cut}, \tag{F.24}$$

where $\chi^2_T(\mathbf{a}^*_i)$ is minimized and evaluated only for data which remains after the truncation. In the end the model weight $pr(M_i|\mathbf{D})$ reads

$$pr(M_i|\mathbf{D}) \propto e^{-\frac{AIC_i}{2}}. \tag{F.25}$$

By constructing the model weight in such a manner we naturally encompass the principle of Ockham's razor[2]. Models which describe the data badly have a large χ^2_T and are penalized for that, on the other side models with a large number of parameters or small number of data points ('overfitting') are penalized by a factor $2k$ or $2N_{cut}$, respectively.

[2] 'Frustra fit per plura quod potest fieri per pauciora', or in English it is vain to do with more what can be done with fever.

F.4 Systematic averaging

Sometimes the model averaging based on the AIC fails, in that case one could use a systematic averaging scheme. Here we illustrate this scheme with the extraction of a single parameter a_0.

We know that different models yield different estimates and variances for the desired parameter a_0

$$\langle a_0 \rangle_i \pm \sigma_{a_0,i}, \qquad \text{for } i = 1, \ldots, N, \tag{F.26}$$

where N denotes the number of models. By using the formulas presented in section F.2, we can process the results for the parameter a_0 into a single model-independent result

$$\langle a_0 \rangle \pm \sigma_{a_0}, \tag{F.27}$$

which represents our inference about the parameter a_0. This is the quint-essence of the Bayesian model averaging procedure, however, this procedure might fail in certain cases. We have made the experience that Bayesian model averaging fails if we have very noisy data in combination with vastly different models. In such cases, one would ideally investigate the Gaussian approximate posterior (GAP) and come up with a different information criterion (instead of the AIC one), which is more conservative and takes the noisy data and the differences between the models into account.

Instead, for the sake of simplicity, we present a method which allows us to perform model averaging without the construction of a complex model weight $pr(M_i|\mathbf{D})$. In order to obtain a more conservative, model-independent estimate of a paramater a_0, we utilize once again the formulas presented in section F.2. This time, we modify the weights such that

$$pr(M_i|\mathbf{D}) = \frac{1}{\sigma^2_{a_0,i}} \frac{1}{\sum_{j=1}^{N} \frac{1}{\sigma^2_{a_0,j}}}, \tag{F.28}$$

where N denotes the number of models. This method was presented and used by the twisted mass collaboration in Refs. [64, 65] and is applied in this thesis in cases where "traditional" Bayesian model averaging is problematic.

G Analytical results for the Schwinger model

In this section we present some analytical results concerning the Schwinger model. We start with the derivation of the axial anomaly in the 1-flavour Schwinger model, as discussed in subsection 2.1.3. In section G.2 we turn to the 2-flavour Schwinger model and discuss Lüscher's formula for the finite volume effects on the pion mass. Next, we investigate the average plaquette $\langle P \rangle$, which is used to confirm the validity of our quenched simulations. We finish this chapter by proving the often mentioned reflection symmetry of the canonical determinants.

G.1 Axial anomaly

Here we sketch the derivation of the axial anomaly for the 1-flavour Schwinger model using the Ward-Takahashi identity. In this section we work in Minkowski spacetime and closely follow the derivation in Peskin (see Ref. [23]). Consider the fermionic functional integral

$$\mathcal{Z} = \int \mathcal{D}\psi \mathcal{D}\bar{\psi} \exp\left[iS_F[\bar{\psi}, \psi, A_\mu]\right], \tag{G.1}$$

where S_F denotes the fermionic part of the action at mass zero ($m_0 = 0$) in Minkowski spacetime[1]

$$S_F[\bar{\psi}, \psi, A_\mu] = \int d^2x \bar{\psi} i \not{D} \psi. \tag{G.2}$$

Let $\mathcal{O}$ be a product of local fields $\psi, \bar{\psi}$, then the expectation value of $\mathcal{O}$ is given by

$$\langle \mathcal{O} \rangle = \frac{1}{\mathcal{Z}} \int \mathcal{D}\psi \mathcal{D}\bar{\psi} \mathcal{O} \exp\left[iS_F[\bar{\psi}, \psi, A_\mu]\right]. \tag{G.3}$$

Suppose now, that we perform an infinitesimal local, chiral transformation

$$\psi \to \psi' = (1 + i\tilde{\Lambda}(x)\gamma^5)\psi \qquad \text{and} \qquad \bar{\psi} \to \bar{\psi}' = \bar{\psi}(1 + i\tilde{\Lambda}(x)\gamma^5), \tag{G.4}$$

where $\tilde{\Lambda}(x)$ is chosen such that it vanishes at infinity. The expectation value $\langle \mathcal{O} \rangle$ cannot be affected by an infinitesimal variation of the fields, therefore

$$\delta\langle \mathcal{O} \rangle = \langle \delta \mathcal{O} \rangle + \langle \mathcal{O}(i\delta S_F) \rangle + \langle \mathcal{O} \delta \mathcal{J}^{-2} \rangle \stackrel{!}{=} 0, \tag{G.5}$$

where the last term arises due to a non-trivial transformation behaviour of the Dirac fields and is related to the Jacobian $\mathcal{J}$ via

$$\mathcal{D}\bar{\psi}' \mathcal{D}\psi' = \mathcal{J}^{-2} \mathcal{D}\bar{\psi} \mathcal{D}\psi. \tag{G.6}$$

Equation (G.5) is also often referred to as the Ward-Takahashi identity in the path integral formalism. For the derivation of the axial anomaly we will use a reduced form of this identity, we consider the case with $\mathcal{O} = \mathbb{1}$, such that

$$\langle i\delta S_F + \delta \mathcal{J}^{-2} \rangle = 0. \tag{G.7}$$

We will show, that the appearance of the axial anomaly is related to the non-trivial transformation behaviour of the Jacobian. Consider the fermionic functional integral after a change of variable given by eq. (G.4)

$$\begin{aligned} \mathcal{Z} &= \int \mathcal{D}\psi \mathcal{D}\bar{\psi} \mathcal{J}^{-2} \exp\left[i \int d^2x \left[\bar{\psi} i \not{D} \psi - (\partial_\mu \tilde{\Lambda}(x))(\bar{\psi}\gamma^\mu\gamma^5\psi)\right]\right], \\ &= \int \mathcal{D}\psi \mathcal{D}\bar{\psi} \mathcal{J}^{-2} \exp\left[i \int d^2x \left[\bar{\psi} i \not{D} \psi + \tilde{\Lambda}(x)\partial_\mu(\bar{\psi}\gamma^\mu\gamma^5\psi)\right]\right], \end{aligned} \tag{G.8}$$

[1] Note, that after a so-called Wick rotation the Minkowski action can be written as an Euclidean action, turning the functional integral into a partition function (see section A.1).

where we immediately identify the axial current $J_A^\mu = \bar{\psi}\gamma^\mu\gamma^5\psi$ and

$$\delta S_F = \int d^2x \tilde{\Lambda}(x)\partial_\mu J_A^\mu. \tag{G.9}$$

The derivation of the Jacobian is a bit more involved, but can also be done in a straightforward way.

Consider a basis of eigenstates of $i\not{D}$, with right and left eigenvectors such that

$$i\not{D}\phi_m = \lambda_m\phi_m \qquad \text{and} \qquad \tilde{\phi}(i\not{D}) = -iD_\mu\tilde{\phi}\gamma^\mu = \lambda_m\tilde{\phi}. \tag{G.10}$$

For vanishing background fields $A_\mu = 0$, the eigenvectors are just plane waves, with eigenvalues $\lambda_m = k^2 = (k^0)^2 - \vec{k}^2$. These eigenfunctions can be used to expand the fermion fields

$$\psi(x) = \sum_m a_m\phi_m(x) \qquad \text{and} \qquad \bar{\psi}(x) = \sum_m \tilde{a}_m\tilde{\phi}_m(x), \tag{G.11}$$

where $a_m, \tilde{a}_m$ are anticommuting coefficients multiplying the c-number eigenfunctions. The functional measure can now be defined as

$$\mathcal{D}\psi\mathcal{D}\bar{\psi} = \prod_m da_m d\tilde{a}_m \qquad \text{and} \qquad \mathcal{D}\psi'\mathcal{D}\bar{\psi}' = \prod_m da'_m d\tilde{a}'_m. \tag{G.12}$$

The transformation we perform, relates the coefficients to each other via an infinitesimal linear transformation $(1 + C)$. The determinant of this transformation yields the Jacobian $\mathcal{J}$. We compute this transformation by expanding the coefficients a'_m as

$$a'_m = \sum_n \langle\phi'_m, \phi_n\rangle a_n = \sum_n \int d^2x \left(\phi_m^\dagger(x)(1 + i\tilde{\Lambda}(x)\gamma^5)\phi_n(x)\right) a_n = \sum_n \left(\delta_{mn} + C_{mn}\right) a_n. \tag{G.13}$$

Since the parameter C_{nn} is related to $\tilde{\Lambda}$ and therefore an infinitesimal correction, we can expand the sought-after Jacobian $\mathcal{J}$ as

$$\mathcal{J} = \det(1 + C) = \exp\left[\mathrm{Tr}[\log(1 + C)]\right] \approx \exp\left[\sum_n C_{nn} + \text{corrections}\right], \tag{G.14}$$

such that, after ignoring higher order terms, we arrive at

$$\log(\mathcal{J}) \approx \sum_n C_{nn} = i\int d^2x\tilde{\Lambda}(x)\sum_n \phi_n^\dagger(x)\gamma^5\phi_n(x). \tag{G.15}$$

The sum over all eigenvectors, resp. eigenstates must be regularized in a gauge-invariant way. Such a regularization reads

$$\sum_n \phi_n^\dagger(x)\gamma^5\phi_n(x) \to \lim_{M\to\infty}\sum_n \phi_n^\dagger(x)\gamma^5\phi_n(x)e^{\lambda_m^2/M^2}, \tag{G.16}$$

where we used the eigenvalues introduced in eq. (G.11) and introduced a hard momentum cut-off M, which will be taken to infinity in the end. Since the sign of λ_m^2 will be negative after a Wick rotation, the overall sign in the exponent of the convergence factor is given correctly. Utilizing operator rules we can write the above equation in operator form

$$\sum_n \phi_n^\dagger(x)\gamma^5\phi_n(x) \to \lim_{M\to\infty}\sum_n \phi_n^\dagger(x)\gamma^5 e^{(i\not{D})^2/M^2}\phi_n(x) \tag{G.17}$$

$$\to \lim_{M\to\infty}\langle x|\gamma^5 e^{(i\not{D})^2/M^2}|x\rangle \tag{G.18}$$

$$\to \lim_{M\to\infty}\langle x|\gamma^5 e^{-\frac{D^2}{M^2} - \frac{g}{2M^2}\sigma^{\mu\nu}F_{\mu\nu}}|x\rangle, \tag{G.19}$$

where we used that

$$\begin{aligned}(i\not{D})^2 &= -\gamma^\mu\gamma^\nu D_\mu D_\nu \\ &= -D^2 - \frac{1}{2}\sigma^{\mu\nu}F_{\mu\nu}, \quad \text{with} \quad \sigma^{\mu\nu} = \frac{i}{2}[\gamma^\mu, \gamma^\nu].\end{aligned}$$

Since $\mathrm{Tr}[\gamma^5] = 0$, we must bring down Dirac matrices from the exponent by expanding it. The leading contribution, yields a non-zero trace and is given by $(\sigma^{\mu\nu}F_{\mu\nu})$. Since we take the limit $M \to \infty$, we can ignore the background fields A_μ in the derivative, such that we arrive at an expression with two independent contributions

$$\sum_n \phi_n^\dagger(x)\gamma^5\phi_n(x) \to \lim_{M\to\infty} \underbrace{\mathrm{Tr}[\gamma^5(-\frac{g}{2M^2}\sigma^{\mu\nu}F_{\mu\nu})]}_{\text{Part 1}} \underbrace{\langle x|e^{-\frac{\partial^2}{M^2}}|x\rangle}_{\text{Part 2}}, \tag{G.20}$$

which can be evaluated separately. Thanks to $\gamma^5 = \gamma^0\gamma^1$, we have

$$\sigma^{\mu\nu} = \frac{i}{2}[\gamma^\mu, \gamma^\nu] = i\epsilon^{\mu\nu}\gamma^5, \tag{G.21}$$

where $\epsilon^{\mu\nu}$ denotes the totally antisymmetric Levi-Civita tensor with $\epsilon^{01} = 1$. The first part can be computed to be

$$\text{Part 1} = -\frac{ig}{2M^2}\epsilon^{\mu\nu}F_{\mu\nu}\,\mathrm{Tr}[\gamma^5.\gamma^5] = -\frac{ig}{M^2}\epsilon^{\mu\nu}F_{\mu\nu}. \tag{G.22}$$

The second part can be obtained after using the Fourier representation of the matrix element and performing a Wick rotation

$$\text{Part 2} = \lim_{x\to y}\int \frac{d^2k}{(2\pi)^2}e^{-ik(x-y)}e^{\frac{k^2}{M^2}} \tag{G.23}$$

$$= i\int \frac{d^2k_E}{(2\pi)^2}e^{-\frac{k_E^2}{M^2}} = i\frac{M^2}{4\pi}. \tag{G.24}$$

After combining the two contributions and taking the (trivial) limit $M \to \infty$, we obtain

$$\sum_n \phi_n^\dagger(x)\gamma^5\phi_n(x) \to \frac{g}{4\pi}\epsilon^{\mu\nu}F_{\mu\nu}. \tag{G.25}$$

Consequently, up to first order, the Jacobian can be written as

$$\mathcal{J} = \exp\left[i\int d^2x\tilde{\Lambda}(x)\frac{g}{4\pi}\epsilon^{\mu\nu}F_{\mu\nu}\right], \tag{G.26}$$

and the transformed fermionic functional integral (eq. (G.8)) becomes

$$\mathcal{Z} = \int \mathcal{D}\psi\mathcal{D}\bar{\psi}\exp\left[i\int d^2x\left[\bar{\psi}i\not{D}\psi + \tilde{\Lambda}(x)\{\partial_\mu J_A^\mu - \frac{g}{2\pi}\epsilon^{\mu\nu}F_{\mu\nu}\}\right]\right]. \tag{G.27}$$

We can immediately read off the contribution arising from the axial anomaly

$$\partial_\mu J_A^\mu = \frac{g}{2\pi}\epsilon^{\mu\nu}F_{\mu\nu}. \tag{G.28}$$

Alternatively, one obtains this relation by using the Ward-Takahashi identity eq. (G.5), with δS_F given by eq. (G.9) and

$$\delta\mathcal{J}^{-2} = -i\int d^2x\tilde{\Lambda}(x)\frac{g}{2\pi}\epsilon^{\mu\nu}F_{\mu\nu}. \tag{G.29}$$

G.2 Lüscher's formula for finite volume effects

For the rest of this chapter we will be working in Euclidean spacetime on a lattice of extent $L \times L_t$ and with a lattice spacing of one, $a = 1$. We consider a scalar field theory in two dimensions describing a single self-interacting particle of mass m_0. After imposing restrictions on the lattice Lüscher derived a formula for the finite volume effects on the particle mass (see Ref. [29]). We require a lattice whose temporal extent is sufficiently large (ideally $L_t = \frac{1}{T} = \infty$), such that finite temperature corrections are negligible. Also the lattice spacing needs to be small enough, such that lattice artefacts can be considered

absent. If we further restrict ourselves to large lattices (Lüscher suggests $m_0 L \geq 3.0$), Lüscher's formula for finite volume corrections to the particle mass is given by

$$m_0(L) = m_0 - \underbrace{\lambda^2 m_0^{-3} \frac{1}{8\pi} (\frac{4\pi}{\sqrt{3}}\xi)^{\frac{1}{2}} K_{-\frac{1}{2}}(\frac{\sqrt{3}}{2}\xi)}_{\text{Part 1}} - \underbrace{\frac{1}{2m_0} \int \frac{dq}{(2\pi)2q_0} e^{-q_0 L} F(iq_1)}_{\text{Part 2}}, \tag{G.30}$$

where $m_0(L)$ denotes the finite volume particle mass, m_0 the infinite volume particle mass, λ is the effective 3-particle coupling, K_l the modified Besselfunction, $\xi = m_0 L$ and $F(iq_1)$ denotes some forward scattering amplitude. We sketch in detail the modifications which have to be made to obtain eq. (2.63). We start by examining the first correction (Part 1), proportional to the effective 3-particle coupling λ. In order to work with Lüscher's formula, we write down the expansion of the modified Bessel function (see nr. 8.432 in Ref. [66])

$$K_\alpha(z) = \int e^{-z\cosh(t)} \cosh(\alpha t) dt, \tag{G.31}$$

for large values of z, which reads

$$K_\alpha(z) \approx \sqrt{\frac{\pi}{2z}} e^{-z} \left(1 + \frac{4\alpha^2 - 1}{8z} + \text{higher order}\right). \tag{G.32}$$

However, the expansion naturally truncates for $\alpha = -\frac{1}{2}$, such that

$$K_{-\frac{1}{2}}(z) \stackrel{!}{=} \sqrt{\frac{\pi}{2z}} e^{-z}, \quad \text{for all } z \geq 0. \tag{G.33}$$

Using this expression with $z = \frac{\sqrt{3}}{2}\xi$, we can simplify Part 1 greatly and obtain

$$\text{Part 1} \to \left(\frac{\lambda^2}{4\sqrt{3} m_0^3}\right) e^{-\frac{\sqrt{3}}{2}\xi}. \tag{G.34}$$

Similarly we can proceed with Part 2, which can be rewritten using $q_1 = \frac{k_1}{L}$ such that

$$\frac{1}{2m_0} \int \frac{dq_1}{(2\pi)2q_0} e^{-q_0 L} F(iq_1) \approx \frac{1}{4m_0^2 2\pi} \frac{F(0)}{L} \int \frac{dk_1}{\sqrt{1 + \frac{k_1^2}{\xi^2}}} e^{-\sqrt{1+\frac{k_1^2}{\xi^2}}\xi}, \tag{G.35}$$

where we used that for large lattices $F(\frac{ik_1}{L}) \approx F(0)$. In order to obtain the large ξ behaviour one expands the integrand, such that

$$\frac{e^{-\sqrt{1+\frac{k_1^2}{\xi^2}}\xi}}{\sqrt{1 + \frac{k_1^2}{\xi^2}}} \approx e^{-\xi - \frac{k_1^2}{2\xi}}. \tag{G.36}$$

After performing the Gaussian integration we obtain

$$\text{Part 2} \to \frac{1}{\sqrt{\xi}} \left(\frac{F(0)}{4m_0\sqrt{2\pi}}\right) e^{-\xi}. \tag{G.37}$$

After combining both parts we can describe the finite volume effects using the formula

$$m_0(L) = m_0 - \left(\frac{\lambda^2}{4\sqrt{3} m_0^3}\right) e^{-\frac{\sqrt{3}}{2}\xi} - \frac{1}{\sqrt{\xi}} \left(\frac{F(0)}{4m_0\sqrt{2\pi}}\right) e^{-\xi}. \tag{G.38}$$

For decreasing volumes the pion mass becomes artificially inflated due to the self-interactions via the boundaries, meaning that finite volume effects on the pion mass are always positive. As a next step, we modify eq. (G.38) such that the positive sign of the corrections becomes evident. It was argued by Gutsfeld et al. in Ref. [21], that $F(0) \propto -m_0^2$, showing that the contribution of $F(0)$ is negative. Upon fixing $F(0)$ as negative, we investigated finite volume effects on the pion mass in the 2-flavour Schwinger

model. We found out that the finite volume corrections proportional to the 3-particle coupling (given by Part 1), are positive as well.

In order keep the notation simple, we make the replacements

$$\lambda \to i\lambda, \quad \text{and} \quad F(0) \to -F(0), \tag{G.39}$$

where λ is now assumed to be real and $F(0)$ is considered positive. As a result, we obtain the formula for finite volume corrections presented in eq. (2.63) which are used throughout this thesis

$$m_\pi(L) = m_\pi + \left(\frac{\lambda^2}{4\sqrt{3}m_\pi^3}\right) e^{-\frac{\sqrt{3}}{2}\xi} + \frac{1}{\sqrt{\xi}}\left(\frac{F(0)}{4m_\pi\sqrt{2\pi}}\right) e^{-\xi}. \tag{G.40}$$

G.3 Pure gauge susceptibility

Throughout this thesis, we work mostly with quenched simulations and access the desired configuration space by using reweighting techniques, as explained in section C.9. One of the easiest ways to test whether our quenched simulations provide correctly generated configurations is to find observables which can be derived analytically and measure them on the generated ensembles. One such observable is given by the pure gauge plaquette

$$\langle P \rangle = \langle \frac{1}{2\Omega} \sum_P \left(U^P + U^{P,\dagger}\right) \rangle, \quad \text{with} \quad \Omega = L \cdot L_t, \tag{G.41}$$

whose behaviour can be analytically derived, as shown by Elser in Ref. [19]. We write down the full partition function of the quenched Schwinger model which reads

$$\mathcal{Z} = \int \mathcal{D}U e^{-S_g[U]} = \int \mathcal{D}U e^{-\beta \sum_P [1 - \frac{1}{2}(U^P + U^{P,\dagger})]}, \tag{G.42}$$

where U^P denotes the contribution around an elementary plaquette, which is given by eq. (A.57), that is

$$\begin{aligned} U^P_{\mu\nu}(n) &= U_{n,n+\hat{\mu}} U_{n+\hat{\mu},n+\hat{\mu}+\hat{\nu}} U^\dagger_{n+\hat{\nu},n+\hat{\mu}+\hat{\nu}} U^\dagger_{n,n+\hat{\nu}} && \text{(G.43)} \\ &= \exp\left(i(\phi_\mu(n) + \phi_\nu(n+\hat{\mu}) - \phi_\mu(n+\hat{\nu}) - \phi_\nu(n))\right) && \text{(G.44)} \\ &= \exp(i\theta_P(n)). && \text{(G.45)} \end{aligned}$$

We choose to characterize a plaquette based on its point on the very bottom to the left and follow the gauge-links in a counterclockwise direction s.t.

$$U^P(n) = \exp\left(i(\phi_1(n) + \phi_0(n+\hat{1}) - \phi_1(n+\hat{0}) - \phi_0(n))\right) = \exp(i\theta_P(n)). \tag{G.46}$$

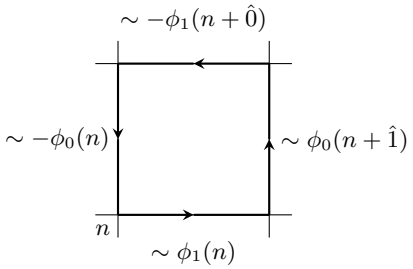

Figure G.1: Orientation of the plaquette, the gauge fields are characterized by angles $\phi_i(n)$.

Now we can rewrite the partition function as

$$\begin{aligned} Z &= e^{-\beta\Omega} \int \prod_{n_1} \left(\frac{d\phi_0(n_1)}{2\pi}\frac{d\phi_1(n_1)}{2\pi}\right) e^{\beta \sum_{n_2} \cos(\theta_P(n_2))} && \text{(G.47)} \\ &= e^{-\beta\Omega} \int \prod_{n_1} \left(\frac{d\phi_0(n_1)}{2\pi}\frac{d\phi_1(n_1)}{2\pi}\right) \prod_{n_2} e^{\beta \cos(\theta_P(n_2))}. && \text{(G.48)} \end{aligned}$$

Next, we introduce the Fourier-transform of the exponential

$$e^{\beta\cos(\phi)} = \sum_{n=-\infty}^{\infty} c_n e^{in\phi}, \tag{G.49}$$

where the coefficients can be identified with the modified Bessel-functions (see Ref. [67])

$$c_n = \frac{1}{2\pi}\int_{-\pi}^{\pi} e^{\beta\cos(\phi)}e^{-in\phi}d\phi = \frac{1}{\pi}\int_0^{\pi} e^{\beta\cos(\phi)}\cos(n\phi)d\phi = I_n(\beta). \tag{G.50}$$

Now, the partition function reads

$$\begin{aligned}\mathcal{Z} =& e^{-\beta\Omega}\left(\prod_{n_2}\sum_{k_{n_2}}\right)\int\prod_n\left(\frac{d\phi_0(n)}{2\pi}\frac{d\phi_1(n)}{2\pi}\right)\\ &\times\prod_{n_2}\left(e^{i\beta k_{n_2}(\phi_1(n_2)-\phi_1(n_2+\hat{0})+\phi_0(n_2+\hat{1})-\phi_0(n_2))}I_{k_{n_2}}(\beta)\right).\end{aligned} \tag{G.51}$$

The evaluation of this partition function can be simplified, once we order all the contributions accordingly and evaluate the integrals step-by-step. Each integration picks up two (multiplicative) factors from the integrand. For example, if we perform the integration over $d\phi_0(n)$ we obtain

$$\int\frac{d\phi_0(n)}{2\pi}e^{-i\beta k_{n_1}\phi_0(n_1)+i\beta k_{n_1-\hat{1}}\phi_0(n_1)} = \delta_{n,n_1}\delta_{k_{n_1},k_{n_1-\hat{1}}}, \tag{G.52}$$

where $k_{n_1-\hat{1}}$ just denotes one of the summation indices $\{k_1, k_2, \ldots, k_\Omega\}$, which is being summed over. After evaluating all the integrals in the same manner and relabelling $n_2 \to n$, we obtain

$$\mathcal{Z} = e^{-\beta\Omega}\left(\prod_n\sum_{k_n}\right)\prod_n(\delta_{k_n,k_{n-\hat{1}}}\delta_{k_n,k_{n-\hat{0}}}I_{k_n}(\beta)), \tag{G.53}$$

which is non-zero only if all the indices are the same s.t.

$$k_1 = k_{1-\hat{0}} = k_{1-\hat{1}} = \ldots, \qquad \text{resp.} \qquad k_1 = k_2 = k_3 = \cdots = k.$$

Now the evaluation of the partition function is straightforward and we obtain

$$Z = e^{-\beta\Omega}\sum_{k\in\mathbb{Z}}I_k(\beta)^\Omega = e^{-\beta\Omega}\left(I_0(\beta)^\Omega + 2\sum_{k=1}^{\infty}I_k(\beta)^\Omega\right), \tag{G.54}$$

where we used a symmetry-property of the modified Bessel-function $I_n(x) = I_{-n}(x)$ for all $n \in \mathbb{N}$ and $x \in \mathbb{R}$. In order to extract the plaquette, we use

$$\langle P\rangle = 1 + \frac{1}{Z\Omega}\frac{\partial Z}{\partial\beta} \quad \text{and} \quad \frac{\partial I_n(\beta)}{\partial\beta} = \frac{1}{2}\left(I_{n-1}(\beta) + I_{n+1}(\beta)\right) \tag{G.55}$$

and after some calculus we obtain the desired result, presented in section 4.2, that is

$$\langle P\rangle = \frac{\frac{I_1(\beta)}{I_0(\beta)} + \sum_{n=1}^{\infty}\left[\left(\frac{I_n(\beta)}{I_0(\beta)}\right)^{\Omega-1}\left(\frac{I_{n-1}(\beta)}{I_0(\beta)} + \frac{I_{n+1}(\beta)}{I_0(\beta)}\right)\right]}{1 + 2\sum_{n=1}^{\infty}\left(\frac{I_n(\beta)}{I_0(\beta)}\right)^{\Omega}}. \tag{G.56}$$

G.4 Reflection symmetry of the canonical determinant

After discussing the dimensional reduction in chapter 3, in this section we derive the reflection symmetry of the canonical determinants

$$\det{}_k^*(\mathbf{K}) = \det{}_{-k}(\mathbf{K}), \quad \forall k \in \{0, 1, \ldots, L\}. \tag{G.57}$$

as mentioned in subsection 3.3.5. As in chapter 3 we will be working on a lattice of extent $L \times L_t$ and we set the lattice spacing to one ($a = 1$) for the sake of readability. Consider the canonical determinant as derived in eq. (3.59), that is

$$\det{}_k(\mathbf{K}[U]) = \left(\prod_{i=1}^{L_t} |B_i||2\kappa U_i^\dagger|\right) \sum_{I,|I|=k+L} \det(\mathcal{T}^{II}) = \left(\prod_{i=1}^{L_t} |B_i||2\kappa U_i^\dagger|\right) E_{k+L}(\mathcal{T}) \tag{G.58}$$

and make the replacement $E_{k+L}(\mathcal{T})$ and $S_{k+L}(\mathcal{T})$ as illustrated in section D.1 such that

$$\det{}_k(\mathbf{K}[U]) = \left(\prod_{i=1}^{L_t} |B_i||2\kappa U_i^\dagger|\right) S_{k+L}(\mathcal{T}). \tag{G.59}$$

For the sake of readability, we abbreviate $n = L$ and recapitulate the definition of the symmetric function, discussed in section D.1. Let $A \in \mathrm{Mat}(m, \mathbb{C})$ and assume that the spectrum of A is given by $\sigma(A) = \{\lambda_1, \ldots, \lambda_m\}$. Then the k'th elementary symmetric function reads

$$S(A) = S_k(\lambda_1, \ldots, \lambda_m) = \sum_{1 \le i_1 \le \cdots \le i_k \le m} \prod_{j=1}^{k} \lambda_{i_j}. \tag{G.60}$$

We showed in subsection 3.3.5 that the spectrum of the transfer matrix $\mathcal{T}$ can be written as

$$\sigma(\mathcal{T}) = \{\lambda_1, \ldots, \lambda_n, \frac{1}{\lambda_1^*}, \ldots, \frac{1}{\lambda_n^*}\} = \{r_1 e^{i\phi_1}, \ldots, r_n e^{i\phi_n}, \frac{1}{r_1} e^{i\phi_1}, \ldots, \frac{1}{r_n} e^{i\phi_n}\}, \tag{G.61}$$

and that the determinant is given by

$$\det \mathcal{T} = \prod_{i=1}^{L_t} \det(U_i)^2 \overset{!}{=} e^{2i(\phi_1 + \cdots + \phi_n)} = e^{2i\Phi}, \tag{G.62}$$

where we defined

$$\Phi = \sum_{i=1}^{n} \phi_i. \tag{G.63}$$

We extract the temporal gauge-link dependence of the bulkfactor via

$$\left(\prod_{i=1}^{L_t} |B_i||2\kappa U_i^\dagger|\right) = \left(\prod_{i=1}^{L_t} |B_i||2\kappa|\right) \prod_{i=1}^{L_t} \det U_i^\dagger = \left(\prod_{i=1}^{L_t} |B_i||2\kappa|\right) e^{-i\Phi}, \tag{G.64}$$

which then leads to

$$\det{}_k(\mathbf{K}[U]) = \left(\prod_{i=1}^{L_t} |B_i||2\kappa|\right) e^{-i\Phi} S_{n+k}(\mathcal{T}). \tag{G.65}$$

Note that the prefactor $\left(\prod_{i=1}^{L_t} |B_i||2\kappa|\right)$ is now completely real. The potentially complex part is now given by

$$\tilde{S}_k(\mathcal{T}) = e^{-i\Phi} S_k(\mathcal{T}). \tag{G.66}$$

If we can prove the reflection property of the quantity $\tilde{S}_k(\mathcal{T})$, that is

$$\tilde{S}^*_{n-k}(\mathcal{T}) = \tilde{S}_{n+k}(\mathcal{T}), \quad \text{for } k \in \{0, 1, \ldots n\}, \tag{G.67}$$

then we have proven the reflection symmetry for the canonical determinant as well.

G.4.1 Reflection symmetry of $\tilde{S}_{n+k}(\mathcal{T})$

We argued that in order to prove reflection symmetry of the canonical determinants, we can show that the rescaled symmetric functions $\tilde{S}_{n+k}(\mathcal{T})$ have a reflection property, such that

$$\tilde{S}^*_{n-k}(\mathcal{T}) = \tilde{S}_{n+k}(\mathcal{T}), \quad \text{for } k \in \{0, 1, \dots n\}, \quad \text{with} \quad \sigma(\mathcal{T}) = \{\lambda_1, \dots, \lambda_n, \frac{1}{\lambda_1^*}, \dots, \frac{1}{\lambda_n^*}\}. \tag{G.68}$$

To prove this we take an arbitrary k and we show that for every summand q in $\tilde{S}_{n-k}(\mathcal{T})$, there exists a summand p in $\tilde{S}_{n+k}(\mathcal{T})$ which is exactly complex conjugated i.e. $p = q^*$. Then every summand in $\tilde{S}_{n-k}(\mathcal{T})$ has a complex conjugated "partner" in $\tilde{S}_{n+k}(\mathcal{T})$ and it is therefore trivially true that

$$\tilde{S}^*_{n-k}(\mathcal{T}) = \tilde{S}_{n+k}(\mathcal{T}). \tag{G.69}$$

Take some arbitrary summand q in $\tilde{S}_{n-k}(\mathcal{T})$ which is built from a combination of $n-k$ eigenvalues of $\mathcal{T}$. We assume that $a \leq n$ eigenvalues have been taken from the subset $\{\lambda_1, \dots, \lambda_n\} \subseteq \sigma(\mathcal{T})$ and $b \leq n$ eigenvalues have been chosen from $\{\frac{1}{\lambda_1^*}, \dots, \frac{1}{\lambda_n^*}\}$, such that $a + b = n - k$. We denote these collections of eigenvalues with

$$\{\lambda_{i_1}, \lambda_{i_2}, \dots, \lambda_{i_a}\} \quad \text{and} \quad \{\frac{1}{\lambda^*_{i_1}}, \frac{1}{\lambda^*_{i_2}}, \dots, \frac{1}{\lambda^*_{i_b}}\}, \tag{G.70}$$

respectively. Then we can write down the summand q in $\tilde{S}_{n-k}(\mathcal{T})$ as

$$q = e^{-i\Phi} \prod_{j=1}^{a} \lambda_{i_j} \prod_{k=1}^{b} \frac{1}{\lambda^*_{i_k}}, \quad \text{with } a + b = n - k. \tag{G.71}$$

Upon utilizing the "normalization" of the eigenvalues

$$\det(\mathcal{T}) = \prod_{i=1}^{n} \lambda_i \prod_{i=1}^{n} \frac{1}{\lambda_i^*} \stackrel{!}{=} e^{2i\Phi}, \tag{G.72}$$

we can relate the chosen eigenvalues for q, to the ones which have been omitted

$$\prod_{j=1}^{a} \lambda_{i_j} \prod_{k=1}^{b} \frac{1}{\lambda^*_{i_k}} = e^{2i\Phi} \prod_{j=a+1}^{n} \frac{1}{\lambda_{i_j}} \prod_{k=b+1}^{n} \lambda^*_{i_k}, \tag{G.73}$$

where on the r.h.s we have $n + k$ factors. However, this means that we can write down q as a product of $n + k$ eigenvalues,

$$q = e^{i\Phi} \underbrace{\prod_{j=a+1}^{n} \frac{1}{\lambda_{i_j}} \prod_{k=b+1}^{n} \lambda^*_{i_k}}_{n+k \text{ eigenvalues of } \sigma(\mathcal{T}).}, \tag{G.74}$$

and upon defining the complex conjugate as p

$$p = e^{-i\Phi} \prod_{j=a+1}^{n} \frac{1}{\lambda^*_{i_j}} \prod_{k=b+1}^{n} \lambda_{i_k} \tag{G.75}$$

we see that that $p = q^*$ takes the form of a summand in $\tilde{S}_{n+k}(\mathcal{T}) = e^{-i\Phi} S_{n+k}(\mathcal{T})$, which concludes the proof.

H Numerical results details

Here we want to include the details for the numerical results, which have been omitted in chapter 5. In the following sections we present a detailed description of the performed calculations, the precise numerical details can be found in the tables at the end of each section. Throughout this chapter we set the lattice spacing to $a = 1$.

H.1 Datasets

In order to examine the 2-flavour Schwinger model in the canonical formalism we performed quenched simulations, that is simulations with no fermion content. We vary the coupling $\beta = \frac{1}{(ag)^2}$, where g denotes the bare coupling, such that $\beta \in \{3.0, 5.0, 7.0\}$. For each coupling we perform measurements for different volumes L and temperatures $T = \frac{1}{L_t}$, in steps of $\Delta L = 2$ and $\Delta L_t = 2$, such that

$$L \in \{4, 6, 8, \ldots, 38, 40\} \quad \text{and} \quad L_t \in \{4, 6, 8, \ldots, 58, 60\}. \tag{H.1}$$

Utilizing the prescription presented in the appendix section C.9, we can reweight those quenched simulations into simulations of the mass-degenerate 2-flavour Schwinger model where we have an *up* and a *down* quark. After reweighting those simulations, we obtain five different datasets which will be labelled with A3, A5, A7, B5 and B7. For the datasets A3, A5 and A7 the bare masses are tuned in such a way that we have a fixed infinite volume pion mass $m_\pi/g \approx 0.75$, while the remaining two datasets are fixed such that $m_\pi/g \approx 0.44$. A summary of the used datasets is given in table H.1.

Datasets	β	m	κ	am_π	m_π/g
A3	3.0	0.0000	0.5000	0.4330(3)	0.7500(5)
A5	5.0	0.0220	0.4892	0.3387(2)	0.7574(3)
A7	7.0	0.0266	0.4870	0.2859(1)	0.7564(3)
B5	5.0	-0.0400	0.5208	0.1921(4)	0.4296(8)
B7	7.0	-0.0220	0.5112	0.1701(6)	0.450(2)

Table H.1: Datasets used in chapter 5.

H.2 Extrapolation to zero temperature

Consider one of the datasets presented in table H.1. For each dataset we have calculated the ground state energies $E_{n\pi}(L, L_t)$, for $n \in \{1, 2, 3\}$ and L, L_t given in eq. (H.1). In this section we want to discuss in detail the extraction of the ground state energies in multi-meson sectors. From the discussion in section 3.5 we know that the ground state energies of the multi-meson sectors are given by multi-pion states. The ground state energies of those multi-pion states are obtained by measuring the free energy difference between the corresponding canonical sectors (as explained in section 3.6) and extrapolating to zero temperature. The needed formula is given by

$$E_{n\pi} = \lim_{T\to 0} E_{n\pi}(T) = -\lim_{T\to 0} T \log\left(\frac{\mathcal{Z}_{(n,-n)}(T)}{\mathcal{Z}_{(0,0)}(T)}\right), \tag{H.2}$$

which has been referred to as the master formula in chapter 5. For fixed volumes, the finite temperature behaviour differs depending on the volume L and the isospin sector which is being considered. In chapter 5 we present some plots for the dataset A5 (figures 5.1,5.2,5.6,5.7 and 5.13), showing the temperature behaviour of the ground state energies as a function of the volume and the meson sector. In order

to describe the temperature behaviour, we use different models, resp. fit functions, which have been motivated in section 3.5. The measured energies for fixed meson sector and fixed volume $E_{n\pi}(L, L_t)$ can then be fitted to those models, allowing us to extract the ground state energies as a function of the volume. The detailed procedure involves Bayesian model averaging and systematic averaging as explained in the appendix in chapter F.

H.2.1 Isospin $I = 1$ sector and the extraction of $E_\pi(L) = m_\pi(L)$

For a fixed volume we can examine the behaviour of the ground state energy of the isospin $I = 1$ sector, that is $E_\pi(L, L_t) = m_\pi(L, L_t)$, as a function of the temperature, which is related to the temporal lattice extent via $T = \frac{1}{L_t}$. Following the discussion in subsection 3.6.5 an ansatz we are going to use for the extraction of m_π is given by

$$E_\pi(T) \approx m_\pi - T \log\left(\frac{1 + 2\sum_{i=1}^{\frac{L}{2}} e^{-(E_{\pi^+}^{(i)} - m_\pi)/T} + e^{-(m_{a_0} - m_\pi)/T} + 2\sum_{i=1}^{\frac{L}{2}} e^{-(E_{a_0}^{(i)} - m_\pi)/T}}{1 + e^{-m_\pi/T} + 2\sum_{i=1}^{\frac{L}{2}} e^{-E_{\pi^0}^{(i)}/T}}\right), \tag{H.3}$$

which, after making the replacement $T \to \frac{1}{L_t}$, can be used to derive three different fit functions

$$\mathrm{M}_{m_\pi,1}(L_t, m_\pi) = m_\pi, \tag{H.4}$$

$$\mathrm{M}_{m_\pi,2}(L_t, m_\pi) = m_\pi - \frac{1}{L_t}\log\left(\frac{1 + 2\sum_{i=1}^{\frac{L}{2}} e^{-(E_{\pi^+}^{(i)} - m_\pi)L_t}}{N}\right), \tag{H.5}$$

$$\mathrm{M}_{m_\pi,3}(L_t, m_\pi, m_{a_0}) = m_\pi - \frac{1}{L_t}\log\left(\frac{Z}{N}\right), \tag{H.6}$$

where we introduced some abbreviations such as

$$Z = 1 + 2\sum_{i=1}^{\frac{L}{2}} e^{-(E_{\pi^+}^{(i)} - m_\pi)L_t} + e^{-(m_{a_0} - m_\pi)L_t} + 2\sum_{i=1}^{\frac{L}{2}} e^{-(E_{a_0}^{(i)} - m_\pi)L_t},$$

$$N = 1 + e^{-m_\pi L_t} + 2\sum_{i=1}^{\frac{L}{2}} e^{-E_{\pi^0}^{(i)} L_t}.$$

We vary the fit ranges for each ansatz, for the constant fit $\mathrm{M}_{m_\pi,1}(L_t, m_\pi)$ we fix the upper limit of the fit range $L_t^{\text{max.}}$ in such a way that $L_t^{\text{max.}} \in \{60, 58, 56, 54, 52, 50\}$. The lower fit boundary of the fit $L_t^{\text{min.}}$ is chosen in such a way, that there is at least a difference of $\Delta L_t = 10$, such that $L_t^{\text{min.}} \in \{4, 6, 8, \ldots, L_t^{\text{max.}} - 10\}$, yielding a total of 129 combinations of $[L_t^{\text{min.}}, L_t^{\text{max.}}]$ and therefore 129 fits. This choice of fit ranges, specifically restricting the upper boundary $L_t^{\text{max.}}$, ensures good quality fits in the low temperature regime, where the energy reaches a constant plateau.

Similar considerations play a role when fitting $\mathrm{M}_{m_\pi,2}(L_t, m_\pi)$ and $\mathrm{M}_{m_\pi,3}(L_t, m_\pi, m_{a_0})$. We choose the fit ranges in such a way, that the fits turn out well. Since we have an additional correction term we need to set the lower boundary $L_t^{\text{min.}}$ of the fit in such a way that temperature corrections are taken into account. For $\mathrm{M}_{m_\pi,2}$ we fix $L_t^{\text{max.}} \in \{60, 58, 56, 54, 52, 50, 48, 46\}$ and choose $L_t^{\text{min.}} \in \{26, 24, 22, 20, \ldots, 4\}$, which yields a total of 108 fits. For the model $\mathrm{M}_{m_\pi,3}(L_t, m_\pi, m_{a_0})$ we take even more corrections into account and by adding an additional mass parameter m_{a_0}. Upon fixing the upper boundary to $L_t^{\text{max.}} \in \{60, 58, 56, 54, 52, 50, 48, 44\}$, we have to vary the lower boundary in a high temperature regime, to obtain reliable results, which is why we choose $L_t^{\text{min.}} \in \{18, 16, 14, \ldots, 4\}$.

Note that these fit ranges, although somewhat ambiguous, have been determined after multiple tests and trials. We summarize the results

$$\mathrm{M}_{m_\pi,1}(L_t, m_\pi), \quad L_t^{\text{max.}} \in \{60, 58, 56, 54, 52, 50\}, \qquad L_t^{\text{min.}} \in \{L_t^{\text{max.}} - 10, \ldots, 6, 4\}, \tag{H.7}$$

$$\mathrm{M}_{m_\pi,2}(L_t, m_\pi), \quad L_t^{\text{max.}} \in \{60, 58, 56, 54, 52, 50, 48, 46\}, \qquad L_t^{\text{min.}} \in \{26, 24, 22, 20, \ldots, 4\}, \tag{H.8}$$

$$\mathrm{M}_{m_\pi,3}(L_t, m_\pi, m_{a_0}), \quad L_t^{\text{max.}} \in \{60, 58, 56, 54, 52, 50, 48, 46, 44\}, \quad L_t^{\text{min.}} \in \{18, 16, 14, \ldots, 4\}. \tag{H.9}$$

For each model (with their corresponding) fit ranges we perform the least-squares fits and determine the pion mass $m_\pi = \lim_{L_t \to \infty} m_\pi(L_t)$. Note, that we do not use any priors in our definition of the χ_T^2 and just utilize the standard χ_0^2, that is

$$\chi_T^2 = \chi_0^2 = \sum_{L_t}\left(\frac{\mathrm{M}_{m_\pi,i}(L_t, \cdot) - m_\pi(L_t)}{s m_\pi(L_t)}\right)^2, \qquad \forall i \in \{1, 2, 3\} \tag{H.10}$$

where $m_\pi(L_t)$ denotes the measurement for the ground state energy as a function of temperature and $sm_\pi(L_t)$ its error. We consider each model separately and perform Bayesian model averaging as explained in chapter F, where the used Akaike information criterion (AIC, the most general form is given by eq. (F.24)) is given by

$$AIC = \chi^2_T + 2k + 2N_{cut}. \tag{H.11}$$

The number of fit parameters k for the three different fit functions is given by $k = 1, 1, 2$, respectively. The parameter N_{cut} is given by the number of data points which have been left out.

H.2.2 Isospin $I = 2, 3$ sector and the extraction of $E_{2\pi}(L)$, resp. $E_{3\pi}(L)$

The very same strategy can be performed for investigating the ground state energies of the isospin $I = 2$ and isospin $I = 3$ sectors. The used fit functions are motivated by the discussion in subsection 3.6.5 and are given by

$$\mathrm{M}_{E_{2\pi},1}(T, E_{2\pi}) = E_{2\pi} \tag{H.12}$$

$$\mathrm{M}_{E_{2\pi},2}(T, E_{2\pi}, A_1, A_2) = E_{2\pi} - T \log\left(\frac{1 + A_2 e^{-A_1/T}}{1 + e^{-m_\pi/T} + 2\sum_{i=1}^{\frac{L}{2}} e^{-E^{(i)}_{\pi^0}/T}}\right), \tag{H.13}$$

and

$$\mathrm{M}_{E_{3\pi},1}(T, E_{3\pi}) = E_{3\pi} \tag{H.14}$$

$$\mathrm{M}_{E_{3\pi},2}(T, E_{3\pi}, B_1, B_2) = E_{3\pi} - T \log\left(\frac{1 + B_2 e^{-B_1/T}}{1 + e^{-m_\pi/T} + 2\sum_{i=1}^{\frac{L}{2}} e^{-E^{(i)}_{\pi^0}/T}}\right), \tag{H.15}$$

respectively. Note, that the values for m_π have been determined beforehand from the zero temperature extrapolation of the 1-pion ground state energy. The fit ranges are also chosen similarly as for the ground state energies of the 1-pion state. The constant fits $\mathrm{M}_{E_{2\pi},1}(T, E_{2\pi})$ and $\mathrm{M}_{E_{3\pi},1}(T, E_{3\pi})$ have the same fit ranges as $\mathrm{M}_{m_\pi,1}(L_t, m_\pi)$ given in eq. (H.7). The fit ranges for the exponential corrections on the other hand are chosen to be the same as the fit ranges for $\mathrm{M}_{m_\pi,3}(L_t, m_\pi, m_{a_0})$ in eq. (H.9). We summarize all the used fit functions for the 2- and 3-pion ground state energies, such that

$$\mathrm{M}_{E_{2\pi},1}(T, E_{2\pi}), \quad L_t^{\text{max.}} \in \{60, 58, 56, 54, 52, 50\}, \quad L_t^{\text{min.}} \in \{L_t^{\text{max.}} - 10, \ldots, 6, 4\}, \tag{H.16}$$

$$\mathrm{M}_{E_{2\pi},2}(T, E_{2\pi}, A_1, A_2), \quad L_t^{\text{max.}} \in \{60, 58, \ldots, 46, 44\}, \quad L_t^{\text{min.}} \in \{18, 16, 14, \ldots, 4\}, \tag{H.17}$$

$$\mathrm{M}_{E_{3\pi},1}(T, E_{3\pi}), \quad L_t^{\text{max.}} \in \{60, 58, 56, 54, 52, 50\}, \quad L_t^{\text{min.}} \in \{L_t^{\text{max.}} - 10, \ldots, 6, 4\}, \tag{H.18}$$

$$\mathrm{M}_{E_{3\pi},2}(T, E_{3\pi}, B_1, B_2), \quad L_t^{\text{max.}} \in \{60, 58, \ldots, 46, 44\}, \quad L_t^{\text{min.}} \in \{18, 16, 14, \ldots, 4\}. \tag{H.19}$$

After executing all the fits and performing Bayesian model averaging with each model separately, we obtain the model-dependent volume dependence of the 2- and 3-pion ground state energies $E_{2\pi}(L)$ and $E_{3\pi}(L)$. The results, including the extracted pion masses $m_\pi(L)$, are nicely summarized for each dataset in tables H.2 to H.6.

H.2.3 Systematic averaging

After performing the Bayesian model averaging for each model, we do not have final results for $m_\pi(L)$, $E_{2\pi}(L)$ and $E_{3\pi}(L)$ yet. For each volume, we have model-dependent results, which need to be averaged consistently. To estimate the systematics, as conservatively as possible we propose systematic averaging as explained in section F.4.

For the sake of completeness, we would like to discuss the reason for this somewhat odd approach used for the analysis of the data. It is evident, that one also could have used Bayesian model averaging to average over all available models, this is exactly what Bayesian model averaging is used for, after all. However, in our investigations, we found out, that this prescription does not lead to satisfactory results. The reason for that, is the combination of fluctuating data and different fit models, with different asymptotic behaviour. The Bayesian model averaging procedure (utilized with the Akaike Information Criterion (AIC)) is not conservative enough, and usually favours one of the models, while heavily discriminating against the others. If the favoured fit model is the same for all volumes this is not a big

problem, however, if the favoured models fluctuate with the volume, we obtain vastly fluctuating data for the ground state energies $m_\pi(L), E_{2\pi}(L)$ and $E_{3\pi}(L)$. This is why we choose the more conservative approach given by a "systematic averaging" of the models. This approach is not only being used for the extrapolation to zero temperature, but also in future calculations.

The very final, model-independent results for $m_\pi(L), E_{2\pi}(L)$ and $E_{3\pi}(L)$ are now given tables H.7,H.8 and H.9. The results for $m_\pi(L)$ were used for the discussion of finite volume effects on the pion mass in the next section.

	Extraction $m_\pi(L)$			Extraction $E_{2\pi}(L)$		Extraction $E_{3\pi}(L)$	
L	$M_{m\pi,1}$	$M_{m\pi,2}$	$M_{m\pi,3}$	$M_{E2\pi,1}$	$M_{E2\pi,2}$	$M_{E3\pi,1}$	$M_{E3\pi,2}$
4	0.85322(30)	0.85340(31)	0.85352(31)	2.52507(87)	2.52566(33)	4.50446(59)	4.5072(11)
6	0.59915(26)	0.59919(26)	0.59937(28)	1.92127(40)	1.92082(20)	3.66680(38)	3.66682(24)
8	0.50842(40)	0.50837(35)	0.50857(34)	1.57875(37)	1.57898(28)	3.08776(41)	3.08788(40)
10	0.47167(85)	0.46953(59)	0.46952(43)	1.36835(73)	1.36806(47)	2.68113(96)	2.67966(66)
12	0.45086(87)	0.44988(59)	0.44989(59)	1.2352(12)	1.23435(75)	2.3858(15)	2.3873(12)
14	0.44348(84)	0.44185(39)	0.44244(54)	1.14266(90)	1.1427(19)	2.1678(13)	2.1658(11)
16	0.43746(93)	0.43591(74)	0.43559(87)	1.0813(16)	1.0799(18)	2.0096(16)	2.0049(20)
18	0.4376(12)	0.43418(58)	0.43393(50)	1.0347(20)	1.0289(16)	1.8816(46)	1.8738(14)
20	0.43395(77)	0.43344(58)	0.43355(67)	0.9990(20)	1.0027(37)	1.7798(23)	1.7817(38)
22	0.43566(82)	0.43273(79)	0.43259(76)	0.9758(33)	0.9723(32)	1.7106(30)	1.7075(44)
24	0.4367(11)	0.43170(42)	0.43187(36)	0.9613(20)	0.9569(59)	1.6460(26)	1.6490(52)
26	0.4320(23)	0.43219(55)	0.43218(49)	0.9401(27)	0.9398(20)	1.6039(24)	1.6016(53)
28	0.43070(94)	0.43413(48)	0.43371(73)	0.9305(18)	0.9363(64)	1.5603(27)	1.5653(82)
30	0.4282(12)	0.43271(56)	0.43226(57)	0.9190(17)	0.9237(55)	1.5245(33)	1.5286(67)
32	0.4325(10)	0.43424(55)	0.43561(67)	0.9180(19)	0.9208(31)	1.5071(28)	1.5085(68)
34	0.4249(16)	0.43185(43)	0.43207(40)	0.9150(25)	0.9251(91)	1.4845(55)	1.4776(66)
36	0.4309(10)	0.43357(73)	0.43415(85)	0.9080(33)	0.912(10)	1.4649(27)	1.4557(65)
38	0.4290(15)	0.43450(63)	0.43436(66)	0.9010(22)	0.911(10)	1.4532(25)	1.460(14)
40	0.4254(12)	0.43385(55)	0.43416(64)	0.8998(18)	0.915(13)	1.4399(33)	1.453(16)

Table H.2: Extracted values of the volume dependent pion masses, 2-pion and 3-pion ground state energies $m_\pi(L), E_{2\pi}(L), E_{3\pi}(L)$, for each volume (dataset A3).

	Extraction $m_\pi(L)$			Extraction $E_{2\pi}(L)$		Extraction $E_{3\pi}(L)$	
L	$M_{m\pi,1}$	$M_{m\pi,2}$	$M_{m\pi,3}$	$M_{E2\pi,1}$	$M_{E2\pi,2}$	$M_{E3\pi,1}$	$M_{E3\pi,2}$
4	0.85634(29)	0.85626(22)	0.85647(22)	2.55702(25)	2.55665(17)	4.59490(66)	4.59768(100)
6	0.56785(17)	0.56785(17)	0.56795(16)	1.903660(84)	1.903708(77)	3.68285(21)	3.68294(17)
8	0.45550(21)	0.45550(20)	0.45540(18)	1.52939(15)	1.52938(11)	3.05828(22)	3.05833(16)
10	0.40205(22)	0.40190(23)	0.40205(22)	1.29602(19)	1.29593(15)	2.61775(38)	2.61784(24)
12	0.37452(25)	0.37449(22)	0.37458(26)	1.14148(32)	1.14126(23)	2.29846(33)	2.29880(40)
14	0.35917(38)	0.35903(26)	0.35907(27)	1.03422(55)	1.03378(32)	2.06002(60)	2.05955(34)
16	0.35008(47)	0.34965(27)	0.34975(23)	0.95635(50)	0.95647(33)	1.87620(87)	1.87602(39)
18	0.34483(37)	0.34502(21)	0.34517(26)	0.90135(71)	0.9022(14)	1.73363(52)	1.73409(70)
20	0.34298(43)	0.34214(31)	0.34209(23)	0.86024(81)	0.8594(16)	1.62245(76)	1.62215(73)
22	0.34144(38)	0.34065(22)	0.34063(22)	0.82240(85)	0.82277(69)	1.5320(11)	1.5329(12)
24	0.33854(90)	0.33947(23)	0.33941(16)	0.7976(13)	0.7982(11)	1.45647(85)	1.45695(96)
26	0.33860(46)	0.33903(23)	0.33892(30)	0.77838(90)	0.7800(13)	1.3977(11)	1.3984(12)
28	0.33653(50)	0.33842(19)	0.33858(17)	0.7621(17)	0.7605(17)	1.3504(12)	1.3486(25)
30	0.33595(88)	0.33849(26)	0.33840(23)	0.74806(87)	0.7508(12)	1.3048(12)	1.3071(18)
32	0.33507(75)	0.33870(22)	0.33859(19)	0.7393(11)	0.7413(13)	1.2706(14)	1.2723(25)
34	0.33415(49)	0.33853(22)	0.33864(18)	0.7301(17)	0.7348(23)	1.2408(16)	1.2424(18)
36	0.33435(53)	0.33818(27)	0.33833(21)	0.7190(14)	0.7226(14)	1.2161(38)	1.2158(32)
38	0.33238(82)	0.33805(25)	0.33814(22)	0.7143(18)	0.7144(17)	1.1935(25)	1.1925(44)
40	0.3304(11)	0.33799(33)	0.33808(26)	0.7121(26)	0.7137(61)	1.1739(29)	1.1755(59)

Table H.3: Extracted values of the volume dependent pion masses, 2-pion and 3-pion ground state energies $m_\pi(L), E_{2\pi}(L), E_{3\pi}(L)$, for each volume (dataset A5).

	Extraction $m_\pi(L)$			Extraction $E_{2\pi}(L)$		Extraction $E_{3\pi}(L)$	
L	$M_{m\pi,1}$	$M_{m\pi,2}$	$M_{m\pi,3}$	$M_{E2\pi,1}$	$M_{E2\pi,2}$	$M_{E3\pi,1}$	$M_{E3\pi,2}$
4	0.86114(21)	0.86114(19)	0.86123(18)	2.57105(17)	2.57117(15)	4.62974(65)	4.63139(50)
6	0.55661(18)	0.55661(18)	0.55667(17)	1.89866(10)	1.89862(10)	3.68860(25)	3.68885(21)
8	0.43398(20)	0.43398(20)	0.43401(20)	1.50921(13)	1.50921(12)	3.04495(21)	3.04503(21)
10	0.37240(21)	0.37241(21)	0.37249(22)	1.26355(26)	1.26377(19)	2.59008(21)	2.59010(21)
12	0.33827(22)	0.33828(22)	0.33831(22)	1.09923(22)	1.09932(22)	2.25841(25)	2.25835(24)
14	0.31791(26)	0.31799(23)	0.31803(22)	0.98396(26)	0.98402(24)	2.00917(30)	2.00913(30)
16	0.30574(28)	0.30569(23)	0.30575(24)	0.89986(31)	0.90006(29)	1.81786(32)	1.81797(33)
18	0.29808(27)	0.29802(20)	0.29805(22)	0.83750(62)	0.83687(42)	1.66775(41)	1.66772(37)
20	0.29325(32)	0.29330(21)	0.29343(22)	0.78955(54)	0.78986(50)	1.54745(42)	1.54784(46)
22	0.29013(33)	0.29071(26)	0.29078(27)	0.75152(53)	0.75176(46)	1.45101(68)	1.45136(60)
24	0.28861(53)	0.28848(24)	0.28854(22)	0.72166(75)	0.72167(62)	1.36954(59)	1.37014(61)
26	0.28737(71)	0.28764(23)	0.28758(25)	0.69856(96)	0.69850(68)	1.3050(15)	1.30530(95)
28	0.28584(40)	0.28660(20)	0.28668(20)	0.67830(58)	0.67922(79)	1.24803(89)	1.24900(91)
30	0.28543(47)	0.28621(20)	0.28628(18)	0.66462(78)	0.66536(81)	1.2035(13)	1.2042(14)
32	0.28500(57)	0.28601(22)	0.28613(19)	0.65041(75)	0.65085(79)	1.16541(92)	1.1675(29)
34	0.28443(50)	0.28612(17)	0.28611(17)	0.64049(82)	0.64015(77)	1.1301(10)	1.1294(10)
36	0.28132(45)	0.28557(19)	0.28572(18)	0.6295(25)	0.6317(22)	1.1006(20)	1.1028(50)
38	0.28282(32)	0.28580(22)	0.28592(20)	0.62395(86)	0.6250(12)	1.0740(13)	1.0744(16)
40	0.28151(53)	0.28568(17)	0.28576(18)	0.6191(10)	0.6139(17)	1.0521(19)	1.0481(19)

Table H.4: Extracted values of the volume dependent pion masses, 2-pion and 3-pion ground state energies $m_\pi(L), E_{2\pi}(L), E_{3\pi}(L)$, for each volume (dataset A7).

	Extraction $m_\pi(L)$			Extraction $E_{2\pi}(L)$		Extraction $E_{3\pi}(L)$	
L	$M_{m\pi,1}$	$M_{m\pi,2}$	$M_{m\pi,3}$	$M_{E2\pi,1}$	$M_{E2\pi,2}$	$M_{E3\pi,1}$	$M_{E3\pi,2}$
4	0.84889(31)	0.84881(24)	0.84903(25)	2.52614(29)	2.52572(19)	4.52904(77)	4.5321(12)
6	0.53958(20)	0.53958(20)	0.53969(19)	1.86239(14)	1.86244(12)	3.61761(33)	3.61782(26)
8	0.40552(29)	0.40555(27)	0.40543(23)	1.467772(84)	1.467838(84)	2.97975(27)	2.97998(22)
10	0.33219(24)	0.33220(23)	0.33230(24)	1.21211(17)	1.212060(85)	2.52044(28)	2.52070(27)
12	0.28766(31)	0.28760(30)	0.28765(35)	1.03610(17)	1.03629(21)	2.18097(31)	2.18112(30)
14	0.25836(45)	0.25822(39)	0.25816(42)	0.90972(48)	0.90893(24)	1.92263(69)	1.92247(40)
16	0.23769(48)	0.23745(39)	0.23749(31)	0.81420(43)	0.81426(27)	1.71974(59)	1.71976(43)
18	0.22389(49)	0.22394(38)	0.22408(48)	0.74374(65)	0.7448(19)	1.55941(59)	1.55968(62)
20	0.21551(70)	0.21485(54)	0.21460(50)	0.68989(85)	0.6883(18)	1.43204(88)	1.43187(81)
22	0.21086(92)	0.20845(57)	0.20940(49)	0.63894(86)	0.63962(70)	1.3270(13)	1.3285(20)
24	0.20292(85)	0.20297(53)	0.20307(59)	0.6032(12)	0.6039(11)	1.2364(10)	1.23678(87)
26	0.20005(94)	0.19950(49)	0.19973(52)	0.5758(12)	0.5781(26)	1.1634(16)	1.1642(13)
28	0.19816(96)	0.19725(54)	0.19740(66)	0.5504(19)	0.5492(11)	1.1065(13)	1.1034(27)
30	0.19519(90)	0.19617(47)	0.19660(62)	0.5294(11)	0.5338(26)	1.0465(14)	1.0517(33)
32	0.1950(11)	0.19454(60)	0.19474(84)	0.5120(13)	0.5136(15)	1.0022(16)	1.0034(31)
34	0.1963(11)	0.19392(65)	0.19451(81)	0.4994(14)	0.5049(31)	0.9618(17)	0.9643(29)
36	0.1950(12)	0.19178(73)	0.19237(79)	0.4820(14)	0.4889(20)	0.9251(22)	0.9276(25)
38	0.1916(13)	0.19245(81)	0.19355(83)	0.4768(21)	0.4771(36)	0.8974(32)	0.8936(64)
40	0.1896(17)	0.19119(78)	0.1914(10)	0.4598(23)	0.4641(30)	0.8575(36)	0.8596(28)

Table H.5: Extracted values of the volume dependent pion masses, 2-pion and 3-pion ground state energies $m_\pi(L), E_{2\pi}(L), E_{3\pi}(L)$, for each volume (dataset B5).

	Extraction $m_\pi(L)$			Extraction $E_{2\pi}(L)$		Extraction $E_{3\pi}(L)$	
L	$M_{m\pi,1}$	$M_{m\pi,2}$	$M_{m\pi,3}$	$M_{E2\pi,1}$	$M_{E2\pi,2}$	$M_{E3\pi,1}$	$M_{E3\pi,2}$
4	0.85731(23)	0.85731(19)	0.85737(19)	2.54859(19)	2.54868(19)	4.58007(70)	4.58188(56)
6	0.54011(18)	0.54011(18)	0.54014(17)	1.87219(10)	1.87221(10)	3.64358(28)	3.64380(20)
8	0.40352(18)	0.40352(18)	0.40354(19)	1.470410(82)	1.470410(80)	2.99319(25)	2.99329(20)
10	0.32808(24)	0.32805(23)	0.32810(21)	1.20976(18)	1.210004(93)	2.52627(21)	2.52641(24)
12	0.28093(22)	0.28092(22)	0.28090(21)	1.03020(13)	1.03021(11)	2.18034(26)	2.18038(26)
14	0.24918(25)	0.24925(23)	0.24923(23)	0.90033(16)	0.90037(15)	1.91659(29)	1.91661(28)
16	0.22737(33)	0.22729(27)	0.22733(26)	0.80300(22)	0.80314(21)	1.71141(35)	1.71153(35)
18	0.21224(33)	0.21193(28)	0.21204(26)	0.72836(57)	0.72802(31)	1.54819(36)	1.54842(49)
20	0.20045(35)	0.20041(29)	0.20069(32)	0.66968(46)	0.67015(43)	1.41533(41)	1.41583(44)
22	0.19303(59)	0.19280(36)	0.19284(37)	0.62222(51)	0.62243(43)	1.30740(76)	1.30790(71)
24	0.18635(54)	0.18647(44)	0.18645(39)	0.58336(88)	0.58353(58)	1.21524(59)	1.21612(62)
26	0.1841(10)	0.18241(37)	0.18271(50)	0.5522(12)	0.55266(64)	1.1416(17)	1.1417(12)
28	0.17860(98)	0.17858(39)	0.17880(39)	0.52526(92)	0.52659(87)	1.07363(96)	1.07515(92)
30	0.1759(11)	0.17583(49)	0.17576(54)	0.50472(93)	0.5060(12)	1.0198(17)	1.0209(24)
32	0.17538(93)	0.17417(58)	0.17440(48)	0.4845(10)	0.48526(90)	0.9741(12)	0.9745(26)
34	0.17501(83)	0.17306(51)	0.17388(62)	0.4689(10)	0.46977(75)	0.9305(12)	0.9304(11)
36	0.1725(12)	0.17208(53)	0.17196(46)	0.4560(27)	0.4573(18)	0.8952(17)	0.8929(42)
38	0.17237(81)	0.17060(51)	0.17105(82)	0.4449(13)	0.4468(19)	0.8582(16)	0.8590(18)
40	0.1705(14)	0.17061(41)	0.17114(48)	0.4351(17)	0.4327(32)	0.8269(23)	0.8288(21)

Table H.6: Extracted values of the volume dependent pion masses, 2-pion and 3-pion ground state energies $m_\pi(L), E_{2\pi}(L), E_{3\pi}(L)$, for each volume (dataset B7).

	$m_\pi(L)$				
L	A3	A5	A7	B5	B7
4	0.85337(33)	0.85636(25)	0.86118(20)	0.84891(28)	0.85733(20)
6	0.59923(28)	0.56788(17)	0.55663(18)	0.53962(20)	0.54012(18)
8	0.50846(37)	0.45546(21)	0.43399(20)	0.40549(26)	0.40353(18)
10	0.46983(94)	0.40201(23)	0.37243(22)	0.33223(24)	0.32808(23)
12	0.45007(76)	0.37453(24)	0.33829(22)	0.28763(32)	0.28092(22)
14	0.44223(75)	0.35907(29)	0.31798(24)	0.25824(43)	0.24922(24)
16	0.4362(11)	0.34975(31)	0.30573(25)	0.23751(38)	0.22733(28)
18	0.4344(12)	0.34504(28)	0.29805(23)	0.22396(45)	0.21205(31)
20	0.43360(69)	0.34225(44)	0.29334(25)	0.21489(66)	0.20052(34)
22	0.4336(16)	0.34075(37)	0.29060(39)	0.20927(99)	0.19286(42)
24	0.4321(12)	0.33941(26)	0.28852(27)	0.20300(62)	0.18644(45)
26	0.43218(63)	0.33894(33)	0.28760(29)	0.19966(60)	0.18264(66)
28	0.4335(14)	0.33839(52)	0.28655(34)	0.19745(73)	0.17868(47)
30	0.4321(15)	0.33835(55)	0.28619(31)	0.19616(75)	0.17581(60)
32	0.4345(12)	0.33851(71)	0.28602(35)	0.19466(79)	0.17445(71)
34	0.4317(13)	0.3383(12)	0.28602(44)	0.1945(12)	0.17369(95)
36	0.4332(15)	0.3379(11)	0.2853(12)	0.1925(14)	0.17206(59)
38	0.4340(17)	0.3379(11)	0.2854(12)	0.1928(12)	0.17109(97)
40	0.4331(27)	0.3378(14)	0.28551(94)	0.1910(12)	0.17082(59)

Table H.7: Extracted values of the volume dependent pion masses $m_\pi(L)$, for each volume and for all datasets after the systematic averaging.

	$E_{2\pi}(L)$				
L	A3	A5	A7	B5	B7
4	2.52559(48)	2.55677(26)	2.57112(17)	2.52585(30)	2.54864(20)
6	1.92091(31)	1.903686(84)	1.89864(10)	1.86241(13)	1.87220(10)
8	1.57890(34)	1.52938(13)	1.50921(12)	1.467805(90)	1.470410(81)
10	1.36815(57)	1.29596(17)	1.26370(24)	1.21207(11)	1.20995(15)
12	1.23459(98)	1.14133(28)	1.09928(22)	1.03618(21)	1.03021(12)
14	1.1427(12)	1.03389(44)	0.98399(25)	0.90909(44)	0.90035(15)
16	1.0807(18)	0.95644(39)	0.89996(32)	0.81424(33)	0.80307(22)
18	1.0311(33)	0.90153(95)	0.83707(57)	0.74385(93)	0.72810(41)
20	0.9998(29)	0.8601(11)	0.78972(54)	0.6896(13)	0.66993(50)
22	0.9740(36)	0.82262(78)	0.75166(50)	0.63935(84)	0.62234(48)
24	0.9609(29)	0.7979(12)	0.72167(68)	0.6036(12)	0.58348(69)
26	0.9399(23)	0.7789(13)	0.69852(79)	0.5762(18)	0.55255(82)
28	0.9309(28)	0.7613(19)	0.67863(79)	0.5496(15)	0.5260(11)
30	0.9194(26)	0.7490(16)	0.66498(88)	0.5301(22)	0.5052(12)
32	0.9188(26)	0.7401(15)	0.65062(80)	0.5127(16)	0.4849(10)
34	0.9157(42)	0.7318(30)	0.64031(82)	0.5003(27)	0.46946(96)
36	0.9084(46)	0.7207(23)	0.6308(26)	0.4843(37)	0.4569(22)
38	0.9015(37)	0.7143(18)	0.6243(11)	0.4769(25)	0.4455(18)
40	0.9001(32)	0.7123(34)	0.6177(26)	0.4614(33)	0.4346(23)

Table H.8: Extracted values of the volume dependent 2-pion ground state energies $E_{2\pi}(L)$, for each volume and for all datasets after the systematic averaging.

	$E_{3\pi}(L)$				
L	A3	A5	A7	B5	B7
4	4.5051(14)	4.5957(15)	4.63079(97)	4.5300(17)	4.5812(11)
6	3.66682(29)	3.68291(19)	3.68875(26)	3.61774(31)	3.64373(25)
8	3.08782(41)	3.05831(18)	3.04499(21)	2.97988(27)	2.99325(23)
10	2.6801(10)	2.61782(29)	2.59009(21)	2.52057(30)	2.52633(24)
12	2.3867(15)	2.29859(40)	2.25838(24)	2.18105(31)	2.18036(26)
14	2.1666(16)	2.05966(47)	2.00915(30)	1.92251(49)	1.91660(28)
16	2.0079(29)	1.87605(51)	1.81791(33)	1.71976(49)	1.71147(35)
18	1.8745(29)	1.73379(63)	1.66773(38)	1.55954(62)	1.54827(42)
20	1.7803(29)	1.62229(76)	1.54762(48)	1.43195(85)	1.41556(49)
22	1.7096(38)	1.5324(12)	1.45120(66)	1.3274(17)	1.30767(77)
24	1.6466(35)	1.45668(93)	1.36983(67)	1.23660(96)	1.21565(75)
26	1.6035(32)	1.3980(12)	1.3052(11)	1.1639(15)	1.1416(14)
28	1.5607(39)	1.3501(17)	1.2485(10)	1.1059(21)	1.0744(12)
30	1.5253(45)	1.3056(18)	1.2038(14)	1.0473(26)	1.0202(20)
32	1.5073(37)	1.2711(19)	1.1656(14)	1.0025(21)	0.9741(15)
34	1.4817(69)	1.2414(19)	1.1298(11)	0.9625(24)	0.9304(11)
36	1.4636(48)	1.2159(35)	1.1009(28)	0.9262(27)	0.8949(23)
38	1.4534(37)	1.1933(31)	1.0742(14)	0.8966(44)	0.8585(18)
40	1.4405(54)	1.1742(37)	1.0501(27)	0.8588(33)	0.8279(24)

Table H.9: Extracted values of the volume dependent 3-pion ground state energies $E_{3\pi}(L)$, for each volume and for all datasets after the systematic averaging.

H.3 Extrapolation to infinite volume and extraction of $a^2\lambda$ and $a^2F(0)$

By utilizing the final model-independent results for $m_\pi(L)$ in table H.7, we can use Lüscher's formula, that is eq. (2.63)

$$m_\pi(L) = m_\pi + \left(\frac{\lambda^2}{4\sqrt{3}m_\pi^3}\right) e^{-\frac{\sqrt{3}}{2}m_\pi L} + \frac{1}{\sqrt{m_\pi L}}\left(\frac{F(0)}{4m_\pi\sqrt{2\pi}}\right) e^{-m_\pi L}, \tag{H.20}$$

and determine the infinite volume pion mass $m_\pi = \lim_{L\to\infty} m_\pi(L)$, the 3-pion coupling λ and the forwards scattering amplitude $F(0)$. Also here, we perform a combination of Bayesian model averaging and systematic averaging, as explained in chapter F. The fit functions we use are variations of eq. (H.20) and given by

$$\mathrm{M}_1^{\mathrm{FVE}}(L) = m_\pi + \left(\frac{\lambda^2}{4\sqrt{3}m_\pi^3}\right) e^{-\frac{\sqrt{3}}{2}m_\pi L} + \frac{1}{\sqrt{m_\pi L}}\left(\frac{F(0)}{4m_\pi\sqrt{2\pi}}\right) e^{-m_\pi L}, \tag{H.21}$$

$$\mathrm{M}_2^{\mathrm{FVE}}(L) = m_\pi + \left(\frac{\lambda^2}{4\sqrt{3}m_\pi^3}\right) e^{-\frac{\sqrt{3}}{2}m_\pi L}, \tag{H.22}$$

$$\mathrm{M}_3^{\mathrm{FVE}}(L) = m_\pi + \frac{1}{\sqrt{m_\pi L}}\left(\frac{F(0)}{4m_\pi\sqrt{2\pi}}\right) e^{-m_\pi L}, \tag{H.23}$$

with varying fit ranges from $L^{\min}$ to $L^{\max}$. The fit ranges have been chosen based on the dataset and not based on the model. Only the lower boundaries have been varied among the datasets, to ensure good quality fits

$$\text{A3}: \quad L^{\min} \in \{4,6,8\} \qquad L^{\max} \in \{16,18,\ldots,40\}, \tag{H.24}$$

$$\text{A5}: \quad L^{\min} \in \{4,6,8,10\} \qquad L^{\max} \in \{16,18,\ldots,40\}, \tag{H.25}$$

$$\text{A7}: \quad L^{\min} \in \{4,6,8,10\} \qquad L^{\max} \in \{16,18,\ldots,40\}, \tag{H.26}$$

$$\text{B5}: \quad L^{\min} \in \{4,6,8,10\} \qquad L^{\max} \in \{16,18,\ldots,40\}, \tag{H.27}$$

$$\text{B7}: \quad L^{\min} \in \{4,6,8,10,12\} \qquad L^{\max} \in \{16,18,\ldots,40\}. \tag{H.28}$$

The next step is to perform those fits and perform Bayesian model averaging to get separate model-dependent values for the infinite volume pion mass m_π, the 3-pion coupling and the forward scattering amplitude. The results are summarized in tables H.10 to H.14.

In each table we first show the results for $\mathrm{M}_1^{\mathrm{FVE}}$, then $\mathrm{M}_2^{\mathrm{FVE}}$ and finally $\mathrm{M}_3^{\mathrm{FVE}}$. However, we only show the fits which have $\chi^2/\text{d.o.f} \leq 2.0$ and where the relative errors on the fit parameters do not exceed 50%. As a result we can see that for all datasets the third model $\mathrm{M}_3^{\mathrm{FVE}}$ can be completely discarded, not yielding a single reasonable fit. This indicates, that the contributions arising from the 3-pion coupling are more dominant than the ones from the forward scattering term. For the smaller pion mass $m_\pi/g \approx 0.44$, i.e. dataset B5 and B7 (table H.13 and H.14), we can see that the complete fit function $\mathrm{M}_1^{\mathrm{FVE}}$ is necessary to obtain a reasonable fit. This is reasonable, given that we are working in a much smaller volume. On the other hand for datasets A5 and A7 (table H.11 and H.12) the only model yielding good results is $\mathrm{M}_2^{\mathrm{FVE}}$. Intuitively one would think that also $\mathrm{M}_1^{\mathrm{FVE}}$ would describe the data well, however, as it turns out, the fit parameters become numerically unstable after adding the additional fitting term proportional to $F(0)$.

We summarize, that for all datasets $\mathrm{M}_3^{\mathrm{FVE}}$ needs to be completely discarded. In addition to that, we discard $\mathrm{M}_1^{\mathrm{FVE}}$ for A5 and A7, and $\mathrm{M}_2^{\mathrm{FVE}}$ for B5 and B7. This means that for A5, A7, B5 and B7 we only consider results from one fit model and we directly adopt the results obtained after Bayesian model averaging. For dataset A3 we must perform systematic averaging as explained in section F.4. The model-dependent results are depicted in table H.15, after the systematic averaging we obtain the very final model-independent results shown in table H.16.

am_π	$a^2\lambda$	$a^2F(0)$	fit range	χ^2/ndof	ndof
0.43421(58)	0.853(13)	2.90(44)	6 - 18	1.80	4
0.43366(45)	0.861(12)	2.62(39)	6 - 20	1.89	5
0.43363(45)	0.862(12)	2.60(39)	6 - 22	1.59	6
0.43343(43)	0.864(12)	2.50(39)	6 - 24	1.62	7
0.43304(35)	0.870(11)	2.29(36)	6 - 26	1.81	8
0.43306(34)	0.870(11)	2.31(35)	6 - 28	1.62	9
0.43301(33)	0.870(11)	2.28(35)	6 - 30	1.50	10
0.43311(32)	0.869(11)	2.33(35)	6 - 32	1.48	11
0.43304(31)	0.870(11)	2.29(35)	6 - 34	1.44	12
0.43304(30)	0.870(11)	2.30(35)	6 - 36	1.33	13
0.43307(30)	0.869(11)	2.31(35)	6 - 38	1.26	14
0.43307(30)	0.869(11)	2.31(35)	6 - 40	1.17	15
0.43329(42)	0.9239(23)	-	8 - 20	0.90	5
0.43328(41)	0.9239(23)	-	8 - 22	0.75	6
0.43314(40)	0.9239(23)	-	8 - 24	0.81	7
0.43286(34)	0.9240(23)	-	8 - 26	0.96	8
0.43289(32)	0.9240(23)	-	8 - 28	0.88	9
0.43285(32)	0.9240(23)	-	8 - 30	0.82	10
0.43295(31)	0.9240(23)	-	8 - 32	0.90	11
0.43289(30)	0.9240(23)	-	8 - 34	0.89	12
0.43290(29)	0.9240(23)	-	8 - 36	0.82	13
0.43293(29)	0.9240(23)	-	8 - 38	0.79	14
0.43293(29)	0.9240(23)	-	8 - 40	0.74	15

Table H.10: Results for the finite volume fits of the 1-pion ground state energies (resp. pion mass m_π) for dataset A3. We only show results with χ^2/d.o.f ≤ 2.0 and relative error on the fit parameters smaller than 50%. The first fits are given by $\mathrm{M}_1^{\mathrm{FVE}}(L)$ (both fitting contributions), the second ones by $\mathrm{M}_2^{\mathrm{FVE}}(L)$ (only one contribution proportional to λ^2). At the very bottom, we would have fits performed with $\mathrm{M}_3^{\mathrm{FVE}}(L)$, however, this fit model is unreliable and we have no fits to present.

am_π	$a^2\lambda$	$a^2F(0)$	fit range	χ^2/ndof	ndof
0.33912(19)	0.56704(92)	-	10 - 22	1.28	5
0.33889(16)	0.56727(91)	-	10 - 24	1.99	6
0.33875(14)	0.56741(90)	-	10 - 28	1.99	8
0.33872(13)	0.56745(90)	-	10 - 30	1.89	9
0.33871(13)	0.56746(90)	-	10 - 32	1.72	10
0.33870(13)	0.56746(90)	-	10 - 34	1.58	11
0.33869(13)	0.56747(90)	-	10 - 36	1.49	12
0.33868(13)	0.56748(90)	-	10 - 38	1.41	13
0.33868(13)	0.56749(90)	-	10 - 40	1.34	14

Table H.11: Results for the finite volume fits of the 1-pion ground state energies (resp. pion mass m_π) for dataset A5. We only show results with χ^2/d.o.f ≤ 2.0 and relative error on the fit parameters smaller than 50%. The first fits would be given by $\mathrm{M}_1^{\mathrm{FVE}}(L)$ (both fitting contributions), however, as we see, we do not obtain any reliable fits for dataset A5. The second fits are given by $\mathrm{M}_2^{\mathrm{FVE}}(L)$ (only one contribution proportional to λ^2), these are the only ones which work here. The fits performed with $\mathrm{M}_3^{\mathrm{FVE}}(L)$ are of bad quality, which is why they do not show up as well.

am_π	$a^2\lambda$	$a^2F(0)$	fit range	χ^2/ndof	ndof
0.28612(17)	0.40810(43)	-	10 - 22	0.66	5
0.28605(15)	0.40805(42)	-	10 - 24	0.68	6
0.28603(13)	0.40804(42)	-	10 - 26	0.59	7
0.28597(12)	0.40801(42)	-	10 - 28	0.73	8
0.28592(12)	0.40798(42)	-	10 - 30	0.81	9
0.28589(11)	0.40796(42)	-	10 - 32	0.78	10
0.28589(11)	0.40796(42)	-	10 - 34	0.72	11
0.28588(11)	0.40796(42)	-	10 - 36	0.69	12
0.28588(11)	0.40795(42)	-	10 - 38	0.66	13
0.28587(11)	0.40795(42)	-	10 - 40	0.62	14

Table H.12: Results for the finite volume fits of the 1-pion ground state energies (resp. pion mass m_π) for dataset A7. We only show results with χ^2/d.o.f ≤ 2.0 and relative error on the fit parameters smaller than 50%. The first fits would be given by $\mathrm{M}_1^{\mathrm{FVE}}(L)$ (both fitting contributions), however, as we see, we do not obtain any reliable fits for dataset A7. The second fits are given by $\mathrm{M}_2^{\mathrm{FVE}}(L)$ (only one contribution proportional to λ^2), these are the only ones which work. The fits performed with $\mathrm{M}_3^{\mathrm{FVE}}(L)$ are of bad quality and do not show up.

am_π	$a^2\lambda$	$a^2F(0)$	fit range	χ^2/ndof	ndof
0.19333(95)	0.1508(25)	1.002(82)	10 - 22	0.65	4
0.19271(72)	0.1517(22)	0.958(68)	10 - 24	0.70	5
0.19237(55)	0.1523(20)	0.934(59)	10 - 26	0.68	6
0.19227(47)	0.1525(19)	0.926(55)	10 - 28	0.60	7
0.19229(42)	0.1524(19)	0.928(52)	10 - 30	0.52	8
0.19222(38)	0.1526(19)	0.922(50)	10 - 32	0.48	9
0.19226(37)	0.1525(18)	0.925(50)	10 - 34	0.44	10
0.19219(36)	0.1526(18)	0.919(49)	10 - 36	0.45	11
0.19216(34)	0.1527(18)	0.916(48)	10 - 38	0.42	12
0.19201(33)	0.1530(18)	0.903(47)	10 - 40	0.57	13

Table H.13: Results for the finite volume fits of the 1-pion ground state energies (resp. pion mass m_π) for dataset B5. We only show results with χ^2/d.o.f ≤ 2.0 and relative error on the fit parameters smaller than 50%. The first fits are given by $\mathrm{M}_1^{\mathrm{FVE}}(L)$ (both fitting contributions). Next we would have fits performed with $\mathrm{M}_2^{\mathrm{FVE}}(L)$ and $\mathrm{M}_3^{\mathrm{FVE}}(L)$, but since they are of bad quality they do not show up here.

am_π	$a^2\lambda$	$a^2F(0)$	fit range	χ^2/ndof	ndof
0.17322(60)	0.1163(11)	0.916(37)	10 - 22	0.93	4
0.17251(51)	0.1168(10)	0.883(33)	10 - 24	1.52	5
0.17237(46)	0.1170(10)	0.876(31)	10 - 26	1.34	6
0.17146(71)	0.1209(20)	0.751(67)	12 - 24	0.73	4
0.17144(62)	0.1210(19)	0.750(62)	12 - 26	0.59	5
0.17083(48)	0.1221(17)	0.702(54)	12 - 28	0.90	6
0.17042(43)	0.1229(16)	0.669(50)	12 - 30	1.20	7
0.17028(39)	0.1232(15)	0.657(47)	12 - 32	1.12	8
0.17028(37)	0.1232(15)	0.657(46)	12 - 34	1.00	9
0.17008(32)	0.1236(14)	0.640(42)	12 - 36	1.03	10
0.17000(31)	0.1238(14)	0.632(41)	12 - 38	1.00	11
0.16987(28)	0.1241(14)	0.621(40)	12 - 40	0.98	12

Table H.14: Results for the finite volume fits of the 1-pion ground state energies (resp. pion mass m_π) for dataset B7. We only show results with χ^2/d.o.f $\leq$ 2.0 and relative error on the fit parameters smaller than 50%. The first fits are given by $\mathrm{M}_1^{\mathrm{FVE}}(L)$ (both fitting contributions). Fits performed with $\mathrm{M}_2^{\mathrm{FVE}}(L)$ and $\mathrm{M}_3^{\mathrm{FVE}}(L)$ are of bad quality and do not show up here.

Dataset	$(am_\pi)_{\mathrm{M}_1^{\mathrm{FVE}}}$	$(am_\pi)_{\mathrm{M}_2^{\mathrm{FVE}}}$	$(am_\pi)_{av.}$	$(a^2F(0))_{\mathrm{M}_1^{\mathrm{FVE}}}$	$(a^2F(0))_{\mathrm{M}_2^{\mathrm{FVE}}}$	$(a^2F(0))_{av.}$
A3	0.7501(5)	0.7499(5)	0.7500(5)	2.31(35)	N/A	2.31(35)
A5	N/A	0.7574(3)	0.7574(3)	N/A	N/A	N/A
A7	N/A	0.7564(3)	0.7564(3)	N/A	N/A	N/A
B5	0.4296(8)	N/A	0.4296(8)	0.913(49)	N/A	0.913(49)
B7	0.450(2)	N/A	0.450(2)	0.644(63)	N/A	0.644(63)
Dataset	$(a^2\lambda)_{\mathrm{M}_1^{\mathrm{FVE}}}$	$(a^2\lambda)_{\mathrm{M}_2^{\mathrm{FVE}}}$	$(a^2\lambda)_{av.}$	$(\lambda/g^2)_{\mathrm{M}_1^{\mathrm{FVE}}}$	$(\lambda/g^2)_{\mathrm{M}_2^{\mathrm{FVE}}}$	$(\lambda/g^2)_{av.}$
A3	0.869(11)	0.9240(23)	0.922(11)	2.608(33)	2.7720(68)	2.765(34)
A5	N/A	0.56747(90)	0.56747(90)	N/A	2.8373(45)	2.8373(45)
A7	N/A	0.40796(42)	0.40796(42)	N/A	2.8557(29)	2.8557(29)
B5	0.1528(18)	N/A	0.1528(18)	0.7639(91)	N/A	0.7639(91)
B7	0.1235(19)	N/A	0.1235(19)	0.865(13)	N/A	0.865(13)

Table H.15: Results for the different parameters describing finite volume effects after performing Bayesian model averaging.

Dataset	m_π/g	$a^2\lambda$	λ/g^2	$a^2F(0)$
A3	0.7500(5)	0.922(11)	2.765(34)	2.31(35)
A5	0.7574(3)	0.56747(90)	2.8373(45)	N/A
A7	0.7564(3)	0.40796(42)	2.8557(29)	N/A
B5	0.4296(8)	0.1528(18)	0.7639(91)	0.913(49)
B7	0.450(2)	0.1235(19)	0.865(13)	0.644(63)

Table H.16: Final model-independent results for the 3-pion coupling and the forward scattering amplitude $a^2\lambda$, λ/g^2 and $a^2F(0)$, after systematic averaging.

H.4 Scattering phase shift

In this section we want to provide the details, which have been omitted during the discussion of the scattering phase shift in section 5.4. After extracting the infinite volume pion mass m_π and the 2-pion ground state energies $E_{2\pi}(L)$, as explained in section H.2 and section H.3, we can discuss the extraction of the scattering phase shift via

$$\delta(k(L)) = -\frac{kL}{2} \equiv \delta(L), \tag{H.29}$$

where the relative momentum k is extracted from the bosonic lattice dispersion relation given by

$$E_{2\pi}(L) = 2\cosh^{-1}(\cosh(m_\pi) + 1 - \cos(k(L))). \tag{H.30}$$

The numerical results for the scattering phase shift $\delta(x)$, with $x = x(L) = \frac{k(L)}{m_\pi}$ are given by table H.18 and H.17.

	A3		
L	$x = x(L)$	$\delta(x(L)) = \delta(L)$	$ak(L)$
4	3.1953(28)	0.37447(83)	1.38356(41)
6	2.1490(20)	0.35002(82)	0.93052(27)
8	1.6086(17)	0.3555(12)	0.69652(31)
10	1.2727(17)	0.3863(24)	0.55106(47)
12	1.0492(22)	0.4157(47)	0.45432(78)
14	0.8847(27)	0.4601(72)	0.3831(10)
16	0.7649(40)	0.492(13)	0.3312(17)
18	0.6608(77)	0.566(30)	0.2861(33)
20	0.5891(72)	0.591(31)	0.2551(31)
22	0.5250(96)	0.641(45)	0.2273(41)
24	0.4900(83)	0.595(43)	0.2122(36)
26	0.4297(71)	0.723(40)	0.1860(30)
28	0.4014(93)	0.708(56)	0.1738(40)
30	0.3630(93)	0.784(60)	0.1572(40)
32	0.3606(95)	0.643(66)	0.1561(41)
34	0.350(15)	0.57(11)	0.1514(67)
36	0.322(19)	0.63(15)	0.1395(81)
38	0.294(16)	0.72(13)	0.1274(69)
40	0.288(14)	0.65(12)	0.1247(62)

Table H.17: Scattering phase shifts $\delta(x)$, as a function of $x = \frac{k}{m_\pi}$ for dataset A3.

	A5			A7		
L	$x = x(L)$	$\delta(x(L)) = \delta(L)$	$ak(L)$	$x = x(L)$	$\delta(x(L)) = \delta(L)$	$ak(L)$
4	4.2729(22)	0.24713(44)	1.44723(22)	5.1634(21)	0.18938(29)	1.47610(15)
6	2.8483(15)	0.24746(26)	0.964711(85)	3.4337(14)	0.19669(24)	0.981634(79)
8	2.1294(12)	0.25673(45)	0.72122(11)	2.5667(12)	0.20653(35)	0.733767(89)
10	1.6905(11)	0.27881(73)	0.57256(15)	2.0394(11)	0.22642(78)	0.58303(16)
12	1.3939(11)	0.3089(13)	0.47211(22)	1.68467(99)	0.25193(91)	0.48161(15)
14	1.1793(13)	0.3457(24)	0.39941(34)	1.4295(10)	0.2809(13)	0.40867(18)
16	1.0161(12)	0.3885(26)	0.34414(33)	1.2364(11)	0.3139(19)	0.35346(23)
18	0.8933(25)	0.4187(71)	0.30254(79)	1.0851(17)	0.3497(38)	0.31021(43)
20	0.7946(28)	0.4505(93)	0.26911(93)	0.9653(16)	0.3821(42)	0.27595(42)
22	0.6988(22)	0.5381(80)	0.23668(73)	0.8635(16)	0.4261(45)	0.24687(41)
24	0.6308(36)	0.578(14)	0.2137(12)	0.7786(21)	0.4707(70)	0.22257(58)
26	0.5748(41)	0.611(18)	0.1947(14)	0.7090(25)	0.5066(91)	0.20269(70)
28	0.5190(62)	0.681(29)	0.1758(21)	0.6455(27)	0.558(11)	0.18454(76)
30	0.4772(57)	0.717(29)	0.1616(19)	0.5994(31)	0.571(13)	0.17134(87)
32	0.4452(58)	0.729(31)	0.1508(19)	0.5479(31)	0.636(14)	0.15662(87)
34	0.413(12)	0.762(68)	0.1400(40)	0.5085(33)	0.670(16)	0.14536(94)
36	0.367(10)	0.903(62)	0.1244(35)	0.470(11)	0.724(56)	0.1343(31)
38	0.3383(84)	0.965(54)	0.1146(28)	0.4421(49)	0.740(27)	0.1264(14)
40	0.329(17)	0.92(11)	0.1113(56)	0.412(12)	0.785(69)	0.1178(35)
	B5			B7		
L	$x = x(L)$	$\delta(x(L)) = \delta(L)$	$ak(L)$	$x = x(L)$	$\delta(x(L)) = \delta(L)$	$ak(L)$
4	7.606(15)	0.21889(50)	1.46135(25)	8.723(32)	0.17335(38)	1.48412(19)
6	5.128(10)	0.18596(36)	0.98521(12)	5.856(22)	0.15273(42)	0.99629(14)
8	3.8637(77)	0.17230(46)	0.74232(11)	4.407(17)	0.14253(64)	0.74977(16)
10	3.0873(64)	0.17584(68)	0.59315(14)	3.521(14)	0.1462(10)	0.59907(20)
12	2.5621(56)	0.1881(11)	0.49224(19)	2.923(12)	0.1579(14)	0.49728(23)
14	2.1819(52)	0.2072(22)	0.41920(32)	2.492(10)	0.1737(19)	0.42399(27)
16	1.8945(46)	0.2298(22)	0.36398(27)	2.1671(95)	0.1921(25)	0.36868(31)
18	1.6769(53)	0.2420(56)	0.32218(62)	1.9129(90)	0.2125(37)	0.32545(41)
20	1.5051(57)	0.2498(81)	0.28918(81)	1.7120(84)	0.2289(47)	0.29127(47)
22	1.3413(47)	0.3069(65)	0.25770(59)	1.5439(80)	0.2523(53)	0.26266(49)
24	1.2207(56)	0.327(10)	0.23452(85)	1.4030(79)	0.2773(73)	0.23869(61)
26	1.1253(73)	0.331(16)	0.2162(12)	1.2877(80)	0.2937(91)	0.21907(70)
28	1.0290(65)	0.374(15)	0.1977(11)	1.1855(84)	0.318(12)	0.20170(89)
30	0.9558(90)	0.387(24)	0.1836(16)	1.1032(88)	0.326(15)	0.18769(99)
32	0.8882(73)	0.411(20)	0.1706(13)	1.0205(84)	0.364(15)	0.17361(94)
34	0.838(12)	0.404(37)	0.1610(22)	0.9549(83)	0.380(16)	0.16246(95)
36	0.771(17)	0.475(57)	0.1481(31)	0.900(13)	0.385(34)	0.1531(19)
38	0.738(12)	0.446(41)	0.1419(22)	0.849(11)	0.399(29)	0.1444(15)
40	0.668(16)	0.575(61)	0.1283(31)	0.798(13)	0.428(41)	0.1357(20)

Table H.18: Scattering phase shifts $\delta(x)$, as a function of $x = \frac{k}{m_\pi}$ for the four datasets A5, A7, B5 and B7.

H.5 Effective range expansion

After calculating $\delta(x(L)) \equiv \delta(L)$, we can use the data and fit it to some ansatz. Motivated by the discussion in subsection 2.7.2 we will fit the data to a so-called effective range expansion, given by eq. (2.102), that is

$$k \tan(\delta_0(k)) = \frac{1}{a_0} + \frac{r_0}{2} k^2 + \mathcal{O}(k^4), \tag{H.31}$$

where a_0 denotes the scattering length and r_0 the effective range. From the extracted scattering phase shifts we compute $f(x) = x \tan(\delta(x(L)))$, which can be described using the following three fit models, motivated by the effective range expansion

$$\mathrm{M}_1^\delta(x, c_0, c_1) = c_0 + c_1 x^2 \tag{H.32}$$

$$\mathrm{M}_2^\delta(x, c_0, c_1, c_2) = c_0 + c_1 x^2 + c_2 x^4 \tag{H.33}$$

$$\mathrm{M}_3^\delta(x, c_0, c_1, c_2, c_3) = c_0 + c_1 x^2 + c_2 x^4 + c_3 x^6, \tag{H.34}$$

where $c_0 = 1/(m_\pi a_0)$ and $c_1 = \frac{1}{2}(m_\pi r_0)$. The fit ranges used for each model are characterized by values of $x = x(L)$, the larger the volume L the smaller is $x(L)$. For each model we perform fits for different fit ranges which are then being averaged using Bayesian model averaging. The fit ranges are given by

$$\mathrm{M}_1^\delta(x, c_0, c_1), \quad x_{min} \in \{x(L = 40), x(38), \ldots, x(34)\}, \qquad x_{max} \in \{x(16), \ldots, x(4)\} \tag{H.35}$$

$$\mathrm{M}_2^\delta(x, c_0, c_1, c_2), \quad x_{min} \in \{x(40), x(38), \ldots, x(34)\}, \qquad x_{max} \in \{x(10), \ldots, x(4)\} \tag{H.36}$$

$$\mathrm{M}_3^\delta(x, c_0, c_1, c_2, c_3), \quad x_{min} \in \{x(40), x(38), \ldots, x(34)\}, \qquad x_{max} \in \{x(10), \ldots, x(4)\}. \tag{H.37}$$

The numerical results are depicted in subsection in tables H.19 to H.23, where we only show the results with $\chi^2/\text{d.o.f} \leq 2.0$ and relative error smaller than 50%. Note, that for the datasets A7 (and A5 as well), we obtain somewhat odd fit results, see table H.21 for the last fit function M_3^δ. Because of over fitting, for some of the fits the parameter c_1 changes the sign. This indicates that those fits converged to a different area in parameter space. This is normally not a problem, however, to obtain reliable results after model averaging the fit parameters need to be somewhat consistent. Consequently, we discard the fits in A5 and A7 which have negative values for c_1 and proceed to average the remaining ones.

After Bayesian model averaging we end up with the values for $\{c_0, c_1\}$ in table H.24, where the last column shows the results for each dataset after performing systematic averaging. The last column will be used for the extraction of $a_0 m_\pi$ and $r_0 m_\pi$, yielding the very final results, which have been presented in section 5.5 and are summarized in table H.25.

To make predictions for the 3-pion ground state energy, we must restrict ourselves to a single final fit for $\delta(x)$, which will be used to solve the 3-particle quantization conditions. This is needed to correctly take into account correlations between the fit parameters. Since we want to describe as much of the data as possible, we fix the lower bound of the fits to $x_{min} = x(L = 40)$ and choose the upper bound of the fit range $x_{max} = x(L)$ as large as possible, i.e. we choose L as small as possible. Next, we choose between the three fit models and we take the one which allows us to describe the data with a reasonable χ^2 and the smallest number of parameters. For the 5 datasets the following fits have been used:

$$\text{A3} \sim \mathrm{M}_3^\delta(x, c_0, c_1, c_2, c_3), \quad \text{with} \quad [x_{min}, x_{max}] = [x(40), x(6)], \tag{H.38}$$

$$\text{A5} \sim \mathrm{M}_2^\delta(x, c_0, c_1, c_2), \quad \text{with} \quad [x_{min}, x_{max}] = [x(40), x(8)], \tag{H.39}$$

$$\text{A7} \sim \mathrm{M}_2^\delta(x, c_0, c_1, c_2), \quad \text{with} \quad [x_{min}, x_{max}] = [x(40), x(8)], \tag{H.40}$$

$$\text{B5} \sim \mathrm{M}_2^\delta(x, c_0, c_1, c_2), \quad \text{with} \quad [x_{min}, x_{max}] = [x(40), x(6)], \tag{H.41}$$

$$\text{B7} \sim \mathrm{M}_2^\delta(x, c_0, c_1, c_2), \quad \text{with} \quad [x_{min}, x_{max}] = [x(40), x(6)], \tag{H.42}$$

as a result we obtain the fit results depicted in table H.26. Remarkably, almost the full range of data points, that is between 17 and 18 data points, can be described using the presented fit models with 3 and 4 fit parameters only.

c_0	c_1	c_2	c_3	fit range	χ^2/d.o.f	ndof
0.289(18)	0.226(41)	-	-	40 - 16	1.51	11
0.303(14)	0.178(21)	-	-	40 - 14	1.52	12
0.326(12)	0.129(12)	-	-	40 - 12	1.84	13
0.3398(80)	0.1108(53)	-	-	40 - 10	1.87	14
0.298(18)	0.208(41)	-	-	38 - 16	1.38	10
0.310(15)	0.168(21)	-	-	38 - 14	1.36	11
0.332(12)	0.124(12)	-	-	38 - 12	1.61	12
0.3426(80)	0.1089(53)	-	-	38 - 10	1.60	13
0.3628(34)	0.09131(80)	-	-	38 - 6	1.99	15
0.302(19)	0.200(42)	-	-	36 - 16	1.46	9
0.314(15)	0.163(22)	-	-	36 - 14	1.40	10
0.334(12)	0.121(13)	-	-	36 - 12	1.62	11
0.3440(80)	0.1079(53)	-	-	36 - 10	1.58	12
0.3630(34)	0.09124(80)	-	-	36 - 6	1.95	14
0.308(19)	0.189(42)	-	-	34 - 16	1.45	8
0.318(15)	0.157(22)	-	-	34 - 14	1.36	9
0.337(12)	0.118(13)	-	-	34 - 12	1.54	10
0.3456(80)	0.1068(53)	-	-	34 - 10	1.47	11
0.3642(51)	0.0907(20)	-	-	34 - 8	1.98	12
0.3633(34)	0.09117(80)	-	-	34 - 6	1.83	13
0.306(15)	0.190(30)	-0.04(1)	-	40 - 10	1.57	13
0.323(11)	0.147(12)	-0.016(3)	-	40 - 8	1.60	14
0.314(16)	0.176(30)	-0.03(1)	-	38 - 10	1.40	12
0.327(11)	0.142(12)	-0.014(3)	-	38 - 8	1.39	13
0.3573(42)	0.0960(15)	-0.0008(1)	-	38 - 4	1.95	15
0.317(16)	0.169(31)	-0.03(1)	-	36 - 10	1.43	11
0.329(11)	0.139(12)	-0.014(3)	-	36 - 8	1.39	12
0.3576(42)	0.0958(15)	-0.0008(1)	-	36 - 4	1.93	14
0.332(11)	0.136(12)	-0.013(3)	-	34 - 8	1.31	11
0.3581(41)	0.0957(15)	-0.0008(1)	-	34 - 4	1.82	13
0.253(23)	0.480(96)	-0.4(1)	0.13(4)	40 - 10	1.12	12
0.295(18)	0.238(44)	-0.09(3)	0.016(7)	40 - 8	1.46	13
0.313(12)	0.176(18)	-0.038(8)	0.0047(10)	40 - 6	1.48	14
0.265(24)	0.437(100)	-0.4(1)	0.12(4)	38 - 10	1.05	11
0.318(12)	0.168(18)	-0.035(8)	0.0043(10)	38 - 6	1.29	13
0.270(25)	0.42(10)	-0.3(1)	0.11(4)	36 - 10	1.12	10
0.321(12)	0.164(18)	-0.033(8)	0.0042(10)	36 - 6	1.30	12
0.277(25)	0.39(10)	-0.3(1)	0.10(4)	34 - 10	1.12	9
0.324(12)	0.160(18)	-0.031(8)	0.0039(10)	34 - 6	1.24	11

Table H.19: Fits for the scattering phase shift $\delta(x)$, for the 3 fit models M_1^δ,M_2^δ,M_3^δ (dataset A3). We only show the fits with χ^2/d.o.f. ≤ 2.0 and where the relative errors of the fit parameters are less than 50%.

c_0	c_1	c_2	c_3	fit range	χ^2/d.o.f	ndof
0.3953(55)	0.0199(47)	-	-	40 - 14	1.48	12
0.3865(40)	0.0294(23)	-	-	40 - 12	1.62	13
0.3952(55)	0.0200(47)	-	-	38 - 14	1.60	11
0.3864(40)	0.0294(23)	-	-	38 - 12	1.74	12
0.3941(56)	0.0209(48)	-	-	36 - 14	1.51	10
0.3859(40)	0.0298(23)	-	-	36 - 12	1.63	11
0.3934(56)	0.0215(48)	-	-	34 - 14	1.54	9
0.3856(40)	0.0300(23)	-	-	34 - 12	1.64	10
0.3859(37)	0.0262(24)	0.0026(4)	-	40 - 8	1.63	14
0.3859(37)	0.0263(24)	0.0026(4)	-	38 - 8	1.75	13
0.3854(37)	0.0266(24)	0.0026(4)	-	36 - 8	1.64	12
0.3850(37)	0.0268(24)	0.0026(4)	-	34 - 8	1.65	11
0.3912(43)	0.0181(36)	0.0060(9)	-0.00040(7)	40 - 6	1.43	14
0.3911(43)	0.0182(36)	0.0060(9)	-0.00040(7)	38 - 6	1.54	13
0.3905(43)	0.0188(36)	0.0058(9)	-0.00039(7)	36 - 6	1.43	12
0.3900(43)	0.0191(36)	0.0057(9)	-0.00038(7)	34 - 6	1.44	11

Table H.20: Fits for the scattering phase shift $\delta(x)$, for the 3 fit models M_1^δ,M_2^δ,M_3^δ (dataset A5). We only show the fits with χ^2/d.o.f. ≤ 2.0 and where the relative errors of the fit parameters are less than 50%. Note, that dataset A5 also has some fits of M_3^δ with negative values for c_1. However, since the relative errors were large enough they do not show here. Those fits will not be used for the model averaging procedure.

c_0	c_1	c_2	c_3	fit range	χ^2/d.o.f	ndof
0.3840(33)	0.0130(19)	-	-	40 - 14	1.04	12
0.3760(27)	0.0194(11)	-	-	40 - 12	1.86	13
0.3839(33)	0.0130(19)	-	-	38 - 14	1.12	11
0.3759(27)	0.0194(11)	-	-	38 - 12	1.99	12
0.3835(33)	0.0133(19)	-	-	36 - 14	1.17	10
0.3895(42)	0.0067(33)	-	-	34 - 16	0.89	8
0.3834(33)	0.0134(19)	-	-	34 - 14	1.25	9
0.3865(37)	0.0063(30)	0.0034(6)	-	40 - 10	0.97	13
0.3770(28)	0.0165(15)	0.0012(2)	-	40 - 8	1.76	14
0.3864(37)	0.0063(30)	0.0033(6)	-	38 - 10	1.03	12
0.3769(28)	0.0166(15)	0.0012(2)	-	38 - 8	1.87	13
0.3859(37)	0.0067(30)	0.0033(6)	-	36 - 10	1.08	11
0.3766(28)	0.0168(15)	0.0012(2)	-	36 - 8	1.93	12
0.3857(37)	0.0068(30)	0.0033(6)	-	34 - 10	1.15	10
0.4027(58)	-0.0252(94)	0.019(5)	-0.0022(6)	40 - 10	0.37	12
0.3811(31)	0.0117(21)	0.0027(4)	-0.00013(2)	40 - 6	1.38	14
0.4025(59)	-0.0250(95)	0.019(5)	-0.0021(6)	38 - 10	0.40	11
0.3810(31)	0.0117(21)	0.0027(4)	-0.00013(2)	38 - 6	1.46	13
0.4021(60)	-0.0244(97)	0.019(5)	-0.0021(6)	36 - 10	0.43	10
0.3806(32)	0.0120(21)	0.0026(4)	-0.00012(2)	36 - 6	1.51	12
0.4018(60)	-0.0240(98)	0.018(5)	-0.0021(6)	34 - 10	0.47	9
0.3805(31)	0.0121(21)	0.0026(4)	-0.00012(2)	34 - 6	1.61	11

Table H.21: Fits for the scattering phase shift $\delta(x)$, for the 3 fit models M_1^δ,M_2^δ,M_3^δ (dataset A7). We only show the fits with χ^2/d.o.f. ≤ 2.0 and where the relative errors of the fit parameters are less than 50%. Note, that for the fit model M_3^δ we do have some fits with negative values of c_1 showing up here. These fits will not be considered for the model averaging procedure, we just show them for the sake of completeness.

c_0	c_1	c_2	c_3	fit range	χ^2/d.o.f	ndof
0.3755(94)	0.0182(27)	-	-	40 - 16	1.33	11
0.3777(80)	0.0173(19)	-	-	40 - 14	1.23	12
0.3798(60)	0.01652(91)	-	-	40 - 12	1.14	13
0.3727(45)	0.01827(42)	-	-	40 - 10	1.29	14
0.3743(95)	0.0186(27)	-	-	38 - 16	1.39	10
0.3769(80)	0.0175(19)	-	-	38 - 14	1.28	11
0.3794(59)	0.01659(91)	-	-	38 - 12	1.19	12
0.3725(45)	0.01830(42)	-	-	38 - 10	1.33	13
0.3762(96)	0.0180(28)	-	-	36 - 16	1.46	9
0.3782(81)	0.0171(19)	-	-	36 - 14	1.33	10
0.3802(59)	0.01646(91)	-	-	36 - 12	1.22	11
0.3728(45)	0.01825(42)	-	-	36 - 10	1.39	12
0.3759(96)	0.0181(28)	-	-	34 - 16	1.64	8
0.3781(80)	0.0172(19)	-	-	34 - 14	1.47	9
0.3801(59)	0.01647(91)	-	-	34 - 12	1.34	10
0.3728(44)	0.01826(42)	-	-	34 - 10	1.51	11
0.3842(82)	0.0136(24)	0.0004(2)	-	40 - 10	1.21	13
0.3843(58)	0.0135(10)	0.00039(5)	-	40 - 8	1.12	14
0.3756(43)	0.01612(45)	0.00024(1)	-	40 - 6	1.32	15
0.3839(58)	0.0136(10)	0.00038(5)	-	38 - 8	1.17	13
0.3753(42)	0.01615(45)	0.00024(1)	-	38 - 6	1.37	14
0.3850(83)	0.0133(25)	0.0004(2)	-	36 - 10	1.28	11
0.3847(58)	0.0134(10)	0.00039(5)	-	36 - 8	1.18	12
0.3757(42)	0.01610(45)	0.00024(1)	-	36 - 6	1.42	13
0.3850(83)	0.0133(25)	0.0004(2)	-	34 - 10	1.41	10
0.3847(58)	0.0134(10)	0.00039(5)	-	34 - 8	1.28	11
0.3756(42)	0.01611(45)	0.00024(1)	-	34 - 6	1.53	12
0.3867(67)	0.0121(15)	0.0006(1)	-0.000008(3)	40 - 6	1.14	14
0.3830(46)	0.01345(61)	0.00047(3)	-0.0000054(3)	40 - 4	1.09	15
0.3862(67)	0.0122(15)	0.0006(1)	-0.000008(3)	38 - 6	1.19	13
0.3828(46)	0.01349(61)	0.00047(3)	-0.0000054(3)	38 - 4	1.13	14
0.3874(67)	0.0119(16)	0.0006(1)	-0.000009(3)	36 - 6	1.19	12
0.3833(46)	0.01341(61)	0.00048(3)	-0.0000055(3)	36 - 4	1.15	13
0.3873(66)	0.0119(16)	0.0006(1)	-0.000009(3)	34 - 6	1.30	11
0.3832(46)	0.01341(60)	0.00048(3)	-0.0000055(3)	34 - 4	1.24	12

Table H.22: Fits for the scattering phase shift $\delta(x)$, for the 3 fit models M_1^δ,M_2^δ,M_3^δ (dataset B5). We only show the fits with χ^2/d.o.f. ≤ 2.0 and where the relative errors of the fit parameters are less than 50%.

c_0	c_1	c_2	c_3	fit range	χ^2/d.o.f	ndof
0.370(10)	0.0111(18)	-	-	40 - 16	0.18	11
0.3712(90)	0.0107(12)	-	-	40 - 14	0.17	12
0.3700(79)	0.01108(74)	-	-	40 - 12	0.16	13
0.3657(68)	0.01209(45)	-	-	40 - 10	0.29	14
0.3555(57)	0.01390(22)	-	-	40 - 8	1.35	15
0.371(10)	0.0109(18)	-	-	38 - 16	0.19	10
0.3716(89)	0.0106(11)	-	-	38 - 14	0.17	11
0.3703(78)	0.01105(73)	-	-	38 - 12	0.17	12
0.3658(67)	0.01208(44)	-	-	38 - 10	0.31	13
0.3555(57)	0.01390(22)	-	-	38 - 8	1.44	14
0.372(10)	0.0106(18)	-	-	36 - 16	0.15	9
0.3725(88)	0.0104(11)	-	-	36 - 14	0.14	10
0.3708(77)	0.01096(72)	-	-	36 - 12	0.14	11
0.3662(66)	0.01205(44)	-	-	36 - 10	0.30	12
0.3556(56)	0.01389(22)	-	-	36 - 8	1.55	13
0.373(10)	0.0104(18)	-	-	34 - 16	0.14	8
0.3730(87)	0.0104(11)	-	-	34 - 14	0.13	9
0.3711(76)	0.01091(70)	-	-	34 - 12	0.14	10
0.3663(66)	0.01203(43)	-	-	34 - 10	0.32	11
0.3556(55)	0.01389(21)	-	-	34 - 8	1.68	12
0.3738(98)	0.0090(18)	0.0002(1)	-	40 - 10	0.18	13
0.3745(82)	0.0087(10)	0.00023(4)	-	40 - 8	0.16	14
0.3682(67)	0.01055(50)	0.00015(1)	-	40 - 6	0.34	15
0.3743(97)	0.0088(18)	0.0002(1)	-	38 - 10	0.18	12
0.3747(81)	0.0087(10)	0.00024(4)	-	38 - 8	0.16	13
0.3684(66)	0.01054(50)	0.00015(1)	-	38 - 6	0.36	14
0.3755(96)	0.0085(18)	0.00024(10)	-	36 - 10	0.13	11
0.3755(80)	0.00852(99)	0.00024(4)	-	36 - 8	0.12	12
0.3687(65)	0.01050(49)	0.00015(1)	-	36 - 6	0.35	13
0.3762(94)	0.0083(17)	0.00025(10)	-	34 - 10	0.12	10
0.3759(79)	0.00844(98)	0.00025(4)	-	34 - 8	0.11	11
0.3688(65)	0.01048(48)	0.00015(1)	-	34 - 6	0.37	12
0.3761(90)	0.0078(14)	0.00035(8)	-0.000004(1)	40 - 6	0.18	14
0.3738(71)	0.00862(66)	0.00029(2)	-0.0000027(2)	40 - 4	0.18	15
0.3765(89)	0.0077(14)	0.00036(8)	-0.000004(1)	38 - 6	0.18	13
0.3740(70)	0.00859(65)	0.00029(2)	-0.0000027(2)	38 - 4	0.19	14
0.3775(88)	0.0075(14)	0.00037(8)	-0.000004(1)	36 - 6	0.13	12
0.3745(70)	0.00852(64)	0.00029(2)	-0.0000027(2)	36 - 4	0.15	13
0.3780(87)	0.0073(14)	0.00038(8)	-0.000004(1)	34 - 6	0.12	11
0.3747(69)	0.00848(63)	0.00029(2)	-0.0000027(2)	34 - 4	0.15	12

Table H.23: Fits for the scattering phase shift $\delta(x)$, for the 3 fit models M_1^δ,M_2^δ,M_3^δ (dataset B7). We only show the fits with χ^2/d.o.f. ≤ 2.0 and where the relative errors of the fit parameters are less than 50%.

Dataset	c_0 from M_1^δ	c_0 from M_2^δ	c_0 from M_3^δ	Final result for c_0
A3	0.319(24)	0.324(16)	0.282(34)	0.318(25)
A5	0.3914(67)	0.3856(37)	0.3907(44)	0.3883(53)
A7	0.3846(40)	0.3863(38)	0.3810(31)	0.3835(43)
B5	0.3771(70)	0.3825(70)	0.3842(56)	0.3817(71)
B7	0.3687(81)	0.3726(85)	0.3747(77)	0.3721(85)
Dataset	c_1 from M_1^δ	c_1 from M_2^δ	c_1 from M_3^δ	Final result for c_1
A3	0.156(46)	0.151(28)	0.35(16)	0.157(51)
A5	0.0240(61)	0.0265(25)	0.0186(38)	0.0241(48)
A7	0.0123(31)	0.0064(31)	0.0118(21)	0.0106(35)
B5	0.0173(15)	0.0140(17)	0.0130(12)	0.0145(23)
B7	0.0114(10)	0.0093(14)	0.0083(10)	0.0098(18)

Table H.24: Results for c_0 and c_1 after performing Bayesian model averaging for the three fitting functions separately. The last column denotes the results after the systematic averaging.

Dataset	c_0	$a_0 m_\pi$	c_1	$r_0 m_\pi$
A3	0.318(25)	3.147(80)	0.157(51)	0.31(10)
A5	0.3883(53)	2.576(14)	0.0241(48)	0.0482(96)
A7	0.3835(43)	2.607(11)	0.0106(35)	0.0212(71)
B5	0.3817(71)	2.620(19)	0.0145(23)	0.0290(46)
B7	0.3721(85)	2.688(23)	0.0098(18)	0.0195(35)

Table H.25: Summary of all the extracted parameters after taking the systematic average.

Dataset	c_0	c_1	c_2	c_3	fit range	χ^2/d.o.f	ndof
A3	0.313(12)	0.176(18)	-0.0379(77)	0.00473(97)	40 - 6	1.48	14
A5	0.3859(37)	0.0262(24)	0.00265(39)	N/A	40 - 8	1.63	14
A7	0.3770(28)	0.0165(15)	0.00120(18)	N/A	40 - 8	1.76	14
B5	0.3756(43)	0.01612(45)	0.000240(14)	N/A	40 - 6	1.32	15
B7	0.3682(67)	0.01055(50)	0.000147(13)	N/A	40 - 6	0.34	15

Table H.26: Choice of the best fits for each dataset. For dataset A3 we choose the fit model given by M_3^δ, while for all other datasets M_2^δ is being used.

H.6 Calculation 3-pion ground state energy $E^{\delta}_{3\pi}$ based on $\delta(k)$

In order to make predictions for the 3-pion ground state energy $E^{\delta}_{3\pi}$ we first want to establish the needed measurements. For each dataset we require the following quantities

- The model-independent infinite volume pion mass m_π, extracted in section H.3.
- The best model-fit for the scattering phase shift $\delta(x)$, with $x = \frac{k}{m_\pi}$, which is needed to solve the 3-particle quantization conditions. These fits have been discussed in section H.5 and are given in table H.26.

As explained in section 5.7, we use the pion mass m_π and the scattering phase shift $\delta(x)$ to solve the quantization conditions in the center of mass frame, that is

$$\cot\left(\delta\left(\frac{x}{2}\right) + \delta(x)\right) + \cot\left(\frac{x \cdot (m_\pi L)}{2}\right) = 0, \quad \text{with} \quad x = \frac{k}{m_\pi}. \tag{H.43}$$

Note that due to the periodicity of the cotangens, there are several solutions for x, which solve the quantization condition. Since we are looking for the smallest possible 3-pion ground state energy $E^{\delta}_{3\pi}$, we start with the largest volume $m_\pi L^{max}$ and choose the smallest solution x of the quantization condition. Next, we continuously decrease the volume $m_\pi L$, such that also the solutions for the quantization condition vary continuously. This allows us to predict the 3-pion ground state energies $E^{\delta}_{3\pi}$ in a consistent well-behaved way. In the end we obtain the solutions presented in figure 5.15 and 5.16.

Bibliography

[1] J. N. Guenther, *Overview of the qcd phase diagram: Recent progress from the lattice*, *Eur. Phys. J. A* **57** (2021) 136, [2010.15503].

[2] A. Hasenfratz and D. Toussaint, *Canonical ensembles and nonzero density quantum chromodynamics*, *Nucl. Phys. B* **371** (1992) 539–549.

[3] S. Kratochvila and P. de Forcrand, *The Canonical approach to finite density QCD*, *PoS* **LAT2005** (2006) 167, [hep-lat/0509143].

[4] Z. Fodor, K. K. Szabo and B. C. Toth, *Hadron spectroscopy from canonical partition functions*, *JHEP* **08** (2007) 092, [0704.2382].

[5] A. Alexandru, M. Faber, I. Horvath and K.-F. Liu, *Lattice QCD at finite density via a new canonical approach*, *Phys. Rev. D* **72** (2005) 114513, [hep-lat/0507020].

[6] K. Steinhauer and U. Wenger, *Loop formulation of supersymmetric Yang-Mills quantum mechanics*, *JHEP* **12** (2014) 044, [1410.0235].

[7] A. Alexandru, G. Bergner, D. Schaich and U. Wenger, *Solution of the sign problem in the Potts model at fixed fermion number*, *Phys. Rev. D* **97** (2018) 114503, [1712.07585].

[8] S. Burri and U. Wenger, *The Hubbard model in the canonical formulation*, *PoS* **LATTICE2019** (2019) 249, [1912.09361].

[9] U. Wenger and P. Bühlmann, *Heavy-dense QCD at fixed baryon number without a sign problem*, *PoS* **LATTICE2021** (2022) 584, [2110.15021].

[10] A. Alexandru and U. Wenger, *QCD at non-zero density and canonical partition functions with Wilson fermions*, *Phys. Rev. D* **83** (2011) 034502, [1009.2197].

[11] J. S. Schwinger, *Gauge Invariance and Mass*, *Phys. Rev.* **125** (1962) 397–398.

[12] J. S. Schwinger, *Gauge Invariance and Mass. 2.*, *Phys. Rev.* **128** (1962) 2425–2429.

[13] S. Coleman, R. Jackiw and L. Susskind, *Charge shielding and quark confinement in the massive schwinger model*, *Annals of Physics* **93** (1975) 267 – 275.

[14] S. Coleman, *More about the massive schwinger model*, *Annals of Physics* **101** (1976) 239 – 267.

[15] W. Detmold, M. J. Savage, A. Torok, S. R. Beane, T. C. Luu, K. Orginos et al., *Multi-Pion States in Lattice QCD and the Charged-Pion Condensate*, *Phys. Rev. D* **78** (2008) 014507, [0803.2728].

[16] H. J. Rothe, K. D. Rothe and J. A. Swieca, *Screening versus confinement*, *Phys. Rev. D* **19** (May, 1979) 3020–3023.

[17] S. Coleman, *Quantum sine-gordon equation as the massive thirring model*, *Phys. Rev. D* **11** (Apr, 1975) 2088–2097.

[18] S. Durr and C. Hoelbling, *Staggered versus overlap fermions: A Study in the Schwinger model with N(f)=0, 1, 2*, *Phys. Rev. D* **69** (2004) 034503, [hep-lat/0311002].

[19] S. Elser, *The Local bosonic algorithm applied to the massive Schwinger model*, hep-lat/0103035.

[20] M. Luz, *Cutoff effects of wilson fermions in the absence of spontaneous chiral symmetry breaking*, Master's thesis, Humboldt-Universität zu Berlin, Mathematisch-Naturwissenschaftliche Fakultät I, 2006. http://dx.doi.org/10.18452/14059.

[21] C. Gutsfeld, H. A. Kastrup and K. Stergios, *Mass spectrum and elastic scattering in the massive SU(2)(f) Schwinger model on the lattice*, *Nucl. Phys. B* **560** (1999) 431–464, [hep-lat/9904015].

[22] R. F. Dashen, B. Hasslacher and A. Neveu, *Particle spectrum in model field theories from semiclassical functional integral techniques*, *Phys. Rev. D* **11** (Jun, 1975) 3424–3450.

[23] M. E. Peskin and D. V. Schroeder, *An Introduction to quantum field theory*. Addison-Wesley, Reading, USA, 1995.

[24] H. J. Rothe, *Lattice Gauge Theories : An Introduction (Fourth Edition)*, vol. 43. World Scientific Publishing Company, 2012, 10.1142/8229.

[25] H. Nielsen and M. Ninomiya, *A no-go theorem for regularizing chiral fermions*, *Physics Letters B* **105** (1981) 219 – 223.

[26] I. Hip, C. B. Lang and R. Teppner, *Chiral symmetry in the two flavor lattice Schwinger model*, *Nucl. Phys. B Proc. Suppl.* **63** (1998) 682–684, [hep-lat/9709030].

[27] M. Lüscher and U. Wolff, *How to calculate the elastic scattering matrix in two-dimensional quantum field theories by numerical simulation*, *Nuclear Physics B* **339** (1990) 222 – 252.

[28] M. Lüscher, *Volume dependence of the energy spectrum in massive quantum field theories*, *Communications in Mathematical Physics* **104** (Jun, 1986) 177–206.

[29] M. Lüscher, *On a Relation Between Finite Size Effects and Elastic Scattering Processes*. Springer US, Boston, MA, 1984, 10.1007/978-1-4757-0280-4_15.

[30] D. Delphenich, J. Schechter and S. Vaidya, *Pion pion scattering in two-dimensions*, *Phys. Rev. D* **59** (1999) 056004, [hep-ph/9806349].

[31] D. Delphenich and J. Schechter, *Multiflavor massive Schwinger model with nonAbelian bosonization*, *Int. J. Mod. Phys. A* **12** (1997) 5305–5324, [hep-th/9703120].

[32] E. Witten, *Nonabelian Bosonization in Two-Dimensions*, *Commun. Math. Phys.* **92** (1984) 455–472.

[33] D. J. Griffiths and D. F. Schroeter, *Introduction to quantum mechanics; 3rd ed.* Cambridge University Press, Cambridge, Jul, 2018.

[34] M. Luscher, *Volume Dependence of the Energy Spectrum in Massive Quantum Field Theories. 2. Scattering States*, *Commun. Math. Phys.* **105** (1986) 153–188.

[35] P. Guo, *One spatial dimensional finite volume three-body interaction for a short-range potential*, *Phys. Rev. D* **95** (2017) 054508, [1607.03184].

[36] P. Guo and T. Morris, *Multiple-particle interaction in (1+1)-dimensional lattice model*, *Phys. Rev. D* **99** (2019) 014501, [1808.07397].

[37] J. H. Eberly, *Quantum scattering theory in one dimension*, *American Journal of Physics* **33** (1965) 771–773.

[38] V. E. Barlette, M. M. Leite and S. K. Adhikari, *Quantum scattering in one dimension*, *European Journal of Physics* **21** (aug, 2000) 435–440.

[39] V. E. Barlette, M. M. Leite and S. K. Adhikari, *Integral equations of scattering in one dimension*, *American Journal of Physics* **69** (2001) 1010–1013.

[40] H. A. Bethe, *Theory of the Effective Range in Nuclear Scattering*, *Phys. Rev.* **76** (1949) 38–50.

[41] J. D. Jackson and J. M. Blatt, *The interpretation of low energy proton-proton scattering*, *Rev. Mod. Phys.* **22** (Jan, 1950) 77–118.

[42] T. Ohmura, Y. Hara and T. Yamanouchi, *Low Energy Electron-Hydrogen Scattering*, *Progress of Theoretical Physics* **20** (07, 1958) 82–88.

[43] C. Gattringer and C. B. Lang, *Quantum chromodynamics on the lattice*, vol. 788. Springer, Berlin, 2010, 10.1007/978-3-642-01850-3.

[44] C. Panagiotakopoulos, *Topology of 2d lattice gauge fields*, *Nuclear Physics B* **251** (1985) 61–76.

[45] M. Luscher, *Topology of Lattice Gauge Fields*, *Commun. Math. Phys.* **85** (1982) 39–48.

[46] W. Bietenholz, *Hadron Physics from Lattice QCD*, *Int. J. Mod. Phys. E* **25** (2016) 1642008, [1605.08103].

[47] M. Luscher and S. Schaefer, *Lattice QCD without topology barriers*, *JHEP* **07** (2011) 036, [1105.4749].

[48] D. A. Carsten Urbach, "Hybrid-monte carlo for the schwinger model." https://github.com/urbach/schwinger.

[49] F. Bruckmann, C. Gattringer, T. Kloiber and T. Sulejmanpasic, *Grand Canonical Ensembles, Multiparticle Wave Functions, Scattering Data, and Lattice Field Theories*, *Phys. Rev. Lett.* **115** (2015) 231601, [1509.05189].

[50] F. Romero-López, A. Rusetsky and C. Urbach, *Two- and three-body interactions in φ^4 theory from lattice simulations*, *Eur. Phys. J. C* **78** (2018) 846, [1806.02367].

[51] R. A. Horn and C. R. Johnson, *Matrix Analysis*. Cambridge University Press, 1990.

[52] A. Wipf, *Statistical Approach to Quantum Field Theory: An Introduction*, vol. 992 of *Lecture Notes in Physics*. 10, 2021, 10.1007/978-3-030-83263-6.

[53] P. Hasenfratz and F. Karsch, *Chemical Potential on the Lattice*, *Phys. Lett. B* **125** (1983) 308–310.

[54] D. Dummit and R. Foote, *Abstract Algebra*. Wiley, 2003.

[55] P. Cameron, S. Cameron, J. Bruce and C. Series, *Permutation Groups*. London Mathematical Society Student Texts. Cambridge University Press, 1999.

[56] K. Binder and D. P. Landau, *A Guide to Monte Carlo Simulations in Statistical Physics*. Cambridge University Press, 2 ed., 2000.

[57] B. Efron and R. J. Tibshirani, *An Introduction to the Bootstrap*. No. 57 in Monographs on Statistics and Applied Probability. Chapman & Hall/CRC, Boca Raton, Florida, USA, 1993.

[58] R. Iwami, S. Ejiri, K. Kanaya, Y. Nakagawa, D. Yamamoto and T. Umeda, *Multipoint reweighting method and its applications to lattice QCD*, *Phys. Rev. D* **92** (2015) 094507, [1508.01747].

[59] D. Bailey, *Mpfun2015: A thread-safe arbitrary precision computation package (full documentation)*, 2015.

[60] D. S. Sivia and J. Skilling, *Data Analysis - A Bayesian Tutorial*. Oxford Science Publications. Oxford University Press, 2nd ed., 2006.

[61] S. Konishi and G. Kitagawa, *Information Criteria and Statistical Modeling*. Springer series in statistics. Springer, 2008.

[62] W. I. Jay and E. T. Neil, *Bayesian model averaging for analysis of lattice field theory results*, *Phys. Rev. D* **103** (2021) 114502, [2008.01069].

[63] G. P. Lepage, B. Clark, C. T. H. Davies, K. Hornbostel, P. B. Mackenzie, C. Morningstar et al., *Constrained curve fitting*, *Nucl. Phys. B Proc. Suppl.* **106** (2002) 12–20, [hep-lat/0110175].

[64] Extended Twisted Mass collaboration, C. Alexandrou et al., *Quark masses using twisted-mass fermion gauge ensembles*, *Phys. Rev. D* **104** (2021) 074515, [2104.13408].

[65] European Twisted Mass collaboration, N. Carrasco et al., *Up, down, strange and charm quark masses with N_f = 2+1+1 twisted mass lattice QCD*, *Nucl. Phys. B* **887** (2014) 19–68, [1403.4504].

[66] R. Gradshteyn, *Table of integrals, series, and products.* Academic Press, New York, 5 ed., 1996.

[67] W. Press, S. Teukolsky, W. Vetterling and B. Flannery, *Numerical Recipes: The Art of Scientific Computing.* Cambridge University Press, 3 ed., 2007.

Selbstständigkeitserklärung

gemäss Art. 18 PromR Phil.-nat. 2019

Name/Vorname: Bühlmann Patrick

Matrikelnummer: 13-101-126

Studiengang: Theoretische Physik, Doktorat
Bachelor ☐ Master ☐ Dissertation ☒

Titel der Arbeit: The Schwinger model in the canonical formulation
Leiter der Arbeit: Prof. Dr. Urs Wenger

Ich erkläre hiermit, dass ich diese Arbeit selbständig verfasst und keine anderen als die angegebenen Quellen benutzt habe. Alle Stellen, die wörtlich oder sinngemäss aus Quellen entnommen wurden, habe ich als solche gekennzeichnet. Mir ist bekannt, dass andernfalls der Senat gemäss Artikel 36 Absatz 1 Buchstabe r des Gesetzes über die Universität vom 5. September 1996 und Artikel 69 des Universitätsstatuts vom 7. Juni 2011 zum Entzug des Doktortitels berechtigt ist. Für die Zwecke der Begutachtung und der Überprüfung der Einhaltung der Selbständigkeitserklärung bzw. der Reglemente betreffend Plagiate erteile ich der Universität Bern das Recht, die dazu erforderlichen Personendaten zu bearbeiten und Nutzungshandlungen vorzunehmen, insbesondere die Doktorarbeit zu vervielfältigen und dauerhaft in einer Datenbank zu speichern sowie diese zur Überprüfung von Arbeiten Dritter zu verwenden oder hierzu zur Verfügung zu stellen.

Datum/Ort: 5. Juli 2022
3012 Bern

Unterschrift:

Bühlmann Patrick